

Ghent University
Department of Physics and Astronomy

Real-space Renormalization Group Methods in the Age of Tensor Network States

Matthias Bal

Dissertation submitted in fulfillment of the requirements for the degree of
Doctor (PhD) in Science: Physics



Academic year: 2017-2018

Supervisor

Prof. Dr. Frank Verstraete

Co-supervisor

Prof. Dr. Jutho Haegeman

Members of the examination committee

Prof. Dr. Jérôme Dubail (Université de Lorraine)

Prof. Dr. Glen Evenbly (Université de Sherbrooke)

Prof. Dr. Jan Ryckebusch (Ghent University)

Prof. Dr. Dimitri Van Neck (Ghent University)

Dr. Karel Van Acoleyen (Ghent University)

Preface

This dissertation contributes to the ongoing effort of understanding the origins and applications of real-space renormalization group methods in tensor network representations of classical and quantum many-body systems.

First, we construct a matrix product operator ansatz to coarse-grain real-space transfer matrices of matrix product state descriptions of one-dimensional quantum spin chains. By treating the physical spin as an impurity, we unravel the virtual entanglement degrees of freedom of matrix product states into a layered structure to reveal an inherent renormalization group scale [1].

Secondly, we rephrase tensor network renormalization for two-dimensional classical lattice models in a manifestly nonnegative way. The resulting real-space renormalization group flow preserves positivity and hence yields an interpretation in terms of Hamiltonian flows, reconciling modern real-space tensor network renormalization methods with traditional block-spin approaches [2].

Thirdly, we study non-local symmetries in tensor networks by expressing two-dimensional classical partition functions in terms of strange correlators of judiciously chosen product states and string-net wave functions [3]. We exhibit and exploit the emerging non-local symmetries of the partition function at criticality and highlight parallels between topological sectors and conformal primary fields in the shared framework of matrix product operator symmetries. Additionally, we provide a complementary perspective on real-space renormalization by recognizing known tensor network renormalization methods as the approximate truncation of an exactly coarse-grained strange correlator.

* * *

- M. Bal, D. J. Williamson, R. Vanhove, N. Bultinck, J. Haegeman, and F. Verstraete, “Mapping topological to conformal field theories through strange correlators”, (2018), arXiv:1801.05959
- M. Bal, M. Mariën, J. Haegeman, and F. Verstraete, “Renormalization Group Flows of Hamiltonians Using Tensor Networks”, *Physical Review Letters* **118**, 250602 (2017), arXiv:1703.00365
- M. Bal, M. M. Rams, V. Zauner, J. Haegeman, and F. Verstraete, “Matrix product state renormalization”, *Physical Review B* **94**, 1 (2016), arXiv:1509.01522

Acknowledgements

First of all, I would like to thank the Flemish, Belgian, and European people for their generous funding of basic research (not all of which is fundamental or important). Being granted time to think—and to think only—is an extraordinary privilege.

Like any work of art, a dissertation is an exercise in absurdity, restraint, acquiescence, and perseverance in the face of futility. Eventually, however, the human spirit prevails and the artist begins to dream anew. I would like to thank the members of the examination committee for their encouraging comments and careful reading of the manuscript. Any remaining errors are my own.

During the last four and a half years, I have been tremendously inspired by both of my supervisors. The contagious excitement of Frank, together with his ability to effortlessly jump between bursts of wild exaltation and sobering lucidity, has taught me the delightful freedom of doing research. I have been equally impressed by Jutho's thorough knowledge, quiet dedication, and eagerness to help at all times. I also learned to make mistakes and came to appreciate the following deep ontological statement on the nature of the physical universe: that what is physical is real only insofar as it can be put into MATLAB.

For all interactions scientific and ridiculous, I would like to thank the past and present members of the quantum crew: Alexis, Benoît, Boye, Bram, Damian, Dominic, Frank, Gertian, Jacob, James, Jonas, Jos, Jutho, Karel, Laurens, Maarten, Marek, Matthew, Matthias, Michaël, Nick, Paul, Robijn, Valentin, Vid, and Volkher. Also thanks to Inge and Gerbrand for the administrative and technical support.

To my cat Pablo and all of his feline friends for the daily interspecies communication.

To my friends and family for their interest in my well-being.

To my parents for their unconditional love and support.

To Nina, whose enthralling presence completely and utterly transcends the triteness of any academic acknowledgement. So let us stop right here and start off somewhere else.

MATTHIAS BAL
March 2018

Contents

Preface	iii
Acknowledgements	v
1 Prelude	1
1.1 General introduction	1
1.2 Overview	1
I Preliminaries	5
2 Renormalization group theory	7
2.1 Problems with many length scales	7
2.2 Collective behavior, criticality, and phase transitions	11
2.2.1 Equilibrium statistical mechanics	11
2.2.2 A selection of simple discrete and continuum models	12
2.2.3 Phase transitions and criticality	13
2.2.4 Quantum criticality and quantum-to-classical mapping	17
2.3 Scaling and homogeneity	18
2.4 Landau free energies and mean-field theory	20
2.4.1 Landau theory	21
2.4.2 Saddle point approximation and mean-field theory	22
2.4.3 The neglected importance of fluctuations on all scales	25
2.4.4 Mean-field theory and anomalous dimensions	26
2.4.5 Symmetry-breaking phases	27
2.5 Renormalization: concepts and ideas	29
2.5.1 Kadanoff's block-spin renormalization group	29
2.5.2 Manifolds and flows	31
2.5.3 Fixed points and universality	34
2.6 Scaling behavior and critical exponents	38
2.6.1 Scaling of free energy	38
2.6.2 Scaling of correlation functions	39
2.6.3 Critical exponents from RG eigenvalues	41
2.6.4 Scaling operators and scaling dimensions	41

2.7	Perturbative RG and effective field theories	42
2.7.1	Universality in quantum field theories	43
2.7.2	The Gaussian fixed point	44
2.7.3	Real-space perturbations	46
2.7.4	Perturbing the Gaussian fixed point: the ϵ -expansion	46
2.7.5	Beyond the Landau-Ginzburg paradigm	49
2.8	Operator product expansion and conformal field theory	50
2.8.1	Conformal invariance and quantum fields	50
2.8.2	The power of the Virasoro algebra	52
2.8.3	Unitary minimal models	53
2.8.4	Finite-size scaling on the cylinder	54
2.8.5	Modular invariance	54
2.8.6	Renormalization group flows and CFT	57
2.8.7	Operators on the lattice and in the continuum	57
2.9	Numerical renormalization group	58
2.10	Real-space renormalization	59
2.10.1	Kadanoff's block-spin RG	60
2.10.2	Migdal-Kadanoff bond moving approximation	64
2.10.3	Niemeijer-van Leeuwen cumulant approximation	65
3	Tensor network states	69
3.1	The renaissance of quantum entanglement	69
3.2	Matrix product states	71
3.2.1	Ansatz and properties	71
3.2.2	Transfer matrix and correlations	73
3.2.3	Renormalization by blocking	75
3.2.4	Variational optimization	77
3.3	Projected entangled pair states	78
3.3.1	Ansatz and properties	78
3.3.2	Topological order and MPO algebras	79
3.3.3	Variational optimization	79
3.4	Multi-scale entanglement renormalization ansatz	81
3.4.1	Ansatz and properties	81
3.4.2	Entanglement structure of MERA: correlations in scale space	84
3.4.3	Causal cone bounds for 1D isometric tensor networks	88
3.5	Real-space renormalization and tensor network states	90
3.5.1	Classical partition functions as tensor networks	90
3.5.2	Tensor renormalization group	92
3.5.3	Tensor network renormalization	93
3.5.4	Real-space RG in the space of tensors	97
II	Results	101
4	Matrix product state renormalization	103
4.1	Background and motivation	103

4.2	Exact and compressed MPS transfer matrices	105
4.3	Coarse-graining transfer matrices	106
4.4	From Euclidean path integral to uniform MPS	108
4.5	Structure of MPS fixed point reduced density matrices	112
4.6	Restricted variational subspaces for excitations	113
4.7	Numerical results	115
4.7.1	MPS ansatz from Wilson MPO	115
4.7.2	MPS excitation ansatz from Wilson MPO	117
4.7.3	Free fermion ansatz	118
4.8	Conclusion	121
4.9	Appendices	122
4.9.1	Path integrals, wave functions, and quantum states	122
4.9.2	Free fermion construction	123
4.9.3	Isometric MPO versus MERA	128
5	Renormalization group flows of Hamiltonians	129
5.1	Background and motivation	129
5.2	Tensor network renormalization	130
5.3	Coarse-graining nonnegative tensor networks	131
5.4	Renormalization group flow	133
5.5	Application to classical partition functions	134
5.6	Effective Hamiltonians	136
5.7	Conclusion	137
5.8	Appendices	138
5.8.1	Nonnegative matrix factorization	138
5.8.2	Details on the TNR ₊ implementation	141
5.8.3	CDL tensors and entanglement filtering	145
5.8.4	Symmetries and tensor network renormalization	146
5.8.5	Approximate scale invariance	146
5.8.6	Conformal data from tensor networks	147
6	Mapping TQFTs to CFTs through strange correlators	151
6.1	Background and motivation	151
6.2	Partition functions from strange correlators	153
6.2.1	Symmetry-enriched string-net models	153
6.2.2	Strange correlators	158
6.2.3	MPO algebra and pulling-through	163
6.2.4	Extension to other minimal models	165
6.3	Exact diagonalization and topological sectors	166
6.3.1	Motivation	166
6.3.2	Topological corrections to the conformal spin	167
6.3.3	Ocneanu's tube algebra and the anyon ansatz	169
6.3.4	Topological sectors of the Ising model	170
6.4	Coarse-graining strange correlators	174
6.4.1	Exact string-net renormalization	174
6.4.2	Coarse-graining map as a PEPO	177

6.4.3	Real-space RG and SC renormalization	179
6.4.4	Kadanoff's block-spin truncation	181
6.4.5	Tensor renormalization group (TRG)	182
6.4.6	Beyond tensor network renormalization (TNR)	183
6.5	Conclusion	184
6.6	Appendices	185
6.6.1	Kramers-Wannier duality	185
6.6.2	Explicit string-net coarse-graining gates	189
	Outlook	195

CHAPTER ONE

Prelude

“Universality makes physics possible.”

1.1 General introduction

The development of renormalization group theory by Kenneth. G. Wilson and his contemporaries in the early 1970s has arguably been one of the most influential developments in post-war theoretical physics. By focusing on theories defined at different length scales, Wilson introduced the notions of flows, fixed points, and universality to understand the behavior of physical systems under a change of scale.

Tensor network states owe their numerical origin to the astonishing accuracy of the density-matrix renormalization group algorithm for one-dimensional quantum spin chains, developed in 1992 by Steve White, a former student of Wilson. Over the years, insights from entanglement theory and condensed-matter physics have helped establish tensor networks as a natural framework for studying the physics of (quantum) many-body systems.

In this dissertation we contribute to the ongoing effort of understanding the origins and applications of real-space renormalization group methods in tensor network representations of classical and quantum many-body systems.

1.2 Overview

We have split this dissertation into two parts for the reader’s convenience. The first part consists of two preliminary chapters on renormalization group theory and tensor network states, which experts can skim-read or read selectively when referred back to from the three chapters in the second part containing our main results. The wide range of topics covered in the introductory chapters is reflective of a style which sets out to be broad and inclusive rather than deep.

Chapter 2 provides a comprehensive, pedagogic overview of renormalization group theory from the point of view of statistical physics and critical phenomena. After introducing the problems with physical systems exhibiting correlations across many length scales, we discuss phase transitions, criticality, scaling, and homogeneity. By going over Landau’s theory of symmetry breaking and its saddle-point approximation, we get an idea of why fluctuations on all length scales are troublesome for

mean-field theory and set the stage for Wilson's groundbreaking contributions to renormalization group theory. We go on to introduce the core ideas of the renormalization group: flows, fixed points, and universality. We emphasize how these insights are shared between the lattice and the continuum by discussing effective field theories and perturbative RG using the seminal example of the ϵ -expansion. We then provide a succinct introduction to conformal field theory and its relation to classical partition functions, which is of crucial importance to understand the physics of critical statistical-mechanical lattice models in two dimensions. We conclude with a sketch of Wilson's numerical renormalization group and some explicit examples of historical real-space renormalization schemes.

Chapter 3 introduces tensor network states as a *lingua franca* for understanding (quantum) many-body physics. We trace their origins to the renaissance of quantum entanglement in the nineties and discuss basic properties of matrix product states (MPS), projected-entangled pair states (PEPS), and the multi-scale entanglement renormalization ansatz (MERA). Focusing on their renormalization properties, we highlight a natural real-space RG transformation for MPS and examine the entanglement structure of scale invariant MERAs in scale space. After demonstrating how to encode classical partition functions as tensor networks, we show how real-space RG transformations on the level of tensor networks lead to numerical algorithms such as the tensor renormalization group (TRG) and tensor network renormalization (TNR) which vastly outperform the old-school methods discussed in Chapter 2. We conclude by summarizing TRG and TNR in terms of RG flows in the space of tensors.

Chapter 4 describes a matrix product operator (MPO) ansatz to coarse-grain real-space transfer matrices associated to MPS descriptions of one-dimensional quantum spin chains. We interpret MPS truncation as an application of Wilson's numerical renormalization group along the imaginary time direction appearing in the path integral representation of the quantum state. Treating the physical spin as an impurity, we identify a uniform MPS representation which takes the entanglement degrees of freedom that are relevant to the impurity into account. We numerically show that the layered decomposition of the MPS bond dimension obtained in this way is related to a renormalization group scale by probing the spectrum of elementary excitations using a restricted variational excitation ansatz.

Chapter 5 rephrases tensor network renormalization for two-dimensional classical lattice models in a manifestly nonnegative way using nonnegative matrix factorization. The resulting real-space renormalization group flow preserves positivity and hence yields an interpretation in terms of RG flows of effective Hamiltonians, reconciling modern real-space tensor network renormalization methods with traditional block-spin approaches. We derive algebraic relations for fixed point tensors, calculate critical exponents, and benchmark our method on the Ising model and the six-vertex model.

Chapter 6 studies non-local symmetries in tensor networks by expressing two-dimensional classical partition functions in terms of strange correlators of judiciously chosen product states and topological string-net wave functions. We show how the

topological properties of the string-net ensure that (part of) the emerging non-local symmetries of the scaling limit of the classical partition function at criticality are already present at the ultraviolet level, highlighting parallels between topological sectors and conformal primary fields in the shared framework of MPO symmetries. In particular, we numerically identify the emergent anyonic excitations in finite-size conformal field theory spectra of twisted partition functions on the torus. Additionally, we provide a complementary perspective on real-space renormalization by recognizing known tensor network renormalization methods as the approximate truncation of a coarse-grained strange correlator.

* * *

Regarding the scope of this dissertation, we would like to remind the reader of Freeman Dyson's binary classification of mathematicians (or of creative human activities in general for that matter) into frogs and birds [4]:

“Some mathematicians are birds, others are frogs. Birds fly high in the air and survey broad vistas of mathematics out to the far horizon. They delight in concepts that unify our thinking and bring together diverse problems from different parts of the landscape. Frogs live in the mud below and see only the flowers that grow nearby. They delight in the details of particular objects, and they solve problems one at a time.”

Since we are interested in numerical methods to approximate the explicit RG flows leading from the muddy short-distance physics of lattice models to their universal long-distance behavior, the work in this dissertation is, in many ways, most definitely froggy. We apologize in advance to any high-flying birds who might feel offended by our dragging them back down to the dirt, to the origin of any tree carrying food for birds.

Part I

Preliminaries

Renormalization group theory

In this chapter¹, we provide a pedagogic overview of renormalization group (RG) theory with a bias towards equilibrium statistical physics, critical phenomena, and statistical field theory. After a brief summary of the difficulties posed by many-body systems exhibiting correlations across many length scales, we introduce essential points of phase transitions, criticality, and mean-field theory. Next, we highlight the idea of the renormalization group approach and enumerate its core concepts: scaling, flows, fixed points, and universality. One of the main goals in this chapter is to firmly instill the notion that quantum field theory is completely and utterly unnecessary to understand renormalization group theory. Even though knowledge of renormalization in quantum field theory surely complements our discussion and is extremely useful in its own right, familiarity with its techniques is useful only to the extent that one is interested in swiftly doing perturbative calculations involving Feynman diagrams.

Throughout, we often resort to the Ising model as a guiding example, which, despite its simplicity², captures the gist of a considerable amount of questions physicists ponder when they study many-body systems with an infinite amount of degrees of freedom. What are the possible phases? What is the nature of transitions between these phases and what are the universal properties of these transitions? What does the ground state in each of these phases look like? What about excitations, correlation functions, order parameters, and the interplay between field theory and lattice models? We conclude this chapter with a short introduction to conformal field theory, the numerical renormalization group, and a selection of some historical real-space implementations of the renormalization group, without resorting to tensor networks just yet.

2.1 Problems with many length scales

The reductionist mantra of physics tries to explain macroscopic phenomena in terms of (possibly complex) microscopic behavior. In simple cases, such as hydrodynamics,

¹The material in this chapter does not contain original research and is an amalgamation of articles [5–7], reviews [8], notes [9, 10], textbooks [11–15], and other sources duly cited.

²The Ising model was actually one of the “theorist’s laboratories” Wilson used to shape his ideas on renormalization [16]. Additionally, in the context of real-space renormalization, the Ising model’s simplicity ought to discourage us from succumbing to any form of hubris: as of today, it has still not been truly satisfactorily renormalized in three dimensions.

microscopic fluctuations are seen to average out when considering systems at larger length scales, allowing for an adequate description in terms of continuum equations. Luckily, it seems that length scales in nature have the tendency to decouple to the extent that atomic fluctuations are not important for describing macroscopic fluids.

There however exist numerous phenomena where many scales of length are equally important and fluctuations occur on all scales up to macroscopic wavelengths. One of the most tangible³ examples is critical opalescence, which occurs in the study of critical phenomena and second-order phase transitions. At its critical point, water can no longer boil and the distinction between liquid and gas disappears. Near criticality, density fluctuations develop at all possible length scales, and in particular also at the length scales responsible for strong light scattering. The result is that an otherwise transparent fluid suddenly looks milky and opaque near criticality. In the Kondo effect, electrons of all wavelengths in the conduction band of a metal interact with the magnetic moments of impurities, leading to a strongly-correlated electron system. Other examples include turbulence, where a cascade of eddies spans all length scales down to the millimetre level until viscosity damps the turbulent fluctuations, and quantum field theory, where fluctuations at all momentum scales appear in calculations.

The common trait of these problems is the presence of a lot of strongly coupled degrees of freedom. Originally, *renormalization* referred to the *ad hoc* removal of ultraviolet divergences encountered in the Feynman diagrams of quantum electrodynamics [17]. The solution was to introduce an artificial cutoff in the integrals over momenta of virtual particles, and then removing all dependence on the unwanted cutoff by expressing the bare parameters e_0 and m_0 in terms of finite, experimentally accessible quantities e and m . The *renormalization group* concept was introduced by Gell-Mann and Low [18] to propose a family of parameters e_λ relating the behavior of quantum electrodynamics at an arbitrary momentum scale λ as a means to interpolate between the physical charge e and the bare charge e_0 . The high-energy behavior of the differential equations for e_λ derived by Gell-Mann and Low served as an inspiration for the development of the renormalization group theory as a conceptual framework by Wilson⁴.

Meanwhile, in the field of critical phenomena, people noticed experimentally that a multitude of physical systems at criticality could be grouped into *universality classes* with similar *critical exponents* describing the continuous phase transitions. At criticality, the correlation length in a system diverges and fluctuations proliferate at all length scales. It was noted that Landau's mean-field theory of critical phenomena could not describe the universal large-distance behavior of these transitions for spatial dimensions $d < 4$, since it yielded predictions for critical exponents that were incompatible with, for example, the known exact solution of the Ising model

³In practice, these experiments are done with binary fluid mixtures whose critical point can be reached at much lower pressures. In the case of water, *seeing* critical opalescence requires a glass window capable of withstanding 218 atm at 647 K.

⁴Here, and elsewhere in this dissertation, the term "Wilsonian" refers not to Wilson *per se* but to the combined work of many physicists culminating in the current view on renormalization. Wilson himself was rather modest about his own achievements, and was of the opinion that most of his work would have been discovered sooner or later by his contemporaries [16].

for $d = 2$ and experimentally measured exponents for $d = 3$. The existence of universality classes led to scaling laws involving critical exponents and scaling hypotheses for the singular part of thermodynamic quantities. Kadanoff developed a qualitative, but not completely satisfactory, explanation of the scaling hypothesis in terms of coarse-graining spins by assuming that the diverging correlation length was the only relevant length scale at criticality [19].

Renormalization group theory thus has its roots *both* in particle physics and critical phenomena. It took a physicist familiar with, and, more importantly, appreciative of both disciplines to truly recognize the deep implications of the theory and the unified view on quantum field theory and statistical mechanics it is capable of providing. From a modern point of view, the renormalization group is a set of ideas containing a mathematical procedure to gradually transfigure a physical theory into one with different, effective degrees of freedom, yet in such a way that identical answers are obtained in a certain asymptotic regime of interest. This procedure sounds very impractical, but Wilson discovered that most long-distance physics becomes remarkably simple due to universality, and can be completely characterized by just a few (renormalized) parameters. The clue is to consider the short-distance lattice spacing a of a lattice model (or the momentum cutoff Λ of a quantum field theory) as an integral part of any physical theory. According to Wilson, we should adjust the parameters of the theory in such a way that the long-distance physics survives the coarse-graining procedure when gradually letting the lattice cutoff grow (or momentum cutoff shrink). As we will see, universality is explained in terms of the existence of fixed points in theory space, and the discrete set of universality classes correspond to different realizations of how a system can be scale invariant. Long-distance physics is to a large extent insensitive to what happens at short distances, but the way this decoupling arises is much more subtle and refined than in classical theories.

In practice, there is no single equation. The abstract ideas of the framework have to be adapted to fit the structure of the problem at hand. When a renormalization group approach fails on a particular problem, the qualitative picture of renormalization is most likely not to blame but rather a lack of imagination on the part of the practitioner. The general strategy however amounts to focusing on degrees of freedom that control the asymptotic behavior, which often requires physical intuition. In the presence of a Fermi surface for example, it turns out that the relevant degrees of freedom live close to the Fermi momentum k_F rather than at the origin in momentum space [20]. Even though precise quantitative calculations can and have been carried out, the generality of the framework suggests that it is not even wrong to regard the idea of renormalization as a kind of meta-theory, an overarching physical concept useful to many areas in physics. It is also possible to think about renormalization as nothing more than a computational tool, an efficient way to calculate the partition function one piece at a time⁵.

An important concept implicit in Wilson's work is the notion of an *effective field theory*. All quantum field theories (or all statistical mechanical models, since taking

⁵Going further along this insubstantial utilitarian path, we can regard the partition function as nothing more than a computational device and physics boils down to a counting game.

the continuum limit of a field theory with a cutoff is equivalent to a second-order phase transition) should not be regarded as beautiful, final theories of everything but rather as approximate, equally beautiful theories, which are however only valid in a certain regime. Feeling the need to get rid of ultraviolet divergences is the result of holding on to the absurd notion that field theories should be valid up to arbitrarily short distances. In this light, taking the continuum limit by sending the momentum cutoff to infinity becomes a vacuous statement: by definition of the RG procedure we want the effective theory describing the low-energy physics to be insensitive to what happens at the cutoff scale.

We would like to end this introductory section with a digression that should be kept in the back of one's mind when transitioning from renormalization group theory to tensor network states in Chapter 3. With computational physics being ubiquitous today, it is perhaps hard to imagine that Wilson's work was done in a time when the bulk of theoretical physicists only resorted to computer calculations for work involving the Department of Defense. Using computers to make fundamental progress in theoretical physics was considered a sign of bad taste. Reading Wilson's original papers as well as his popular scientific writing [21], it is striking that he was not only concerned with the physical implications of his work, but also cared a lot about its numerical translation, with numerical insights feeding back into his theoretical work. He devoted a great deal of attention to massaging physical problems into models amenable to practical computer simulations. Wilson himself had access to a \$5 million CDC 7600, which, with its 36.4 MHz CPU, was considered the fastest *digital computing machine* from 1969 up until 1975. Incidentally, the primary reason he even bothered to seriously implement his numerical RG solution for the Kondo problem [5] was to a large extent driven by technological advances, as evident from this interview excerpt [22]:

Q: And looking at the Kondo effect at that stage, does the stimulation for that come from Phil Anderson [23]?

KW: No. It comes from my utter astonishment at the capabilities of the Hewlett-Packard pocket calculator⁶, the one that does exponents and cosines. And I buy this thing and I can't take my eyes off it and I have to figure out something that I can actually do that would somehow enable me to have fun with this calculator . . . What happened was that I worked out a very simple version of a very compressed version of the Kondo problem, which I could run on a pocket calculator. And then I realize that this was something I could set up with a serious calculation on a big computer to be quantitatively accurate.

In a 1975 article [24], Wilson explicitly stated that, in his mind, “the renormalization group is a numerical approach”, and he concluded that same article as follows:

“Where the renormalization group approach has been successful a lot of ingenuity has been required: one cannot write a renormalization

⁶The Hewlett-Packard HP-35 was the first *handheld electronic pocket calculator* and was released in 1972.

group cookbook. (In contrast, Feynman diagrams techniques can be reduced to simple strict rules.) Even if one succeeds in formulating the renormalization group approach for a particular problem, one is likely to have to carry out a complicated computer calculation, which makes most theoretical physicists cringe.”

Anecdotally though these stories may be, we believe they identify a hands-on style of doing physics that has been (sub)consciously absorbed by the tensor network community, and that the primarily Wilsonian roots of this vision all too often goes unacknowledged.

2.2 Collective behavior, criticality, and phase transitions

To understand how the renormalization group, among other things, corrects Landau’s mean-field theory of critical phenomena, it is useful to first of all remind ourselves of some canonical results on phase transitions, criticality, and scaling.

2.2.1 Equilibrium statistical mechanics

The emergence of collective macroscopic properties from the intricate microscopic dynamics of many degrees of freedom lies at the core of statistical mechanics. A macrostate is characterized by a few phenomenological variables (volume, pressure, temperature, entropy, . . .) and often corresponds to a large number of microstates which all contribute to the same macrostate. Rather than trying to derive the macroscopic from the microscopic, statistical mechanics connects both descriptions in a probabilistic way. For example, in the canonical ensemble⁷ at temperature T , each microstate μ gets assigned a probability through the Boltzmann weight $\exp(-\beta H(\{\mu\}))/Z$, where β denotes the inverse temperature $1/k_B T$, $H(\{\mu\})$ the Hamiltonian, and where the normalization is given by the *partition function* $Z = \sum_{\mu} \exp(-\beta H(\{\mu\}))$. Thermodynamic information about the macroscopic state can then be extracted from suitable derivatives of the *free energy* $F = -k_B T \ln Z$, where k_B denotes Boltzmann’s constant.

The microscopic interactions for realistic systems are often however too complicated for an *ab initio* approach, so that it may prove worthwhile to consider averaging out over sufficiently many degrees of freedom to see if one ends up with a simpler description. In this hydrodynamic limit, the averaged variables are no longer a discrete set of degrees of freedom on the lattice but slowly varying continuous fields, leading to the study of statistical mechanics of fields. Phenomenological field approaches are thus of a mesoscopic nature and require a *coarse-graining* procedure to average out over thermal fluctuations with characteristic wavelengths $\lambda > \lambda(T) \approx v\hbar/k_B T \gg a$, where $v\hbar/k_B T$ is the de Broglie wavelength and a the

⁷Rather than relying on the ergodic hypothesis, we can motivate the introduction of statistical ensembles with a mesoscopic approach. By dividing a system into lots of mesoscopic parts, where each part is assumed to be described by a microstate reflecting the complexity of the whole system, the properties of the entire system follow from a spatial rather than a temporal averaging over all subsystems [13].

lattice spacing. By considering an interval $a \ll dx \ll \lambda(T)$ around a point x , we can define an average deformation field $\phi(x)$ which varies slowly over dx . Note that even though we describe $\phi(x)$ as being a continuous field, it does not vary over distances comparable to the lattice spacing, i.e. the remnants of the discrete lattice are still present since there is a physical cutoff given by the lattice spacing. The key principles to construct a phenomenological field theory are locality, translational symmetry, and stability. Since interactions between particles are short-range in most situations, translation invariance constrains the effective interactions to only involve derivatives $\partial\phi/\partial x, \partial^2\phi/\partial^2x, \dots$. Locality then signifies that higher derivative terms are less important. We also require stability since we want to describe fluctuations around an equilibrium solution, which excludes linear terms in ϕ or its derivatives.

2.2.2 A selection of simple discrete and continuum models

The mother of all discrete models is the Ising model, which is defined on a lattice of spins σ_i , each spin taking the value -1 or 1 . For a lattice of N sites there is a total of 2^N different spin configurations or microstates. The Hamiltonian (or the energy for a given configuration $\{\sigma\}$) is given by

$$H[\sigma] = -J \sum_{\langle ij \rangle} \sigma_i \sigma_j - h \sum_i \sigma_i, \quad (2.1)$$

where $\langle ij \rangle$ indicates nearest-neighbor summation, J denotes ferromagnetic ($J > 0$) or antiferromagnetic ($J < 0$) coupling, and h is an external magnetic field. The Ising model can be generalized to the q -state Potts model

$$H_q[\sigma] = -J_q \sum_{\langle ij \rangle} \delta_{\sigma_i \sigma_j}, \quad (2.2)$$

where each spin σ_i now takes one of q possible values, coinciding with the Ising model in zero magnetic field for $q = 2$. This model has a permutation symmetry S_q of the spin labels. The q -state clock model is defined in terms of spins having values among the q -th roots of unity $e^{i\phi}$, where $q\phi \in 2\pi\mathbb{Z}$. The Hamiltonian

$$H_c[\phi] = -J_c \sum_{\langle ij \rangle} \cos(\phi_i - \phi_j), \quad (2.3)$$

has a Z_q symmetry under $\phi_i \rightarrow e^{2\pi i/q} \phi_i$ and a spin-flip symmetry $\phi_i \rightarrow -\phi_i$.

As an example of statistical models with continuous degrees of freedom, let us generalize the local spin to be a unit vector \mathbf{n} , with Hamiltonian

$$H[\mathbf{n}] = -J \sum_{\langle ij \rangle} \mathbf{n}_i \cdot \mathbf{n}_j - \sum_i \mathbf{h} \cdot \mathbf{n}_i, \quad (2.4)$$

which is called the classical $O(n)$ vector model if the vector \mathbf{n} is taken to have n components. The $O(n)$ model contains respectively the Ising model and the XY-model for $n = 1$ and $n = 2$. Going from the lattice to the continuum results

in a continuum Hamiltonian of the form

$$H[\mathbf{n}] = \int d^d x (J \partial_i \mathbf{n} \cdot \partial_i \mathbf{n} - \mathbf{h} \cdot \mathbf{n}), \quad (2.5)$$

where we have introduced the fields $\mathbf{n}(x)$ and $\mathbf{h}(x)$. By replacing the unit vector constraint $\mathbf{n}^2(x) = 1$ at every position by

$$\frac{1}{V} \int d^d x \mathbf{n}^2 = 1, \quad (2.6)$$

we obtain the spherical model. We can also achieve the same effect by adding a quartic potential as a penalty term to the Hamiltonian, leading to

$$H[\mathbf{n}] = \int d^d x \left(\frac{1}{2} \partial_i \mathbf{n} \cdot \partial_i \mathbf{n} + \frac{\mu^2}{2} \mathbf{n}^2 + \frac{u}{4} (\mathbf{n}^2)^2 \right). \quad (2.7)$$

The energy minimum as a function of $|\mathbf{n}|$ depends on the relative values of the couplings μ^2 and u . Note that if $n = 1$, i.e. if \mathbf{n} only has a single component ϕ , we recover the ϕ^4 model

$$H[\phi] = \int d^d x \left(\frac{1}{2} (\nabla \phi)^2 + \frac{\mu^2}{2} \phi^2 + \frac{u}{4} \phi^4 \right), \quad (2.8)$$

which, for $u = 0$ reduces to the exactly solvable Gaussian model.

2.2.3 Phase transitions and criticality

An important consequence of interactions among many degrees of freedom is the possibility of new phases of matter whose collective behavior does not correspond in any way to that of a few particles. A phase transition⁸ occurs when one macroscopic phase transforms to a different one, which involves pronounced changes in various response functions. The point in the phase diagram at which this happens is called the *critical point*. Note that for a finite system of N spins, the number of terms 2^N in the partition function is obviously finite, which ensures the analyticity of the free energy. Phase transitions, and non-analytic behavior in general, can thus only truly take place in the thermodynamic⁹ limit $N \rightarrow \infty$.

First-order or discontinuous transitions are characterized by a finite jump in thermodynamic quantities. Two (or more) phases on either side of the critical point coexist exactly at the critical point. Slightly away from the critical point, there usually exists a unique phase whose properties can be continuously connected to one of

⁸For the subsequent discussion on criticality and renormalization, we will concern ourselves with thermal phase transitions driven by thermal fluctuations as opposed to *quantum phase transitions*. The latter are driven by the purely quantum mechanical competition between ground states at zero temperature when tuning a parameter in the Hamiltonian (see also Section 2.2.4).

⁹For lattice models, we take the thermodynamic limit to refer to $N, V \rightarrow \infty$ while keeping the density $N/V = a^{-d}$ fixed, where a denotes the lattice spacing. In quantum field theory, this limit corresponds to an infinite system with an ultraviolet cutoff.

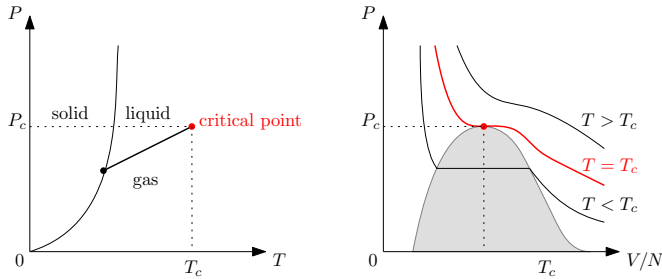


FIGURE 2.1: Qualitative pressure-temperature and pressure-specific volume phase diagrams of the liquid-gas phase transition. The free energy is analytic except for a branch cut along the phase boundary.

the co-existent phases at the critical point. The discontinuities in thermodynamic quantities thus result from going from one stable phase to another stable phase. Additionally, the *correlation length*, which measures the distance over which fluctuations are significantly correlated, generally remains finite in first-order phase transitions.

At a second-order (or continuous) transition, the correlation length effectively becomes infinite and fluctuations are correlated across all length scales. This forces the whole system to be in a unique, critical phase, and phases on either side of the critical point must converge to that same critical phase at the critical point. There are no jumps in thermodynamic quantities since differences like energy density have to smoothly go to zero at the critical point. The derivatives of thermodynamic quantities however, such as the specific heat or the susceptibility, are discontinuous or singular at the critical point. Crucially, the symmetry of one phase, which is usually the low-temperature one, is a subgroup of the symmetry of the other. We will come back to the important concept of symmetry breaking in Section 2.4.5.

Let us consider two simple examples in parallel to illustrate the above points: the condensation of a gas into a liquid (see Fig. 2.1) and the phase transition between paramagnetic and ferromagnetic phases in simple magnets (see Fig. 2.2). In both cases, the first-order transition happens along a coexistence line that terminates at a critical point, where the isotherms exhibit singular behavior. In the vicinity of the critical point, the difference between the densities of the coexisting liquid and gas phases vanishes, while the isothermal compressibility $\kappa = -(\partial V/\partial P)|_T/V \rightarrow \infty$ as $T \rightarrow T_c$. Close to criticality, the fluid looks cloudy due to *critical opalescence*, which signals that the collective density fluctuations occur at long enough wavelengths to scatter visible light. For the ferromagnet, it is the zero-field susceptibility $\chi = (\partial M/\partial H)|_{H=0}$ which diverges as $T \rightarrow T_c$.

In the vicinity of a critical point, the singular behavior is characterized by a set of *critical exponents*, which describe the non-analyticity of various thermodynamic functions. For the case of the ferromagnet¹⁰, let us introduce the reduced temperature $t = (T - T_c)/T_c$, where T_c denotes the Curie temperature, together with the reduced

¹⁰Due to universality, the critical exponents at the gas-liquid critical point are actually identical with those of simple ferromagnets we consider here.

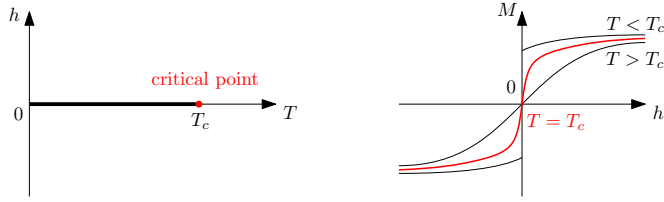


FIGURE 2.2: Qualitative external field-temperature and magnetization-external field phase diagrams for a simple magnet.

external magnetic field $h = H/(k_B T)$. In the limit $t \rightarrow 0$, any thermodynamic quantity is assumed to decompose into a regular part that remains finite (but can be discontinuous), and a singular part, which diverges or has diverging derivatives. The power-law behavior¹¹ of these singular parts is listed below:

- α The heat capacity is the thermal response function, with singularities at zero field described by an exponent α ,

$$C(T, h = 0) \propto |t|^{-\alpha}. \quad (2.9)$$

A positive value of α corresponds to a divergence, while a negative α entails a finite heat capacity, possibly with a cusp.

- β The *order parameter* (see Sec. 2.4.5) is given by the magnetization

$$m(T) = \frac{1}{V} \lim_{h \rightarrow 0^+} M(T, h), \quad (2.10)$$

which, close to the critical point, behaves as

$$m(T, h = 0) \propto (-t)^\beta, \quad (2.11)$$

for $T < T_c$ (it is zero for $T > T_c$).

- γ The susceptibility is the response of the order parameter to its conjugate field, and diverges as

$$\chi(T, h = 0) \propto |t|^{-\gamma}. \quad (2.12)$$

Assuming a local order-parameter density $m(\mathbf{r})$ such that

$$M = \left\langle \int d^3 \mathbf{r} m(\mathbf{r}) \right\rangle, \quad (2.13)$$

¹¹We tacitly assume that the same singularity governs both sides of the transition, so that, for example, the identification $\alpha_+ = \alpha_- \equiv \alpha$ holds.

it is straightforward to show that, for the connected correlation functions

$$\Gamma_c(\mathbf{r}) = \langle m(\mathbf{r})m(0) \rangle - \langle m(\mathbf{r}) \rangle \langle m(0) \rangle, \quad (2.14)$$

the following special case of the fluctuation-dissipation theorem holds:

$$\chi = \frac{V}{k_B T} \int d^3\mathbf{r} \Gamma_c(\mathbf{r}), \quad (2.15)$$

which relates a bulk response function to microscopic fluctuations. If g then denotes a typical value of the correlation function for $|\mathbf{r}| < \xi$, we find $k_B T/V < g\xi^3$, i.e. a diverging susceptibility implies a diverging correlation length. If we imagine a spin system near the critical point as an aggregate of droplets of different magnetizations, we can already appreciate that spins have to fluctuate over all length scales from the lattice spacing up to the (diverging) correlation length. Indeed, if this were not the case, the connected correlation function would have a peak near $|\mathbf{r}| \sim \xi$ and be small below that scale.

δ At $T = T_c$, the magnetization vanishes along the critical isotherm as

$$m(T = T_c, h) \propto |h|^{1/\delta}. \quad (2.16)$$

ν, η Let us assume the Ornstein-Zernike form for the asymptotic correlation functions near criticality,

$$\Gamma_c(\mathbf{r}) \sim \frac{e^{-|\mathbf{r}|/\xi}}{|\mathbf{r}|^p}, \quad t \rightarrow 0. \quad (2.17)$$

The critical exponent ν associated to the correlation is defined by

$$\xi(T, h = 0) \propto |t|^{-\nu}, \quad (2.18)$$

while for $t = 0$, where $\xi = \infty$, there is no longer exponential but power-law decay of correlations with

$$p = d - 2 + \eta, \quad (2.19)$$

where η is the critical exponent associated to the power-law decay of correlations at the critical point.

Note that the significance of the critical exponents was, at first, wholly experimental. Series of experiments on widely different systems, with critical temperatures orders of magnitude apart, could be grouped into classes which shared approximately the same critical exponents. We mention this because the definitions of $\{\alpha, \beta, \gamma, \delta\}$ given above are rooted in experimental convenience. We will see later on in Sec. 2.6 and Sec. 2.8 that other linear combinations of the critical exponents are actually a lot more fundamental from a theoretical perspective.

2.2.4 Quantum criticality and quantum-to-classical mapping

In the previous sections, we have focused on critical behavior in classical systems described by statistical mechanics for reasons of clarity. At finite temperatures, thermal fluctuations usually dominate quantum effects, but there are of course many scenarios where quantum effects do become of fundamental importance, e.g. in low dimensional strongly-correlated quantum systems¹² and in most quantum field theory applications. Classical statistical mechanics however remains important as a very good approximation to quantum statistical mechanics when the correlation length exceeds the typical de Broglie wavelength of the system. In that case, there is no need to invoke quantum mechanics¹³. For system with a characteristic velocity v (speed of light, Fermi velocity, ...), the de Broglie wavelength at temperature T is $\lambda_T = v\hbar/k_B T \propto \beta$, so that, for large enough temperatures or very close to a finite temperature critical point where $\xi \gg \lambda_T$, classical statistical mechanics takes over.

Mathematically, the formalism for describing quantum field theories and statistical mechanics of continuous phase transitions is very similar. For statistical mechanical models defined in the continuum, the analogy with quantum field theory is particularly manifest. For example, consider the partition function of the Hamiltonian for the ϕ^4 -model given in Eq. (2.8),

$$Z = \int \mathcal{D}\phi \exp \left(-\beta \int d^d x \left(\frac{1}{2} (\nabla\phi)^2 + \frac{\mu^2}{2} \phi^2 + \frac{u}{4} \phi^4 \right) \right), \quad (2.20)$$

The partition function of this d -dimensional statistical model is a sum over all possible configurations of a field, i.e. a functional integral entirely analogous to the Euclidean generating functional of a quantum field in d space-time dimensions. By rescaling the field as $\phi \rightarrow \sqrt{\beta}\phi$ and the ϕ^4 -coupling as $u \rightarrow (1/\beta)u$, we can even remove the explicit temperature dependence,

$$Z = \int \mathcal{D}\phi \exp \left(- \int d^d x \left(\frac{1}{2} (\nabla\phi)^2 + \frac{\mu^2}{2} \phi^2 + \frac{u}{4} \phi^4 \right) \right), \quad (2.21)$$

so that changing the temperature is seen to correspond to rescaling the field and adjusting couplings appropriately.

The partition function of a d -dimensional quantum system described by a density operator¹⁴ $\rho = \exp(-\beta H)$ follows from the path integral formalism by a Wick rotation $t \rightarrow -i\tau$ and restricting Euclidean time τ to a finite strip of extent β ,

$$Z = \text{Tr} (\exp(-\beta H)) = \int [\mathcal{D}\phi(\tau)] e^{-S_E(\phi(\tau))}. \quad (2.22)$$

At zero temperature, the extent of the additional dimension becomes infinite and

¹²We will touch upon some aspects of the critical behavior of quantum systems at zero temperature when discussing matrix product state renormalization in Chapter 4. Quantum criticality is intimately related to the existence of gapless excitations in the system, i.e. a continuum of excited states arbitrarily close in energy to the ground state.

¹³This is an example of the decoupling of scales we mentioned in Sec. 2.1.

¹⁴The quantum Hamiltonian generally depends on non-commuting operators.

we recover the generating functional in Euclidean time. At finite temperatures, the quantum partition function of a d -dimensional system looks like that of a $(d + 1)$ -dimensional classical system defined on a strip of width β . This quantum-to-classical mapping is quite general, but apart from a few special cases, it is less illuminating than one might think because there is usually no “easier” side to the mapping. Related to the above is the *transfer matrix* formalism¹⁵, which is the statistical mechanical analogue of the operator formalism in quantum field theory. Recognizing the transfer matrix T as an evolution operator $U(a)$ acting over a lattice spacing a in the temporal direction allows for the definition of a Hamiltonian operator given by $T = \exp(-aH)$. The correlation length ξ is then related to the mass gap m of the associated Euclidean quantum field theory by

$$\xi = \frac{1}{ma}. \quad (2.23)$$

A diverging correlation length in the vicinity of a critical point thus corresponds to the field theory’s renormalized mass going to zero for a fixed lattice cutoff a , i.e. a critical system is equivalent to a massless quantum field theory, if the lattice spacing a remains finite. Let us rephrase this statement slightly differently. Removing the cutoff by taking the *continuum limit* of a field theory with a cutoff is equivalent to taking the limit in which the correlation length is infinitely large compared to the cutoff: the continuum limit *is* a second-order phase transition [25].

2.3 Scaling and homogeneity

To explain the scaling behavior of thermodynamic quantities near the critical point, the scaling hypothesis postulates that the correlation length ξ is the only important length scale near criticality, in terms of which all other lengths must be measured. The singular form of the free energy density (and any other thermodynamic quantity for that matter) in the neighborhood of the critical point is then assumed to be given by a homogeneous function of its parameters,

$$f(t, h) \sim |t|^{2-\alpha} \mathcal{F} \left(\frac{h}{|t|^\Delta}, \dots, \frac{g_j}{|t|^{\phi_j}}, \dots \right), \quad (2.24)$$

where \mathcal{F} is a scaling function (see next paragraph). The gap exponent $\Delta = \beta + \delta$ determines how h scales with t , while the ϕ_j are the *cross-over exponents* for possible other conjugate-variable pairs in the theory¹⁶. The homogeneous form of $f(t, h)$ has been chosen to reproduce the singularity of the heat capacity at $h = 0$, since $C \sim -\partial^2 f / \partial t^2 \sim |t|^{-\alpha} \mathcal{C}(h/t^\Delta)$, where $\mathcal{C}(h/t^\Delta)$ denotes the homogeneous function resulting from differentiating Eq. (2.24) twice.

¹⁵We will come back transfer matrices in Sec. 2.10.1.1 and in the context of tensor network states, where these objects are of crucial importance (see Chapter 3 and Chapter 4).

¹⁶In RG parlance, the cross-over exponents control the relative importance of these fields near $t = 0$ in the vicinity of a particular critical point. In original scaling formulations, these additional exponents were absent because they more often than not correspond to *irrelevant* operators (see Sec. 2.5.3).

Before sketching the implications of this ansatz, let us introduce a short intermezzo to explain homogeneous functions and their intimate relation to power laws. A function $f(x)$ of one variable $x > 0$ is called homogeneous if $f(\lambda^a x) = \lambda f(x)$ for all $\lambda > 0$, and a power law if $f(x) = x^{1/a} f(1)$ with exponent $1/a$, where $f(1)$ is the value of the function evaluated at $x = 1$. It is easy to show that a function is homogeneous if and only if it is a power law, with the important property that the relative change $f(\lambda^a x)/f(x) = \lambda$ is a constant independent of x . A function $f(x, y)$ of two variables is called a generalized homogeneous function if

$$f(\lambda^a x, \lambda^b y) = \lambda f(x, y), \quad \text{for all } \lambda > 0, \quad (2.25)$$

and if it satisfies a *scaling form* with exponent $1/a$ if

$$f(x, y) = |x|^{1/a} \mathcal{F}_{\pm} \left(y/|x|^{b/a} \right), \quad (2.26)$$

where $\mathcal{F}_{\pm} (y/|x|^{b/a}) = f(\pm 1, y/|x|^{b/a})$ is called the *scaling function*, which evaluates the function $f(x, y)$ at $x = \pm 1$ and rescaled variable $y/|x|^{b/a}$. One can show that $f(x, y)$ is a generalized homogeneous function Eq. (2.25) if and only if it can be rewritten in the scaling form Eq. (2.26), satisfying the property that $f(\lambda^a x, \lambda^b y)/f(x, y) = \lambda$ is independent of x . Even without knowing the explicit functional form $f(x, y)$, it is possible to check if $f(x, y)$ is a generalized homogeneous function by plotting the transformed function $x^{-1/a} f(x, y)$ versus the rescaled argument $y/x^{b/a}$ and checking if the data collapses onto the scaling function \mathcal{F} .

The fact that the correlation length is the most important length scale at criticality and solely responsible for singular contributions to thermodynamic quantities actually determines the leading singular behavior of the free energy. Let us divide a system of linear size L into approximately independent components of size ξ . Because $\ln Z(t, h)$ is extensive and dimensionless, it must look something like

$$\ln Z = \left(\frac{L}{\xi} \right)^d g_{\xi} + \dots + \left(\frac{L}{a} \right)^d g_a, \quad (2.27)$$

where a is the lattice spacing, and g_{ξ} and g_a are non-singular functions of dimensionless parameters. The first term determines the leading singular behavior, so that

$$f_s(t, h) \sim \frac{\ln Z}{L^d} \sim \xi^{-d} \sim |t|^{d\nu} g \left(\frac{h}{|t|^{\Delta}} \right) \quad (2.28)$$

where we have made use of the more fundamental assumption that the correlation length is a homogeneous function, i.e. $\xi(t, h) \sim |t|^{-\nu} g(h/|t|^{\Delta})$. Identifying the expression for the singular part of the free energy with Eq. (2.24) immediately yields a first example of a *scaling law*: $2 - \alpha = d\nu$ (Josephson's law).

Other scaling laws follow from identifying critical exponents in thermodynamic

quantities calculated using Eq. (2.24). The magnetization equals

$$m(t, h) \sim \frac{\partial f}{\partial h} \sim |t|^{2-\alpha-\Delta} \mathcal{M}\left(\frac{h}{|t|^\Delta}\right). \quad (2.29)$$

In the limit $x \rightarrow 0$, $\mathcal{M}(x)$ is a constant, so that

$$m(t, h = 0) \sim |t|^{2-\alpha-\Delta} \quad \longrightarrow \quad \beta = 2 - \alpha - \Delta. \quad (2.30)$$

For $x \rightarrow \infty$ on the other hand, we have $\mathcal{M}(x) \sim x^p$ and

$$m(t = 0, h) \sim |t|^{2-\alpha-\Delta} \left(\frac{h}{|t|^\Delta}\right)^p, \quad (2.31)$$

which, since this limit should be independent of t , requires $2 - \alpha - \Delta = \Delta p$, hence

$$m(t = 0, h) \sim h^{(2-\alpha-\Delta)/\Delta} \quad \longrightarrow \quad \delta = \frac{\Delta}{\beta}. \quad (2.32)$$

Similarly, the susceptibility yields

$$\chi(t, h = 0) \sim \left.\frac{\partial f}{\partial h}\right|_{h=0} \sim |t|^{2-\alpha-2\Delta} \quad \longrightarrow \quad \gamma = 2\Delta - 2 + \alpha. \quad (2.33)$$

Together, these relations lead to $\alpha + 2\beta + \gamma = 2$ (Rushbrooke's law) and $\gamma = \beta(\delta - 1)$ (Widom's law). Another scaling law is obtained from looking at the decay of the correlations functions at criticality, which is governed by η . Since we have seen that

$$\Gamma(\mathbf{x}) \sim \frac{1}{|\mathbf{x}|^{d-2+\eta}}, \quad (2.34)$$

we can integrate the connected correlation functions to get an additional exponent identity

$$\chi \sim \int d^d \mathbf{x} \Gamma(\mathbf{x}) \sim \int^\xi \frac{d^d \mathbf{x}}{|\mathbf{x}|^{d-2+\eta}} \sim \eta^{2-\eta} \sim |t|^{-\nu(2-\eta)}, \quad (2.35)$$

namely $\gamma = \nu(2 - \eta)$ (Fisher's law).

2.4 Landau free energies and mean-field theory

Let us now come back to phenomenological field theories and consider the example of a ferromagnet¹⁷ to discuss the mean-field theory predictions for critical behavior. As we will see, mean-field theory is the saddle point approximation to the Landau-Ginzburg partition function. More generally, Landau theory is a phenomenological

¹⁷Even though the origin of magnetism is quantum mechanical, a phenomenological Landau theory of magnetism considers only the long-wavelength, collective excitations of spins to be important close to the phase transition.

field approach primarily suited to be used in the vicinity of a critical point, where the order parameter is small. Note that the importance of the contributions of Landau theory to physics is of far greater significance than the brief exposition below suggests.

2.4.1 Landau theory

Consider an n -component coarse-grained order parameter field $\vec{m}(\mathbf{x})$ living in a d -dimensional space. As already mentioned in Sec. 2.2.1, we should think of $\vec{m}(\mathbf{x})$ as a mesoscopic coarse-grained quantity with an implicit cutoff (since it contains no fluctuations smaller than the lattice spacing a). The key idea is that, by going from the microscopic to a mesoscopic scale, non-analyticities associated with microscopic degrees of freedom are washed out, and the probability distribution for the coarse-grained degrees of freedom $\vec{m}(\mathbf{x})$ close to the critical point can be obtained by an analytic expansion in powers of \vec{m} . Non-analyticities at the macroscopic scale are also avoided as these involve an infinite number of degrees of freedom, which we steer clear of by adhering to the mesoscopic regime.

It will become clear that the dimensionality of the order parameter together with the spatial dimension are important in distinguishing *universality classes*. The case $n = 1$ includes liquid-gas transitions, binary mixtures, as well as the uniaxial magnets we have been considering as an example. The case $n = 2$ captures superfluidity, superconductivity, and planar magnets while $n = 3$ corresponds to classical magnets. While most down-to-earth situations occur in $d = 3$, phenomena on surfaces ($d = 2$) and chains or wires ($d = 1$) are also of interest. We should also not forget to mention the case $d = 4$, which includes relativistic quantum field theories.

Explicitly, coarse-graining amounts to a change of variables from the original microscopic degrees of freedom to the field $\vec{m}(\mathbf{x})$ by integrating over all allowed configurations to construct new, effective probabilities for the field configurations. This mesoscopic perspective suggests the introduction of an effective reduced¹⁸ Hamiltonian

$$\beta H[\vec{m}(\mathbf{x}), \vec{h}(\mathbf{x})] = \int d^d \mathbf{x} \Psi[\vec{m}(\mathbf{x}), \vec{h}(\mathbf{x})], \quad (2.36)$$

where $\vec{h}(\mathbf{x}) = \beta \vec{H}(\mathbf{x})$ denotes the reduced magnetic field conjugate to the order parameter and where Ψ is the *Landau free energy*¹⁹ [26]. Close to the critical point, where \vec{m} can be safely assumed to be small, we expect to be able to expand the

¹⁸Note that while the probability of a particular configuration is indeed given by the Boltzmann weights $\exp(-\beta H[\vec{m}(\mathbf{x})])$, this does not imply that all terms in the exponent are actually proportional to β . Such a dependence only holds for the true microscopic Hamiltonian; in general the mesoscopic parameters will be analytic functions of the external parameters such as temperature. This, in a way, is exactly the whole point of the Landau approach.

¹⁹By including the work against the external field, we are actually dealing with the Gibbs canonical ensemble. We will continue to write F though.

effective free energy as something resembling

$$\Psi[\vec{m}(\mathbf{x}), \vec{h}(\mathbf{x})] = \frac{1}{2}(\nabla\vec{m})^2 - \vec{m}(\mathbf{x}) \cdot \vec{h}(\mathbf{x}) + \frac{1}{2}r_0m^2(\mathbf{x}) + s_0m^3(\mathbf{x}) + u_0m^4(\mathbf{x}) + \dots, \quad (2.37)$$

where we assumed the external field to be weak by only introducing a linear coupling. In principle, any term compatible with the symmetries of the system is allowed, since microscopic symmetries survive the coarse-graining process and constrain the effective Hamiltonian. Together with the usual assumptions of locality and uniformity, this enumeration of constraints limits the number of possible interactions.

To describe rotationally invariant magnetic systems, it is sufficient to include only a few terms, leading to the Landau-Ginzburg Hamiltonian

$$\beta H = \beta F_0 + \int d^d\mathbf{x} \left(\frac{t}{2}\vec{m}^2(\mathbf{x}) + u\vec{m}^4(\mathbf{x}) + \frac{K}{2}(\nabla\vec{m}(\mathbf{x}))^2 + \dots - \vec{h} \cdot \vec{m}(\mathbf{x}) \right) \quad (2.38)$$

where the constant term βF_0 is an analytical contribution to the free energy coming from the integration over short-range degrees of freedom. The couplings $\{t, u, K, \dots\}$ are phenomenological parameters obtained after coarse-graining the microscopic degrees of freedom while constraining their average to $\vec{m}(\mathbf{x})$. These parameters are non-universal functions of both microscopic interaction parameters and external parameters²⁰.

2.4.2 Saddle point approximation and mean-field theory

In principle, we can now calculate various thermodynamic functions (and their singularities) from the partition function

$$Z = \int [d\vec{m}(\mathbf{x})] e^{-\beta H[\vec{m}(\mathbf{x})]}, \quad (2.39)$$

where $H[\vec{m}(\mathbf{x})]$ corresponds to the Landau-Ginzburg Hamiltonian Eq. (2.38). Even though we have a well-defined lattice spacing a , this functional integral is still hard to do. Mean-field theory boils down to considering the saddle point approximation by replacing the functional integral by the maximum value of the integrand, which corresponds to the most probable field configuration of $\vec{m}(\mathbf{x})$. Since the interactions favor keeping the magnetization vectors parallel, the parameter K is expected to be positive and any variation in magnitude or direction of $\vec{m}(\mathbf{x})$ will result in an energy penalty from the term $K(\nabla\vec{m})^2/2$. This suggests that the field is uniform in its most probable configuration for constant \vec{h} , so that

$$Z \approx e^{-\beta F_0} \int d\vec{m} \exp \left(-V \left(\frac{t}{2}m^2 + um^4 + \dots - \vec{h} \cdot \vec{m} \right) \right), \quad (2.40)$$

²⁰See footnote 18.

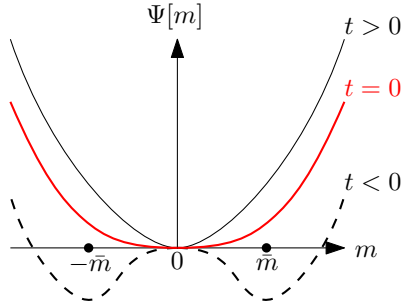


FIGURE 2.3: Sketch of the Landau free energy Eq. (2.42) at different temperatures. A second-order phase transition at $t = 0$ leads to spontaneous symmetry breaking for $t < 0$.

where V is the volume of the system. For $V \rightarrow \infty$, this integral is dominated by the saddle point \vec{m} which maximizes the exponent of the integrand. The saddle point free energy is then

$$\beta F = -\ln Z \approx \beta F_0 + V \min_{\vec{m}} \underbrace{\left[\frac{t}{2} m^2 + um^4 + \dots - \vec{h} \cdot \vec{m} \right]}_{\Psi[\vec{m}, \vec{h}]}, \quad (2.41)$$

where we have identified the appropriate Landau free energy $\Psi[\vec{m}, \vec{h}]$ for this theory. The most probable magnetization is obtained by picking a magnetization $\vec{m} = \vec{m}\vec{h}/\|\vec{h}\|$ aligned to the external field, with a constant magnitude \vec{m} . Let us now *choose* to only take the following terms into account:

$$\Psi[m, h] = \frac{t}{2} m^2 + um^4 - hm, \quad (2.42)$$

where we, from now on, restrict to the scalar case of $n = 1$ for simplicity. The behavior of this quartic function is plotted in Fig. 2.3. The magnitude \vec{m} is obtained from

$$\frac{\partial \Psi}{\partial m} = t\vec{m} + 4u\vec{m}^3 - h = 0, \quad (2.43)$$

To match our model with the experimental phase diagram of a ferromagnet, we now have to *impose* physical conditions on the phenomenological parameters. Since the parameters are assumed to be analytic functions of temperature in the vicinity of the critical point, they can be expanded as

$$t(T, \dots) = a_0 + a_1(T - T_c) + O((T - T_c)^2), \quad (2.44)$$

$$u(T, \dots) = u + u_1(T - T_c) + O((T - T_c)^2). \quad (2.45)$$

The parameter t should be a monotonic function of temperature which vanishes at

T_c , so that $a_0 = 0$ and $a_1 = a > 0$. Stability of the ferromagnetic phase requires $u > 0$ (recall that we also assumed $K > 0$). Note that these constraints are the most minimal and natural ones. This remarkably simple model can qualitatively describe second-order²¹ phase transitions and illustrates how a phase transition from a regime where $\bar{m} = 0$ to a regime where $\bar{m} \neq 0$ can be captured by a continuous function Ψ . For $h = 0$, the Landau free energy is invariant under $m \rightarrow -m$, but this symmetry is *spontaneously broken* when $t < 0$ (see Sec. 2.4.5). A crucial observation is that a perfectly regular Landau free energy $\Psi[m, h, T]$ can lead to singularities in the saddle point free energy. The point is that the value \bar{m} which minimizes Ψ is allowed to be a singular function of h and T , i.e. the singularities are introduced by the non-analytic minimization procedure.

Let us now derive the mean-field predictions for the critical exponents:

□ α The saddle point free energy Eq. (2.42) for $h = 0$ is given by

$$\beta F = \beta F_0 + V\Psi(\bar{m}) = \beta F_0 + V \begin{cases} 0 & \text{for } t > 0 \\ -\frac{t^2}{16u} & \text{for } t < 0 \end{cases} \quad (2.46)$$

where we have used that $t = a(T - T_c)$ up to leading order. In that case, we also have that $\partial/\partial T \approx a\partial/\partial t$, so that in the vicinity of T_c we find

$$C(h = 0) = -T \frac{\partial^2 F}{\partial T^2} \approx -T_c a^2 \frac{\partial^2 k_B T_c \beta F}{\partial T^2} = C_0 + V k_B a^2 T_c^2 \times \begin{cases} 0 & \text{for } t > 0 \\ \frac{1}{8u} & \text{for } t < 0 \end{cases} \quad (2.47)$$

Since the saddle point predicts a discontinuity instead of a divergence, insisting on the power law form $t^{-\alpha}$ suggests $\alpha = 0$. For all spatial dimensions, mean-field theory predicts that no divergence occurs.

□ β For $h = 0$, we can obtain the magnitude of the magnetization directly from Eq. (2.43), which has real solutions

$$\bar{m}(h = 0) = \begin{cases} 0 & \text{for } t > 0 \\ \pm \sqrt{\frac{a}{4u}}(T_c - T)^{1/2} & \text{for } t < 0 \end{cases} \quad (2.48)$$

so that $\beta = 1/2$.

□ γ Differentiating Eq. (2.43) with respect to \bar{m} at $h = 0$ gives the inverse longitudinal susceptibility,

$$\chi^{-1} = \left. \frac{\partial h}{\partial \bar{m}} \right|_{h=0} = t + 12u\bar{m}^2 = \begin{cases} t & \text{for } t > 0 \\ -2t & \text{for } t < 0. \end{cases} \quad (2.49)$$

²¹This is a second-order phase transition because \bar{m} is continuous at $t = 0$, as can be seen from Eq. (2.48).

Table 2.1: Critical exponents for the Ising model universality class ($n = 1$).

Critical exponents	Ising $d = 2$	Ising $d = 3$ [27]	Mean field $d \geq 4$
α	0	0.11008	0
β	1/8	0.326419	1/2
γ	7/4	1.237075	1
δ	15	4.78984	3
ν	1	0.629971	1/2
η	1/4	0.036298	0

Identifying $\chi \propto |t|^{-\gamma}$ predicts $\gamma = 1$.

δ At $t = 0$, Eq. (2.43) gives

$$\bar{m}(t = 0) = \left(\frac{h}{4u} \right)^{1/3}, \quad (2.50)$$

yielding $\delta = 3$.

ν, η The correlation length can be obtained by considering small fluctuations on top of the (Gaussian) mean-field solution, yielding the asymptotic solutions for the connected correlation function $\Gamma_c(x) \sim x^{2-d}$ for $x \ll \xi$ and $\Gamma_c(x) \sim \xi^{(3-d)/2} \exp(-x/\xi)/x^{(d-1)/2}$ for $x \gg \xi$, where $\xi \sim (at)^{-1/2}$ for $t > 0$ and $\xi \sim (-2at)^{-1/2}$ for $t < 0$. We thus identify $\nu = 1/2$ and $\eta = 0$.

The critical exponents for the Ising universality class are summarized in Table 2.1. Note that the mean-field predictions contain a flair of universality since they do not depend on microscopic details. They are however too universal in the sense that there is no differentiation between spatial dimensions. In the next sections, we will argue why mean-field theory fails for $d < 4$.

2.4.3 The neglected importance of fluctuations on all scales

Recall that mean-field theory is the saddle-point approximation to a theory characterized by a Landau free energy. Below the so-called *upper critical dimension* d_u , mean-field theory is no longer reliable because fluctuations start modifying the saddle-point conclusions²². For d less than the *lower critical dimension* ($d_l = 2$ for continuous symmetries and $d_l = 1$ for discrete symmetries) fluctuations are strong enough to destroy the ordered phase. In between $d_l < d < d_u$, they are strong enough to invalidate saddle point results, but not sufficiently powerful to completely destroy the ordered phase.

The importance of fluctuations can be roughly estimated by comparing fluctuations of $m(x)$ over a distance ξ with its average value \bar{m} . If fluctuations are small,

²²Note that the value of the upper critical dimension depends on the nature of the critical point, e.g. for a tricritical point we have $d_u = 3$.

then

$$\frac{\Gamma(\xi)}{\bar{m}^2} = \frac{\xi^{2-d}}{-at/4u} \ll 1, \quad (2.51)$$

or, using $\xi \sim (-at)^{-1/2}$, we find $u(a|t|)^{(d-4)/2} \ll 1$. We see that this particular instance of the *Ginzburg criterion* can be fulfilled for $t \rightarrow 0$ only if $d > 4$. More generally, long wavelength fluctuations dominate the critical behavior in spatial dimensions $d < 4$, and it is exactly these fluctuations which are ignored in mean-field theory when the correlation length diverges. To properly deal with long-wavelength fluctuations, one must average step-by-step, accounting for all length scales.

Put differently, Landau theory fails for $d < 4$ because it only considers fluctuations with wavelengths $\lambda < L$ where L is a mesoscopic averaging scale $a \leq L \leq \xi$. Since the average magnetization $m(x)$ is averaged over a region of size L , one can average over microscopic variations in the magnetization only if the average $m(x)$ remains unchanged. So fluctuations with wavelengths $\lambda < L$ can be taken into account statistically, but those for which $L < \lambda \leq \xi$ are left out of the picture. It is of course these fluctuations which proliferate as one approaches the critical point where $\xi \rightarrow \infty$. In this sense, Landau theory is a compromise between statistical mechanics and hydrodynamics [28]. We will see in Sec. 2.5 that the renormalization group tries to solve this problem by taking all wavelengths $a \leq L \leq \xi$ into account. The difference will turn out to be that the couplings t and u , which were constant in Landau theory, now actually have to depend on the coarse-graining scale L for $a \leq L \leq \xi$. More precisely, the couplings have to flow if we want physical results to be independent of L , and since $\xi \rightarrow \infty$ at criticality, all intermediate wavelength fluctuations have to be taken into account.

2.4.4 Mean-field theory and anomalous dimensions

By restricting to mean-field theory in this section, we might have given the wrong impression that the Landau free energy prescription leads to macroscopic theories which yield physical answers without any reference to the lattice cutoff a . We would like to stress that, except for the mean-field approximation, the limit $a \rightarrow 0$ cannot be taken straightforwardly because it can be shown to lead to ultraviolet divergences in the free energy. In Sec. 2.7.2, we will discuss the Gaussian model, which is almost identical to the mean-field theory described before. There, it will become clear that the correct procedure to deal with these divergences is to let the couplings flow. Note that the fact that ultraviolet divergences do not affect infrared singularities only happens in trivial models like the Gaussian model. This is important to keep in the back of one's mind, since critical exponents are determined by the nature of infrared divergences.

Another way to understand the dangers of boldly sending lattice spacings to zero is by considering dimensional analysis. The scaling hypothesis boils down to measuring any quantity X with dimensions $[X] = L^{-y}$, where L denotes a length, to be proportional to ξ^{-y} in the vicinity of the critical point. Since βF is dimensionless,

$\beta F/V = \beta f$ has dimension L^{-d} , and, from Eq. (2.34), $[\Gamma(x)] = L^{2-d-\eta}$, so that

$$[M/V] = [\langle m(x) \rangle] = L^{(2-d-\eta)/2}. \quad (2.52)$$

The dimension of $m(x)$ is however $[m(x)] = L^{(2-d)/2}$. The naïve conclusion is that ensemble averaging should not change the dimension, and hence $\eta = 0$. Ensemble averaging does however change the dimension in a subtle way because it introduces a length scale into the problem: the ultraviolet cutoff a . Indeed, under a scale transformation $x' = x/b$, we have that $m(x/b) = b^{(2-d)/2}m(x)$, while an anomalous contribution arises for

$$\langle m(x/b) \rangle \equiv f(x/b; a/b) = b^{(2-d-\eta)/2} f(x; a). \quad (2.53)$$

Anomalous dimensions have their origin in the changes to the finite, effective cutoff under a scale transformation. In models more complicated than (Gaussian) mean-field theory, the arbitrary RG scale set by the lattice spacing influences the infrared singularity at $t = 0$, leading to anomalous dimensions $\eta \neq 0$, which we will encounter in Sec. 2.7.4 and Sec. 2.8.

2.4.5 Symmetry-breaking phases

A cornerstone of the Landau–Ginzburg paradigm is the intimate relation between phase transitions and the concept of symmetry breaking. Spontaneously broken symmetries are symmetries of the Hamiltonian (or of the action) which are no longer reflected in the macrostate of the statistical system (or in the ground state of the quantum system). Broken symmetries can be either discrete (e.g. \mathbb{Z}_2 spin-flip invariance in the Ising model) or continuous (e.g. rotation in $O(n)$ scalar field theory). In both cases, symmetry-breaking phases of matter are characterized by an *order parameter* which captures a quantity that is not invariant under the symmetry under consideration and has a non-zero expectation value in the broken phase. The phase with broken symmetry is often referred to as the ordered phase, since it establishes a long-range order, while the unbroken, high-temperature phase is called the symmetric phase. Note that we have seen in Eq. (2.21) that the analogue of temperature in field theories is some nonlinear coupling constant. In the context of symmetry breaking, this implies that phase transitions in field theory occur as a function of a coupling constant instead of the temperature. The resulting physics is however indistinguishable.

As an example for the discrete case, consider the breaking of the spin-flip symmetry $\sigma_i \rightarrow -\sigma_i$ in the Ising model in the limit of zero external field. The order parameter is given by $\langle \sigma_i \rangle$ since the magnetization is nonzero in the low-temperature phase where the symmetry is broken. The case of continuous symmetries is rather more interesting because spontaneously breaking a continuous symmetry is intimately tied to the presence of gapless excitations. These so-called Nambu–Goldstone modes are associated with long-wavelength fluctuations of the order parameter. Familiar examples include phonons in crystals breaking translation invariance, spin waves in ferromagnets breaking rotational invariance, and Higgs modes breaking

local gauge symmetry in superconductors and electro-weak theory. At finite temperature, long-wavelength thermal fluctuations of the order parameter destroy the long-range order, and prevent spontaneous symmetry breaking from happening in one- and two-dimensional systems with short-range interactions. This is the content of the Mermin-Wagner-Coleman theorem. The implications for quantum systems²³ follow from the analogy between a quantum system in d spatial dimensions and a classical system in $d + 1$ dimensions, where the additional imaginary time dimension has an extent determined by the inverse temperature β . For any non-zero temperature, there exist fluctuations of the continuous order parameter at length scales greater than $v\beta$, where v denotes the characteristic velocity of the system²⁴, and these fluctuations are governed by classical statistical mechanics. The Mermin-Wagner-Coleman theorem thus implies that no continuous symmetry can be broken in two dimensions except at zero temperature, i.e. two-dimensional systems with a continuous symmetry cannot be ordered at finite temperature. For one-dimensional quantum systems, such breaking can remain impossible even at zero temperature due to quantum fluctuations restoring the symmetry. This behavior confirms the trend that as we go to lower dimensions, fluctuations become more proficient at destroying any potential order.

Interestingly, there are ways to avoid the ruthless Mermin-Wagner-Coleman theorem. A famous and Nobel-prize winning example is the infinite-order Berezinskii-Kosterlitz-Thouless (KT) phase transition in the two-dimensional XY -model, which is the $n = 2$ case of the $O(n)$ model defined by

$$H = -J \sum_{\langle ij \rangle} \cos(\theta_i - \theta_j) - \sum_j h_j \cos \theta_j, \quad (2.54)$$

where we have parametrized the unit-length rotor of Eq. (2.4) as $\mathbf{n}_i = (\cos \theta, \sin \theta)$. In contrast to the continuous phase transitions we have discussed up to now, the KT-transition does not break any symmetry. If we were to take the spontaneous magnetization as the local order parameter, we would find that $\langle \mathbf{n}_i \rangle = 0$ at both sides of the transition. At any finite temperature $T > 0$, there is no true long-range order but there still appears to be a phase transition for a critical temperature T_c , separating a low-temperature quasi-ordered phase with algebraically decaying correlation functions, where the power law depends on the temperature, from a high-temperature disordered phase with exponentially decaying correlation functions. The relevant degrees of freedom turn out to be vortices, stable topological defects, which are bound in pairs below T_c and deconfined above that temperature, rendering the KT-transition the epitome of a *topological phase transition*.

²³Note that we implicitly consider infinite quantum many-body systems since the “breaking” inherent to spontaneous symmetry breaking requires all degenerate ground states to be orthogonal to each other in the infinite volume limit, leading to super-selection sectors.

²⁴Here we have again invoked the de Broglie wavelength as a measure of the applicability of classical statistical mechanics.

2.5 Renormalization: concepts and ideas

Having provided a sufficient background to understand the task ahead, let us now introduce the Wilsonian concepts and ideas of the renormalization group.

2.5.1 Kadanoff's block-spin renormalization group

The success of the scaling hypothesis Eq. (2.24) in predicting scaling relations between critical exponents strongly suggests that the only relevant length scale close to the critical point is the (diverging) correlation length ξ . In this sense, critical behavior is determined by statistically self-similar fluctuations up to the scale set by $\xi \rightarrow \infty$.

In 1966, Kadanoff exploited this insight to derive the known scaling relations (and new *hyperscaling*²⁵ relations involving the spatial dimension d) by mapping a near-critical system onto itself while reducing the amount of effective, correlated degrees of freedom [19]. Following Kadanoff, we consider the Ising Hamiltonian,

$$H = -J \sum_{\langle ij \rangle} \sigma_i \sigma_j - h \sum_i \sigma_i, \quad (2.55)$$

on a hypercubic d -dimensional lattice with lattice spacing a . Actually, we will be interested in the *reduced Hamiltonian*,

$$H[\{\sigma\}; t, h] \equiv \beta H = -J \sum_{\langle ij \rangle} \sigma_i \sigma_j - h \sum_i \sigma_i, \quad (2.56)$$

where $J \equiv J/(k_B T)$ and $h \equiv h/(k_B T)$ are now understood to be reduced couplings. We have also introduced a dimensionless variable $t = (J - J_c)/J_c$ to measure the deviation from criticality, so that the tuple $(t, h) = (0, 0)$ tunes the Hamiltonian to criticality. We now treat all b^d spins σ_i in a block I of linear size ba as a single effective spin Σ_I and rescale the system back to its original scale $\mathbf{x}' = \mathbf{x}/b$. After one step, the number of spins N is reduced by a factor of b^{-d} . Crucially, we then assume that after the coarse-graining²⁶ and rescaling in this way, the near-critical system can be equally well described by a nearest-block-neighbor Hamiltonian of the same form,

$$H'[\{\Sigma\}; t', h'] = -J' \sum_{\langle IJ \rangle} \Sigma_I \Sigma_J - h' \sum_I \Sigma_I, \quad (2.57)$$

but with different couplings (t', h') . For this equivalence to be of any value, we need to be able to relate the “bare” couplings (t, h) to the “renormalized” couplings

²⁵Hyperscaling relations are however not generally valid for $d > 4$, which was only later understood via RG arguments. For $d > 4$, a dangerously irrelevant variable (see footnote 36) appears whose influence forces $d \equiv (2 - \alpha)/\nu$ to remain at 4 for $d > 4$ [29].

²⁶In practice, the coarse-graining procedure can be implemented for example using a simple majority rule $\Sigma_I = b^{-d} \sum_{i \in I} \sigma_i$ or a decimation rule $\Sigma_I = (\text{central spin} \in I)$, but note that the explicit details of the coarse-graining map are of no importance here (see Sec. 2.10 for several explicit real-space RG prescriptions).

(t', h') . Kadanoff achieved this by arguing that this is plausible since we assume that $b \ll \xi/a$, i.e. the block size is larger than the lattice spacing but smaller than the correlation length. Indeed, because $\xi \rightarrow \infty$ at criticality, we can, asymptotically, choose the value of our blocking parameter b rather arbitrarily. This idea was an absolutely crucial insight. In particular, Kadanoff argued, we can choose it such that the coupling of the magnetic field h to a block Σ_I of b^d spins is approximately equal to the coupling to b^d average spins,

$$\Sigma_I \simeq \frac{1}{b^d \zeta(b)} \sum_{i \in I} \sigma_i, \quad (2.58)$$

where $\zeta(b)$ is a renormalization factor ensuring that the variations of the fluctuations of the effective spins match those of the original ones²⁷. Introducing a similar, thermal renormalization factor $\theta(b)$, we arrive at the approximate recursion relations,

$$t' \approx \theta(b)t, \quad h' \approx b^d \zeta(b)h, \quad (2.59)$$

Starting slightly away from criticality, the initial system has a finite but large correlation length $\xi(t, h)$, which is reduced by a factor b after a single iteration due to the spatial rescaling. The renormalized Hamiltonian is then even less critical and the above recursion relations continue to push the parameters further away from the origin. The scaling factors $\theta(b)$ and $\zeta(b)$ thus have to be positive. In fact, we can even deduce their functional form, since we have the trivial no-scaling expression $\theta(1) = 1$ and the semigroup property $t'' = \theta(b_2)t' = \theta(b_2)\theta(b_1)t = \theta(b_1 b_2)t$. The unique functional solution of these equations is a *power law* $\theta(b) = b^\lambda$, so that

$$t' \approx b^\lambda t, \quad h' \approx b^{d-\omega} h, \quad (2.60)$$

where we have similarly rewritten the magnetic scaling factor $\zeta(b) = b^{-\omega}$. What Kadanoff actually assumes here is that $t'(t, h)$ is an analytic function of t , even at criticality, hoping that only spins in the neighborhood of the block are of any importance in calculating t' . In this way, non-analyticities can only arise for quantities involving the entire lattice [25].

Note that the assumptions of Kadanoff's picture leading to Eq. (2.60) already allow us to derive the scaling form of the free energy, of correlation functions, and of other bulk quantities derived from the free energy. We will however postpone these derivations to Sec. 2.6, where it will become clear that $\lambda = 1/\nu$ and $\omega = \beta/\nu = (d - 2 + \eta)/2$. Using these results, all six critical exponents can be expressed in terms

²⁷Using the metaphor of a pixelated image, coarse-graining corresponds to decreasing the resolution by changing the pixel size, rescaling restores the original resolution, and the renormalization step changes the contrast of the image so that it matches the original [15].

of just two independent ones (ν and η):

$$\alpha = 2 - \nu d, \quad (2.61)$$

$$\beta = \nu(d - 2 + \eta)/2, \quad (2.62)$$

$$\gamma = \nu(2 - \eta) \quad (2.63)$$

$$\delta = (d + 2 - \eta)/(d - 2 + \eta). \quad (2.64)$$

To accentuate the importance of Wilson's contribution to renormalization group theory, it is crucial to emphasize that Kadanoff's block-spin picture does not *explain* why the renormalized Hamiltonian should resemble the original one at all. This assertion only holds exactly for the one-dimensional Ising model, and quickly fails in higher dimensions as demonstrated in Sec. 2.10. Spins have to be allowed to fluctuate at many length scales at once, and a single effective coupling is flagrantly insufficient. The Kadanoff picture however correctly suggests that a small, fixed number of couplings is sufficient to capture the scaling behavior near criticality, but, again, provides no explanation. There also seems to be no inherent reason why the power-law scaling factors λ and ω cannot be completely different for every physical system.

It is becoming painfully clear that we have been rather schizophrenic up to now by tacitly assuming and simultaneously avoiding to explain the notion of *universality*²⁸. Let us now elucidate the general Wilsonian framework which not only supports and explains the intuition behind Kadanoff's heuristic scaling picture, but also paves the way for quantitative RG calculations.

2.5.2 Manifolds and flows

Consider yet again a spin system in d dimensions consisting of N spins denoted by $\sigma(\mathbf{x})$. Instead of calculating the partition function in one fell swoop, we will split the set $\{\sigma(\mathbf{x})\}$ into two parts: $N' = N/b^d$ spins $\{\sigma_{<}(\mathbf{x})\}$ which we leave untouched as fluctuating variables and $N - N'$ remaining spins $\{\sigma_{>}(\mathbf{x})\}$ which we integrate (or sum) over. This separation of degrees of freedom entails a coarse-graining procedure without explicitly specifying any details. In this way, the partial trace implicitly defines an *effective Hamiltonian*

$$e^{H_{\text{eff}}\{\{\sigma_{<}\}\}} = \text{Tr}_{N-N'}^{\sigma_{>}} \left(e^{H\{\{\sigma_{<}\} \cup \{\sigma_{>}\}\}} \right), \quad (2.65)$$

²⁸At the risk of spoiling the remainder of this chapter: some people are of the opinion that Wilson's formalism also does not *truly* explain universality (whatever *truly* explaining something might mean), and that the underlying assumptions have merely shifted to assumptions on the topology of an infinite parameter space: the existence of critical surfaces, flows, and fixed points. We find this judgement to be a sign of bad taste.

where we have defined the reduced Hamiltonian²⁹ as

$$H[\{\sigma(\mathbf{x})\}] \equiv -\frac{H[\{\sigma(\mathbf{x})\}]}{k_B T}. \quad (2.66)$$

This transformation is exact; if we trace over the renormalized spins, we recover the original partition function again, since

$$\begin{aligned} Z_{N'}[H'] &= \text{Tr}_{N'}^{\sigma'} \left(e^{H[\{\sigma'\}]} \right) = \text{Tr}_{N'}^{\sigma_{<}} \left(e^{H_{\text{eff}}[\{\sigma_{<}\}]} \right) \\ &= \text{Tr}_{N'}^{\sigma_{<}} \left(\text{Tr}_{N-N'}^{\sigma_{>}} \left(e^{H[\{\sigma_{<}\} \cup \{\sigma_{>}\}] } \right) \right) \\ &= \text{Tr}_N^{\sigma} \left(e^{H[\{\sigma\}] } \right) = Z_N[H], \end{aligned} \quad (2.67)$$

where $\{\sigma\} = \{\sigma_{<}\} \cup \{\sigma_{>}\}$ contains all spins. Note that the definition Eq. (2.65) implies not only that the partition functions (which are numbers) remain the same, but also that the probability distributions of quantities which only depend on coarse-grained spins are preserved. These include correlations between the long-wavelength degrees of freedom, so that the formal RG procedure leaves the large-scale physics of the system intact. One can of course always conjure up some arbitrarily complicated effective Hamiltonian resulting from the coarse-graining, but a tacit assumption of the renormalization group is that the *dominant* interactions of effective Hamiltonians will always be short-ranged³⁰.

If we now rescale spatial coordinates by $\mathbf{x}' = \mathbf{x}/b$ and relabel $\sigma'(\mathbf{x}') \equiv \sigma_{<}(\mathbf{x})$, we get a renormalized Hamiltonian $H'[\sigma'] \equiv e^{H_{\text{eff}}[\{\sigma_{<}\}]}$. Formally, this procedure defines an explicit renormalization group transformation with spatial rescaling factor b ,

$$H'[\{\sigma'\}] = \mathcal{R}_b(H[\{\sigma\}]), \quad (2.68)$$

which can be iterated to generate a sequence of renormalized reduced Hamiltonians $H^{(s)}$, recursively given by

$$H^{(s)} = \mathcal{R}_b \left(H^{(s-1)} \right) = \mathcal{R}_{b^s} \left(H^{(0)} \right), \quad (2.69)$$

where $H^{(0)} \equiv H$ and $H^{(1)} \equiv H'$ in the previous notation. Essentially, the operation \mathcal{R}_b describes the effect of a scale transformation on the Hamiltonian of the system when coarse-graining over blocks of size ba where a denotes the lattice spacing

²⁹Note that the same remark as in the case of the effective Landau-Ginzburg Hamiltonian in Sec. 2.4.1 applies here as well: only in the microscopic Hamiltonian do the couplings, which are implicit in our notation, scale with the temperature T .

³⁰Long-range interactions lead, among other things, to corrections to the discussion below and to different universality classes [12]. We will not consider long-range interactions.

cutoff. Note that we have made use of the semi-group property³¹

$$\mathcal{R}_b \mathcal{R}_{b'} = \mathcal{R}_{bb'} = \mathcal{R}_{b'} \mathcal{R}_b \quad (2.70)$$

to connect subsequent transformations.

Because we have rescaled and relabeled the renormalized spins after the exact coarse-graining, we expect them to be completely equivalent to the original variables. Upon closer inspection, it is easy to see that this assumption fails, and we cannot expect the original form of the Hamiltonian to be reproduced. For an initial Ising Hamiltonian in zero magnetic field with a (reduced) nearest-neighbor interaction $K_1 = J/(k_b T)$, the effective Hamiltonian eventually involves an infinite number of non-vanishing spin couplings for every conceivable and allowed interaction between local products of spins.

Let us illustrate Wilson's solution [6, 7] to this conundrum for the case of the Ising model. The key idea is to initially already introduce an infinite number of couplings by considering generalized Ising models

$$H = K_0 N + K_1 \sum_{\langle ij \rangle} \sigma_i \sigma_j + K_2 \sum_{\langle\langle ij \rangle\rangle} \sigma_i \sigma_j + K_3 \sum_{\text{plaquettes}} \sigma_i \sigma_j \sigma_k \sigma_l + \dots, \quad (2.71)$$

where K_0 is a constant coupling term, which acts as a physically immaterial yet important free energy offset. These Hamiltonians are characterized by a tuple $K = (K_1, K_2, \dots)$, marking a point on the manifold of (infinite) reduced couplings associated to that family of Hamiltonians. The familiar Ising model is recovered by setting $K = (K_1, 0, 0, \dots)$. In the infinite coupling space, the discrete RG flow can then be described by iterating

$$K' = \mathcal{R}_b(K). \quad (2.72)$$

After one iteration, the generalized Ising model looks like

$$H' = K'_0 N' + K'_1 \sum_{\langle IJ \rangle} \sigma_I \sigma_J + K'_2 \sum_{\langle\langle IJ \rangle\rangle} \sigma_I \sigma_J + K'_3 \sum_{\text{plaquettes}} \sigma_I \sigma_J \sigma_K \sigma_L + \dots, \quad (2.73)$$

where we have summed over all configurations $\{\sigma_i\}$ consistent with $\{\sigma_I\}$.

It is this remarkable insight of Wilson which eliminates the absurdity inherent in Kadanoff's block-spin idea: we should not be surprised that an infinite number of interactions show up when coarse-graining, since they have been there all along (their initial couplings were just set to zero). The renormalization group transformation Eq. (2.72) takes us out of the way too small submanifold of nearest-neighbor Ising models and allows an infinite number of couplings to flow and adjust during the

³¹Renormalization group transformations are not necessarily invertible, i.e. it is not always possible to unambiguously retrace one's steps when coarse-graining. In this sense, RG transformations generically only constitute a semi-group (and a discrete one on the lattice).

coarse-graining process. Additionally, the picture of flows in theory space explains how sharp non-analytical phase transitions can emerge from smooth, analytic initial data by iterating a well-behaved recursion formula an infinite number of times.

2.5.3 Fixed points and universality

The smoothness of the RG transformation is the consequence of the fact that at every iteration we only consider a finite number of degrees of freedom, and implies that universal critical properties are preserved under renormalization. It also helps ensuring that the critical point of the original Hamiltonian maps onto that of every subsequent effective Hamiltonian. In this way, *critical trajectories* can emanate from a physical critical point, whose topology could in general be horrifically complicated. For well-designed RG transformations however, it seems to be the case that critical trajectories asymptotically terminate in a *fixed point* reduced Hamiltonian H^* whose reduced couplings we will denote by $K^* = (K_1^*, K_2^*, \dots)$, a point on the previously introduced manifold of (infinite) reduced couplings.

Fixed points³² are solutions of the fixed-point equation

$$K^* = \mathcal{R}_b(K^*), \quad (2.74)$$

and correspond to Hamiltonians describing statistically self-similar configurations. The correlation length $\xi(K)$, which is a function of the parameters in the Hamiltonian, behaves as $\xi(K) = b\xi(\mathcal{R}_b(K))$, which implies that the correlation length at a fixed point must either be zero or infinity. Correlation length $\xi(K^*) = 0$ fixed points are either trivial, corresponding to independent fluctuations at each point which describe either complete disorder (infinite temperature) or complete order (zero temperature), or are topologically ordered³³. A non-trivial fixed point with $\xi(K^*) = \infty$ describes a critical point and defines a *universality class* of critical behavior which attracts all systems whose critical trajectories eventually end up in the fixed point K^* .

The stability of the fixed point can be studied by using the analyticity of the RG transformation to linearize the recursion relations in the neighborhood $K^* + \delta K$ of the fixed point,

$$\mathcal{R}_b(K^* + \delta K) = K^* + \delta K'(K) = K^* + [\mathfrak{R}_b]\delta K, \quad (2.75)$$

where we have defined the matrix

$$[\mathfrak{R}_b]_{\alpha\beta} = \left. \frac{\partial K'_\alpha}{\partial K_\beta} \right|_{K^*}. \quad (2.76)$$

³²Note that fixed points are but the simplest kind of asymptotic behavior of RG flows. Other asymptotic behavior, such as limit cycles, can also occur and has been studied [30].

³³Similar to symmetry-breaking phase transitions, there also exist topological phase transitions between topological phases or between a topological phase and a trivial phase. Additionally, topological phases can be further characterized based on their interplay with symmetries (see Sec. 2.7.5).

Close to K^* , the RG flow thus boils down to

$$K'_\alpha - K_\alpha^* = \sum_\beta [\mathfrak{R}_b]_{\alpha\beta} (K_\beta - K_\beta^*). \quad (2.77)$$

Diagonalizing \mathfrak{R}_b yields left³⁴ eigenvectors $\{e^i\}$ and corresponding eigenvalues $\{\lambda^i(b)\}$. The *scaling fields* $u_i = \sum_\alpha e_\alpha^i (K_\alpha - K_\alpha^*)$ are made up of linear combinations of the deviations from the fixed point and transform multiplicatively close to the fixed point:

$$u'_i = \sum_\alpha e_\alpha^i (K'_\alpha - K_\alpha^*) = \sum_{\alpha,\beta} e_\alpha^i [\mathfrak{R}_b]_{\alpha\beta} (K_\beta - K_\beta^*) \quad (2.78)$$

$$= \lambda^i(b) \sum_\beta e_\beta^i (K'_\beta - K_\beta^*) = \lambda^i(b) u_i \quad (2.79)$$

The semi-group property Eq. (2.70) additionally implies that the linearized matrices \mathfrak{R}_b for different b commute and can thus be diagonalized simultaneously, i.e. the eigenvectors $\{u_i\}$ are actually independent of the rescaling factor b . It also implies that

$$u_i \mathfrak{R}_b \mathfrak{R}_{b'} = \lambda^i(b) \lambda^i(b') u_i = u_i \mathfrak{R}_{bb'} = \lambda^i(bb') u_i, \quad (2.80)$$

which, together with the condition $\lambda^b(1) = 1$ for $b = 1$ (no scaling), yields a power law form $\lambda^i(b) = b^{y_i}$ for the eigenvalues, so that

$$u'_i = b^{y_i} u_i. \quad (2.81)$$

The $\{y_i\}$ are called *renormalization group eigenvalues* or *anomalous dimensions*, and will turn out to be related to the critical exponents. Even though quantities such as critical exponents should be independent of the arbitrary scaling factor b , it is important to note that approximate values obtained from approximate RG flows such as block-spin RG (see Sec. 2.10) or tensor network renormalization methods (see Sec. 3.5) may contain a weak dependence on b and other details of the RG transformation.

Assuming³⁵ that $y_i \in \mathbb{R}$, there are three cases for the flow behavior of the $\{u_i\}$ near the fixed point:

- $y_i > 0$ (relevant): the deviation of the fixed point along the direction u_i increases under scaling since $b^{y_i} > 1$; the RG flow is driven away from the fixed point

³⁴The linearised RG flow matrix $[\mathfrak{R}_b]_{\alpha\beta}$ is not necessarily symmetric so its left eigenvectors need not coincide with its right eigenvectors.

³⁵Complex eigenvalues can occur since \mathfrak{R}_b is not symmetric in general, but these lead to RG strange trajectories which spiral around the fixed point, either converging if $\text{Re}(y_i < 0)$ or diverging if $\text{Re}(y_i > 0)$.

- $y_i < 0$ (irrelevant³⁶): the deviation of the fixed point along the direction u_i decreases under scaling since $b^{y_i} < 1$; the RG flow is driven towards the fixed point
- $y_i = 0$ (marginal): the linearised equations are insufficient to determine the flow behavior since $b^{y_i} = 1$; higher order terms are necessary to determine whether the u_i is marginally relevant, marginally irrelevant, or exactly marginal

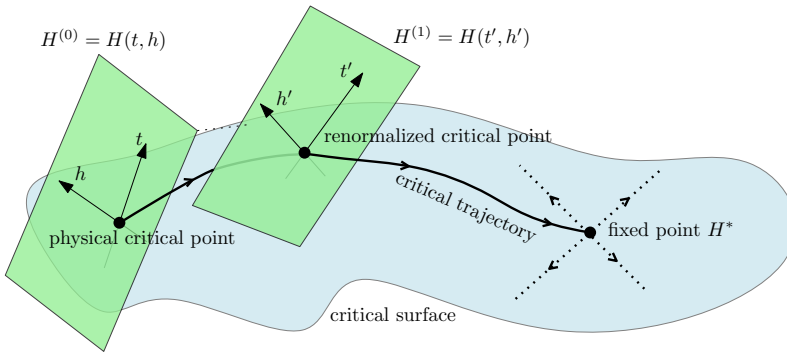


FIGURE 2.4: Renormalization group flow of a critical theory along the critical trajectory towards the fixed point on the critical surface in infinite coupling space.

Consider a fixed point with k relevant eigenvalues and a total number of couplings k' (which is actually infinite). Near the fixed point, the codimension- k subspace spanned by the $(k' - k)$ irrelevant eigenvectors is called the *critical surface* of the fixed point K^* and contains all nearby points with $\xi(K_c) = \infty$ which are attracted to the fixed point³⁷. In order to end up on the critical surface, one has to tune the k relevant couplings to zero. The resulting RG flow then guarantees that the long-distance properties of all points on the critical surface are determined by the same fixed point K^* in the infinite coupling space (see Fig. 2.4). This is the origin of *universality*, namely that Hamiltonians which only differ in terms of irrelevant operators will give rise to identical critical behavior. More realistic systems have more complicated phase diagrams, including multiple non-trivial fixed points, tricritical fixed points, and intricate RG flows which can exhibit *cross-over behavior*: at different length scales, different fixed points influence the properties of the same physical system. Note that critical fixed points can act as ultraviolet or infrared fixed points depending on the RG trajectories. Non-critical fixed points however always act as infrared sinks because they do not support relevant directions.

³⁶Irrelevant operators can also be *dangerously irrelevant*, meaning that, notwithstanding their irrelevant nature, their effects can still be felt close to the fixed point [31]

³⁷For a point K_c on the critical surface, $\xi(K_c) = \infty$ since $\xi(K)$ decreases under the RG flow and $\xi(K^*) = \infty$.

Example: Ising model

At the risk of being tedious, let us provide a very explicit example of the general framework. For the critical short-range Ising model, we have $k = 2$ relevant eigenvalues, corresponding respectively to the thermal and symmetry-breaking magnetic eigenvalue y_t and y_h with scaling fields $u_1 = t = (T - T_c)/T_c$ (reduced temperature) and $u_2 = h = H/(k_B T_c)$ (reduced magnetic field). All remaining scaling fields are irrelevant but vitally important. Indeed, for an RG trajectory to lay on the critical surface, we must tune t and h to zero. Note that this in itself does not constitute an RG flow, we are merely tuning the temperature and external magnetic field “knobs” of our microscopic model. The flow will then be confined to the critical surface and the system will be attracted to the non-trivial fixed point as the irrelevant variables vanish. Any RG trajectory that starts close to but not quite on the critical surface also flows towards the non-trivial fixed point as the irrelevant variables decrease at longer length scales. However, the increasing importance of the relevant scaling fields at even longer length scales will eventually drive the flow away from the critical surface to either the low-or high-temperature fixed point where $\xi(K) = 0$.

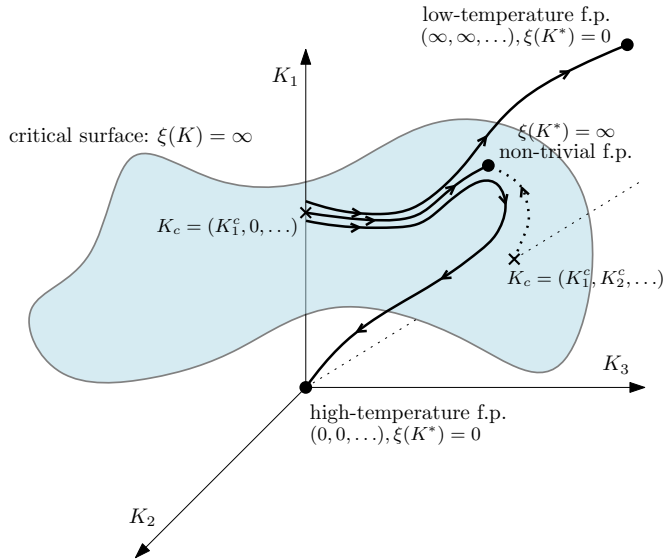


FIGURE 2.5: Projection of the infinite coupling space $K = (K_1, K_2, \dots)$ onto three couplings. The critical surface is shaded in blue and two critical points, corresponding to the nearest-neighbor Ising model and the generalized Ising model, are indicated with a cross. Both flow along the critical surface spanned by all irrelevant couplings of the non-trivial fixed point. For the nearest-neighbor Ising model, two other flows are drawn which are obtained by tuning the temperature away from T_c and which respectively lead to the trivial low- and high-temperature fixed points.

To really understand what is going on, let us consider the familiar Ising model in zero magnetic field with just one relevant variable for clarity (see Fig. 2.5). As

the temperature is varied, we find the tuple $K^c = (K_1^c, 0, 0, \dots)$ in the infinite coupling space as the intersection of K_1 with the codimension-1 critical surface. The associated correlation length is $\xi(K_c) = \infty$, and the model flows along the critical surface under the RG transformation to the fixed point K^* . Note that the temperature acts as some kind of rescaling with respect to the origin in the coupling space. A generalized Ising model in zero magnetic field becomes critical at a completely different intersection point $K^c = (K_1^c, K_2^c, K_3^c, \dots)$ when varying the temperature. Under the RG transformation along the critical surface, this critical generalized model flows to the exact same fixed point K^* in the infinite coupling space. We can thus appreciate that the *critical point* of any microscopic model in the same universality class is generically found some finite distance away from the universal attractive *fixed point* in infinite coupling space and differs in terms of couplings to irrelevant operators. Away from criticality, initial points flow to the respective trivial low-or high-temperature sinks³⁸ (∞, ∞, \dots) and $(0, 0, \dots)$, depending on the position with respect to the critical surface, which acts as a separatrix.

2.6 Scaling behavior and critical exponents

After a finite number of iterations of the analytic RG transformation, the values u_i should still depend analytically on the deviations (t, h) of the original theory from its critical point. The relevant variables must also vanish when $t \rightarrow 0, h \rightarrow 0$, so that, by symmetry, the leading order parameter transformation is given by

$$u'_t(t, h) = b^{y_t} t + \dots \quad (2.82)$$

$$u'_h(t, h) = b^{y_h} h + \dots, \quad (2.83)$$

coinciding with Kadanoff's scaling proposal Eq. (2.60).

2.6.1 Scaling of free energy

Because of the preservation Eq. (2.67) of the partition function under RG, we can consider the flow of the reduced free energy per site

$$f(\{K\}) = -N^{-1} \ln Z, \quad (2.84)$$

which gives

$$e^{-Nf(\{K\})} = e^{-Ng(\{K\}) - N'f(\{K'\})}, \quad (2.85)$$

where $N' = b^{-d}N$. The constant term $Ng(\{K\})$ corresponds to the free energy offset encountered in Eq. (2.71) and contains integrated-out short-range correlations within each block. We thus see that the complete free energy transforms

³⁸Or in terms of the coupling strength: strongly- or weakly-coupled fixed points.

inhomogeneously under the renormalization group,

$$f(\{K\}) = g(\{K\}) + b^{-d} f(\{K'\}), \quad (2.86)$$

but that the singular part (the second term) does transform homogeneously,

$$f_s(\{K\}) = b^{-d} f_s(\{K'\}). \quad (2.87)$$

In the vicinity of the fixed point, we can write the above equation explicitly in terms of the scaling fields,

$$f_s(u_t, u_h) = b^{-d} f_s(b^{y_t} u_t, b^{y_h} u_h), \quad (2.88)$$

where we have ignored³⁹ the irrelevant fields u_3, \dots . Let us now iterate the RG transformation n times

$$f_s(u_t, u_h) = b^{-nd} f_s(b^{ny_t} u_t, b^{ny_h} u_h), \quad (2.89)$$

until $|b^{ny_t} u_t| = u_{t0}$, where u_{t0} is arbitrary but sufficiently small so that the linear approximations in Eq. (2.82) and Eq. (2.83) remain valid. We find the homogeneous function

$$f_s(u_t, u_h) = |u_t/u_{t0}|^{d/y_t} f_s\left(\pm u_{t0}, \frac{u_h}{|u_t/u_{t0}|^{y_h/y_t}}\right), \quad (2.90)$$

which, in terms of t and h looks like

$$f_s(t, h) = |t/t_0|^{d/y_t} \mathcal{F}_{\pm}\left(\frac{h/h_0}{|t/t_0|^{y_h/y_t}}\right), \quad (2.91)$$

where $\mathcal{F}_{\pm} = f_s\left(\frac{h/h_0}{|t/t_0|^{y_h/y_t}}\right)$ is a universal scaling function. All non-universal dependence resides in the scale factors t_0 and h_0 . Note that we have recovered Widom's scaling ansatz Eq. (2.24).

2.6.2 Scaling of correlation functions

The renormalization group preserves not only the partition function, but also the probability measure of all long-wavelength degrees of freedom and thus the large-distance behavior of correlation functions. The spin-spin correlation function in the Ising model⁴⁰

$$G(\mathbf{x}_1 - \mathbf{x}_2, H) = \langle \sigma(\mathbf{x}_1) \sigma(\mathbf{x}_2) \rangle_H - \langle \sigma(\mathbf{x}_1) \rangle_H \langle \sigma(\mathbf{x}_2) \rangle_H \quad (2.92)$$

³⁹As we cannot assume that the initial constant u_3^0 in the Taylor expansion of an irrelevant eigenvalue in terms of t and h is zero, a non-zero value u_3^0 can lead to non-universal corrections to the asymptotic universal scaling behavior.

⁴⁰We have explicitly denoted dependence of the ensemble on (the couplings in) the Hamiltonian H .

can be obtained from the free energy by adding a source term $-\sum_{\mathbf{x}} h(\mathbf{x})\sigma(\mathbf{x})$ to the Hamiltonian and differentiating,

$$G(\mathbf{x}_1 - \mathbf{x}_2, H) = \frac{\partial^2}{\partial h(\mathbf{x}_1)\partial h(\mathbf{x}_2)} \ln Z[h]|_{h(\mathbf{r})=0} \quad (2.93)$$

Assuming short-range interactions and a block-spin renormalization, we can ignore the fact that $h(\mathbf{r})$ is actually slowly varying and regard it as a weak uniform field. This suggests that the renormalized Hamiltonian is of the same form

$$H'(\sigma') - \sum_{\mathbf{x}'} h'(\mathbf{x}')\sigma'(\mathbf{x}') \quad (2.94)$$

with $h'(\mathbf{x}') = b^{y_h} h(\mathbf{x})$. Since the renormalization group preserves the partition function, we must have

$$\frac{\partial^2 \ln Z'[h']}{\partial h'(\mathbf{x}'_1)\partial h'(\mathbf{x}'_2)} = \frac{\partial^2 \ln Z[h]}{\partial h(\mathbf{x}_1)\partial h(\mathbf{x}_2)}. \quad (2.95)$$

The left hand side is simply $G((\mathbf{x}_1 - \mathbf{x}_2)/b, H')$. The right hand side involves infinitesimally changing $h'(\mathbf{x}'_1) \rightarrow h'(\mathbf{x}'_1) + \delta h'(\mathbf{x}'_1)$ within the block labelled by \mathbf{x}'_1 , which boils down to changing all local fields $h(\mathbf{x})$ acting on the fine-grained spins within that block by an amount $\delta h(\mathbf{x}) = b^{-y_h} \delta h'(\mathbf{x}')$. The right hand side is thus equal to

$$b^{-2y_h} \langle (\sigma_1^{\mathbf{x}'_1} + \sigma_2^{\mathbf{x}'_1} + \dots)(\sigma_1^{\mathbf{x}'_2} + \sigma_2^{\mathbf{x}'_2} + \dots) \rangle_H, \quad (2.96)$$

where one includes all b^d spins in each block labelled by \mathbf{x}'_1 and \mathbf{x}'_2 on the coarse-grained lattice. If $|\mathbf{x}_1 - \mathbf{x}_2| \gg b$, all of these b^{2d} two-point correlations should be almost identical. Close to the fixed point, we thus find

$$G((\mathbf{x}_1 - \mathbf{x}_2)/b, H') = b^{2(d-y_h)} G(\mathbf{x}_1 - \mathbf{x}_2, H). \quad (2.97)$$

Note that this kind of reasoning is very similar to the operator product expansion we will encounter in Sec. 2.8. For large enough distances and isotropic interactions, the correlator depends only on the distance $x = |\mathbf{x}_1 - \mathbf{x}_2|$. Near the critical point, we let $h \rightarrow 0$ and find

$$G(x, t) = b^{-2(d-y_h)} G(x/b, b^{y_h} t). \quad (2.98)$$

Iterating the RG transformation n times until $b^{ny_h} t = t_0$, we end up with

$$G(x, t) = \left| \frac{t}{t_0} \right|^{2(d-y_h)/y_h} \mathcal{G} \left(\frac{x}{|t/t_0|^{-1/y_h}} \right). \quad (2.99)$$

2.6.3 Critical exponents from RG eigenvalues

From the scaling of the singular part of the free energy Eq. (2.91), one can obtain the critical exponents $\{\alpha, \beta, \gamma, \delta\}$ for the Ising universality class by taking appropriate limits of derivatives of the singular part of the free energy and identifying the powers in the resulting power laws,

$$\alpha = 2 - \frac{d}{y_t}, \quad \beta = \frac{d - y_h}{y_t}, \quad \gamma = \frac{2y_h - d}{y_t}, \quad \delta = \frac{y_h}{d - y_h}. \quad (2.100)$$

From the scaling of the spin-spin correlation function, the exponents $\{\nu, \eta\}$ can be obtained as follows. Away from criticality, we expect the correlation function Eq. (2.99) to decay as $e^{-r/\xi}$ for large r (where t is also large and mean-field theory is valid), leading to the identification $\xi \propto |t|^{-1/y_t}$. At the critical point $t = 0$, we iterate Eq. (2.98) until $r/b^n = O(r_0)$, where r_0 is a fixed distance much larger than the lattice spacing a or the range of the interactions, so that $G(r) \propto r^{-2(d-y_h)}$. Identifying the critical exponents, we find

$$\nu = \frac{1}{y_t}, \quad \eta = d + 2 - 2y_h. \quad (2.101)$$

All of the above critical exponents are given in terms of the RG eigenvalues y_t and y_h , which naturally explains the *scaling relations* between critical exponents we encountered in Sec. 2.3. What were once magical relations between universal numbers, turn out to be trivial algebraic identities involving RG eigenvalues.

2.6.4 Scaling operators and scaling dimensions

Before moving on, we want to point out an important subtlety. Near the fixed point, the scaling fields u_i constructed from the eigenvectors are linear combinations of the deviations ($K_\alpha - K_\alpha^*$) of the couplings from their fixed point values. Perturbing a relevant scaling field u_i for example, thus corresponds to changing the couplings in front of the corresponding linear combination of operators in the Hamiltonian. The latter corresponds to a set $\{S_\alpha\}$ of local products of spins $\sigma(\mathbf{x})$ for the effective Hamiltonian of the Ising model or to monomials of the fields in the effective action of a quantum field theory. Simple-looking operators in the effective Hamiltonian (like a nearest-neighbor spin interaction) could very well consist of a complicated arrangement of many different RG eigenoperators.

Having a continuum limit of a statistical mechanical model in mind, we can introduce *scaling operators* $\{\phi_i\}$ which couple to the scaling fields u_i . As $|\mathbf{x}_1 - \mathbf{x}_2| \rightarrow \infty$, one can show that their correlation functions behave as⁴¹

$$\langle \phi_i(\mathbf{x}_1) \phi_i(\mathbf{x}_2) \rangle \propto |\mathbf{x}_1 - \mathbf{x}_2|^{-2\Delta_i} \quad (2.102)$$

⁴¹Note that pure power law behavior only applies to scaling operators at the *fixed* point and not at the *critical* point. As we have seen, the critical point differs from the fixed point in terms of irrelevant operators, whose presence leads (among other effects) to corrections of the form $|\mathbf{x}_1 - \mathbf{x}_2|^{-\Delta_i - \Delta_j - \sum_k |y_k|}$, where the sum over k runs over a subset of irrelevant operators [12].

where we have defined the *scaling dimension*

$$\Delta_i = d - y_i. \quad (2.103)$$

Indeed, in the vicinity of the fixed point one can perturb by

$$\sum_i u_i \int \frac{d^d \mathbf{x}}{a^d} \phi_i(\mathbf{x}) \xrightarrow{\text{RG flow}} \sum_i b^{y_i} u_i \int \frac{d^d \mathbf{x}}{(ba)^d} \phi_i(\mathbf{x}), \quad (2.104)$$

which leaves the partition function invariant if we require that

$$\phi_i(\mathbf{x}) \rightarrow b^{\Delta_i} \phi_i(\mathbf{x}), \quad (2.105)$$

where Δ_i denotes the scaling dimension defined in Eq. (2.103). This definition of the scaling dimension relates the RG eigenvalue y_i of a scaling field to the asymptotic behavior of the two-point correlation function of the scaling operator to which that field couples, and corrects the naïve classical scaling dimension. The idea behind scaling operators and scaling dimensions will become more clear in connection to Sec. 2.8 for conformal field theories, where we will shift our attention from critical exponents to scaling dimensions and their associated scaling operators, which seem even more fundamental since all critical exponents follow from the values of the scaling dimensions.

2.7 Perturbative RG and effective field theories

“The ideas of this paper can be applied to relativistic quantum field theory. So the ideas of this paper are not special to the problem of critical phenomena. The basic problem causing the difficulties in understanding critical phenomena is the problem of the infinite number of degrees of freedom. This problem is also the bottleneck in quantum field theory and in many of the stubborn problems in solid-state physics.”

K. G. Wilson, 1971 [7]

Before sketching the results of the ϵ -expansion, let us first qualitatively connect the framework introduced in the previous sections to renormalization in quantum field theory (QFT). If we consider infinitesimal RG transformations where $b = \exp(l) \approx 1 + \delta l$, then the couplings of the action in the infinite coupling space will also transform infinitesimally,

$$K'_\alpha(b) = K_\alpha(1 + \delta l) = K_\alpha + \delta l \frac{dK_\alpha}{dl} + O(\delta l^2). \quad (2.106)$$

Expanding the recursion relations up to first order in δl , we thus find at a set of differential RG equations for the couplings,

$$\frac{d}{dl} K_\alpha = \beta_\alpha(K), \quad (2.107)$$

where the β -functions are components of the vector field generating the RG flow. These are called *renormalization group beta functions* in quantum field theory, where they usually differ by a sign and are expressed in momentum space rather than real space. The fixed points now correspond to the zeroes of the beta functions, and the RG eigenvalues y_i are the eigenvalues of the matrix $\partial\beta_a/\partial K_\beta$, evaluated at the zeroes of the beta functions. We can actually repeat the formal development of the previous sections by substituting the Hamiltonian for the action $S[\phi; g_i]$ of a field $\phi(\mathbf{x})$ whose interactions are captured by a set of running couplings $\{g_i\}$. In particular, the discussion about scaling operators Eq. (2.105) translates to the breakdown of naïve dimensional analysis.

Note that the scale invariance of a classical action certainly does not imply scale invariance at the quantum level. A quantum field theory makes no sense without a regularization prescription, which necessarily introduces a length scale into the theory. This regularization scale breaks the dilatation symmetry (or conformal symmetry, see Sec. 2.8), except at very particular points in the coupling space, where the theory becomes truly scale invariant (or conformally invariant) even in the presence of interactions. These points coincide with RG fixed points.

2.7.1 Universality in quantum field theories

For Wilson, the action of a generic QFT involves all types of operators, including irrelevant ones, and thus resides somewhere off the critical surface. The irrelevant operators are however quickly suppressed under the RG flow while the relevant ones become more important, which suggests that the flow of a generic QFT, if it starts off in the right basin of attraction, is very much attracted to the critical trajectory emanating from a fixed point. Its infrared behavior will resemble that of a fixed point theory perturbed by relevant operators. This is just another manifestation of universality, assuring us that properties of theories in the infrared are determined by a few relevant couplings. This brings us to the notion of an *effective field theory*. In fact, we have already encountered examples in Sec. 2.4, since the family of Landau-Ginzburg Hamiltonians can of course be regarded as an effective description of a wide variety of phenomena. In condensed-matter physics applications of field theory, it is generally very natural to construct effective actions by guessing the low-energy degrees of freedom and appropriate symmetries of the physical system under consideration. Even beyond the Landau-Ginzburg paradigm of symmetry breaking (see Sec. 2.7.5), the idea of effective actions survives in the sense that topological states of matter can be described using unitary topological quantum field theories which capture the low-energy behavior.

The situation seems reversed in the context of high-energy physics, where it is more conventional to start from a short-distance description that is potentially extremely complicated, even if we are solely interested in describing long-distance physics accessible to experiment⁴². Appreciating the concept of effective field

⁴²Here, we think of arbitrarily convoluted microscopic field theories and not of string theory, which might very well invalidate this point of view. Note that we do not reject the idea of grand mathematical theories of everything, and the statements in this paragraph carry no such indictments; they are purely pragmatic and in line with the theme of renormalization.

theories in high-energy physics boils down to acknowledging the fact that there can be no infinities arising from UV-divergent loop diagrams if we respect the ultraviolet cutoff for what it is: a limitation on the validity of field theories. There are of course examples of UV-complete quantum field theories, such as asymptotically free gauge theories in four dimensions. Quantum chromodynamics is well-defined at arbitrarily short distance scales since asymptotic freedom allows it to be traced back to a free field theory in the ultraviolet, where it can then be perturbed by a relevant operator. But this is of course a purely mathematical conclusion; physically, there are valid reasons to suspect new structure at sufficiently short length scales.

2.7.2 The Gaussian fixed point

Let us now apply the renormalization group framework to the Gaussian model, paving the way for the ϵ -expansion. The Gaussian model for an n -component field $\vec{m}(\mathbf{x})$ is obtained by keeping only the quadratic terms in the Landau-Ginzburg expansion Eq. (2.38), leading to the partition function

$$Z = \int \mathcal{D}\vec{m}(\mathbf{x}) \exp \left(- \int d^d \mathbf{x} \left(\frac{t}{2} m^2 + \frac{K}{2} (\nabla m)^2 + \frac{L}{2} (\nabla^2 m)^2 + \dots - \vec{h} \cdot \vec{m} \right) \right),$$

and is only defined for $t \geq 0$ since there is no quartic term to guarantee stability⁴³. The phase transition is thus approached from the disordered side $t \rightarrow 0+$.

For perturbative calculations involving continuum models, momentum-space renormalization techniques are preferred. Defining the Fourier modes

$$\vec{m}(\mathbf{q}) = \int d^d \mathbf{x} e^{i\mathbf{q} \cdot \mathbf{x}} \vec{m}(\mathbf{x}), \quad (2.108)$$

the partition function becomes

$$Z \sim \int \mathcal{D}\vec{m}(\mathbf{q}) \exp \left(- \int_0^\Lambda \frac{d^d \mathbf{q}}{(2\pi)^d} \left(\frac{t + Kq^2 + Lq^4 + \dots}{2} \right) |\vec{m}(\mathbf{q})|^2 + \vec{h} \cdot \vec{m}(\mathbf{0}) \right),$$

where the hypercubic Brillouin zone is approximated by a hypersphere of radius Λ , which implements the cutoff.

Instead of removing fluctuations at scales $a < x < ba$, we now remove Fourier modes in the momentum shell $\Lambda/b < q < \Lambda$ to implement the coarse-graining. By splitting the momenta into two subsets $\{\vec{m}(\mathbf{q})\} = \{\vec{m}(\mathbf{q}^<)\} \oplus \{\vec{m}(\mathbf{q}^>)\}$, the

⁴³For $t < 0$, a quartic term $um^4(\mathbf{x})$ with $u > 0$ is required to ensure a finite magnetization.

partition function decouples trivially,

$$Z \sim \exp\left(-\frac{n}{2}V \int_{\Lambda/b}^{\Lambda} \frac{d^d \mathbf{q}}{(2\pi)^d} \ln(t + Kq^2 + Lq^4 + \dots)\right) \times \int \mathcal{D}\tilde{\mathbf{m}}(\mathbf{q}) \\ \times \exp\left(-\int_0^{\Lambda/b} \frac{d^d \mathbf{q}}{(2\pi)^d} \left(\frac{t + Kq^2 + Lq^4 + \dots}{2}\right) |\tilde{\mathbf{m}}(\mathbf{q})|^2 + \vec{h} \cdot \tilde{\mathbf{m}}(\mathbf{0})\right).$$

The rescaling step $\mathbf{q}' = b\mathbf{q}$ then restores the cutoff to its original value, leading to the following rescaled partition function (up to a constant)

$$Z \sim \int \mathcal{D}\tilde{\mathbf{m}}(\mathbf{q}') \exp\left(-\int_0^{\Lambda} \frac{d^d \mathbf{q}'}{(2\pi)^d} b^{-d} \left(\frac{t + Kb^{-2}q'^2 + Lb^{-4}q'^4 + \dots}{2}\right) |\tilde{\mathbf{m}}(\mathbf{q}')|^2 + \vec{h} \cdot \tilde{\mathbf{m}}(\mathbf{0})\right),$$

Finally, we renormalize⁴⁴ the modes according to $\tilde{\mathbf{m}}'(\mathbf{q}') = \tilde{\mathbf{m}}(\mathbf{q}')/z$, leading to

$$Z \sim \int \mathcal{D}\tilde{\mathbf{m}}'(\mathbf{q}') \exp\left(-\int_0^{\Lambda} \frac{d^d \mathbf{q}'}{(2\pi)^d} b^{-d} z^2 \left(\frac{t + Kb^{-2}q'^2 + Lb^{-4}q'^4 + \dots}{2}\right) |\tilde{\mathbf{m}}'(\mathbf{q}')|^2 + z\vec{h} \cdot \tilde{\mathbf{m}}'(\mathbf{0})\right),$$

We can now read off the renormalized parameters

$$t' = z^2 b^{-d} t, \quad h' = zh, \quad K' = z^2 b^{-d-2} K, \quad L' = z^2 b^{-d-4} L, \dots \quad (2.109)$$

The Gaussian fixed point $(t, h) = (0, 0)$ is mapped to itself if we make sure that the remaining terms stay fixed, which can be done by choosing the renormalization factor as $z = b^{1+d/2}$. In that case, $K' = K$, and all remaining parameters scale to zero under repeated iteration. From the scaling of the two relevant directions

$$t' = b^2 t, \quad h' = b^{1+d/2} h, \quad (2.110)$$

we can infer that $y_t = 2$ and $y_h = 1 + d/2$, from which we can calculate the critical exponents⁴⁵ using Eq. (2.100),

$$\alpha = \frac{4-d}{2}, \quad \beta = \frac{d-2}{4}, \quad \gamma = 1, \quad \delta = \frac{d+2}{d-2}, \quad \nu = \frac{1}{2}, \quad \eta = 0. \quad (2.111)$$

⁴⁴This renormalization step corresponds to rescaling spins with $\zeta(b)$ in the block-spin approach of Sec. 2.5.1 (“changing the contrast of the image”).

⁴⁵The critical exponent β is actually not physical in the Gaussian model since the ordered phase $t < 0$ is not stable.

Note that all critical exponents immediately follow from the infinitesimal RG transformation, which expresses the rate of change of the coupling constants. Looking back at the mean-field theory critical exponents in Table 2.1, we observe that the value of α only agrees with mean-field theory for $d = 4$. This disagreement again indicates that we cannot ignore fluctuations for $d < 4$ (see Sec. 2.4.3).

2.7.3 Real-space perturbations

The fixed point Hamiltonian for the Gaussian model in real space (with lattice cutoff a) looks like

$$\beta H^* = \frac{K}{2} \int d^d \mathbf{x} (\nabla m)^2. \quad (2.112)$$

Under a combined spatial ($\mathbf{x} \rightarrow \mathbf{x}'$) and field rescaling $\vec{m}(\mathbf{x}) \rightarrow \zeta \vec{m}'(\mathbf{x}')$, scale invariance can be achieved by choosing $\zeta = b^{1-d/2}$. This tells us that a small perturbation with a general power of $\vec{m}(\mathbf{x})$ close to the fixed point behaves as

$$\beta H^* + u_k \int d^d \mathbf{x} m^k \xrightarrow{\text{RG flow}} \beta H^* + u_k b^d \zeta^k \int d^d \mathbf{x}' m'^k, \quad (2.113)$$

which suggests

$$u'_k = b^d b^{k(1-d/2)} u_k, \quad (2.114)$$

so that we find RG eigenvalues $y_k = k - d(k/2 - 1)$. This formula reproduces y_h and y_t respectively for $k = 1$ and $k = 2$, and indicates that the majority of operators are irrelevant at the Gaussian fixed point for $d > 2$. The operator we will now focus on is associated to $y_4 = 4 - d$, which is irrelevant for $d > 4$ but relevant for $d < 4$.

2.7.4 Perturbing the Gaussian fixed point: the ϵ -expansion

Let us now describe Wilson and Fisher's perturbative RG method that was among the first to quantitatively produce non-classical critical exponents by combining perturbation theory and renormalization group theory [25, 32]. The idea is to approach the Landau-Ginzburg Hamiltonian by perturbing the Gaussian model. We consider the reduced Hamiltonian with only lowest order Gaussian terms in zero magnetic field,

$$\beta H_0 + U = \int d^d \mathbf{x} \left(\frac{t}{2} m^2 + \frac{K}{2} (\nabla m)^2 \right) + u \int d^d \mathbf{x} m^4 + \dots \quad (2.115)$$

Even though higher order interactions will be generated by the flow, we do not include any higher order Gaussian terms nor higher powers and derivatives of m since we make use of the *a posteriori* information that all of these interactions will

turn out to be perturbatively irrelevant⁴⁶.

Carefully calculating Feynman diagrams up to second order in u leads to a coarse grained Hamiltonian containing several new interactions proportional to m^2 , m^4 , and m^6 , i.e. the parameter space (K, t, u) is not closed at this order. Given the remark in the previous paragraph however, we will pretend that this is not the case, and immediately state the resulting differential equations governing the RG flow⁴⁷:

$$\frac{dt}{dl} = 2t + \frac{4(n+2)K_d\Lambda^d}{t + K\Lambda^2}u - A(t, K, \Lambda)u^2, \quad (2.116)$$

$$\frac{du}{dl} = (4-d)u - \frac{4(n+8)K_d\Lambda^d}{(t + K\Lambda^2)^2}u^2, \quad (2.117)$$

where $K_d = 2\pi^{d/2}/((2\pi)^d\Gamma(d/2))$ and $A(t, K, \Lambda)$ is a numerical prefactor of u^2 in the coarse-grained Hamiltonian. The step from recursion relations to differential equations was done using the infinitesimal flow recipe given in the introduction of Sec. 2.7. The renormalization factor

$$z = b^{1+d/2+O(\epsilon^2)} \quad (2.118)$$

is actually unmodified up to second order in $\epsilon = 4 - d$ and is again chosen such that $K' = K$. In addition to the Gaussian fixed point $u^* = t^* = 0$, we now find the *Wilson-Fisher fixed point*⁴⁸ at

$$u_{\text{WF}}^* = \frac{K^2}{4(n+8)K_4}\epsilon + O(\epsilon^2) \quad (2.119)$$

$$t_{\text{WF}}^* = -\frac{(n+2)}{2(n+8)}K\Lambda^2\epsilon + O(\epsilon^2), \quad (2.120)$$

which has been expanded to first order in $\epsilon = 4 - d$. Linearizing around this non-trivial fixed point leads to a positive eigenvalue

$$y_t = 2 - \frac{(n+2)}{(n+8)}\epsilon + O(\epsilon^2), \quad (2.121)$$

and a second eigenvalue

$$y_u = -\epsilon + O(\epsilon^2), \quad (2.122)$$

which is negative for $d < 4$. The critical surface associated to the Wilson-Fisher fixed point is thus codimension-1 (one relevant eigenvalue) and can capture phase transitions. In Fig. 2.6, we schematically depict the topology of the second-order

⁴⁶One can do a perturbative stability analysis around the non-trivial Wilson-Fisher fixed point to show that, at least to first order in $\epsilon = 4 - d$, all additional interactions are irrelevant.

⁴⁷Note that the perturbation parameter u is not dimensionless and has dimensions $[u] = L^{d-4}$.

⁴⁸Even though the ϵ -expansion was a major breakthrough in the study of critical phenomena, this was not the direction Wilson intended to develop his formalism for he considered it a return to perturbation theory [33].

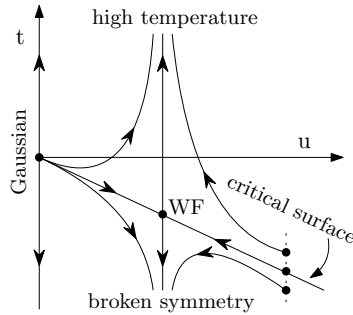


FIGURE 2.6: Schematic perturbative RG flows for $d < 4$. The critical surface of the Wilson-Fisher fixed point is the separatrix between trivial low- and high-temperature fixed points.

perturbative RG flows. Note that all dependence on microscopic parameters such as K and Λ has vanished from the final eigenvalues, which depend only on the number of components n of the field and the spatial dimension $d = 4 - \epsilon$. These eigenvalues characterize the universality class of rotational symmetry breaking in $d < 4$ for systems with short-ranged interactions. For $d > 4$, the non-trivial fixed point is unstable since both scaling fields are relevant. In that case, the approximation breaks down because the fixed point lies in the unphysical $u < 0$ region, signifying that we need to include the m^6 term to stabilize the system. The fixed point associated to the m^6 interaction then suggests an expansion in $\epsilon = 3 - d$.

The critical exponents ν and α can then be straightforwardly calculated from the RG eigenvalues:

$$\nu = \frac{1}{y_t} = \frac{1}{2} + \frac{1}{4} \frac{n+2}{n+8} \epsilon + O(\epsilon^2), \quad (2.123)$$

$$\alpha = 2 - d\nu = \frac{4-n}{2(n+8)} \epsilon + O(\epsilon^2). \quad (2.124)$$

By adding a term $-\vec{h} \cdot \vec{m}(\mathbf{q} = \mathbf{0})$ to the initial Hamiltonian, we can obtain the renormalized coupling h of the symmetry breaking field from $h' = zh = b^{1+d/2}h$ since the term is not affected by coarse-graining or rescaling, so that

$$y_h = 1 + \frac{d}{2} + O(\epsilon^2) = 3 - \frac{\epsilon}{2} + O(\epsilon^2). \quad (2.125)$$

The critical exponents β and γ are then given by:

$$\beta = \frac{d - y_h}{y_t} = \frac{1}{2} - \frac{3}{2(n+8)} \epsilon + O(\epsilon^2), \quad (2.126)$$

$$\gamma = \frac{2y_h - d}{y_t} = 1 + \frac{n+2}{2(n+8)} \epsilon + O(\epsilon^2). \quad (2.127)$$

The anomalous dimension η only becomes non-zero when going to higher orders

[8],

$$\eta = \frac{(n+2)}{2(n+8)^2} \epsilon^2 + O(\epsilon^3). \quad (2.128)$$

We would like to end this discussion with a few remarks. Since the original work of Wilson and Fisher, the ϵ -expansion has been carried out to fifth order using more advanced field theoretical RG schemes involving dimensional regularization and resummation methods. The perturbative results do however not necessarily get better by adding more orders, which is indicative of the non-convergent behavior of an asymptotic series expansion. Even though the predictions of the ϵ -expansion might not be numerically accurate per se, they are useful in the sense that they determine what types of universality classes one can expect in different dimensions. The crucial point is that the topology of flow diagrams such as Fig. 2.6 does not change when moving away from the upper critical dimension $d_u = 4$, since it is determined by the *signs* of the RG eigenvalues. This robustness also explains why it is not completely unreasonable to substitute $d = 3$ and even $d = 2$ into an $\epsilon = (4 - d)$ -expansion.

2.7.5 Beyond the Landau-Ginzburg paradigm

When Wilson mentioned that the ϵ -expansion is an example of renormalization group theory yielding results beyond Landau, it should be noted that he was referring to the possibility of obtaining non-classical critical exponents beyond the mean-field values obtained in Sec. 2.4.2 [28]. In recent years however, the phrase *beyond Landau* has taken on quite a different meaning. Since the observation of the fractional quantum Hall effect [34, 35], it has become clear that not all phases and phase transitions can be classified according to order parameters, symmetry breaking, and long-range correlations. Indeed, in terms of entanglement, all states associated to symmetry-breaking fixed points described by local order parameters are basically product states. Even in the absence of a global symmetry, gapped quantum phases at zero temperature are seen to break up into inequivalent classes, which correspond to distinct topologically ordered phases that cannot be connected to product states using local unitary transformations.

Topological phases of matter can then be defined through an equivalence class of local Hamiltonians [36, 37] whose low-energy physics is captured by a unitary topological quantum field theory (TQFT) [38, 39]. Systems with intrinsic topological order can exhibit a topological ground state degeneracy, protected gapless excitations on the edge, and anyonic excitations. In the presence of a global symmetry, symmetry-protected topological (SPT) phases can arise when no symmetry-preserving local unitary transformation is able to connect the state to a product state. Even though these SPT states do not possess intrinsic topological order, they cannot be treated in the Landau-Ginzburg framework of symmetry breaking since distinct SPT phases can have the same symmetry. The interplay between global symmetries and intrinsic topological order leads to so-called symmetry-enriched topological (SET) phases. We will come back to topological order in the context of tensor network states in Sec. 3.3.2 and in Chapter 6 where we will, quite surprisingly, relate the overlaps

of two *quantum* wave functions to the real-space RG flow of a *classical* partition function.

2.8 Operator product expansion and conformal field theory

Let us now shift our attention to the development of conformal field theory (CFT), which signified a major advance in the understanding of QFT and its applications to critical phenomena. For our purposes, we will be mainly interested in unitary *minimal models*, which are a particular class of analytically tractable (1+1)-dimensional CFTs corresponding to the scaling limit of statistical-mechanical models with Hermitian transfer matrices. In particular, we will see that conformal invariance and unitarity (or reflection positivity for statistical systems) puts strong constraints on the possible values of the critical exponents [40].

The important dynamical principle in CFT is the associativity of the operator algebra rather than Hamiltonians and Lagrangians. Indeed, the structure of CFTs allows one to define theories that are based solely on symmetry properties of correlation functions, without reference to any action or path integral. The key question is then to find a set of local operators which transform among themselves under conformal transformations. This point of view is already present in the operator product expansion (OPE), which, given a set of local operators, states that the product of two local operators can be rewritten as a (possibly infinite) linear combination of other local operators⁴⁹

$$\phi_i(\mathbf{x})\phi_j(\mathbf{y}) = \sum_k C_{ij}^k(\mathbf{x} - \mathbf{y})\phi_k(\mathbf{y}), \quad (2.129)$$

where the $C_{ij}^k(\mathbf{x} - \mathbf{y})$ are expansion coefficients. We can interpret singularities in this formula as a manifestation of the infinite fluctuations which occur at short distances as $\mathbf{x} \rightarrow \mathbf{y}$. Conformal bootstrap methods use OPE equations to constrain and solve CFTs, which has been very successful in two dimensions. Recently, this program has witnessed a revival in higher dimensions with the determination of extremely accurate critical exponents of the CFT capturing the critical three-dimensional Ising model [27].

Since it is not our intention to provide a full introduction to the topic of conformal field theories nor to overindulge in formalism we will not use later on, we will restrict ourselves to the most elementary notions.

2.8.1 Conformal invariance and quantum fields

We have already seen in previous sections that the invariance of a system under dilatation symmetry leads to the notions of scale invariance and self-similarity. In contrast to other symmetries, it is hard to see how dilatation symmetry constrains

⁴⁹Similar ideas were developed around the same time by (at least) Polyakov [41], Wilson [42, 43] and Kadanoff [44]. Note also the similarity to the reasoning in Sec. 2.6.2 where we estimated the behavior of correlation functions under block-spin RG.

the effective Hamiltonian. One exception occurs in two dimensions, where Polyakov [45] showed that a two-dimensional system which is invariant under translations, rotations, and global dilatations, is also automatically locally scale invariant, i.e. invariant under the larger class of angle-preserving conformal transformations $\mathbf{x} \rightarrow \mathbf{x}'$ leaving the metric tensor $g'_{\mu\nu}(\mathbf{x}') = \Lambda(\mathbf{x})g_{\mu\nu}(\mathbf{x})$ invariant up to a local scale factor corresponding to nonuniform rescaling and rotation.

A (1+1)-dimensional conformal field theory is described in terms of correlation functions of a set of conformal fields $\phi(z, \bar{z})$, where $z = x_1 + ix_2$ and $\bar{z} = x_1 - ix_2$ denote complex coordinates. Invariance under local conformal transformations can be thoroughly exploited because the local conformal group coincides with the set of all, not necessarily invertible, holomorphic mappings. Under any conformal map $z \rightarrow w(z)$, $\bar{z} \rightarrow \bar{w}(\bar{z})$, primary⁵⁰ fields $\phi(z, \bar{z})$ transform as

$$\phi'(w, \bar{w}) = \left(\frac{dw}{dz}\right)^{-h} \left(\frac{d\bar{w}}{d\bar{z}}\right)^{-\bar{h}} \phi(z, \bar{z}), \quad (2.130)$$

where we have introduced the holomorphic conformal dimension h and its anti-holomorphic counterpart \bar{h} . These fields can be interpreted as operators and their correlation functions as vacuum expectation values. The two-point correlation function of two primary fields is constrained by conformal symmetry to be of the form

$$\langle \phi_1(z_1, \bar{z}_1) \phi_2(z_2, \bar{z}_2) \rangle = \frac{C_{12}}{(z_1 - z_2)^{2h} (\bar{z}_1 - \bar{z}_2)^{2\bar{h}}}, \quad (2.131)$$

where $h_1 = h_2 = h$ and $\bar{h}_1 = \bar{h}_2 = \bar{h}$ and where C_{12} is a constant coefficient. In particular,

$$\langle \phi(re^{i\theta}, re^{-i\theta}) \phi(0, 0) \rangle = r^{-2(h+\bar{h})} e^{-2i\theta(h-\bar{h})}, \quad (2.132)$$

so that

$$\Delta = h + \bar{h}, \quad s = h - \bar{h}, \quad (2.133)$$

where Δ denotes the scaling dimension and s the conformal spin associated to the primary field ϕ . Note that from Eq. (2.132), we can identify the critical exponent associated to the algebraic decay of correlation functions at criticality with

$$\eta = 2\Delta, \quad (2.134)$$

which is consistent with the definition of the (anomalous) scaling dimension in Eq. (2.103) in terms of RG eigenvalues.

⁵⁰All primary fields are quasi-primary but not all quasi-primary fields are primary. Indeed, a field may transform like Eq. (2.130) only under (an element of) the global conformal group $SL(2, \mathbb{C})$.

2.8.2 The power of the Virasoro algebra

From an algebraic point of view, local conformal transformations on the CFT Hilbert space are generated by the Virasoro operators L_n and \bar{L}_n . In particular, the operators L_{-1} , L_0 , and L_1 (together with their antiholomorphic counterparts) generate the global conformal transformations. For example, $L_0 + \bar{L}_0$ generates dilatations $(z, \bar{z}) \rightarrow \lambda(z, \bar{z})$ (which amount to time translations in radial quantization so that $L_0 + \bar{L}_0$ is proportional to the Hamiltonian of the system), while $L_0 - \bar{L}_0$ generates rotations. The Virasoro operators satisfy $L_n^\dagger = L_{-n}$ and $\bar{L}_n^\dagger = \bar{L}_{-n}$, and obey the commutation relations of the famous Virasoro algebra

$$[L_n, L_m] = (n - m)L_{n+m} + \frac{c}{12}n(n^2 - 1)\delta_{n+m,0} \quad (2.135)$$

$$[L_n, \bar{L}_m] = 0 \quad (2.136)$$

$$[\bar{L}_n, \bar{L}_m] = (n - m)\bar{L}_{n+m} + \frac{c}{12}n(n^2 - 1)\delta_{n+m,0}, \quad (2.137)$$

where the conformal (or central) charge c is a model-dependent constant describing the particular realization of conformal symmetry. It appears as the central term in the Virasoro algebra and its nature is determined by the short-distance behavior of the theory. It is also called the *conformal anomaly* since it reflects how a system responds when introducing a macroscopic length scale (see Sec. 2.8.4).

The vacuum state $|0\rangle$ must be invariant under global conformal transformations, so it should be annihilated by L_{-1} , L_0 , L_{+1} and their antiholomorphic counterparts. Additionally, the vacuum should be annihilated by all the lowering operators L_n , \bar{L}_n , $n > 0$, implying $L_n|0\rangle = 0$ and $\bar{L}_n|0\rangle = 0$ for $n \geq -1$. Primary fields ϕ acting on the vacuum create lowest-weight eigenstates $|h, \bar{h}\rangle = \phi(0, 0)|0\rangle$ of the Hamiltonian $L_0 + \bar{L}_0$ satisfying $L_0|h, \bar{h}\rangle = h|h, \bar{h}\rangle$ and $\bar{L}_0|h, \bar{h}\rangle = \bar{h}|h, \bar{h}\rangle$. Since the holomorphic and antiholomorphic parts form identical commuting Virasoro algebras, we can restrict to the holomorphic case. A basis for the excited states in the N -th level can be obtained by successively applying the raising operators L_{-n} , $n > 0$ to the state $|h\rangle$ in all possible ways, leading to

$$L_{-k_1}, \dots, L_{-k_m}|h\rangle, \quad (2.138)$$

where $1 \leq k_1 \leq \dots \leq k_m$ and $\sum_i k_i = N$. These states are eigenstates of L_0 with eigenvalue $h' = h + \sum_i k_i = h + N$, and are called descendants of the asymptotic state $|h\rangle$ with the integer N labeling the level of the descendant.

The number of linearly independent states at level N is the number $P(N)$ of partitions of N . Together with its infinite tower of descendants, a primary field ϕ constitutes a conformal family $[\phi]$ whose states transform among themselves, i.e. a subspace of the full Hilbert space which is closed under the action of the Virasoro generators and forms a lowest weight representation, or Verma module $V(c, h)$ of the Virasoro algebra, where c denotes the central charge and h the conformal dimension of the primary field. The total Hilbert space of physical theories is then constructed out of tensor products of holomorphic and antiholomorphic modules.

2.8.3 Unitary minimal models

In two dimensions, rational conformal field theories (RCFTs) are CFTs with a finite number of conformal families where all conformal dimensions (and the central charge) are rational numbers that can be calculated from consistency conditions. The most famous examples are the so-called minimal models. For these models, the Verma modules $V(c, h)$ can be shown to contain null states, which can be quotiented out to arrive at irreducible representations $M(c, h)$, the building blocks of minimal models. They are important for our purposes because they capture familiar statistical mechanical models (e.g. the Ising model, the tricritical Ising model, the Potts model, ...) at their critical points.

For values of the central charge $c < 1$, unitarity restricts the allowed values of the central charge to [40]

$$c = 1 - \frac{6}{m(m+1)}, \quad m = 2, 3, 4, \dots \quad (2.139)$$

and the associated primary field dimensions for these values of c can be shown to be rational numbers restricted to

$$h_{r,s} = \frac{((m+1)r - ms)^2 - 1}{4m(m+1)}, \quad 1 \leq r < m-1, 1 \leq s < m-1. \quad (2.140)$$

A generic Hilbert space for a minimal model looks like

$$\mathbb{H} = \bigoplus_{h, \bar{h}} M(c, h) \otimes \bar{M}(c, \bar{h}). \quad (2.141)$$

However, the particular way of combining the components of a minimal model into the physical tensor product theory is not obvious. Modular invariance provides the connection between decoupled holomorphic and antiholomorphic sectors and physically sensible theories defined in terms of modular invariant partition functions. We will come back to modular invariance and partition functions on a torus in Sec. 2.8.5. A simple way of taking the tensor product is to associate the corresponding antiholomorphic module to each holomorphic module, leading to so-called diagonal models

$$\mathbb{H} = \bigoplus_{r,s} M(c, h_{r,s}) \otimes \bar{M}(c, \bar{h}_{r,s}). \quad (2.142)$$

The critical Ising model corresponds to the simplest nontrivial unitary minimal model $m = 3$ with central charge $c = 1/2$. It contains the identity operator 1 and two local scaling operators: the Ising spin σ (a continuum version of the lattice spin σ_i), and the energy density ε (a continuum version of the lattice energy $\sigma_i \sigma_{i+1}$). The conformal dimensions are given by

$$(h, \bar{h})_1 = (0, 0), \quad (h, \bar{h})_\sigma = \left(\frac{1}{16}, \frac{1}{16}\right), \quad (h, \bar{h})_\varepsilon = \left(\frac{1}{2}, \frac{1}{2}\right), \quad (2.143)$$

consistent with $h_{1,1} = h_{2,3} = 0$, $h_{2,1} = h_{1,3} = 1/2$, and $h_{2,2} = h_{1,2} = 1/16$. The non-trivial fusion rules are given by

$$\sigma \times \sigma = 1 + \varepsilon, \quad (2.144)$$

$$\sigma \times \varepsilon = \sigma, \quad (2.145)$$

$$\varepsilon \times \varepsilon = \varepsilon, \quad (2.146)$$

which are compatible with the \mathbb{Z}_2 symmetry $\sigma_i \rightarrow -\sigma_i$ of the Ising model. The critical exponents η and ν are defined by the critical behavior of the correlators

$$\langle \sigma_i \sigma_{i+n} \rangle = \frac{1}{|n|^\eta}, \quad \langle \varepsilon_i \varepsilon_{i+n} \rangle = \frac{1}{|n|^{4-2/\nu}}. \quad (2.147)$$

2.8.4 Finite-size scaling on the cylinder

The conformal map $w = (L/2\pi) \log z$ maps the complex z -plane with a punctured origin to an infinitely long cylinder with circumference L . Writing $w = t + iu$, we can think of imaginary time t running along the cylinder and u as compactified space. The Hamiltonian on the cylinder, which generates infinitesimal translations in t , looks like

$$H = \frac{2\pi}{L} (L_0 + \bar{L}_0) - \frac{\pi c}{6L} = \frac{2\pi}{L} \left(L_0 + \bar{L}_0 - \frac{c}{12} \right) \quad (2.148)$$

Similarly, the momentum operator, which generates infinitesimal translations in u takes on the form

$$P = \frac{2\pi}{L} (L_0 - \bar{L}_0) \quad (2.149)$$

Although straightforward at first sight, these formulas relate the scaling dimensions of primary fields to the spectra of H and P on the cylinder. For lattice models with a lattice spacing a whose scaling limit is described by a CFT, diagonalizing the transfer matrix $T \approx 1 - aH$ thus gives direct numerical access to the scaling dimensions, up to finite-size corrections in (a/L) [46]. In particular, the lowest eigenvalue of H (or the dominant eigenvalue of the transfer matrix) corresponds to

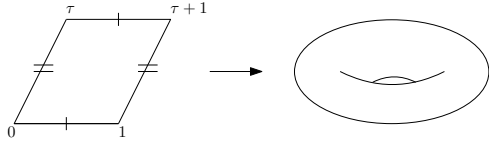
$$E_0 = \frac{2\pi}{L} \left(\Delta_0 - \frac{c}{12} \right) \quad (2.150)$$

where Δ_0 denotes the lowest possible scaling dimension. For unitary CFTs, this scaling dimension corresponds to the identity field $h = \bar{h} = 0$, yielding an estimate for the central charge c from the finite-size scaling behavior in L .

2.8.5 Modular invariance

In Sec. 2.8.2, we found the algebraic description of CFTs in terms of a set of ground states $|h, \bar{h}\rangle = \phi(0, 0) |0\rangle$ for the holomorphic and antiholomorphic Virasoro alge-

bras to act upon. Which combinations of ground states actually occur in physical theories is not immediately clear, even for the minimal models discussed in Sec. 2.8.3 where we know what primary fields might appear. To determine which fields will actually appear requires the physical consistency condition of modular invariance on the torus.


(2.151)

By making use of symmetry considerations, we can specify a torus by imposing periodic boundary conditions on a parallelogram $(0, 1, \tau + 1, \tau)$ with vertices in the complex plane, where the modular parameter τ is a complex number with positive imaginary part. Starting from a finite cylinder of circumference $L = 1$ and length $\text{Im}(\tau)$, we can twist one end by $\text{Re}(\tau)$ and glue the ends together to get a torus. This torus is invariant under the transformations $T : \tau \rightarrow \tau + 1$ and $S : \tau \rightarrow -1/\tau$, where S interchanges space u and imaginary time t . These transformations satisfy $(ST)^3 = S^2 = 1$ and generate the modular group

$$\tau \rightarrow \frac{a\tau + b}{c\tau + d}, \quad ad - bc = 1, \quad (2.152)$$

for $a, b, c, d \in \mathbb{Z}$.

The scaling limit of the partition function of a lattice model on the torus should be invariant under reparametrizations of the torus and should hence be modular invariant. The non-trivial part of this statement is that the partition function can be expressed in terms of the spectrum of scaling dimensions of the CFT in a way which is not manifestly modular invariant [10]. Constructing the partition function on the torus by twisting the cylinder and gluing the ends together leads to

$$Z = \text{Tr} e^{-\text{Im}(\tau)H + i\text{Re}(\tau)P}. \quad (2.153)$$

Substituting the previously stated expressions for H and P for $L = 1$ gives a general definition of CFT partition functions,

$$Z = e^{\text{Im}(\tau)\pi c/6} \text{Tr} e^{2\pi i\tau L_0} e^{-2\pi i\bar{\tau}\bar{L}_0}, \quad (2.154)$$

$$= (q\bar{q})^{-c/24} \text{Tr} q^{L_0} \bar{q}^{\bar{L}_0}, \quad (2.155)$$

where $q \equiv e^{2\pi i\tau}$. Note that this definition does not involve Lagrangians but only the Virasoro operators. The trace sums over all eigenvalues of L_0 and \bar{L}_0 , i.e. over all scaling fields of the CFT. As we have seen in Sec. 2.8.2, these can be grouped into irreducible representations of the Virasoro algebra of the form $(h + N, \bar{h} + \bar{N})$ where h, \bar{h} correspond to primary fields and the non-negative integers N, \bar{N} label the levels of the descendants. In this way, the partition function can be written as a

sesquilinear form,

$$Z = \sum_{h, \bar{h}} M_{h, \bar{h}} \chi_h(q) \chi_{\bar{h}}(\bar{q}), \quad (2.156)$$

where $M_{h, \bar{h}}$ is the multiplicity of primary fields with lowest weights labelled by (h, \bar{h}) , and where we also introduced the characters, which effectively trace over all descendants,

$$\chi_h(q) = q^{-c/24+h} \sum_{N=0}^{\infty} d_h(N) q^N, \quad (2.157)$$

where $d_h(N)$ denotes the degeneracy of the representation at level N . Modular invariance under T implies that all fields must have integer conformal spin⁵¹, since the characters, expressed in terms of τ , transform as

$$\chi_h(\tau + 1) = e^{2\pi i(h - \frac{c}{24})} \chi_h(\tau). \quad (2.158)$$

In matrix form this looks like

$$\chi_h(\tau + 1) = \sum_{\bar{h}} T_{h\bar{h}} \chi_{\bar{h}}(\tau), \quad (2.159)$$

where T is a diagonal matrix containing phases. Invariance under S entails that Z can equally well be expressed as a power series in $\tilde{q} = e^{-2\pi i/\tau}$ and $\tilde{\bar{q}}$ instead, resulting in

$$\chi_h\left(-\frac{1}{\tau}\right) = \sum_{\bar{h}} S_{h\bar{h}} \chi_{\bar{h}}(\tau), \quad (2.160)$$

where S is a unitary and symmetric matrix. The conditions for modular invariance of the partition function can be expressed in terms of the matrix equations

$$[M, T] = [M, S] = 0, \quad M_{h, \bar{h}} \in \mathbb{Z}, \quad M_{h, \bar{h}} \geq 0, \quad (2.161)$$

with the additional requirement that there is a unique vacuum labelled by 0 so that $M_{00} = 1$. The trivial solution is given by $M_{h, \bar{h}} = \delta_{h, \bar{h}}$, which, applied to the minimal models of Sec. 2.8.3, leads to the diagonal models Eq. (2.142). The diagonal modular invariant partition of the Ising model is obtained by choosing the three ground states $|0, 0\rangle$, $|\frac{1}{2}, \frac{1}{2}\rangle$, and $|\frac{1}{16}, \frac{1}{16}\rangle$. Using the state-operator correspondence, these correspond to three primary fields that create the ground states from the vacuum, which we referred to as 1 , ε and σ previously. Other non-diagonal combinations for the Ising model also exist, whose modular invariant partition functions we will encounter in Chapter 6.

⁵¹This holds for periodic boundary conditions. For other kinds of boundary conditions on the torus, topological corrections to the conformal spin modify the possible values (see Sec. 6.3.2).

2.8.6 Renormalization group flows and CFT

Operators in a given CFT are classified as relevant, marginal, or irrelevant according to their scaling dimension Eq. (2.133). The RG flow close to the critical fixed point is then determined by deformations by these operators, and leads to conformal perturbation theory. Knowledge of the behavior of correlators away from criticality is also very important to compare predictions with experimental data, since no real physical system is ever tuned exactly to the critical point⁵². In the context of CFTs, it is interesting to perturb by a marginal operator because this preserves conformal symmetry at zeroth order. Exactly marginal operators can even genuinely perturb the CFT without breaking conformal invariance. This special class of perturbations constitute a whole family of CFTs near the original fixed point, with RG flows connecting the different fixed points on a conformal manifold in the space of couplings.

We should also mention Zamolodchikov's result for two-dimensional CFTs on the existence of a positive real function $c(g)$, depending on the coupling constants $g = \{g^i\}$, which decreases monotonically under the RG flow,

$$\frac{d}{dl}c = \sum_i \beta^i(g) \frac{\partial}{\partial g^i} c(g) \leq 0. \quad (2.162)$$

This flow quantifies the irreversibility of the renormalization group and takes on the value of the central charge $c(g^*) = c$ at the RG fixed point, where $\beta^i(g) = 0$ [47].

2.8.7 Operators on the lattice and in the continuum

Let us conclude this succinct introduction to CFTs with a comment on the correspondence between microscopic operators on the lattice and their emergent large-distance continuum fields. Even though the connection between lattice and continuum descriptions alluded to in Sec. 2.6.4 is a little less vague for systems that can be described in terms of two-dimensional CFTs, i.e. for one-dimensional quantum critical points with a linear dispersion relation and two-dimensional rotationally invariant statistical mechanical systems, it remains hard to make the correspondence truly precise in general [48]. The problem involves figuring out how to expand microscopic lattice operators in terms of continuum fields at criticality, or, conversely, which combination of microscopic lattice operators yields a particular primary field as the dominant contribution in such an expansion. In particular, relating lattice operators to chiral continuum fields is notoriously difficult [49, 50].

For the Ising model, we identified the ultraviolet lattice and the infrared continuum operators in Sec. 2.8.3 by symmetry considerations. The spin field σ is the most relevant operator which is odd under a global spin flip, so that the microscopic spin operator has the field σ as its leading contribution in the continuum limit. The only symmetry-preserving relevant operator is the thermal field ε , whose

⁵²Nor does the correlation length ξ really tend to infinity, as impurities and inhomogeneities in most materials limit ξ to the order of a few thousand sites (which, apparently, is enough to observe near-critical behavior in experiments).

lattice incarnation perturbs the classical Ising model away from the critical point by changing the temperature. Additionally, the non-local chiral operators ψ and $\bar{\psi}$ can be understood in terms of a product of spin and disorder operators on the lattice since they are non-interacting [51]. More complicated theories than the Ising model leave room for multiple continuum operators behaving similarly under discrete conformal transformations. Lattice operators are then inevitably made up of some linear combinations of continuum operators, which obscures any identification. In Chapter 6, we will come back to aspects of this conundrum.

2.9 Numerical renormalization group

“My work on the Kondo problem is the work that seems least likely to have been produced by someone else if I had not done it. To my knowledge, no one else was thinking about the momentum slice approach to the renormalization group, let alone developing the skills needed to mount a large-scale computation based on it.”

K. G. Wilson, 2004 [16]

In light of our digression on the interplay between theoretical physics and numerics in Sec. 2.1 and the MPS impurity picture of transfer matrix renormalization to be discussed in Chapter 4, we cannot leave out a short discussion on Wilson’s numerical renormalization group (NRG) [5, 52]. Wilson’s solution to the Kondo problem provides a prime example where the renormalization group framework has been successfully carried out in all of its non-perturbative glory and has led to the development of a whole field devoted to the study of quantum impurity problems.

In quantum impurity problems, a small system with very few degrees of freedom is coupled to a large non-interacting system which acts as an environment. Crucially, both systems have to be treated quantum mechanically. For the case of the Kondo effect, the impurity is magnetic and interacts with the conduction electrons of nonmagnetic metals. Hence the environment consists of a quasi-continuum over a wide range of energy scales, from a high-energy cut-off down to arbitrarily small excitations. The defining energy scale of the problem, the Kondo temperature T_K , marks the cross-over point below which perturbation theory in the spin-exchange coupling J between impurity and conduction band electron spins is no longer trustworthy due to the appearance of diverging $\ln T$ terms in the perturbative expansion. The Kondo problem then boils down to finding a (non-perturbative) solution which does not break down in the low temperature regime.

Building on scaling ideas of Anderson [23], Wilson wrote the single-impurity Anderson model down in a way which allowed for a tractable logarithmic discretization of the conduction band. After introducing a discretization parameter Λ to define a set of points Λ^{-n} , $n = 0, 1, 2, \dots$ in the continuous bath spectrum, the intervals inbetween these points can be approximated by a single representative state. In this way, an effective, discretized Kondo model is mapped onto a semi-infinite chain with the impurity at the first site the chain. Going along the chain corresponds to decreasing energy scales with hopping matrix elements $t_n \propto \Lambda^{-n/2}$.

This effective quantum impurity model is then iteratively diagonalized by successively adding sites to the chain, starting from a small exactly solvable lattice. Each step, the effective Hamiltonian $H^{(L)}$, associated to the lattice with size L , is numerically diagonalized and only the D lowest energy eigenstates are kept. Next, the D -dimensional reduced Hilbert space $\mathbb{H}^{(L)}$ is constructed from the linear span of the D eigenvectors and operators are projected onto $D \times D$ -dimensional operators having support on $\mathbb{H}^{(L)}$. At the end of each step, a lattice site is added so that the Hilbert space for the next step looks like $\mathbb{H}^{(L+1)} = \mathbb{H}^{(L)} \otimes \mathbb{H}_{\text{site}}$. This process is then iterated with $L \rightarrow L + 1$, where the new Hamiltonian $H^{(L+1)}$ is retrieved from an RG equation relating $H^{(L+1)}$ to $H^{(L)}$ [5]. Convergence is obtained at a fixed point where the lowest energy eigenvalues of the Hamiltonian $H^{(L)}$ become independent of the lattice size L .

In essence, the NRG method boils down to recursively diagonalizing the Hamiltonian from large to small energies, meaning that the low-energy modes are affected by their high-energy counterparts but not the other way around. In this way, very accurate results can be produced for systems with a clear separation of energies, such as quantum impurity problems, where the interaction strength decreases exponentially along the chain. The NRG algorithm quickly breaks down as soon as the strongly-correlated physics of the total system cannot be captured by iteratively restricting to isolated subsystems. This problem was solved by White's density-matrix renormalization group (DMRG) [53], which paved the way for the tensor network states we will discuss in Chapter 3.

2.10 Real-space renormalization

In the previous sections, we have seen glimpses of the power of perturbative RG, where one rejoices in exploiting the presence of small parameters to construct asymptotic series expansions in the vicinity of a Gaussian fixed point. In real space however, much less has been achieved because real-space RG schemes require the construction of explicit, intrinsically non-perturbative transformations that can be reliably and accurately iterated. For two-dimensional critical phenomena, one could argue that, luckily, conformal field theory is powerful enough to provide exact results for a collection of universality classes associated to critical points of lattice models (see Sec. 2.8). Unfortunately, we are not *only* interested in the infrared fixed points and small perturbations around those fixed points, but also in formulating approximate yet accurate RG flows which explicitly take us from the intricate short-distance physics of a critical lattice model to its universal long-distance behavior in a tractable way.

We would therefore like to conclude this chapter on renormalization group theory with an introduction to the Delphic art of designing sensible real-space RG transformations⁵³. As should become clear from the historical examples below, there is no obvious way to systematically improve the obtained results nor is there a rigorous mathematical explanation for why these methods ought to give reasonable

⁵³This may be a bit too strong of a hyperbole, as most practitioners of real-space RG are not *deliberately* obscure. Yet most are not particularly clear on why their methods work either.

results at all. In Chapters 3, 5, and 6, we will discuss how tensor networks can be of help in making progress on some of these issues.

2.10.1 Kadanoff's block-spin RG

2.10.1.1 One dimension

In one spatial dimension, Kadanoff's block-spin decimation is an exact real-space RG transformation. Consider a $b = 2$ decimation acting on the one-dimensional ferromagnetic Ising partition function for an N -spin chain

$$Z_N = \sum_{\{\sigma_i\}} \exp \left(K \sum_{\langle ij \rangle} \sigma_i \sigma_j + h \sum_{i=1}^N \sigma_i \right), \quad (2.163)$$

where $K = J/(k_B T)$ denotes the reduced nearest-neighbor coupling and h the reduced external magnetic field. Let's study the flow in the transfer matrix picture, where

$$Z_N = \text{Tr} (T^N), \quad T = \begin{pmatrix} e^{J+h} & e^{-J} \\ e^{-J} & e^{J-h} \end{pmatrix}. \quad (2.164)$$

Blocking two sites then corresponds to a trivial rewriting of the partition function,

$$Z_N = \text{Tr} (T^N) = \text{Tr} \left((T^2)^{N/2} \right). \quad (2.165)$$

Introducing the short-hand notation $x = e^{-J}$ ($0 \leq x \leq 1$) and $y = e^{-h}$ ($0 \leq y \leq 1$), the coarse-grained transfer matrix is

$$T' = T^2 = \begin{pmatrix} \frac{1}{xy} & \frac{1}{x} \\ \frac{1}{x} & \frac{1}{y} \end{pmatrix}^2 = \begin{pmatrix} x^2 + \frac{1}{x^2 y^2} & y + \frac{1}{y} \\ y + \frac{1}{y} & x^2 + \frac{y^2}{x^2} \end{pmatrix}. \quad (2.166)$$

If we now demand that T' is of the same form as the original T up to an overall factor,

$$T' \equiv C \begin{pmatrix} \frac{1}{x'y'} & \frac{1}{x'} \\ \frac{1}{x'} & \frac{1}{y'} \end{pmatrix}, \quad (2.167)$$

we find the coarse-grained parameters

$$u' = \frac{\sqrt{v + v^{-1}}}{(u^4 + u^{-4} + v^2 + v^{-2})^{1/4}}, \quad (2.168)$$

$$v' = \frac{\sqrt{u^4 + v^2}}{\sqrt{u^4 + v^{-2}}}, \quad (2.169)$$

$$C = \sqrt{v + v^{-1}} (u^4 + u^{-4} + v^2 + v^{-2})^{1/4}, \quad (2.170)$$

mapping $(u, v) \rightarrow (u', v')$. The line of $\xi = 0$ fixed points $u = 1$ is stable and corresponds to zero interaction and any external field whatsoever. Even though the $\xi = \infty$ fixed point $(0, 1)$ is unstable (corresponding to an infinite interaction and zero external field), it is not a critical point since there is no way to reach it.

2.10.1.2 Two dimensions

Consider now the $d = 2$ Ising model on a square lattice of N sites in zero external field with partition function [54],

$$Z = \sum_{\{\sigma_i\}} \exp \left(K_1 \sum_{\langle ij \rangle} \sigma_i \sigma_j \right), \quad (2.171)$$

where $K_1 = J/(k_B T)$ denotes the reduced nearest-neighbor coupling. Let us now coarse-grain explicitly by summing over every other spin in the lattice. As a consequence of this decimation, the remaining spins form a square lattice rotated over 45° with lattice spacing $a' = ba = \sqrt{2}a$, so that all length scales have to be reduced by a factor $b = \sqrt{2}$ to arrive at a renormalized lattice model with $N' = N/b$ spins (see Fig. 2.7).

We can isolate the summation over each decimated spin as follows,

$$\begin{aligned} Z &= \sum_{\{\sigma_i\} \in \square} \sum_{\{\sigma_i\} \in \blacksquare} \exp \left(K_1 \sum_{\langle ij \rangle} \sigma_i \sigma_j \right) \\ &= \sum_{\{\sigma_i\} \in \square} \sum_{\{\sigma_i\} \in \blacksquare} \dots \exp \left(K_1 \sigma_5 \blacksquare \left(\sigma_1^\square + \sigma_2^\square + \sigma_3^\square + \sigma_4^\square \right) \right) \dots \\ &= \sum_{\{\sigma_i\} \in \square} \dots 2 \cosh(K_1 \left(\sigma_1^\square + \sigma_2^\square + \sigma_3^\square + \sigma_4^\square \right)) \dots, \end{aligned} \quad (2.172)$$

where we have focused on a single decimated spin σ_5 . Even though the tuple $(\sigma_1, \sigma_2, \sigma_3, \sigma_4)$ can be in 2^4 microstates, the symmetry of the Boltzmann weight only implies three distinct values,

$$\begin{aligned} &2 \cosh(K_1 (\sigma_1 + \sigma_2 + \sigma_3 + \sigma_4)) \\ &= \begin{cases} 2 \cosh(4K_1) & \text{if } \sigma_1 = \sigma_2 = \sigma_3 = \sigma_4 \\ 2 \cosh(2K_1) & \text{if } \begin{cases} -\sigma_1 = \sigma_2 = \sigma_3 = \sigma_4 \\ \sigma_1 = -\sigma_2 = \sigma_3 = \sigma_4 \\ \sigma_1 = \sigma_2 = -\sigma_3 = \sigma_4 \\ \sigma_1 = \sigma_2 = \sigma_3 = -\sigma_4 \end{cases} \\ 2 & \text{if } \begin{cases} \sigma_1 = -\sigma_2 = -\sigma_3 = \sigma_4 \\ \sigma_1 = \sigma_2 = -\sigma_3 = -\sigma_4 \\ \sigma_1 = -\sigma_2 = \sigma_3 = -\sigma_4 \end{cases} \end{cases} \end{aligned} \quad (2.173)$$

By introducing four renormalized coupling constants K'_0 , K'_1 , K'_2 , and K'_3 , we can reinterpret these weights as

$$2 \cosh(K_1 (\sigma_1 + \sigma_2 + \sigma_3 + \sigma_4)) = \exp \left(K'_0 + \frac{K'_1}{2} (\sigma_1 \sigma_2 + \sigma_2 \sigma_3 + \sigma_3 \sigma_4 + \sigma_1 \sigma_4) + K'_2 (\sigma_1 \sigma_3 + \sigma_2 \sigma_4) + K'_3 \sigma_1 \sigma_2 \sigma_3 \sigma_4 \right).$$

The coarse-graining generates a constant coupling term K'_0 which acts just as a free energy offset, a renormalized nearest-neighbor coupling K'_1 , but also effective interaction terms K'_2 and K'_3 representing respectively next-nearest-neighbor and plaquette interactions. We can solve for the values of these effective couplings by using Eq. (2.173), which leads to four equations for four unknowns. The algebraic solution in terms of K_1 is given by

$$K'_0 = \ln \left(2 \sqrt{\cosh 2K_1} (\cosh 4K_1)^{1/8} \right) \quad (2.174)$$

$$K'_1 = \frac{1}{4} \ln (\cosh 4K_1) \quad (2.175)$$

$$K'_2 = \frac{1}{8} \ln (\cosh 4K_1) \quad (2.176)$$

$$K'_3 = \frac{1}{8} \ln (\cosh 4K_1) - \frac{1}{2} \ln (\cosh 2K_1). \quad (2.177)$$

After relabeling the remaining spins, the renormalized partition function looks like

$$Z = \exp(N'K'_0) \sum_{\{\Sigma_I\}} \exp \left(K'_1 \sum_{\langle IJ \rangle} \Sigma_I \Sigma_J + K'_2 \sum_{\langle\langle IJ \rangle\rangle} \Sigma_I \Sigma_J \right) \quad (2.178)$$

$$+ K'_3 \sum_{\text{plaquettes}} \Sigma_I \Sigma_J \Sigma_K \Sigma_L \Big) = \exp(N'K'_0) Z(K'_1, K'_2, K'_3, N'). \quad (2.179)$$

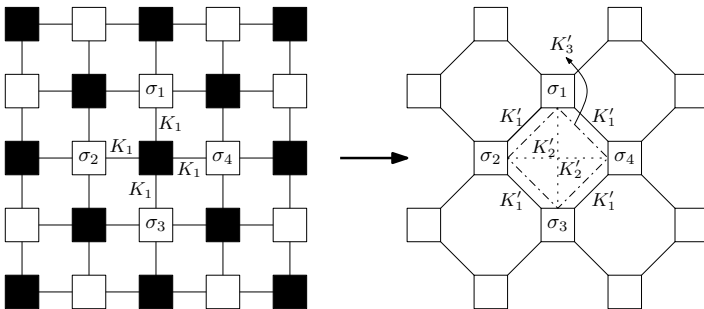


FIGURE 2.7: One decimation step.

It now becomes painfully clear that iterating Kadanoff's block-spin method leads to ever more additional renormalized coupling constants associated to all possible spin interactions allowed by the symmetry of the system. In this case, only interactions involving an even number of spins are allowed due to the Z_2 invariance under spin flips $\sigma_i \rightarrow -\sigma_i$, suggesting we should consider a generalized Ising model involving an infinite number of (even) interactions. The conceptual usefulness of regarding the Hamiltonian description of a physical system as occupying only a small corner in the larger space of all possible Hamiltonians becomes particularly clear now.

Let us check what happens when we truncate the couplings. Ignoring all generated couplings by setting $K'_2 = K'_3 = \dots = 0$, we get

$$K'_0 = \ln \left(2\sqrt{\cosh 2K_1} (\cosh 4K_1)^{1/8} \right) \quad (2.180)$$

$$K'_1 = \frac{1}{4} \ln (\cosh 4K_1). \quad (2.181)$$

This RG flow is similar to the exact one previously obtained in one dimension and has only two fixed points: an unstable zero-temperature ordered fixed point $K_1^* = \infty$ with infinite correlation length due to spontaneous magnetization and a stable infinite-temperature disordered fixed point at $K_1^* = 0$ with zero correlation length, which acts as a sink. Any finite interaction thus renormalizes to zero, so there will always be disorder at sufficiently long length scales. Because only the low- and high-temperature fixed points survive the truncation, we obtain the incorrect prediction that no phase transition takes place in the Ising model for any finite temperature in two dimensions.

Including only K'_2 , the flow becomes

$$K'_0 = \ln \left(2\sqrt{\cosh 2K_1} (\cosh 4K_1)^{1/8} \right) \quad (2.182)$$

$$K'_1 = \frac{1}{4} \ln (\cosh 4K_1) \quad (2.183)$$

$$K'_2 = \frac{1}{8} \ln (\cosh 4K_1) \quad (2.184)$$

Because both K'_1 and K'_2 are both positive and favor the alignment of spins, we can roughly approximate⁵⁴ the flow by introducing an effective nearest-neighbor coupling constant $\tilde{K}'_1 = K'_1 + K'_2$, obeying

$$\tilde{K}'_1 = \frac{3}{8} \ln (\cosh 4\tilde{K}_1). \quad (2.185)$$

We now find that both low- and high temperature fixed points $\tilde{K}'_1^* = \infty$ and $\tilde{K}'_1^* = 0$ are stable fixed points with zero correlation length, with a non-trivial fixed point $\tilde{K}'_1^* \approx 0.507$ in between⁵⁵.

⁵⁴This not completely unreasonable because there are $2N'$ pairs of different nearest-neighbor and next-nearest-neighbor interactions on the square lattice, which, for a system of fully aligned spins, have a total energy $E = 2N'(K'_1 + K'_2)$.

⁵⁵The exact value of the critical temperature is $\beta_c = \log(1 + \sqrt{2})/2 \approx 0.441$.

2.10.2 Migdal–Kadanoff bond moving approximation

For the Ising model on the square lattice, we can also construct a RG scheme with $b = 2$ which decimates every other row/column of spins. To compensate for the generation of new interactions, one can choose to remove the bonds which are not connected to the retained spins, leaving only nearest-neighbor interactions between renormalized spins. But as we have seen previously, this kind of approximation reduces the problem to similar recursion relations as in the one-dimensional case, which contains no critical fixed point. To avoid this breakdown, Migdal and Kadanoff proposed to strengthen the bonds that are left behind by absorbing the unwanted bonds, leading to double bonds of strength $2K_1 \equiv 2K$ between the retained spins [55]. The decimation then yields

$$K'_1 = \frac{1}{2} \ln (\cosh(4K)), \quad (2.186)$$

which has stable fixed points for $\tilde{K}^* = 0$ and $\tilde{K}^* = \infty$. The basins of attraction of the above sinks are separated by a third non-trivial fixed point located at $\tilde{K}^* \approx 0.305$.

This approach can be generalized to higher dimensions, but gives progressively worse results. For a hypercubic lattice in d dimensions, the bond moving step multiplies the coupling with a factor 2^{d-1} , so that after decimation we find

$$K' = \frac{1}{2} \ln (\cosh(2^d K)). \quad (2.187)$$

The high- and low-temperature sinks are stable because $K' \approx 2^{2(d-1)} K^2 \ll K$, for $K \ll 1$, and $K' \approx 2^{d-1} K \gg K$, for $K \gg 1$. The unstable fixed point $K = K^*$ in between corresponds to the non-trivial fixed point. Let us now illustrate a simple application of the general theory by extracting the the critical exponent ν from the behavior of the flow

$$K' = \mathcal{R}(K) = \frac{1}{2} \ln (\cosh(2^d K)) \quad (2.188)$$

close to the non-trivial fixed point K^* . For $(K - K^*)$ small, we make use of the assumed differentiability of the RG transformation to linearize the flow near $K = K^*$,

$$K' \approx \mathcal{R}(K^*) + \mathcal{R}'(K^*)(K - K^*) = K^* + 2^{y_t}(K - K^*), \quad (2.189)$$

where we have introduced $y_t = \ln \mathcal{R}'(K^*) / \ln 2$. In particular, we have

$$2^{y_t} = \left. \frac{\partial K'}{\partial K} \right|_{K=K^*} = 2^{d-1} \tanh(2^d K^*). \quad (2.190)$$

The correlation length scales as $\xi(K) \propto (K - K^*)^{-\nu}$ near criticality, so that,

together with $\xi(K) = 2\xi(K')$, we obtain

$$(K - K^*)^{-\nu} = 2(K' - K^*)^{-\nu} = 2(2^{y_t}(K - K^*))^{-\nu}, \quad (2.191)$$

implying $\nu = 1/y_t$. This simple example based on block-spin RG demonstrates that the existence of critical exponents crucially follows from the assumption of differentiability of the RG transformation at the fixed point.

2.10.3 Niemeijer-van Leeuwen cumulant approximation

For the Ising model on a triangular lattice, Niemeijer and van Leeuwen [56] constructed a $b = \sqrt{3}$ transformation by grouping three spins into a cell I as $\{\sigma_1^I, \sigma_2^I, \sigma_3^I\}$ and then renormalizing the cell using a majority rule

$$\tilde{\sigma}^I = \text{sgn}(\sigma_1^I + \sigma_2^I + \sigma_3^I). \quad (2.192)$$

The renormalized interactions between the renormalized spins $\tilde{\sigma}^I$ are then obtained from the constrained sum

$$e^{-\beta H'[\{\tilde{\sigma}^I\}]} = \sum_{\{\sigma_i^I\} \rightarrow \{\tilde{\sigma}^I\}} e^{-\beta H[\{\sigma^I\}]}. \quad (2.193)$$

To truncate the number of interactions, Niemeijer and van Leeuwen used perturbation theory to decompose the renormalized Hamiltonian into $\beta H = \beta H_0 + U$, where

$$-\beta H_0 = K \sum_I \sum_{\substack{\langle ij \rangle \\ i, j \in I}} \sigma_i^I \sigma_j^I, \quad (2.194)$$

which involves only intracell interactions between decoupled cells. The perturbation involves the remaining intercell interactions,

$$-U = K \sum_{\langle IJ \rangle} \sum_{\substack{\langle ij \rangle \\ i \in I, j \in J}} \sigma_i^I \sigma_j^J. \quad (2.195)$$

Invoking the cumulant expansion to write the expectation value of the exponential as the exponential of expectation values,

$$\langle e^U \rangle_0 = \exp \left(\langle U \rangle_0 + \frac{1}{2} \left(\langle U^2 \rangle_0 - \langle U \rangle_0^2 \right) + \dots \right), \quad (2.196)$$

we find

$$\beta H'[\{\tilde{\sigma}^I\}] = -\ln Z_0[\{\tilde{\sigma}^I\}] + \langle U \rangle_0 - \frac{1}{2} \left(\langle U^2 \rangle_0 - \langle U \rangle_0^2 \right) + \dots \quad (2.197)$$

where $\langle \dots \rangle_0$ refers to the expectation value with respect to βH_0 , with fixed $\tilde{\sigma}^I$, and $Z_0[\{\tilde{\sigma}^I\}]$ denotes the corresponding partition function. This partition function is independent of $\tilde{\sigma}^I$ since it is a product of contributions from independent cells, and can be evaluated to

$$Z_0[\{\tilde{\sigma}^I\}] = (e^{3K} + 3e^{-K})^{N/3}. \quad (2.198)$$

The first cumulant $\langle U \rangle_0$ can also be explicitly calculated,

$$\langle U \rangle_0 = 2K \left(\frac{e^{3K} + e^{-K}}{e^{3K} + 3e^{-K}} \right)^2 \sum_{\langle IJ \rangle} \tilde{\sigma}^I \tilde{\sigma}^J + \dots, \quad (2.199)$$

so that up to first order⁵⁶

$$\beta H'[\{\tilde{\sigma}^I\}] = \frac{N}{3} \ln(e^{3K} + 3e^{-K}) + 2K \left(\frac{e^{3K} + e^{-K}}{e^{3K} + 3e^{-K}} \right)^2 \sum_{\langle IJ \rangle} \tilde{\sigma}^I \tilde{\sigma}^J + \dots \quad (2.200)$$

The nearest-neighbor coupling yields the recursion relation

$$K' = 2K \left(\frac{e^{3K} + e^{-K}}{e^{3K} + 3e^{-K}} \right)^2, \quad (2.201)$$

which has the usual high-temperature ($K^* = 0$) and low-temperature ($K^* = \infty$) zero correlation length sinks. The unstable fixed point in between is given by

$$K^* = \frac{1}{4} \ln(1 + 2\sqrt{2}) \approx 0.336, \quad (2.202)$$

to be compared with the exactly known value of $K^* = 0.2747$ for the triangular lattice.

Since the fixed point occurs for $h^* = 0$, we can easily add an external magnetic field term $h \sum_I \sum_{i \in I} \sigma_i^I$ to the Hamiltonian because it can also be treated perturbatively, leading to the flow equation

$$h' = 3h \left(\frac{e^{3K} + e^{-K}}{e^{3K} + 3e^{-K}} \right). \quad (2.203)$$

In the vicinity of the fixed point $(K^*, 0)$, the RG flow can be linearized as

$$\begin{pmatrix} \delta K' \\ \delta h' \end{pmatrix} = \begin{pmatrix} b^{y_t} & 0 \\ 0 & b^{y_h} \end{pmatrix} \begin{pmatrix} \delta K \\ \delta h \end{pmatrix}, \quad (2.204)$$

with $b^{y_t} = 1.624$ and $b^{y_h} = 2.121$. From these relevant eigenvalues and using

⁵⁶Niemeijer and van Leeuwen actually went to second order, resulting in a three-parameter space with two additional interactions between neighboring spins. The qualitative behavior remains identical.

$b = \sqrt{3}$, the critical exponents are then predicted to be

$$\begin{array}{cccccc} \alpha(0) & \beta(1/8) & \gamma(7/4) & \delta(15) & \nu(1) & \eta(1/4) \\ \hline -0.27 & 0.72 & 0.84 & 2.17 & 1.13 & 1.26 \end{array}$$

Even though the obtained critical exponents differ significantly from the mean-field results in Table 2.1 (which is a good thing), the difference between the predictions and the known exact exponents is rather shocking. This is the result of neglecting higher-order terms in the cumulant expansion Eq. (2.197). Including more terms would however require more couplings to be included in the approximation if we want the effective Hamiltonian to have the same form as the original Hamiltonian.

Tensor network states

In this chapter¹, we introduce tensor network states and describe how they relate to the renormalization group in a way that is relevant for our purposes. In the last decade, tensor networks have emerged as a comprehensive framework capable of providing a fresh perspective on (quantum) many-body physics, mostly due to their focus on states rather than Hamiltonians. Although initially confined to condensed matter and quantum information communities, tensor networks today constitute a *lingua franca* capable of capturing an enormous amount of interesting physics in the same unifying framework of local tensors and their mathematical properties, which are closely related to the physical properties of the model under consideration. The numerical roots of tensor networks lie in the spectacular accuracy of the *density matrix renormalization group* (DMRG) for one-dimensional quantum spin chains, which was developed as a generalization of Wilson's numerical renormalization group for the Kondo problem [53]. From an analytical and a numerical perspective, tensor network states provide both concise models of classical and quantum many-body systems and efficient variational ansätze for the classical simulation of these systems. Their success can be traced back to the fact that they have been intentionally designed to capture the entanglement and correlation structure of physical states using virtual entanglement degrees of freedom.

Given that there exist many recent, excellent reviews on tensor networks and their applications, theoretical underpinnings, and optimization algorithms, we will not attempt to provide an exhaustive introduction and refer the reader to Refs. [57–64] and the references contained therein.

3.1 The renaissance of quantum entanglement

In the last twenty years, the perception of entanglement in quantum mechanics has shifted from an obscure *spukhafte Fernwirkung* to one of the most important concepts in contemporary physics. Rather than a mysterious bottleneck, the entanglement structure of quantum states has become an essential characteristic in classifying quantum phases of matter. Because entanglement has always been present in the postulates of quantum mechanics and the theory itself has also not changed since its conception, it looks like the delay was due to the usual slow and contingent

¹Most of the material in this chapter is not original research apart from some tiny unpublished findings in Section 3.4.

adaptation of human inventiveness. It took physicists more than half a century to realize that entanglement can be used as a resource to do things considered impossible in classical physics, ultimately leading to the development of the thriving fields of quantum information and quantum computation, and an awakening of the aspiration to build a large-scale quantum computer.

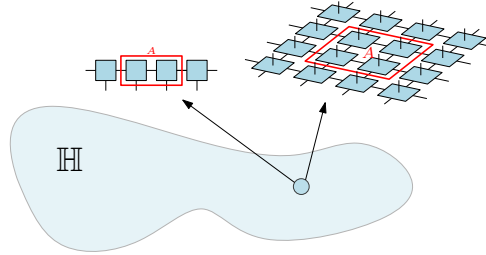
We will be concerned with entanglement in the context of quantum many-body systems, where it is closely related to the curse of dimensionality. Consider the specific example of a one-dimensional spin chain of N sites, where each physical site is associated with a local Hilbert space \mathbb{C}^d . A generic variational ground state wave function then has a tensor product structure

$$|\Psi\rangle = \sum_{i_1, \dots, i_N=1}^d c_{i_1, \dots, i_N} |i_1, \dots, i_N\rangle = \begin{array}{c} \text{---} \boxed{c_{i_1, i_2, \dots, i_N}} \text{---} \\ | \quad | \quad | \quad \dots \quad | \\ i_1 \quad i_2 \quad \dots \quad i_N \end{array} \quad (3.1)$$

where the coefficients $c_{i_1, \dots, i_N} \in (\mathbb{C}^d)^{\otimes N}$ are seen to grow exponentially with the length of the chain. The quantum many-body problem then boils down to how to deal with variational parameters which grow exponentially with the system size. Fortunately, there are good reasons for the practical mind to regard these exponentially large Hilbert spaces as fictitious constructs.

First of all, recall from Chapter 2 that physical Hamiltonians are more often than not short-ranged, i.e. they can be written as a sum of few-body terms $H = \sum_i h_i$. While ground states associated to arbitrarily long-range Hamiltonians can of course explore the exponentially large Hilbert space at will, ground states of local Hamiltonians are naturally less inclined to do so. Secondly, the overwhelming majority of states in the Hilbert space of all quantum many-body states that can be generated by arbitrary time-dependent local Hamiltonians are not physical because they can only be reached after an exponentially long time [65]. Thirdly, the entanglement structure of interacting quantum systems is sculpted by the *area law*. To see this, let us consider the von Neumann entropy $S(\rho_A) = -\text{Tr} \rho_A \log(\rho_A)$ of the reduced density matrix ρ_A of a region A , which quantifies the bipartite entanglement between region A and its complement (the rest of the system). For a random quantum state, we generically find a volume law scaling $S(\rho_A) \sim |A| \log d$, where $|A|$ denotes the number of spins in region A , or, effectively, the volume of region A . Ground states of local Hamiltonians however exhibit an area law $S(\rho_A) \sim |\partial A|$, where $|\partial A|$ denotes the boundary of region A , with possible corrections that are logarithmic in the volume for gapless Hamiltonians [66]. The fact that $S(\rho_A)$ scales as the boundary of ρ_A suggests that the entanglement between region A and its complement is

concentrated along the boundary between the two regions.



From a modern point of view, tensor networks can be regarded as efficient parametrizations of the small, physical corner in Hilbert space which contains the relevant low-energy states for quantum many-body systems. Building on the previous entanglement insights, we will now parade a few variational ansätze for quantum states which have been designed with a specific entanglement structure in mind. Unless explicitly stated otherwise, we will always be interested in the low-energy behavior of translation invariant systems in the thermodynamic limit $N \rightarrow \infty$. Since there are few cases where explicit tensor network equations provide more insight than clear diagrams for our considerations, we will henceforth make extensive use of graphical notation to denote tensor contractions and operations. Not doing so would be nothing short of obfuscation.

3.2 Matrix product states

3.2.1 Ansatz and properties

Matrix product states span the manifold of ground states and low-lying excitations of one-dimensional gapped Hamiltonians. Let us derive their entanglement structure from the general variation wave function Eq. (3.1), which is parametrized in terms of a rank- N tensor c_{i_1, \dots, i_N} . Isolating the first physical index from the rest and doing a singular value decomposition (SVD) gives the Schmidt decomposition

$$|\Psi\rangle = \sum_i \lambda_i |L_i\rangle \otimes |R_i\rangle = \begin{array}{c} L \\ \text{---} \end{array} \begin{array}{c} \lambda \\ \text{---} \end{array} \begin{array}{c} R \\ \text{---} \\ \dots \\ \text{---} \end{array} \quad (3.2)$$

where the singular values λ_i are called Schmidt values and the $|L_i\rangle$ and $|R_i\rangle$ orthonormal basis vectors. The Schmidt values quantify the entanglement across the cut. Repeating this decomposition for the whole chain and absorbing the diagonal λ_i matrices into the local tensors, we get the general form of an MPS with open boundary conditions,

$$|\Psi[A]\rangle = \begin{array}{c} A^{[1]} \\ \text{---} \end{array} \begin{array}{c} A^{[2]} \\ \text{---} \end{array} \begin{array}{c} \text{---} \\ \text{---} \end{array} \dots \begin{array}{c} \text{---} \\ \text{---} \end{array} \begin{array}{c} A^{[N]} \\ \text{---} \end{array} \quad (3.3)$$

Note that we have not really done anything to mitigate the exponential growth so far. From the area law, we however expect the entanglement entropy for any region to be bounded by a constant in one dimension. This implies a fast decay of the Schmidt values across any cut, so that only $D \ll \exp(N)$ non-zero singular values have to be taken into account. In that case, the MPS representation of the state is guaranteed to be an arbitrarily good approximation with a bond dimension D that scales polynomially with N [67]. For translation invariant systems, we can even parametrize the entire wave function in the thermodynamic limit in terms of a uniform MPS which is built out of a single tensor generically containing $O(dD^2)$ parameters.

We will now give a different construction of MPS, which has the advantage that it can be straightforwardly generalized to higher dimensions. Consider a lattice where each physical site corresponds to a local Hilbert space \mathbb{C}^d . Let us now additionally associate two virtual subsystems with bond dimension D to each physical site. We then introduce maximally entangled states $|\omega\rangle = \sum_{i=1}^D |ii\rangle$, where mean-field theory corresponds to taking product states ($D = 1$). Projecting onto the physical level with a judiciously chosen linear map $\mathcal{P}_s = \sum_{i,\alpha,\beta} A_{i,\alpha\beta}^{[s]} |i\rangle \langle\alpha, \beta|$, we obtain

so that the total state of chain is given by

$$|\Psi\rangle = (\mathcal{P}_1 \otimes \mathcal{P}_2 \otimes \dots \otimes \mathcal{P}_N) |\omega\rangle^{\otimes N} \quad (3.5)$$

$$= \sum_{i_1, \dots, i_N} \text{Tr} \left[A_{i_1}^{[1]} A_{i_N}^{[N]} \dots A_{i_N}^{[N]} \right] |i_1, \dots, i_N\rangle. \quad (3.6)$$

This construction satisfies the area law since there are always exactly two maximally entangled states crossing any cut, bounding the entanglement entropy by the constant value $2 \log D$. We end up with the general form of a periodic MPS,

For example, if we pick the entangled state $|\omega\rangle = |00\rangle + |11\rangle$ and the projector $\mathcal{P} = |0\rangle\langle 00| + |1\rangle\langle 11|$, or, equivalently, the MPS tensor

$$A_0 = \begin{pmatrix} 1 & 0 \\ 0 & 0 \end{pmatrix}, \quad A_1 = \begin{pmatrix} 0 & 0 \\ 0 & 1 \end{pmatrix}, \quad (3.8)$$

we get the Greenberger-Horne-Zeilinger state $|\text{GHZ}\rangle = |00\dots 0\rangle + |11\dots 1\rangle$.

Any MPS has a *gauge freedom* in the sense that for any matrix X_s with right-

inverse² X_s^{-1} , the transformation

$$A_i^{[s]} \rightarrow A_i^{[s]} X_s, \quad A_i^{[s+1]} \rightarrow X_s^{-1} A_i^{[s+1]}, \quad (3.9)$$

leaves the state invariant. This property is exploited in numerics for stability to recast an MPS in either left, right, or mixed canonical gauge. For example, an MPS in left gauge has the useful property that its tensors are left-isometric when contracted,

$$\sum_{i=1}^d A_i^\dagger A_i = \left[\begin{array}{c} \boxed{A} \\ \boxed{\bar{A}} \end{array} \right] = \left[\begin{array}{c} \text{---} \\ \text{---} \end{array} \right], \quad (3.10)$$

which enables an efficient calculation of expectation values. Note that matrix product states can be generalized from pure states to density matrices by adding an additional physical leg to the local tensors, leading to so-called matrix product operator (MPO) representations of many-body operators,

$$\cdots \left[\begin{array}{c} \boxed{O} \\ \text{---} \\ \boxed{O} \end{array} \right] \left[\begin{array}{c} \boxed{O} \\ \text{---} \\ \boxed{O} \end{array} \right] \left[\begin{array}{c} \boxed{O} \\ \text{---} \\ \boxed{O} \end{array} \right] \cdots \quad (3.11)$$

The importance of these objects cannot be overstated since they are ubiquitous in many-body physics: from statistical mechanics (see Sec. 3.5.1), where they appear as transfer matrices to the study of topological quantum phases of matter, where they characterize topological symmetries on the virtual level of projected entangled pair states (see Sec. 3.3.2).

3.2.2 Transfer matrix and correlations

A central object in tensor network theory is the *transfer matrix* or *transfer operator*. For MPS, it is constructed by contracting the physical indices of ket and bra,

$$\mathcal{T}_A = \sum_{i=1}^d A \otimes \bar{A} = \left[\begin{array}{c} \boxed{A} \\ \text{---} \\ \boxed{\bar{A}} \end{array} \right] \quad (3.12)$$

The transfer matrix uniquely defines the MPS matrices A up to a local unitaries. Let us now consider a single site operator O_i at site i and calculate its two-point

²The matrix X_s can thus be rectangular and alter the bond dimension.

function through the following tensor network contraction³,

$$\langle \Psi[A] | O_i O_j | \Psi[A] \rangle = \begin{array}{c} \cdots \text{---} \square_A \text{---} \square_A \text{---} \square_A \text{---} \cdots \quad \square_A \text{---} \square_A \text{---} \square_A \text{---} \cdots \\ | \quad | \quad | \quad | \quad | \quad | \quad | \quad | \quad | \quad | \quad | \quad | \quad | \quad | \\ \circ \quad \circ \quad \circ \quad \circ \quad \circ \quad \circ \quad \circ \quad \circ \quad \circ \quad \circ \quad \circ \quad \circ \quad \circ \quad \circ \\ | \quad | \quad | \quad | \quad | \quad | \quad | \quad | \quad | \quad | \quad | \quad | \quad | \\ \cdots \text{---} \square_{\bar{A}} \text{---} \square_{\bar{A}} \text{---} \square_{\bar{A}} \text{---} \cdots \quad \square_{\bar{A}} \text{---} \square_{\bar{A}} \text{---} \square_{\bar{A}} \text{---} \cdots \end{array} \quad (3.13)$$

where we have introduced a modified transfer operator

$$\mathcal{T}_A[O] = \sum_{i,j=1}^d \langle j | O | i \rangle A \otimes \bar{A} = \begin{array}{c} \text{---} \square_A \text{---} \\ | \\ \circ \\ | \\ \text{---} \square_{\bar{A}} \text{---} \end{array} \quad (3.14)$$

In the thermodynamic limit $N \rightarrow \infty$, we assume \mathcal{T}_A to have a unique maximal eigenvalue λ_1 , which we normalize to $\lambda_1 = 1$, with associated eigenvectors $|l\rangle$ and $|r\rangle$. In that case, $\mathcal{T}_A^N \rightarrow |r\rangle \langle l|$, and Eq. (3.13) converges to $\langle l | \mathcal{T}_A[O] \mathcal{T}_A^{i-j} \mathcal{T}_A[O] | r \rangle$. Substituting the expansion $\mathcal{T}_A^k = |r\rangle \langle l| + \sum_{\alpha \geq 2} \lambda_\alpha^k |r_\alpha\rangle \langle l_\alpha|$, where we assume $|\lambda_\alpha| < 1$ for $\alpha \geq 2$, we find that

$$\langle \Psi[A] | O_i O_j | \Psi[A] \rangle = \langle l | \mathcal{T}_A[O] | r \rangle \langle l | \mathcal{T}_A^{i-j} | r \rangle + \sum_{\alpha \geq 2} \lambda_\alpha^{i-j} \langle l | \mathcal{T}_A[O] | r_\alpha \rangle \langle l_\alpha | \mathcal{T}_A[O] | r \rangle. \quad (3.15)$$

The two-point function thus decays exponentially with the distance $|i - j|$ separating the operators and is wholly determined by the spectral properties of the transfer matrix \mathcal{T}_A . Specifically, the *correlation length* measured in units of lattice spacing is given by

$$\xi = - \frac{1}{\ln \left| \frac{\lambda_2}{\lambda_1} \right|}, \quad (3.16)$$

and is related to the gap of the (parent) Hamiltonian. For degenerate largest eigenvalues, the correlation function consists of a long-range part that does not decay together with other contributions which still decay exponentially. It is important to stress that the entanglement structure of MPS is incapable of capturing algebraically decaying correlations. Numerically, it is of course possible to approximate critical ground states. Typically, one observes that the Schmidt values decay much more slowly than off criticality and that the correlation length remains large but finite, since power law correlations are approximated by a sum of exponentials.

Even though we will not further elaborate on the analytical aspects of MPS, note that they can be used as a framework to construct solvable models whose properties can be understood analytically. In particular, MPS have been used to

³Note that these contractions can be evaluated efficiently. For finite MPS, they scale as $O(ND^3)$ for open boundary conditions and as $O(ND^5)$ for periodic boundary conditions, while for uniform MPS the dependence on N drops out.

classify one-dimensional gapped quantum phases of matter [37, 68–70].

3.2.3 Renormalization by blocking

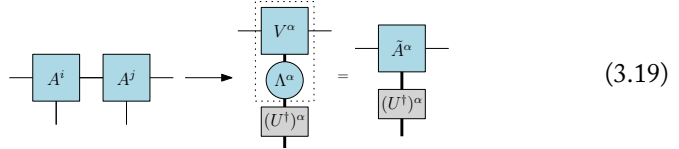
Let us now discuss a simple real-space RG transformation for MPS wave functions, following Ref. [71]. The approach is reminiscent of the block-spin approach discussed in Sec. 2.10, but here we consider a quantum version, and, in line with the spirit of tensor networks, we act on the *state* instead of the Hamiltonian. Recall that we can write any one-dimensional translation invariant state in its MPS form

$$|\Psi[A]\rangle = \sum_{i_1, \dots, i_N=1}^d \text{Tr} [A^{i_1} A^{i_2} \dots A^{i_N}] |i_1, \dots, i_N\rangle, \quad (3.17)$$

where the set of matrices $\{A^i | i = 1, \dots, d\}$ parametrizes the state and the bond dimension $D \leq d^{N/2}$ is left undetermined. We can now define a quantum coarse-graining procedure which maps two neighbouring spins to a single, effective block spin on the level of the MPS tensors. After blocking two tensors $[A^{(ij)}]_{\beta\gamma} \equiv [A^i A^j]_{\beta\gamma}$ and grouping the physical and virtual indices together, we do a singular value decomposition

$$[A^{(ij)}]_{\beta\gamma} \equiv [A^i A^j]_{\beta\gamma} = \sum_{\alpha=1}^{\min(d^2, D^2)} (U^\dagger)_\alpha^{(ij)} \Lambda^\alpha V_{\beta\gamma}^\alpha. \quad (3.18)$$

Graphically, the coarse-graining procedure looks like



$$A^i A^j = \begin{array}{c} \boxed{V^\alpha} \\ \circlearrowleft \Lambda^\alpha \\ \boxed{(U^\dagger)^\alpha} \end{array} = \tilde{A}^\alpha \quad (3.19)$$

The coarse-grained MPS tensor $\tilde{A}^\alpha = \Lambda^\alpha V^\alpha$ is determined up to an isometry U which selects a representative for the equivalence class of the wave function since $|\psi\rangle$ is only defined up to local unitaries, i.e. $|\psi'\rangle \sim |\psi\rangle$ if $|\psi'\rangle = U \otimes U \otimes \dots \otimes U |\psi\rangle$, where the $d^2 \times d^2$ unitary matrix U singles out a local basis. Note that iterating the blocking scheme Eq. (3.18) leads to a bounded physical dimension of the spins. Once the effective physical dimension reaches D^2 , it stays at that value, which implies that we can exactly coarse-grain finite-dimensional matrix product states. For small bond dimensions, we can even enumerate the exact fixed points of the RG flow. Product states, which have bond dimension $D = 1$ and look like $A^1 = 1$, $A^k = 0$ for $k = 2, \dots, d$, are a fixed point of the RG transformation and correspond to the infrared fixed points of massive theories. The GHZ state Eq. (3.8) is also a fixed point, with $U = |0\rangle\langle 00| + |1\rangle\langle 11|$, and corresponds to symmetry-breaking infrared fixed points.

We can get rid of the arbitrary local basis by considering the transfer matrix

$$\mathcal{T}_A = \sum_{i=1}^d A^i \otimes \bar{A}^i = \begin{array}{c} \text{---} A^i \text{---} \\ | \\ \text{---} \bar{A}^i \text{---} \end{array} \quad (3.20)$$

so that the local unitaries automatically drop out when coarse-graining,

$$\begin{array}{c} \text{---} A^i \text{---} \\ | \\ \text{---} \bar{A}^i \text{---} \end{array} \begin{array}{c} \text{---} A^j \text{---} \\ | \\ \text{---} \bar{A}^j \text{---} \end{array} \rightarrow \begin{array}{c} \text{---} \bar{A}^\alpha \text{---} \\ | \\ \text{---} (U^\dagger)^\alpha \text{---} \\ | \\ \text{---} U^\alpha \text{---} \\ | \\ \text{---} \bar{A}^\alpha \text{---} \end{array} = \begin{array}{c} \text{---} \bar{A}^\alpha \text{---} \\ | \\ \text{---} \bar{A}^\alpha \text{---} \end{array} \quad (3.21)$$

and the RG flow in terms of transfer matrices becomes $\mathcal{T}_A \rightarrow \mathcal{T}_{\bar{A}} = \mathcal{T}_A^2$. Fixed points then boil down to characterizing the class of operators $\{\mathcal{T}_A^\infty\} = \{\lim_{n \rightarrow \infty} \mathcal{T}_A^n\}$ which have the structure of an MPS transfer matrix. Since \mathcal{T}_A corresponds to a completely positive map ϕ , which acts as $\phi[\mathcal{T}_A](\rho) = \sum_i A^i \rho A^{i\dagger}$, one can use quantum information theory results on the classification of these maps to classify all $D = 2$ fixed points of the coarse-graining transformation [71].

For injective⁴ MPS, we can always choose the largest non-degenerate eigenvalue of \mathcal{T}_A to be equal to one, and bring the MPS into left gauge to find

$$\mathcal{T}_A^k = \begin{array}{c} \text{---} \rho \text{---} \\ | \\ \text{---} \end{array} \left[\text{---} \right] + O(|\lambda_2|^k) \quad (3.22)$$

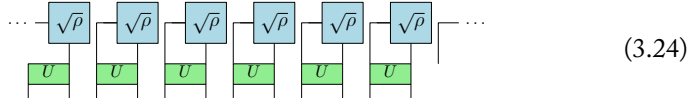
where ρ denotes the full-rank right fixed point and the second eigenvalue $|\lambda_2| < 1$ of the transfer matrix involves subleading corrections. At the fixed point, the trivial scale-invariant state can thus be written in terms of two virtual spin degrees of freedom, which are entangled with their neighbors,

$$\cdots \begin{array}{c} \text{---} \sqrt{\rho} \text{---} \\ | \\ \text{---} \end{array} \begin{array}{c} \text{---} \sqrt{\rho} \text{---} \\ | \\ \text{---} \end{array} \begin{array}{c} \text{---} \sqrt{\rho} \text{---} \\ | \\ \text{---} \end{array} \cdots \quad (3.23)$$

The resulting system has zero correlation length and belongs to the trivial fixed points we encountered in the previous chapter. This confirms the fact that MPS are well-suited to capture gapped systems but much less so for gapless systems. Indeed, the fixed point can be completely disentangled by a finite-depth local quantum

⁴An MPS is said to be injective if there exists a length k such that, after blocking k sites, the map $X \mapsto \sum \text{Tr}[A_{i_1} \dots A_{i_k} X] |i_1, \dots, i_k\rangle$ is injective, meaning that every choice X maps onto a unique physical state associated to that block.

circuit by constructing a unitary U which acts as



$$\dots \begin{array}{c} \sqrt{\rho} \\ U \end{array} \begin{array}{c} \sqrt{\rho} \\ U \end{array} \begin{array}{c} \sqrt{\rho} \\ U \end{array} \begin{array}{c} \sqrt{\rho} \\ U \end{array} \begin{array}{c} \sqrt{\rho} \\ U \end{array} \begin{array}{c} \sqrt{\rho} \\ U \end{array} \dots \quad (3.24)$$

in such a way that the resulting MPS is equal to the product state $|00\dots 0\rangle$. All injective MPS are thus in the same trivial topological phase as a product state. Note that the real-space transformation for matrix product states we have discussed above has recently been extended to matrix product density operators [72].

3.2.4 Variational optimization

Let us now turn to the numerical side of matrix product states. By now, it is understood that the DMRG algorithm amounts to a variational optimization over the manifold of quantum states parametrized by MPS [73, 74]. Explicitly, the ground state of a Hamiltonian is found variationally by solving

$$\arg \min_{|\Psi\rangle \in \mathcal{M}} \frac{\langle \Psi | H | \Psi \rangle}{\langle \Psi | \Psi \rangle}, \quad (3.25)$$

where \mathcal{M} denotes a variational manifold embedded in the physical Hilbert space, which we here restrict to that of (uniform) matrix product states. Using the gauge freedom of MPS in a clever way, the tensor contractions can be efficiently evaluated and the problem for a single tensor reduces to a (generalized) eigenvalue equation. Usually, one optimizes a single tensor at a time and sweeps back and forth until the cost function converges. In this sense, MPS algorithms are greedy, i.e. by locally optimizing for a single tensor at a time we hope to find a global optimum. Numerically, this appears to be the case and the strategy works almost without failing for matrix product states.

There currently exist many ways to optimize MPS wave functions. A particularly elegant one is obtained by a careful adaptation of Dirac's time-dependent variational principle (TDVP) to the language of MPS, which introduces differential geometric notions into the variational optimization procedure [75–77]. The best variational approximation then corresponds to the relentless projection of the quantum state onto the MPS manifold of a given bond dimension. Given a properly optimized ground state $|\Psi[A]\rangle$, the tangent space properties of TDVP additionally suggest a natural excitation ansatz which implements particle-like excitations on top of the ground state [78, 79]. We will make use of these algorithms, as well as their formulation involving MPOs instead of Hamiltonians [63], in Chapters 4, 5, and 6.

3.3 Projected entangled pair states

3.3.1 Ansatz and properties

The construction Eq. (3.4) for MPS can be generalized to higher dimensions to yield the variational class of *projected entangled pair states* (PEPS) [80]. For two dimensions, we instead introduce a (possibly site-dependent) linear operator $\mathcal{P}_s : (\mathbb{C}^D)^{\otimes 4} \rightarrow \mathbb{C}^d$,

$$\mathcal{P}_s = \sum_{i,\alpha,\beta,\gamma,\delta} A_{i,\alpha\beta\gamma\delta}^{[s]} |i\rangle \langle \alpha, \beta, \gamma, \delta|, \quad (3.26)$$

so that

$$|\Psi[A]\rangle = \text{Diagram}, \quad (3.27)$$

which has an entanglement structure compatible with the area law.

Algebraic decay of correlations

As opposed to MPS, PEPS are believed to be able to capture algebraic decay of (thermal) correlations [81]. Suppose we were to consider a classical model $H[s_1, \dots, s_N]$ with a thermal phase transition such as the by now all too familiar Ising model. If we can relate a PEPS to the classical model's partition function Z , then the algebraic decay of (thermal) correlations at the critical inverse temperature β_c ought to be mirrored in the corresponding PEPS description. This is demonstrated by constructing an unnormalized pure state

$$|\psi\rangle = \sum_{\{s_1, \dots, s_N\}} e^{-\frac{\beta}{2} H[s_1, \dots, s_N]} |s_1, \dots, s_N\rangle, \quad (3.28)$$

whose overlap $\langle \psi | \psi \rangle$ matches the partition function $Z = \sum_{\{s_1, \dots, s_N\}} e^{-\beta H[s_1, \dots, s_N]}$. The key insight is that the state Eq. (3.28) has a PEPS representation, which, for the Ising model, looks like

$$\text{Diagram} = e^{-\frac{\beta}{4} (s_i s_\alpha + s_i s_\beta + s_i s_\gamma + s_i s_\delta)}, \quad (3.29)$$

where the Boltzmann weights are encoded in the correlations between virtual spins.

3.3.2 Topological order and MPO algebras

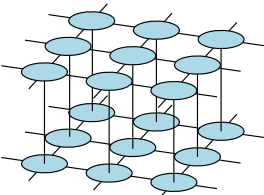
Topologically ordered phases of matter (see Sec. 2.7.5) are wildly popular in condensed matter literature nowadays due to their potential role in realizing large-scale quantum computers by means of topological quantum computation. The idea is to encode qubits using robust, topological degrees of freedom, which are effectively isolated from local interactions with the environment and thus inherently resilient against errors.

In the last few years, it has become clear that two-dimensional nonchiral topological phases of matter can be understood in terms of PEPS by generalizing injectivity conditions to include MPOs acting as generalized symmetries on the virtual level [82–84]. As already noted in Sec. 2.7.5, the interplay of global symmetries with trivial and non-trivial topological phases leads to the possibilities of symmetry-protected topological (SPT) [83] and symmetry-enriched topological (SET) phases [85]. Both of these generalizations can be captured in a unified tensor network formalism which lends itself to numerical simulations [86, 87] due to its focus on states rather than Hamiltonians. It should be noted that the tensor network approach has its origins in local commuting projector Hamiltonians such as Kitaev’s toric code [88] and Levin and Wen’s string-net models [89, 90], which, in turn, are Hamiltonian realizations inspired by known topological quantum field theories (TQFTs).

In Chapter 6, we will introduce parts of the MPO algebra formalism relevant to the specific problem of representing classical partition functions as the overlap of a product state with the PEPS representation of a symmetry-enriched string-net wave function.

3.3.3 Variational optimization

It is important to note that the contraction of PEPS tensor networks can no longer be carried out exactly [91]. Contrary to MPS, there is also no obvious canonical gauge which simplifies calculations. The norm $\langle \Psi[A] | \Psi[A] \rangle$ is given by sandwiching bra and ket,

$$\langle \Psi[A] | \Psi[A] \rangle = \text{Tr} \left(\text{PEPS}_{\text{ket}} \text{PEPS}_{\text{bra}} \right), \quad (3.30)$$


and has to be approximately calculated using MPS techniques [63, 80], corner transfer matrices [92–95], or tensor network renormalization methods (see Sec. 3.5.2). Let us focus on the approximate contraction method which recycles MPS techniques, even though all of them boil down to more or less the same idea. The trick is to

collapse the double-layer tensor network, so that the top view of Eq. (3.30) resembles

$$\langle \Psi[A] | \Psi[A] \rangle = \begin{array}{c} \text{---} \\ \text{---} \\ \text{---} \\ \text{---} \\ \text{---} \\ \text{---} \end{array} \begin{array}{ccc} \circ & \circ & \circ \\ \circ & \circ & \circ \\ \circ & \circ & \circ \end{array} \text{---} \text{---} \text{---} \text{---} \text{---} \text{---}, \quad (3.31)$$

where we have defined the PEPS transfer matrix as

$$\mathcal{T}_A = \begin{array}{c} \circ \\ \text{---} \\ \circ \end{array} \quad (3.32)$$

Since PEPS expectation values cannot be contracted exactly, even the tensor network contractions appearing in variational optimization schemes have to be approximated. So not only do we approximate the quantum state by a PEPS wave function, we also have to approximate the PEPS approximation itself when calculating any kind of overlap. By using the honed tools of Sec. 3.2.4, we can calculate the approximate (uniform) MPS fixed point coming from the top,

$$\begin{array}{c} \square \\ \text{---} \\ \circ \\ \text{---} \\ \text{---} \end{array} \approx \lambda \begin{array}{c} \square \\ \text{---} \\ \text{---} \end{array}, \quad (3.33)$$

and similarly for the bottom. The contraction problem is then reduced to one dimension⁵,

$$\langle \Psi[A] | \Psi[A] \rangle \approx \begin{array}{ccc} \square & \square & \square \\ \text{---} & \text{---} & \text{---} \\ \circ & \circ & \circ \\ \text{---} & \text{---} & \text{---} \\ \square & \square & \square \end{array} \quad (3.34)$$

so that with the leading left and right eigenvectors of the transfer matrix object inside the bounding box, we can evaluate the tensor network to be

$$\langle \Psi[A] | \Psi[A] \rangle \approx \begin{array}{c} \rho_L \quad \rho_R \\ \text{---} \\ \square \\ \text{---} \\ \circ \\ \text{---} \\ \square \\ \text{---} \\ \text{---} \end{array} \quad (3.35)$$

⁵Note that we have ignored eigenvalues and normalizations for clarity here.

This general procedure is referred to as calculating the *environment* of a PEPS tensor and appears in any optimization algorithm which takes the full environment into account. Variational algorithms for PEPS also try to solve Eq. (3.25), but with the variational manifold now corresponding to the class of PEPS wave functions. Most PEPS algorithms (simple-update [96], full-update [97], or fast-full-update [98]) resort to imaginary-time evolution to evolve an initial PEPS state, leading to a projection onto the ground state for long times. This is done by applying quantum gates resulting from the Trotter-Suzuki decomposition of the operator $\exp(\tau H)$ (see Sec. 4.2) to the PEPS, which enlarges the bond dimension and requires truncation. For simple-update, the truncation environment is approximated by a product state, while full-update takes the full environment into account, requiring matrix inverses of possibly badly conditioned effective environments. In Ref. [99], a novel conjugate-gradient algorithm was proposed to directly optimize the global energy functional on the PEPS variational manifold, similar in spirit to the tangent space methods for MPS. It should be noted however that the numerical side of PEPS unfortunately remains shrouded in an air of prohibitive numerical cost, especially for systems close to criticality.

3.4 Multi-scale entanglement renormalization ansatz

In contrast to MPS and PEPS, the multi-scale entanglement renormalization ansatz (MERA) is tailored to capture gapless (critical) ground states in one [100] and two dimensions [101] and implements a real-space RG transformation on quantum states. We will restrict ourselves to the one-dimensional case below.

3.4.1 Ansatz and properties

The MERA has a built-in additional dimension which plays the role of a coarse-graining scale, grouping its tensors in layers. These tensors can either be disentanglers, which are unitary disentangling gates, or isometries, which reduce the number of degrees of freedom. For example, a binary MERA looks like

$$|\Psi\rangle = \text{[Diagram of a binary MERA tensor network]} \quad (3.36)$$

where the physical ultraviolet lattice corresponds to the tensor legs at the bottom and the dotted lines indicate coarse-grained effective lattices at larger length scales. The tensors are constrained to be respectively isometries and unitaries,

$$\text{[Diagram of constraints]} \quad (3.37)$$

which leads to considerable simplifications when computing local expectation values and correlation functions. For states with a finite correlation length, we can cap the network with a *top tensor* after $s \approx \log_2(N)$ layers since all correlations should be dealt with at that point. To impose translation invariance, all disentanglers and isometries of every layer are taken to be identical, even though the ansatz itself is even then clearly not translation invariant. Gapless ground states with a diverging correlation length are expected to be scale invariant, which the MERA can capture by furthermore choosing all layers to be identical⁶. In this way, MERA is able to describe gapless ground states in terms of just a single disentangler and isometry.

Even though most of the literature on MERA is numerically motivated, there have been numerous (semi-)analytical advances over the past few years. Examples include recent work on anomalies and entanglement renormalization [102], the construction of an analytical MERA for the quantum Ising model [103], and the connection between entanglement renormalization and wavelets [103, 104]. Even though we will not discuss the continuous generalization of MERA (cMERA) for Gaussian models [105], we would like to mention that there appear to be many low-hanging fruits left. Looking back at Section 2.7.4, it seems clear that a straightforward step from the known Gaussian solutions towards interacting cMERAs would be to first of all try to reproduce the perturbative RG results for the Wilson-Fisher fixed point. This would rephrase known and well-understood perturbative results in terms of Hamiltonian flows and entanglement renormalization. The key technical step, which makes the derivation nontrivial, is the use of the framework of quasi-adiabatic evolution [36, 106] to treat the unitary (dis)entangling operators perturbatively. From the explicit expression of the coarse-grained Hamiltonian, one should be able to identify the perturbative flow of the couplings.

Algebraically decaying correlations

Let us first of all demonstrate how the tensor constraints Eq. (3.37) simplify the calculation of two-point correlation functions for the ternary MERA,

$$\langle \Psi | O_i O_{i+N} | \Psi \rangle = \text{Diagram} \quad (3.38)$$

⁶In actual numerics, one adds a few transitional layers to flow closer to the fixed point and its associated universal behavior.

Making use of the constraints, we find

$$\langle \Psi | O_i O_{i+N} | \Psi \rangle = \text{Diagram 1} \quad \text{Diagram 2} \quad (3.39)$$

Indeed, all tensors outside the *causal cone* (see also Sec. 3.4.2) of the support of the operators under consideration drop out of the contraction, so that the MERA maps local operators to local operators⁷. After $s \approx \log N$ iterations, two operators which were initially a distance N apart have become nearest-neighbors. From that point on, the scaling behavior of a local operator is completely determined by (a particular instance of) the *ascending superoperator*

$$\mathcal{S}(\phi) = \text{Diagram} \quad (3.40)$$

which is a completely positive, unital map with eigenvalues $|\lambda| \leq 1$ [107]. The two-point correlators of eigenoperators ϕ_i with eigenvalues λ_{ϕ_i} of this map behave as

$$\langle \phi_i(0) \phi_j(x) \rangle \sim \langle \phi_i(0) \phi_j(1) \rangle \lambda_{\phi_i}^{\log_3 x} \lambda_{\phi_j}^{\log_3 x} \sim \frac{\langle \phi_i(0) \phi_j(1) \rangle}{|x|^{\Delta_i + \Delta_j}} \quad (3.41)$$

where we have defined the scaling dimensions $\Delta_i = -\log_3(\lambda_{\phi_i}) \geq 0$. Note the uncanny similarity of the above equations to Sec. 2.8 on conformal field theory. Indeed, the eigenoperators of the superoperator \mathcal{S} can be identified with approximate lattice representations of the CFT primary fields (and their descendants). We will demonstrate some of these features in Sec. 3.4.2.

The previous discussion on correlators suggests that we can interpret the action of MERA as a sequence of unital, completely positive maps acting on local operators. In terms of real-space RG transformations, the MERA approximately conserves the expectation value

$$\langle \Psi_{(0)} | O | \Psi_{(0)} \rangle = \langle \Psi_{(s+1)} | \mathcal{A}_{(s)} \circ \dots \circ \mathcal{A}_{(0)}(O) | \Psi_{(s+1)} \rangle \quad (3.42)$$

for all scales s , where the ascending superoperator $\mathcal{A}_{(s)}$ at layer s is a coarse-graining map from b^{N-s} spins to b^{N-s-1} spins. Thermodynamic observables are then identified as the operators corresponding to fixed points of superoperators *in scale space*.

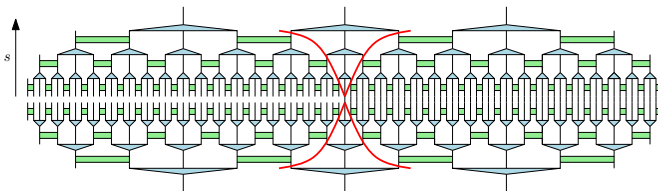
⁷This holds more generally, i.e. not only for the convenient choice of lattice positions we considered here.

3.4.2 Entanglement structure of MERA: correlations in scale space

Let us now study the entanglement properties of the one-dimensional MERA by explicitly constructing effective reduced density matrices in scale space using the causal cone structure. Using the iterative optimization methods developed for MERA in Refs. [108, 109], we set out to numerically quantify the entanglement entropy and mutual information in the auxiliary scale space. Additionally, the features distinguishing MERA from MPS are clearly illustrated in a hands-on way.

3.4.2.1 Semi-infinite density matrix

Consider the problem of calculating the semi-infinite density matrix ρ_A of a wave function parametrized in terms of a numerically optimized ternary MERA with bond dimension χ . By contracting ket and bra to the right of an arbitrary origin, we obtain the reduced density matrix defined on the real-space interval $x \in]-\infty, 0[$, which looks like



The causal cone associated to the origin is drawn in red. All tensors to the right of the causal cone of the origin site drop out due to the unitary and isometric restrictions on the tensors. As we are only interested in the spectrum of ρ_A , the remaining tensors outside the causal cone to the left amount to a big isometry which does not affect the spectrum. So we end up with an effective reduced density matrix along the scale dimension, which takes the form of a matrix product operator (see Eq. (3.11)),

$$\begin{array}{c}
 \xrightarrow{s} \\
 \begin{array}{ccc}
 \begin{array}{c} \text{---} \\ | \\ \text{---} \end{array} & \begin{array}{c} \text{---} \\ | \\ \text{---} \end{array} & \dots \\
 \begin{array}{c} \text{---} \\ | \\ \text{---} \end{array} & \begin{array}{c} \text{---} \\ | \\ \text{---} \end{array} & \dots
 \end{array}
 \end{array}
 \quad (3.43)$$

where the upper indices denote the ket and the lower the bra along the scale dimension. Each lattice site s in scale space is directly related to a real space length scale 3^s . Of course, this semi-infinite MPO still does not allow us to calculate the full semi-infinite density matrix ρ_A , which still grows exponentially in scale. We can, however, calculate arbitrary reduced density matrices of sets of scales by tracing out all other sites.

As an example, consider the reduced density matrix of two sites s and $s + N$. Tracing everything to the left of s gives an identity matrix coming from the left due to the isometric properties of the tensors. Tracing the sites $s + 1$ to $s + N - 1$ amounts to acting with a scale transfer matrix, which is nothing but an instance of

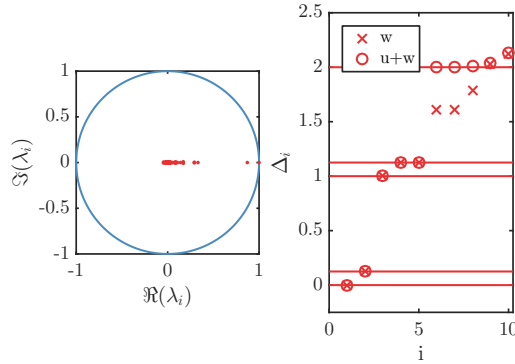


FIGURE 3.1: The transfer matrix in scale space is equivalent to a scaling superoperator, whose dominant eigenvalues λ_i are related to the scaling dimensions $\Delta_i = -\log_3(\lambda_i)$ of the critical theory (quantum Ising model for bond dimension $\chi = 10$). To show that a MERA with $\chi = 10$ is actually more accurate than what the scaling transfer matrix implies, we have also plotted the eigenvalues of MERA's *average descending superoperator*, which is defined on two sites and incorporates the disentangler u [108, 109]. This indicates that, with an increased numerical cost, we could take an (average) origin of two sites to obtain a more accurate scale MPO.

the familiar MERA scaling superoperator we already encountered in Eq. (3.40),

$$\begin{array}{c} \xrightarrow{s} \\ \text{[Diagram of a tensor with two left legs and two right legs]} \\ \text{=} \\ \text{[Diagram of a tensor with two left legs and two right legs]} \end{array} \quad \begin{array}{c} \updownarrow s \end{array} \quad (3.44)$$

where we identify the left indices with the inner ones on the right, and the right indices with the outer ones (as a matrix). Finally, the dominant eigenvector of the above object acts as a fixed point coming from the right of site $s + N$, which is nothing but the dual to the identity operator, i.e. the one-site fixed point reduced density matrix in MERA numerics which represents all upper scales. It is also clear that the entanglement entropy of the reduced density matrix associated to a single scale is trivially constant due to the scale invariant ansatz and the isometric properties of the tensors making up the MPO. Each scale yields a constant contribution to the entanglement entropy by construction.

3.4.2.2 Scale transfer matrix properties

We will restrict ourselves to the scale invariant bulk part of the MPO. The transitional layers drop out anyway due to the isometric properties of the tensors when calculating reduced density matrices of regions having support only in the bulk. As mentioned in Ref. [107] and shown numerically in Fig. 3.1 for an optimized MERA with bond dimension $\chi = 10$, the scale transfer matrix Eq. 3.44 is gapped with correlation

length

$$\xi = -1/\log|\lambda_2/\lambda_1| \approx 7.269 \dots, \tag{3.45}$$

and its low-lying spectrum λ_i is directly related to the scaling dimensions Δ_i of the underlying conformal field theory by

$$\Delta_i = -\log_3(\lambda_i). \tag{3.46}$$

Reversing this reasoning, we expect the exact correlation length in scale space to be $-1/\log(3^{-\Delta_\sigma}) = 1/(0.125 \cdot \log 3) \approx 7.28$ sites (in units of scale space lattice spacing).

Let us now turn to Fig. 3.2 for the spectra of the reduced density matrices associated to a continuous block of n sites in scale space ρ_n , pictorially represented by

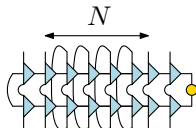


as well as their associated entanglement entropy $S(\rho_n) = -\text{Tr}(\rho_n \log \rho_n)$. The dominant eigenvalues appear to converge to something universal, and a huge amount of irrelevant junk appears after each application of an invariant layer to increase the block size. The trend of the entanglement entropy of a block appears to be linear in scale, recovering the familiar logarithmic scaling with block size for a (1+1)-dimensional CFT with central charge $c = 1/2$ (see Sec. 2.8). Recall that the reduced density matrices of a block of size n in scale space are related to those of blocks of size 3^n in real space and that we are only discussing the spectra of the reduced density matrices; the actual mapping between the support of operators in scale space and real space involves the big spectrum-preserving isometry that we discarded, and is highly non-trivial.

In Fig. 3.3, we plot the mutual information

$$I(A : B) = S(A) + S(B) - S(A \cup B) \tag{3.48}$$

between two single-site ($n = 1$) and two two-site ($n = 2$) regions in scale space in function of the distance N between them,



There is an obvious exponential decay with the distance, which immediately also

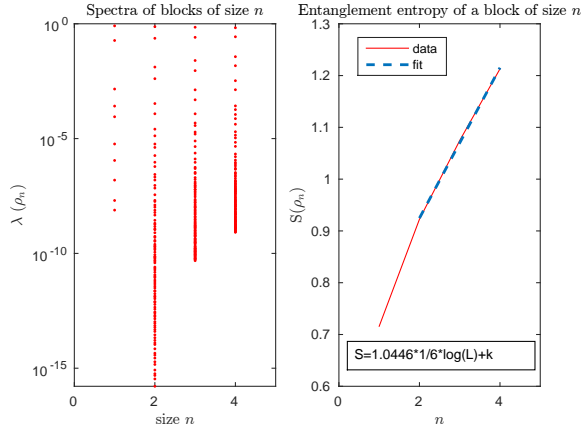


FIGURE 3.2: Spectra (left) and entanglement entropy (right) of blocks of sites in scale space of size $n = 1, 2, 3, 4$ for an optimized $\chi = 10$ MERA and normalization $\text{Tr } \rho_n = 1$.

bounds the correlation functions of observables in scale space, since [110]

$$I(A : B) \geq \frac{(\langle O_A \otimes O_B \rangle - \langle O_A \rangle \langle O_B \rangle)^2}{2 \|O_A\|^2 \|O_B\|^2}. \quad (3.49)$$

Note that the distance N is measured in scale space, so in terms of real space intervals, the decay is polynomial, which is to be expected for critical theories.

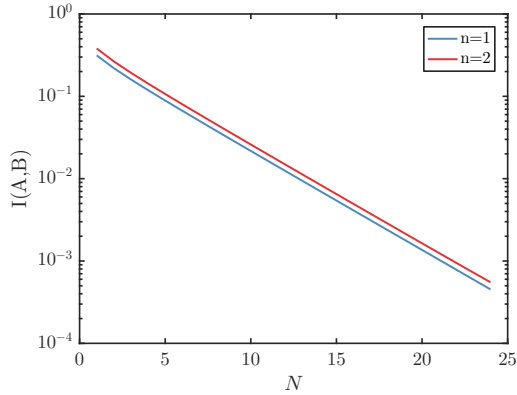


FIGURE 3.3: Mutual information between two single-site ($n = 1$) and two two-site ($n = 2$) regions in scale space in function of distance (in scale) N for an optimized $\chi = 10$ MERA.

3.4.2.3 Musings on excitations in scale space

Let us conclude this section with an overview of the properties of MERA we have encountered. We have seen that the gap of the scale transfer matrix, which is repre-

sented as the trace of an MPO, is directly related to the first non-trivial local scaling dimension. This is a highly non-trivial property of these numerically optimized tensors, and immediately begs the question if studying their robustness using eigenvalue and eigenvector perturbation theory might allow to infer their critical properties and deduce conditions on the elements of the tensors themselves.

Additionally, we calculated the dispersion relation of the scale transfer matrix MPO using the variational excitation ansatz of Sec. 3.2.4 adapted to matrix product operators [63], and found a gapless excitation spectrum⁸. It is known that MPOs with a linear dispersion relation are rare, since they correspond to an *entanglement Hamiltonian* which has a linear (gapless) excitation spectrum. Choosing random isometries in the MPO immediately destroys this linear dispersion relation. Only numerically optimized MERAs can be interpreted as *physical* MERAs in the sense that the scale transfer matrix MPO has the correct structure to reproduce the low-lying CFT spectrum. Even though we did not study perturbations of the numerically optimized tensors, one can already appreciate that the isometric tensors embedded in the scale transfer matrix Eq. (3.44) must be carefully tuned for this spectral behavior to occur.

The above observations suggest that it might be worthwhile to further study the entanglement structure of MERA semi-analytically. Finding explicit conditions on the MERA tensors to ensure a gapless entanglement Hamiltonian together with the correct low-lying CFT spectrum, without having to resort to a black-box numerical optimization procedure, would be quite the achievement.

3.4.3 Causal cone bounds for 1D isometric tensor networks

In this intermezzo, we derive an upper bound for the width of the causal cone in one-dimensional isometric tensor networks which are built by stacking isometries (m, n) which have n incoming legs and m outgoing legs

$$(3.50)$$

Given an initial width x_k of a certain region at layer k , the support of the causal cone in these networks is seen to saturate to a fixed point of a simple Diophantine equation.

Lemma 1 *Consider a one-dimensional isometric tensor network constructed from individual layers, where each layer is characterized by a single isometric tensor M . Let $m \in \mathbb{N}$ and $n \in \mathbb{N}$ respectively denote the number of outgoing and incoming legs of the matrix M*

⁸No dispersion relation is shown here, but see Fig. 5.4 for a very similar plot in the context of tensor network renormalization.

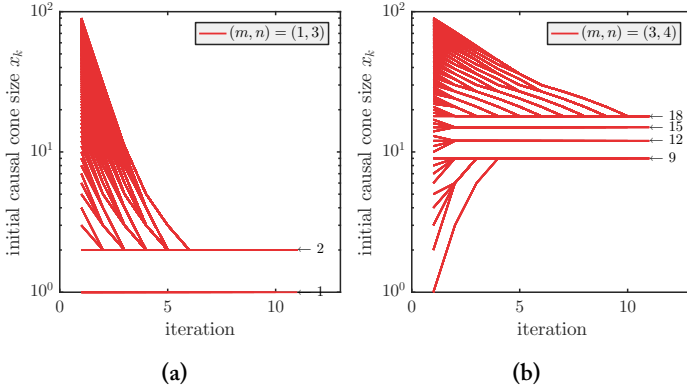


FIGURE 3.4: Fixed points of Eq. (3.54) for a series of initial causal cone sizes $x_k \in [1, 90]$ and isometries (a) $(m, n) = (1, 3)$ and (b) $(m, n) = (3, 4)$.

and assume $m < n$. The worst-case flow for a given causal cone width x_k at a layer k is then given by the recursion relation

$$x_{k+1} = \left(\left\lfloor \frac{x_k - 2}{n} \right\rfloor + 2 \right) m. \quad (3.51)$$

As we are looking for upper bounds on the size of the causal cone, we only consider the worst case scenario for every initial x_k . One can easily check that the largest number of isometries that fit into x_k sites is equal to

$$\left\lfloor \frac{x_k + 2(n-1)}{n} \right\rfloor, \quad (3.52)$$

so that the causal cone grows according to the iterative relation

$$x_{k+1} = \left(\left\lfloor \frac{x_k + 2(n-1)}{n} \right\rfloor \right) m = \left(\left\lfloor \frac{x_k - 2}{n} \right\rfloor + 2 \right) m. \quad (3.53)$$

Lemma 2 *The fixed point of Eq. 3.51 satisfies the Diophantine equation*

$$\frac{x_k}{m} - 2 = \left\lfloor \frac{x_k - 2}{n} \right\rfloor. \quad (3.54)$$

In Fig. 3.4, we have plotted the fixed point behavior for two different configurations of isometries, where one has to keep in mind that these fixed points indicate the worst-case scenario. Like in MERA, there might exist special lattice sites whose causal cone is smaller than expected.

3.5 Real-space renormalization and tensor network states

Let us now turn to real-space RG methods which rely on tensor network states. We have seen that all examples of the old-school methods presented in Sec. 2.10 share the same flaws in that their design is to a large extent model-dependent and there is no obvious way to improve upon the results. One way to understand the breakdown of these real-space RG approaches is through the mutual information Eq. (3.48), which can be shown to satisfy an area law for classical spin systems [110],

$$I(A : B) \leq |\partial A| \log d, \quad (3.55)$$

where the mutual information is expressed in terms of the conditional entropy $H(A|B) = H(A) - I(A : B)$ and d denotes the local dimension. Merely blocking spins will never change the tensor product structure between two regions A and B so that more and more interaction terms will be required for the correlations to keep satisfying an area law under blocking. Additionally, the requirement that a coarse-grained theory should be again expressed in terms of degrees of freedom with the same local dimension is too strong of a constraint on the coarse-graining process. For example, if we are unable to introduce a sufficient amount of effective interactions between Ising spin degrees of freedom, we should try to compensate this lack of effective interactions with an increase in the local dimension, i.e. allow for effective D -dimensional degrees of freedom.

In the upcoming sections, we will see how tensor network representations of classical partition functions enable us to both reshape the tensor product structure and to provide a natural way to let the local dimension grow.

3.5.1 Classical partition functions as tensor networks

There are many ways to represent a classical partition function,

$$Z = e^{\beta F} = \text{Tr}_{\{s_1, s_2, \dots\}} e^{\beta H(s_1, s_2, \dots)}, \quad (3.56)$$

as a tensor network. Degrees of freedom can live on bonds, plaquettes, or vertices, and we are free to construct a tensor network as long as its total contraction sums over all degrees of freedom and matches the partition function.

Let us consider the explicit example of the Ising model on a two-dimensional square lattice, where we associate the spins $\{s_i\}$ to the vertices by means of a tensor

$$\delta_{ijkl} = \begin{array}{c} | \\ \bullet \\ | \end{array} = \begin{cases} 1, & \text{if } i = j = k = l, \\ 0, & \text{otherwise} \end{cases} \quad (3.57)$$

where $i, j, k, l \in \{0, 1\}$. Interactions between the spins live on the bonds in this picture and are given by the matrix

$$a = e^{\beta} \mathbb{1} + e^{-\beta} X = \begin{pmatrix} e^{\beta} & e^{-\beta} \\ e^{-\beta} & e^{\beta} \end{pmatrix}, \quad (3.58)$$

so that we can construct the translation invariant partition function tensor⁹

$$A_{ijkl} = \text{---} \bigcirc A \text{---} = \begin{array}{c} \sqrt{a} \\ \bullet \\ \sqrt{a} \end{array} \begin{array}{c} \sqrt{a} \\ \bullet \\ \sqrt{a} \end{array} \quad (3.59)$$

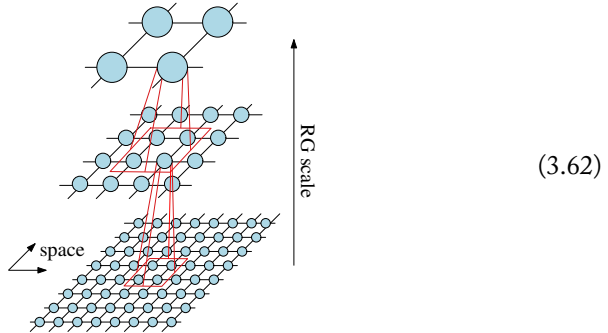
to build the tensor network

$$Z[A] = \text{tTr} \bigotimes A_{ijkl} = \begin{array}{cccc} \bigcirc A & \bigcirc A & \bigcirc A & \bigcirc A \\ \bigcirc A & \bigcirc A & \bigcirc A & \bigcirc A \\ \bigcirc A & \bigcirc A & \bigcirc A & \bigcirc A \\ \bigcirc A & \bigcirc A & \bigcirc A & \bigcirc A \end{array} \quad (3.60)$$

The tensor trace sums over all possible configurations of the spin degrees of freedom, eventually resulting in the partition function. Real-space renormalization can now be interpreted as constructing a sequence of tensor networks

$$Z[A^0] \rightarrow Z[A^1] \rightarrow \dots \rightarrow Z[A^s] \rightarrow \dots, \quad (3.61)$$

where each partition function is defined on a coarser lattice, defining an RG flow in the space of tensors (see Sec. 3.5.4). Pictorially,



In Chapter 6, we will propose more sophisticated tensor network representations of classical partition functions which manifestly encode the non-local symmetries of the underlying CFT fixed point already at the ultraviolet level.

⁹Or the building block of the translation invariant matrix product operator representing the row-to-row or column-to-column transfer matrix.

3.5.2 Tensor renormalization group

The tensor renormalization group (TRG) by Levin and Nave [111] represented arguably the first considerable progress in real-space renormalization in decades. Drawing inspiration from the theory of quantum entanglement and its application to MPS and DMRG, Levin and Nave constructed an improved $b = \sqrt{2}$ block-spin method which is both simple and powerful and is completely based on the singular value decomposition (SVD).

The algorithm is shown in Fig. 3.5, where we have considered a block of four lattice sites. By regarding the partition function tensors as matrices according to the division determined by the dashed diagonals, we can pull the tensors apart using two SVDs,

$$\begin{array}{c} \diagup \\ \bigcirc \\ \diagdown \end{array} \approx \begin{array}{c} \diagup \\ \bigcirc \\ \diagdown \end{array} \approx \begin{array}{c} \diagup \\ \bigcirc \\ \diagdown \end{array} \quad \text{and} \quad \begin{array}{c} \diagup \\ \bigcirc \\ \diagdown \end{array} \approx \begin{array}{c} \diagup \\ \bigcirc \\ \diagdown \end{array} \approx \begin{array}{c} \diagup \\ \bigcirc \\ \diagdown \end{array} \quad (3.63)$$

where the singular values can be truncated¹⁰ and where we have absorbed $\sqrt{\Lambda}$ in U and V^\dagger . The truncations determine the new bond dimension of the coarse-grained partition function tensor, which is obtained by substituting the approximate decompositions Eq. (3.63) respectively at every site of the \ominus - and \otimes -sublattices and exactly blocking four half-sites to restore the isotropy of the lattice.

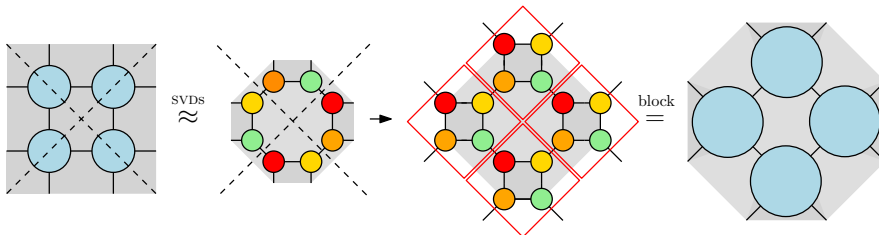


FIGURE 3.5: A single coarse-graining step of the TRG algorithm. Plaquettes containing short-range correlations at the current length scale are denoted by shades of grey. Even though TRG manages to remove some local correlations, its local SVD optimization leaves short-range correlations behind at every step, leading to the failure of TRG at criticality. Away from criticality, the presence of short-range correlations leads to fixed point tensors which depend on microscopic details, challenging their interpretation as RG fixed points.

Like MPS, TRG works extremely well for gapped systems but less so for gapless systems due to similar entanglement and area law constraints. In particular, applying TRG to a critical partition function will not lead to a non-trivial fixed point since every coarse-graining step leaves short-range correlations behind. Away from criticality, these spurious correlations additionally lead to trivial fixed points which depend on microscopic details. The RG flow induced by TRG can thus hardly be called a proper RG flow, since it yields a continuum of trivial fixed points and breaks down when

¹⁰It should by now be clear that the presence of both classical correlations and quantum correlations is reflected in tensor networks by non-zero singular values along bipartite cuts.

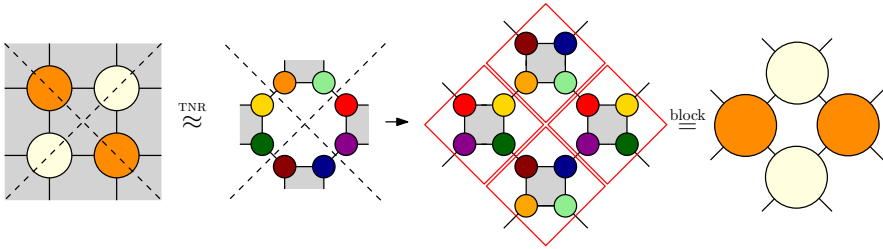


FIGURE 3.6: A single coarse-graining step of a generic TNR algorithm. Even though the diagrams are most closely related to LOOP-TNR, the essential characteristics are shared by all TNR algorithms. The plaquettes of the lattice are initially divided into an A-B structure. A local optimization procedure then removes as many short-range correlations as possible from inside the block (or inside the octagon). After removing local correlations from half of the plaquettes in this way, the exact blocking procedure absorbs the remaining short-range correlations inside the squares to the next coarse-graining scale, where they will be subsequently dealt with.

approaching non-trivial fixed points. Still, extremely accurate critical exponents can be obtained on finite systems using finite-size scaling (see Sec. 3.5.4).

Universal fixed points off criticality have been obtained by including an additional tensor entanglement filtering step before every TRG step, leading to tensor entanglement filtering renormalization (TEFR) [112]. This enhanced TRG algorithm can however still not get rid of short-range correlations at criticality. To counteract the short-range correlation myopia of TRG, other approaches have instead tried to include estimates of the environment. These methods include the second renormalization group [113] and the higher-order renormalization group [114], which all lead to more accurate free energy estimates and expectation values than plain TRG. Crucially, however, none of these TRG-based improvements is capable of yielding non-trivial points tensors at criticality [115].

3.5.3 Tensor network renormalization

Tensor network renormalization (TNR) was recently proposed by Evenbly and Vidal as a real-space RG method capable of sustaining a proper RG flow which includes both an approximate non-trivial fixed point tensor at criticality and unique trivial fixed points off criticality [115]. Additionally, the algorithm yields better accuracies of expectation values and scaling dimensions compared to TRG (see Sec. 3.5.4). Most importantly, the development of TNR has contributed to a better understanding of real-space RG methods in tensor networks.

Before highlighting some aspects of TNR algorithms, let us depict a generic TNR algorithm in Fig. 3.6 in a way that allows for an easy comparison with TRG. The crucial distinction between TRG and TNR is the proper removal of short-range correlations at each length scale. The purely local SVD optimization of TRG is improved by taking a block of four sites into account to determine the optimal truncation. It is important to stress that this is done in an asymmetric way by

removing as many correlations from every other plaquette as possible, so that any remaining correlations are carried over to a larger length scale. Note that we only depict short-range correlations in Fig. 3.5 and Fig. 3.6 since it is these correlations which spoil the RG flow behavior. Long-range correlations, which are of crucial importance at criticality, are assumed to be approximately preserved under the RG transformations (see Sec. 2.6.2).

Let us now parade TNR in its original MERA-TNR incarnation as well as its variations LOOP-TNR and GILT-TNR, both of which are different numerical implementations of the ideas already contained in MERA-TNR. All of them are depicted side by side in Fig. 3.8. We will provide full details on an actual TNR coarse-graining process when discussing TNR_+ in Chapter 5, which is a nonnegative implementation of LOOP-TNR.

3.5.3.1 MERA-TNR

As shown by Evenbly and Vidal, the real-space RG flow of TRG can be significantly improved by thinking in terms of the disentangles and isometries Eq. (3.37) familiar from MERA [115]. Inserting disentangles and isometries inbetween blocks of four lattice sites gets rid of intrablock correlations, see Fig. 3.6(a). By numerically optimizing the isometries and disentangles such that the coarse-grained block resembles the original block as close as possible, the adaptive truncation is able to figure out which short-range correlations can be safely discarded with respect to the block of four sites.

In terms of MERA-TNR, TRG is recovered by setting all unitaries equal to the identity, leaving only local isometries behind. The disentangling power introduced by the additional unitaries can also be appreciated by iterating MERA-TNR on the tensor network representation of an Euclidean path integral in the presence of an open boundary. Pictorially, one can show that this yields a MERA representation of the ground state whereas TRG builds up a tree tensor network [116]. Since a tree tensor network is equivalent to an MPS, the breakdown of TRG at criticality comes as no surprise.

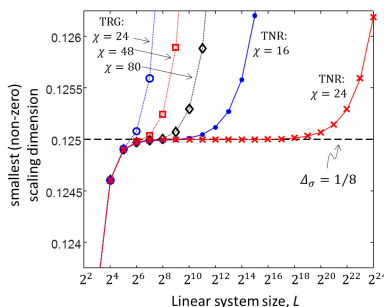


FIGURE 3.7: Smallest non-zero scaling dimension $\Delta_\sigma = 1/8$ of the untwisted Ising CFT spectrum in function of linear system size. Figure from Ref. [115].

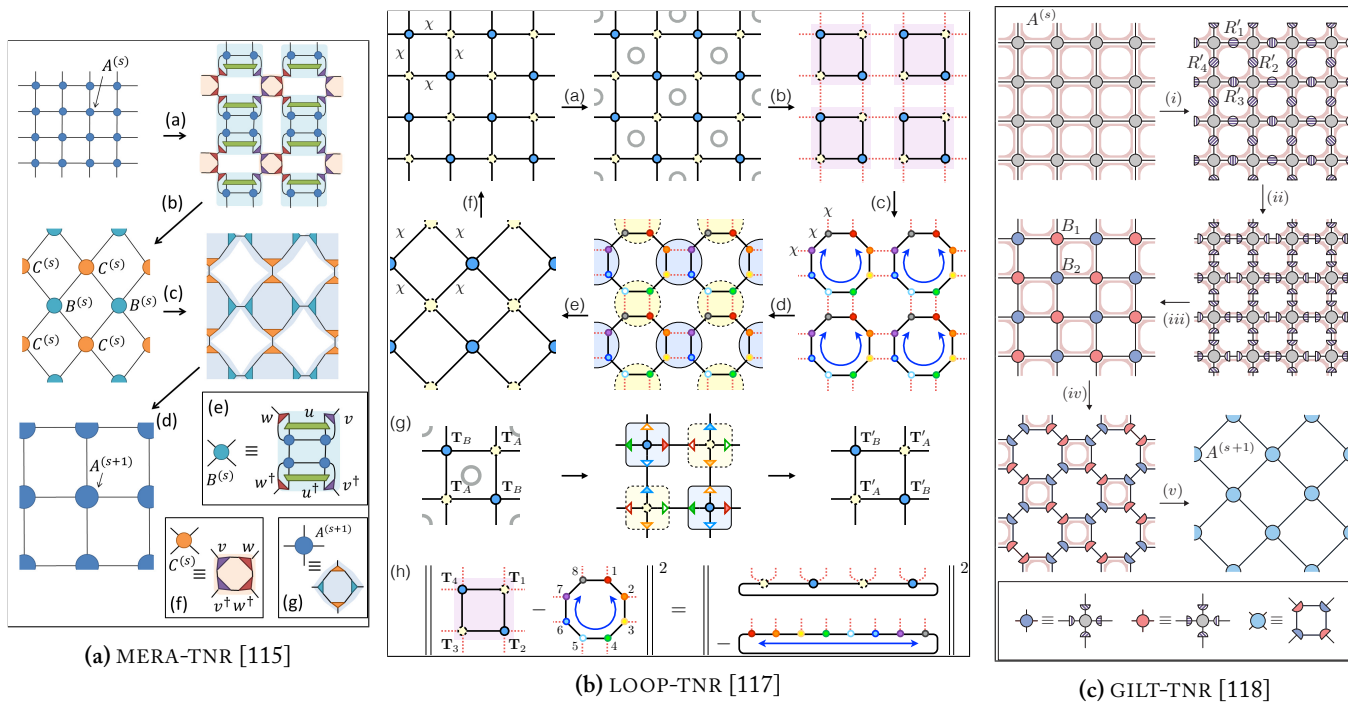


FIGURE 3.8: Overview of TNR coarse-graining algorithms, which respectively get rid of additional short-range correlations in a block of four lattice sites by (a) introducing disentglers, (b) optimizing a periodic MPS, (c) doing a GILT preconditioning step.

To illustrate the improvement of MERA-TNR over TRG, we feature the stability of the RG eigenvalues depicted in Fig. 3.7, where the scaling dimension $\Delta_\sigma = 1/8$ was obtained from diagonalizing the coarse-grained χ -dimensional transfer matrices of the effective partition function at every step (see Sec. 5.8.6.1 for technical details). Upon coarse-graining, TRG is seen to quickly break down whereas MERA-TNR manages to flow closer to the critical fixed point for a considerably larger number of RG steps.

3.5.3.2 LOOP-TNR

As shown in Fig. 3.6(b), LOOP-TNR consists of combination of the entanglement filtering pre-processing step familiar from TEFR improvement of TRG and an additional optimization over a “loop” of trivalent tensors. The key idea is to regard the octagonal loop as a periodic MPS and reformulate the truncation procedure in terms of a well-defined MPS optimization. Due to the sweeping nature of any finite MPS optimization algorithm, correlations inside the loop can be detected and safely discarded. The exact contraction of the squares, which now contain jointly optimized tensors instead of the independently decomposed tensors of TRG, defines the renormalized partition function tensors.

In Chapter 5, we will show that it is possible to implement LOOP-TNR in such a way that the tensor network representation of the classical partition function retains its interpretation in terms of Boltzmann weights, which we will achieve by explicitly preserving nonnegativity in every step of the algorithm.

3.5.3.3 GILT-TNR

The recently developed GILT-TNR algorithm improves TRG by including a graph independent local truncation before every coarse-graining step (see Fig. 3.6(c)). This preconditioning algorithm step is able to locally reduce the bond dimension in an arbitrary tensor network without changing its geometry and is computationally cheaper than MERA-TNR and LOOP-TNR algorithms. Even though the actual renormalization is just a plain TRG step, the accuracy and fixed-point behavior of GILT-TNR matches that of other TNR algorithms (see Table 3.1). As anticipated in Fig. 3.6, the findings of GILT-TNR further indicate that the asymmetric removal of local correlations at every scale is the crucial step distinguishing TRG from TNR.

A most insightful plot is given in Fig. 3.9, where the flow of the singular values across a cut of the partition function tensors Eq. (3.63) is examined along the TRG (top) and GILT-TNR (bottom) flow for different initial temperatures. The upper half of the plots clearly illustrates the shortcomings of TRG: there are no unique trivial fixed points for $T < T_c$ and $T > T_c$ nor is there an approximate critical fixed point for $T = T_c$. The GILT-TNR results in the lower half show unique trivial fixed points which are identical for different initial temperatures. For $T < T_c$, the tensors contain a two degenerate singular values (a GHZ state reflecting all spins up or all spins down) or one singular value (a product state reflecting the independent fluctuations of the spins). At criticality $T = T_c$, an approximate fixed point tensor emerges, which is characterized by invariant singular values. Note that the window of criticality

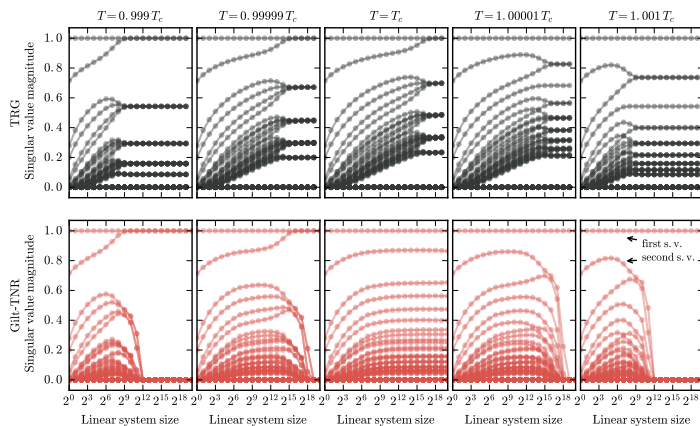


FIGURE 3.9: Comparison of the flow of TRG (top) and GILT-TNR singular values of the coarse-grained Ising partition function tensor for different initial temperatures. Note the difference in fixed point behavior both at and away from criticality $T = T_c$. Figure from Ref. [118]

of the GILT-TNR fixed point tensor is actually consistent with that of MERA-TNR in Fig. 3.7, since the fixed point is not maintained indefinitely. Eventually, the approximate fixed point tensor flows to one of the two unique trivial fixed points [119].

3.5.4 Real-space RG in the space of tensors

Let us now connect the tensor network renormalization group methods discussed above to the general RG framework introduced in Sec. 2.5. It is clear that the assumption on the locality of the dominant interactions under RG is explicit in the tensor network structure. Effective interactions between local degrees of freedom are captured by initially allowing the local dimension d to grow to a larger value χ . This effective local dimension χ is then kept fixed by throwing away negligible entanglement degrees of freedom, which are identified using singular value decomposition (TRG) or a more refined optimization procedure (TNR). Taken together, these two operations try to counteract the growth of interactions in block-spin methods by enlarging the space the local degrees of freedom instead of insisting on keeping the original spin degrees of freedom. This is analogous to the scale invariant MERA for the quantum case (see Sec. 3.4), where one also first introduces transitional layers to grow the local Hilbert space dimension. Only then, in this enlarged Hilbert space, a scale invariant ansatz is imposed.

It is insightful to revisit RG flows but now in the space of tensors¹¹. The qualitative differences between the tensor network renormalization methods we have

¹¹We assume that a similar infinite coupling space structure exists for the space of tensors. One important and obvious complication in a more thorough treatment would be the existence of equivalent tensor network representations of partition functions related by gauge transformations.

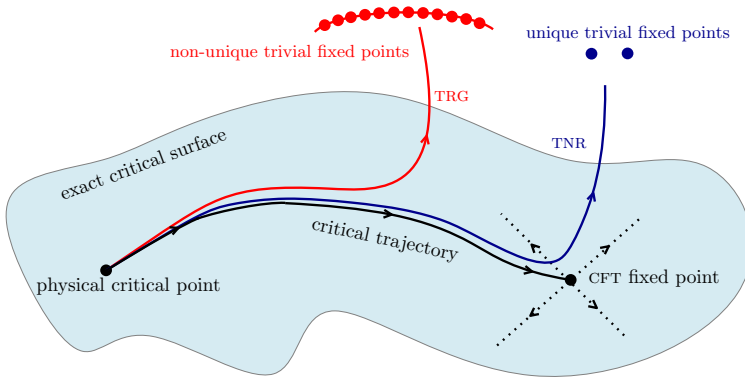


FIGURE 3.10: Qualitative flow behavior of the TRG and TNR tensor network methods for real-space renormalization. The goal is to stay as close as possible to the critical trajectory towards the non-trivial RG fixed point and damp out all irrelevant operators (see Sec. 2.5.3). The truncation steps of TRG and TNR differ in their ability to remove short-range correlations, which is reflected in their fixed-point behavior and accuracy of CFT data.

discussed so far are pictorially indicated in Fig. 3.10. The sketches of TRG and TNR trajectories actually lie in different submanifolds, depending on the bond dimension χ , whose relationship is unclear but which intersect the exact critical surface at least in the physical critical point. Recall that our starting point at criticality is the physical *critical point*, which already encodes the CFT information of the *fixed point* in a non-obvious way, spoiled by irrelevant interactions (see Sec. 2.6.4). We also need to distinguish between fixed points of a particular finite bond dimension RG transformation and the exact, infinite bond dimension CFT fixed point. Even though corner-double line tensors are fixed points of TRG schemes while product states and GHZ states can be fixed points of TNR schemes, it is unknown if these schemes accommodate other, non-trivial fixed points for finite bond dimension.

The task of the RG flow along the critical surface is to wash out all irrelevant operators and drive the partition function tensor to its fixed point tensor. Obviously, this is only exactly possible for infinite bond dimension $\chi \rightarrow \infty$ since the faithful bond dimension has to grow exponentially under blocking. Because any truncation simultaneously restricts both the effective local dimension and the range of the effective interactions, truncating tensors truncates the coupling space in a way that cannot be straightforwardly related to truncating interactions in a Hamiltonian picture. This observation was the inspiration for the restriction of TNR to TNR_+ , a manifestly non-negative implementation of TNR to be discussed in Chapter 5.

A more appropriate question is then how much of an error are we allowed to make when successively approximating the partition function tensor, given that any truncation of the bond dimension induces a highly non-trivial truncation in the infinite coupling space. The key feature of the recently developed TNR methods is that they manage to steer the flow at criticality closer to the exact fixed point for a longer period of time than any previous real-space RG method. Yet we should stress that no TNR scheme is capable of producing a true critical fixed point, since

Table 3.1: Critical exponents for the two-dimensional Ising model from exact diagonalization of linear transfer matrices on finite (coarse-grained) systems [115, 118, 120]. Numbers in brackets denote the (largest) bond dimension used in the respective numerical simulations.

	exact	TRG (120)	MERA-TNR (24)	LOOP-TNR (24)	GILT-TNR (120)
α	0	-0.0004	-0.00018	-0.000012	-0.00004
β	0.125	0.1250180	0.1250117	0.12500085	0.12500265
γ	1.75	1.7503641	1.7501567	1.7500103	1.7500347
δ	15	15.0008961	14.9999488	14.9999872	14.9999808
ν	1	1.0002	1.00009	1.000006	1.00002
η	0.25	0.249986	0.2500008	0.2500002	0.2500003

truncations immediately lead to deviations from the exact critical surface, which throw us off the path towards the fixed point.

However, there exists a window of approximate, critical fixed point behavior, and this critical window is significantly larger in the case of TNR than TRG, where it hardly exists at all. This behavior can also be attributed to the fact that a finite bond dimension introduces a length scale into the system, which acts as an additional relevant scaling variable pushing the flow away from the critical surface, similar in spirit to the cross-over behavior familiar of finite-size scaling¹². Even though every coarse-graining step necessarily introduces a substantial truncation error, it turns out that astonishingly accurate scaling dimensions can be obtained by diagonalizing effective transfer matrices and using CFT finite-size scaling results on a torus (see Sec. 5.8.6.1 and Sec. 6.3.2 for details). In Table 3.1, we compare critical exponents¹³ obtained for the $d = 2$ Ising model universality class. Even though TRG is unable to yield fixed points, accurate critical exponents can still be obtained for finite systems.

In Chapter 6 we will present, among other things, a complementary view on real-space RG which interprets TRG and TNR as different ways of truncating a coarse-grained PEPS wave function. In doing so, it will become clear that the crux of any TNR method is the proper removal of short-range correlations, and of short-range correlations only. We stress the latter point because it runs counter to the usual tensor network intuition where properly accounting for the full environment is of crucial importance to determine an accurate ground state wave function. Coarse-graining a tensor network however requires a different mindset since we want to specifically get rid of short-range correlations.

¹²In MPS theory, the scaling of quantities at criticality in terms of the bond dimension D for $N \rightarrow \infty$ is referred to as finite-entanglement scaling and leads to an effective correlation length $\xi(D) \sim D^\kappa$, where $\kappa = 6/(c(\sqrt{12/c} + 1))$ with c the central charge [121, 122].

¹³The critical exponents have been obtained indirectly from the RG eigenvalues Eq. (2.100) via their relation to the scaling dimensions Eq. (2.103).

Part II

Results

Matrix product state renormalization

In this chapter¹, we investigate the extent to which the MPS transfer matrix can be interpreted as the result of a coarse-graining procedure on the infinite-dimensional quantum transfer matrix originating from the imaginary time path integral representation of a one-dimensional quantum ground state.

4.1 Background and motivation

In recent years, tensor network states have emerged as powerful theoretical and computational tools to investigate strongly correlated quantum many-body systems. By focusing on states rather than Hamiltonians, tensor networks are purposely designed in order to capture the entanglement structure inherent in physically relevant quantum states. For gapped quantum systems, matrix product states (MPS) [123, 124] are known to faithfully represent ground states in one spatial dimension [67], and a plethora of numerical algorithms exist to variationally optimize MPS over the manifold of low-energy states of local Hamiltonians [53, 57, 75, 76, 125, 126]. While local quantities can be approximated to very high precision, long-range behavior is not necessarily captured as accurately due to the exponential decay of correlations in MPS with finite bond dimension. This property is of particular importance in the context of quantum phase transitions, where it has fostered studies of finite entanglement scaling at criticality [122, 127–129].

The multi-scale entanglement renormalization ansatz (MERA) [100] is an altogether different kind of tensor network tailored to the description of scale invariant systems. By introducing unitary disentangling operators, its layered structure is able to accommodate a proper and sustainable renormalization group (RG) flow along the intrinsic scale dimension of the network, even at criticality. Recently, it has been shown that MERA can be reinterpreted as stemming from a novel tensor network renormalization (TNR) scheme for coarse-graining two-dimensional tensor networks [115, 116, 130]. Unlike MPS, the MERA incorporates an explicit scale dimension into its network structure, which renders its real-space coarse-graining properties particularly explicit.

It is well known that the entanglement content of a translation invariant MPS is entirely contained in the dominant eigenvector of its transfer matrix. In a recent

¹The work presented here has been published in Ref. [1] and was done in collaboration with Marek Rams, Valentin Zauner-Stauber, Jutho Haegeman, and Frank Verstraete.

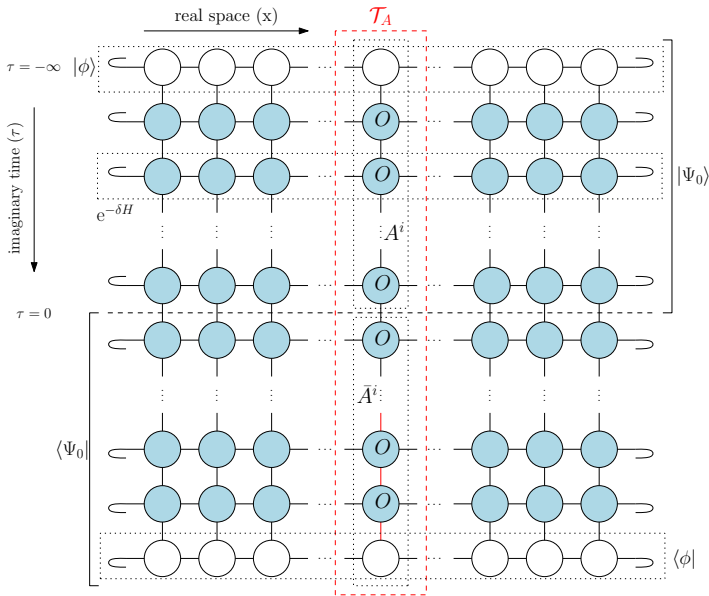


FIGURE 4.1: Two-dimensional tensor network representation of the Euclidean path integral corresponding to the ground state of a local one-dimensional translation invariant lattice Hamiltonian H . Horizontal slices are translation invariant matrix product operators built from a local tensor O (blue circles), and correspond to imaginary time evolution with $e^{-\delta H}$. The MPS ground state $|\Psi_0\rangle$ is obtained by successively applying $e^{-\delta H}$ onto an initial MPS $|\phi\rangle$. Vertical columns can then be interpreted as the MPS transfer matrix $\mathcal{T}_A = \sum_i A^i \otimes \bar{A}^i$, where A^i and \bar{A}^i respectively correspond to the translation invariant ket and bra MPS matrices.

publication [131], it was observed that the other eigenvalues of the MPS transfer matrix contain additional useful information on the elementary excitations and corresponding dispersion relation of the system, providing an intriguing connection between the MPS transfer matrix and the spectral properties of the Hamiltonian. Put differently, there appears to be a highly non-trivial relationship between the excitation spectrum of a local translation invariant Hamiltonian and the local information and static correlations present in its ground state.

In order to gain a better understanding of the origins of the MPS transfer matrix, it was proposed in Ref. [131] to treat the physical spin of a MPS as an impurity in the two-dimensional tensor network arising from the Euclidean path integral representation of the ground state². As depicted in Fig. 4.1, the transfer matrix of an infinite bond dimension MPS can then be identified with the exact quantum transfer matrix at zero temperature. By swapping the interpretation of (Euclidean) time and space, static correlation functions in the MPS are seen to correspond to temporal impurity correlations. The truncated finite-dimensional MPS transfer matrix obtained from numerical simulations will therefore contain

²We refer to Appendix 4.9.1 for a brief summary of path integrals, wave functions, and quantum states.

only the degrees of freedom that are relevant to the impurity dynamics up to some infrared cutoff. This perspective suggests that the state compression involved in variational MPS techniques can be interpreted as an application of Wilson's numerical renormalization group (NRG) [5] (see Sec. 2.9) along the virtual (imaginary time) dimension of the system.

In this chapter, we propose a variational ansatz based on matrix product operators (MPOs) to explicitly coarse-grain transfer matrices and set out to numerically verify the impurity picture proposed in Ref. [131], beyond the analytical results obtained for the XY model in Ref. [132]. Having a layered decomposition of a MPS ground state at our disposal, we benchmark our method on the Ising model, propose an ansatz for the structure of MPS fixed point reduced density matrices, and study the effect of restricting a variational MPS ansatz for elementary excitations to a subspace of variational parameters. We furthermore translate our ansatz to the setting of free fermions, which allows us to further corroborate our findings by exploiting the additional free fermionic structure.

4.2 Exact and compressed MPS transfer matrices

Consider a one-dimensional lattice model and a local translation invariant Hamiltonian $H = \sum_{n \in \mathbb{Z}} h_{n,n+1}$ restricted to nearest-neighbour interactions. The translation invariant ground state of this system can be described by a uniform MPS

$$|\Psi[A]\rangle = \sum_{i=1}^d \mathbf{v}_L^\dagger \left(\prod_{n \in \mathbb{Z}} A^{i_n} \right) \mathbf{v}_R |i\rangle, \quad (4.1)$$

where \mathbf{v}_L^\dagger and \mathbf{v}_R denote boundary vectors irrelevant for bulk properties. The state is hence completely determined by specifying a single tensor $A^i \in \mathbb{C}^{D \times d \times D}$, where D and d , respectively, denote the bond dimension of the virtual level and the physical dimension of the local Hilbert space associated to each lattice site. To each MPS we can associate a transfer matrix

$$\mathcal{T}_A = \sum_i A^i \otimes \bar{A}^i = \begin{array}{c} \text{---} \textcircled{A} \text{---} \\ | \\ \text{---} \textcircled{A} \text{---} \end{array}, \quad (4.2)$$

which is a key object in numerical simulations and is used to calculate static correlation functions with respect to a uniform MPS ground state. We assume that the MPS is injective and normalized such that the transfer matrix has a unique largest eigenvalue equal to 1.

As is well known, a different perspective on the MPS transfer matrix can be provided in terms of a two-dimensional tensor network associated to the uniform MPS representation of the ground state of a local one-dimensional translation invariant Hamiltonian [133–136]. For clarity, an overview of this construction is

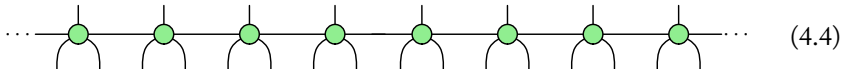
given in Fig. 4.1, where we consider the imaginary time evolution

$$|\Psi_0\rangle = \lim_{\beta \rightarrow \infty} \frac{e^{-\beta H} |\phi\rangle}{\|e^{-\beta H} |\phi\rangle\|}, \quad (4.3)$$

where $|\phi\rangle$ is an initial state assumed to have non-zero overlap with the ground state $|\Psi_0\rangle$. Due to the locality of H , we can split β into small imaginary time steps δ and use a Trotter-Suzuki decomposition $e^{-\delta H} \approx \prod_n e^{-\delta h_{n,n+1}}$ to arrive at a translation invariant MPO representation of $e^{-\delta H}$ (see, e.g., Ref. [137]). This approximation introduces a controllable Trotter error depending on the order of the decomposition, which renders the MPO representation quasi-exact. By grouping tensor contractions along imaginary time, we can identify the *exact* MPS transfer matrix with a single column of the network. Interpreting the tensor network in Fig. 4.1 as an Euclidean path integral, the exact MPS transfer matrix thus coincides with the quantum transfer matrix derived from the partition function $Z_\infty = \lim_{\beta \rightarrow \infty} \text{Tr}(e^{-\beta H})$ at zero temperature. Note however that both these exact transfer matrices have exponentially diverging bond dimensions, and thus differ from the truncated finite-dimensional MPS transfer matrix $\mathcal{T}_{\tilde{A}} = \sum_i \tilde{A}^i \otimes \tilde{A}^i$ defined before, which arises in actual numerical simulations. Similarly, the exact MPS ground state tensor A^i corresponds to a semi-infinite MPO in this picture, and represents the ground state $|\Psi_0\rangle$ up to some Trotter error, of which the truncated finite-dimensional MPS \tilde{A}^i is a compressed version. Stated in these terms, our goal is to shed light on the relationship between the exact MPS A^i and its compressed version \tilde{A}^i .

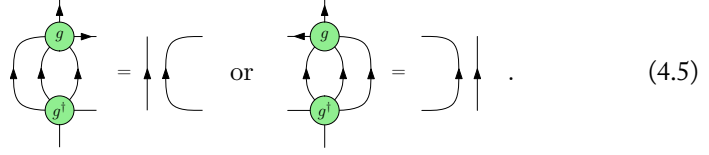
4.3 Coarse-graining transfer matrices

As it is our intention to coarse-grain a translation invariant MPO, defined by a local tensor O having on-site operator dimension d and MPO bond dimension D , a natural way to proceed is to devise a coarse-graining strategy using MPOs in order to retain the matrix product structure. To this end, we introduce an isometric coarse-graining MPO denoted by G , which is characterized locally by a single five-index tensor g ,



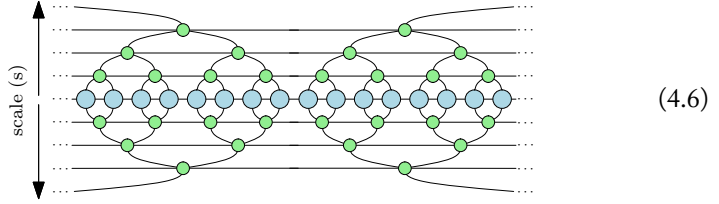
The tensor g is restricted to be an isometry defined by the map $g : \mathbb{I} \otimes \mathbb{I} \otimes \mathbb{W} \rightarrow \mathbb{O} \otimes \mathbb{V}$, where \mathbb{I} , \mathbb{V} , and \mathbb{O} , respectively, refer to the vector spaces of the incoming indices, the virtual indices and the outgoing indices. As such, g satisfies $g^\dagger g = \mathbb{1}_{\mathbb{O} \otimes \mathbb{V}}$ and $g g^\dagger = P$, where P is a projector onto some subspace of $\mathbb{I} \otimes \mathbb{I} \otimes \mathbb{W}$. Let us denote $d = \dim(\mathbb{I})$, $\chi = \dim(\mathbb{V})$ and $d' = \dim(\mathbb{O})$. The isometric constraints on the local tensor g forces the MPO G as a whole to be isometric if $d^2 > d'$, or unitary if $d^2 = d'$. Note that there are two different ways to group operator and virtual indices of g , leading to two possible “gauge” choices, denoted pictorially by the following

equations:



$$(4.5)$$

Let us now consider a finite set $\{G_s\}$ of the kind of MPO isometries defined above, and label them with a discrete scale label $s = 1, 2, \dots, s_{\max}$, where each G_s is allowed to be different. By acting sequentially with each of the $\{G_s\}$ together with their conjugates $\{G_s^\dagger\}$ on the translation invariant MPO to be coarse-grained, we arrive at the MERA-inspired tensor network:



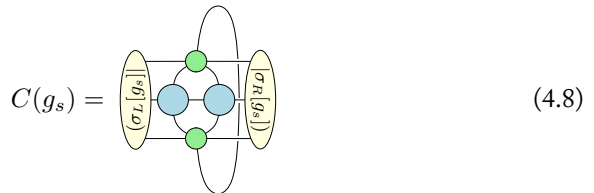
$$(4.6)$$

One way to optimize all of these coarse-graining MPOs, is to perform a single sweep in scale from bottom to top. At each layer s , two tensors O_{s-1} of the previous layer are blocked by acting with g_s and g_s^\dagger to construct



$$(4.7)$$

which is a coarse-grained tensor that redistributes entanglement among virtual and operator dimensions. Tracing over the outgoing indices, as depicted in Eq. (4.8), we can interpret this object as a generalized transfer matrix with $\chi_s^2 D_s$ -dimensional fixed points $(\sigma_L[g_s])$ and $(\sigma_R[g_s])$, where we have emphasized the dependence on the coarse-graining isometry in the notation. By locally maximizing the cost function³



$$(4.8)$$

³Like all tensor network optimization problems, there is no guarantee that a global optimal solution will be found. For our purposes, the optimization procedure was seen to consistently converge to a local optimum.

for the isometry g_s using a conjugate gradient algorithm adapted to unitary manifolds [138], we then iteratively update the left and right fixed points of Eq. (4.7) until convergence of Eq. (4.8) is attained up to some tolerance. The cost function Eq. (4.8) is well-defined for Hermitian MPOs; a possible alternative strategy for non-Hermitian MPOs would be to minimize the norm of the difference between two tensors O_{s-1} and the same two tensors with the projector $P_s = g_s g_s^\dagger$ applied to the outgoing indices. The coarse-grained MPO tensor O_s is obtained by truncating its bond dimension to a fixed number D_s , or up to some tolerance, using conventional MPS methods [139], such that

The diagram shows an equality between two tensor networks. On the left, a blue circle representing a tensor is flanked by two grey trapezoidal shapes labeled W_s and W_s^{-1} . On the right, the same blue circle is shown as part of a larger network of four blue circles arranged in a square, with two green circles above and below the square, connected by lines. The equation is labeled (4.9).

where we have introduced the rank-reducing tensor W_s , with W_s^{-1} denoting the left inverse of W_s such that $W_s^{-1}W_s = \mathbb{1}$ and $W_s W_s^{-1}$ projects onto the truncated subspace. Note that the new on-site operator dimension of the coarse-grained MPO is determined by the output dimension d'_s of the gate g_s . This constitutes the optimization of one layer, and by repeating the above coarse-graining procedure until the top level is reached, we obtain a set of effective MPO tensors $\{O_s\}$, isometric gates $\{g_s\}$ and truncation tensors $\{W_s\}$ for $s = 1, 2, \dots, s_{\max}$. Both the tolerances for the optimization of the cost function and for the truncations provide sensible measures for the errors introduced along the way.

Although our main motivation in this chapter is to coarse-grain the MPOs appearing naturally along the imaginary time direction in the Euclidean path integral picture in Fig. 4.1, there is nothing preventing us from applying the above ansatz along the spatial direction to renormalize, for instance, a Hamiltonian operator or more general transfer matrices arising in two-dimensional lattice models. In particular, local Hamiltonian terms can be seen to renormalize to a sequence of semi-infinite MPO strings to the left or to the right depending on the gauge choice in Eq. (4.5), which follows naturally from the one-sided causal cone structure that arises due to the isometric nature of the coarse-graining gates.

4.4 From Euclidean path integral to uniform MPS

The pioneering work of Wilson on the numerical renormalization group showed that the relevant low-energy subspace for an impurity problem could be obtained by applying real-space RG transformations [5]. Recently, the theory of minimal updates in MERA has related the success of NRG to the inherent causal cone structure of MERA [140]. The causal cone of a region had been originally introduced as the part of the MERA network that is geometrically connected to and able to exert influence on the properties of the state in that region [100]. It has since been interpreted as the collection of tensors that needs to be changed in order to account for a local change of the Hamiltonian in that region, which is understood to be sufficient to

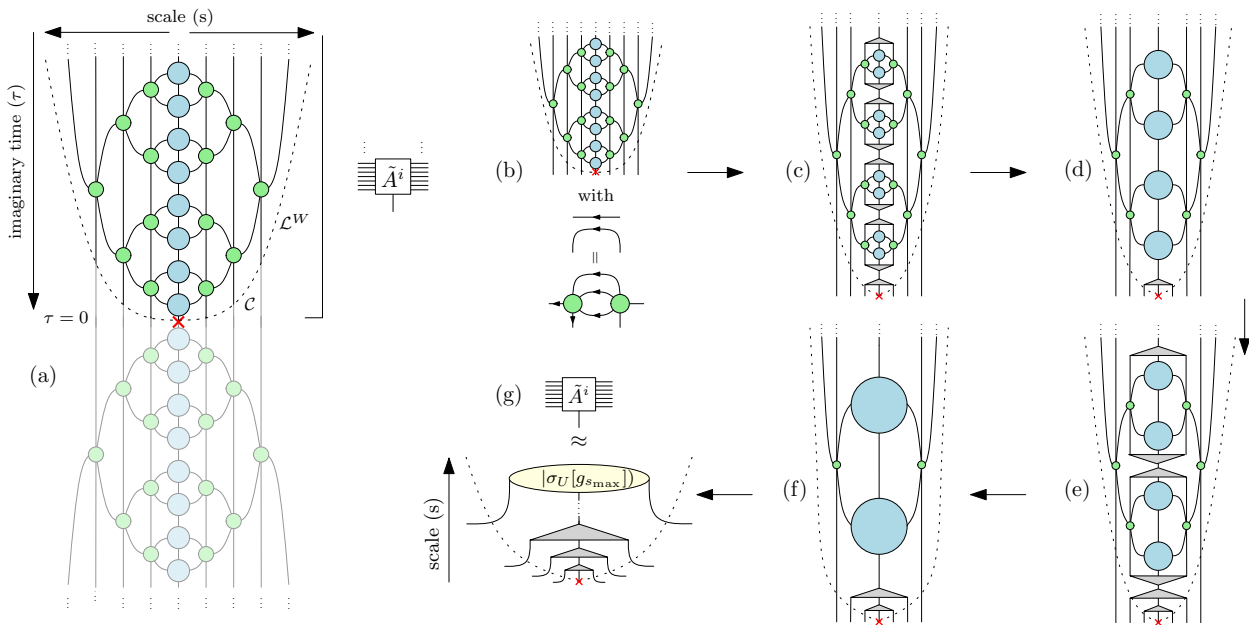


FIGURE 4.2: Uniform MPS from coarse-graining the exact transfer matrix. Location of the physical spin, considered as an impurity at $\tau = 0$, is denoted with a red cross. (a) Bonds crossing the one-sided causal cone \mathcal{C} of the impurity at $\tau = 0$ identify degrees of freedom relevant to the physical spin, which live on the Wilson chain \mathcal{L}^W defined along the boundary of \mathcal{C} . The tensor network outside \mathcal{C} renormalizes the exact transfer matrix \mathcal{T}_A into a new transfer matrix \mathcal{T}_W along \mathcal{L}^W . (b) Contraction of the tensor network outside \mathcal{C} renormalizes the ket, projecting the exact MPS A^i onto the subspace defined by the relevant degrees of freedom along \mathcal{L}^W . (c) Insertion of approximate resolutions of the identity $\mathbb{1} \approx W_1 W_1^{-1}$. (d) Coarse-graining the semi-infinite MPO string to the next layer leaves a single W_1 tensor behind. (e)(f) Repeating this procedure leads to the construction of the Wilson MPO. (g) After introducing an infrared cutoff by capping the Wilson MPO with the fixed point of the uppermost coarse-grained tensor, we retrieve a finite-dimensional MPS \tilde{A}^i .

capture the evolution of that region under successive coarse-graining transformations while maintaining locality [140]. This property can be ultimately traced back to the existence of distinct energy scales in the Hamiltonian. According to the principle of minimal updates, an impurity initially localized in space thus remains localized under coarse-graining, which leads to a very efficient MERA description of systems with boundaries, impurities, or interfaces [141, 142]. The relevant degrees of freedom for an impurity are found to be exactly those living at the boundary of the causal cone.

Although the MPS ansatz we are about to describe bears a resemblance to the impurity MERA construction, the underlying motivation is entirely different. We stress that the main motivation for our proposal is to be able to capture the physics relevant for the physical spin degree of freedom of a quantum state, which, as we will argue, precisely amounts to extracting the degrees of freedom relevant to the spin treated as an impurity in the exact quantum transfer matrix.

Let us now apply the coarse-graining ansatz Eq. (4.6) to the vertical transfer matrix \mathcal{T}_A obtained from the imaginary time evolution network in Fig. 4.1. Note that the physical dimension and virtual dimension in Fig. 4.1 now correspond, respectively, to the bond dimension and the operator dimension of the coarse-graining MPO. We furthermore implicitly assume that $\mathcal{T}_A = e^{-\tilde{H}}$, i.e. the transfer matrix is understood to originate from some Euclidean rotated effective local Hamiltonian \tilde{H} [131]. In general, there is no reason to expect the Hamiltonian \tilde{H} to be related to the physical Hamiltonian H involved in the MPO description of the imaginary time evolution $e^{-\delta H}$.

To arrive at a uniform MPS, we will treat the physical spin connecting the exact MPS representations of ket and bra at $\tau = 0$ as an impurity in \mathcal{T}_A . The arbitrary location of the physical index in imaginary time does not *a priori* introduce an inhomogeneity in \mathcal{T}_A . However, for expectation values of local operators different from the identity, the privileged nature of the physical spin becomes manifest, and an operator insertion at $\tau = 0$ leads to the modified transfer matrix $\mathcal{T}_A^{\mathcal{O}} = \sum_{ij} \mathcal{O}_{ij} A^i \otimes \bar{A}^j$ used in calculating MPS expectation values. As such, a static correlation function between two operators separated by n sites in the physical system corresponds to a “temporal correlator” of the impurity between two operators separated by n steps of evolution with $\mathcal{T}_A = e^{-\tilde{H}}$, where \tilde{H} again denotes not the physical Hamiltonian H but the Euclidean rotated effective local Hamiltonian. We will thus construct a truncated MPS representation \tilde{A}^i by extracting the relevant degrees of freedom for the “Euclidean dynamics” of the impurity from the exact quantum transfer matrix \mathcal{T}_A .

In what follows, we will focus on the upper semi-infinite MPO describing the ket part $|\Psi[A]\rangle$ of the transfer matrix \mathcal{T}_A , as depicted in Fig. 4.2, and refer to the location of the physical spin as the impurity regardless of whether there is actually an operator inserted at $\tau = 0$. To explicitly construct the approximated ket tensor \tilde{A}^i associated to the uniform MPS $|\Psi[\tilde{A}]\rangle$ in Fig. 4.1, we first apply our ansatz to the infinite quantum transfer matrix, and optimize for s_{\max} layers as if no impurity were present. We then insert the impurity at $\tau = 0$ and draw its causal cone \mathcal{C} in Fig. 4.2(a), where the inside of the causal cone stretches out to the left and to the right, and the degrees of freedom affecting the impurity at $\tau = 0$ arise from

contracting the network outside the causal cone. By ignoring the bottom half of the network, we can identify the part of the coarse-graining network which acts on the semi-infinite ket part of the MPO.

In retrospect, the impurity naturally suggests which isometric restriction in Eq. (4.5) to impose on the coarse-graining tensors during the optimization, as the entire tensor network surrounding the original semi-infinite transfer matrix can be interpreted as a projector onto the dominant eigenvector subspace relevant to the impurity, see Fig. 4.2(b).

It is clear that only one index of the MPO coarse-graining tensors crosses the boundary of the causal cone for each layer. Together, these legs constitute the sites of an effective lattice system \mathcal{L}^W defined along the boundary of the causal cone, which is called the Wilson chain. Sites along this chain are labeled by the layer index $s = 1, 2, \dots, s_{\max}$, where site s contains an effective renormalized description, for $d' = d$, of 2^s sites of the original lattice located roughly at a distance 2^s away from the impurity. Moving along the Wilson chain thus corresponds to changing scale and moving away from the impurity. Next, we insert approximate resolutions of the identity at the lowest layer in Fig. 4.2(c) using the rank-reducing tensors $W_1 W_1^{-1}$ obtained during the optimization to reduce the bond dimension in the imaginary time direction. As shown in Fig. 4.2(d), the semi-infinite MPO string is pushed to the next coarse-graining layer, leaving a single tensor W_1 behind. Repeating this procedure for the next layer in Fig. 4.2(e)-(f) leads to the emergence of an inhomogeneous MPO along the imaginary time direction, which we will refer to as the *Wilson* MPO, and which effectively amounts to a sequence of coarse-grained Trotter steps. Even though the bond dimension $\prod_{s=1}^{s_{\max}} \chi_s$ of \tilde{A}^i may become large for large s_{\max} , we can efficiently contract the Wilson MPO sequentially and accurately truncate its bond dimension to some value D . We could partly avoid this additional truncation, which is a consequence of having MPOs corresponding to infinitesimal Trotter times δ , by blocking MPOs initially such that they represent a bigger time step. By introducing the fixed point of the uppermost coarse-grained tensor as an infrared cutoff in Fig. 4.2(g), we arrive at a finite-dimensional approximate Wilson-based MPS with an internal layered structure resulting in the uniform MPS tensor \tilde{A}^i .

The reason for this particular cutoff strategy can be traced back to interpreting the transfer matrix \mathcal{T}_A as a thermal state (or more generally a mixed state) with exponentially decaying correlations. We then expect the coarse graining network to be able to disentangle this state into a product state using a finite number of layers, similar as in the case of ground states of gapped Hamiltonians, such that, after a finite number of layers, we can pictorially denote the RG flow by


(4.10)

If we want the coarse-grained MPO tensor at the top to have a trivial bond dimension $D_{s_{\max}} = 1$, the optimal choice is given by the eigenvectors corresponding to the largest eigenvalue of Eq. (4.7). For a critical MPO, we expect scale invariance to direct the coarse graining process to a fixed point that needs to be iterated forever. In that case, introducing the product state fixed point as an infrared cutoff explicitly breaks the critical properties and can as such only be considered an approximation, whose quality can be assessed by evaluating the energy with respect to the resulting state. Note that all variational, finite bond dimension MPS approximations necessarily contain an implicit infrared cutoff, and that different cutoff implementations might yield different MPS tensors approximating the same gapless state, a point to which we return in Sec. 4.7.1.

In the following two sections, we consider two immediate applications made possible by the structure of our ansatz.

4.5 Structure of MPS fixed point reduced density matrices

From the layered structure of our MPS decomposition, it is straightforward to associate a layered decomposition to the zero-dimensional fixed point reduced density matrices ρ_L and ρ_R of the MPS transfer matrix Eq. (4.2) as well. To see this, let us apply a truncation procedure to the transfer matrix $\mathcal{T}_{\tilde{A}}$ constructed from our ansatz, instead of working solely on the level of the ket $|\Psi[\tilde{A}]\rangle$. By sequentially grouping indices across bra and ket for the truncation step at each layer, we eventually arrive at the norm

$$\langle \Psi[\tilde{A}] | \Psi[\tilde{A}] \rangle = \rho_L \left[\begin{array}{c} \text{Diagram: A diamond-shaped structure with multiple layers of grey triangles (Wilson MPOs) and red triangles (rank-reducing tensors) connected by lines. The structure is symmetric and has a central core. The left and right sides are labeled } \rho_L \text{ and } \rho_R \text{ respectively. The top and bottom vertices are labeled } \tilde{A} \text{ and } \tilde{A} \text{ respectively.} \end{array} \right] \rho_R, \quad (4.11)$$

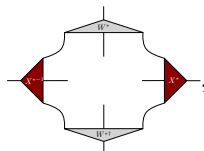
where the grey triangles denote the Wilson MPOs for ket and bra, and the red triangles are now invertible rank-reducing tensors X_s^{-1} (left) and X_s (right), for $s = 1, 2, \dots, s_{\max}$, that can be obtained from lifting the impurity from bottom to top and truncating the effective transfer matrix at each layer s by considering it as a MPS,

$$\left[\begin{array}{c} \text{Diagram: A diamond-shaped structure with a central grey triangle labeled } \mathcal{T}_{\tilde{A}}^s \text{ and two red triangles labeled } X_s^{-1} \text{ and } X_s \text{ on the left and right sides respectively.} \end{array} \right] \approx \left[\begin{array}{c} \text{Diagram: A diamond-shaped structure with a central grey triangle labeled } \mathcal{T}_{\tilde{A}}^{s-1} \text{ and two grey triangles labeled } \tilde{W}_s \text{ on the top and bottom sides respectively.} \end{array} \right] \quad (4.12)$$

Note how we can approximately determine the fixed points of the transfer matrix in a sequential manner without explicitly calculating them, and how only small bond

dimensions are involved in the intermediate truncation processes. A potential application of this insight lies in the problem of efficiently contracting two-dimensional tensor networks, e.g. overlaps of projected entangled pair states [80], where one of the main bottlenecks in variational ground state optimizations can be traced back to calculating high-dimensional MPS fixed points of the MPO transfer matrices needed for the calculation of environment tensors (see Sec. 3.3.3). The feedback of information from high-energy to low-energy in our layered decomposition of these fixed points might lead to a substantial reduction in computational resources, thus allowing the approximation of otherwise intractable MPS fixed points.

Another application concerns scale invariant theories, for which we expect to find a recursive relation, directly from the layered MPS decomposition, whose eigendecomposition ought to contain the scaling operators and scaling dimensions of the underlying conformal field theory (see Sec. 2.8). Suppose we have identified a fixed point truncation tensor W^* and associated X^* in the layered decomposition of our MPS ansatz, characterizing the scale invariant fixed-point behavior. We can then propose a “radial” superoperator


(4.13)

whose eigenvalues and eigenvectors are expected to be related to the scaling dimensions and operators of the underlying conformal field theory (see Sec. 2.8). Forgetting about the Wilson-based MPS origin of the ansatz, we can also build concentric tensor networks from Eq. (4.13), which enforce scale invariance and can be regarded as variational ansätze in their own right [143]. Similar superoperators for extracting scaling fields were of course conceived in MERA [107, 144] and TNR [115] (see Chapter 3), but not in a MPS setting. A partial approach to extract scaling information from a MPS was investigated in Refs. [122, 127–129].

4.6 Restricted variational subspaces for excitations

Given the internal layered structure of the uniform MPS in Fig. 4.2(g), it is tempting to ask how excitations can be interpreted in this framework. Following Wilson’s RG interpretation of the Kondo impurity problem [5], we expect low-energy excitations to live near the top of the Wilson MPO if the layered MPS decomposition obtained from our ansatz can be interpreted as a true renormalization group scale. Note that our ansatz retains translation invariance in space as we effectively construct a uniform MPS, and that the scale dimension in our case refers to coarse-grained imaginary time. We want to emphasize that, even though there is no explicit spatial coarse-graining taking place (as the number of sites remains constant), spatial correlations do arise naturally in our picture as we coarse-grain imaginary time to grow the virtual bond dimension of the MPS. Despite the absence of an explicit coarse-graining in space, the successive MPO layers labeled by s are non-unitary and

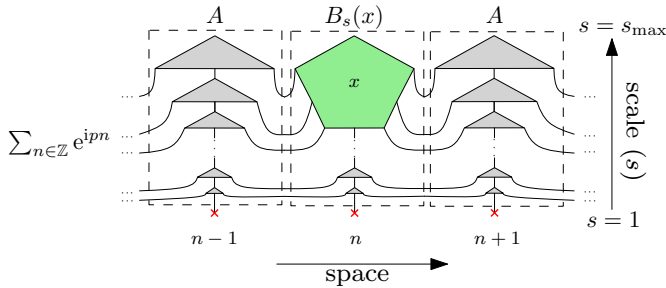


FIGURE 4.3: Example of a restricted variational MPS excitation ansatz $|\Phi_p^{(A)}(B_s)\rangle$ at intermediate layer index s , constructed to allow for targeting the variational parameters x residing in an interval of layers $[s, s_{\max}]$ (green triangles), while the tensors corresponding to layers $[1, s)$ are held fixed.

can therefore shrink the effective Hilbert space at every step. The idea is now to expose this effective reduction of the Hilbert space at higher renormalization scales by perturbing the tensors within the layered structure of the MPS and observing to which part of the spectrum of the Hamiltonian a particular perturbation gives access.

In particular, exploiting the translation invariance which we still have at our disposal, we can use the variational MPS ansatz for localized excitations developed in Refs. [61, 78], given by

$$|\Phi_p^{(A)}(B)\rangle = \sum_{n \in \mathbb{Z}} e^{ipn} \sum_{i_n=1}^d \mathbf{v}_L^\dagger \left(\prod_{m < n} A^{i_m} \right) B^{i_n} \left(\prod_{m' > n} A^{i_{m'}} \right) \mathbf{v}_R |i\rangle. \quad (4.14)$$

Comparing with Eq. (4.1), it is clear that the excitation ansatz is constructed on top of the ground state wave function by changing a single ground state tensor A^i into a tensor B^i and taking a momentum superposition of this localized perturbation. All variational freedom is contained within the tensor B^i , and the variational optimization of the Rayleigh-Ritz quotient

$$\min_B \frac{\langle \Phi_p^{(A)}(B) | H | \Phi_p^{(A)}(B) \rangle}{\langle \Phi_p^{(A)}(B) | \Phi_p^{(A)}(B) \rangle}. \quad (4.15)$$

gives rise to a generalized eigenvalue problem. In order for this generalized eigenvalue problem to be well-defined, it will be necessary to project out so-called null-modes, i.e. (almost) zero eigenvalues of the effective normalization matrix in the right hand side of the generalized eigenvalue equation.

Let us now recast Eq. (4.14) pictorially and substitute our layered MPS decomposition of the MPS ground state to arrive at the variational ansatz depicted in Fig. 4.3. By fixing part of B^i to be equal to A^i using the layered decomposition, we can now design a restricted excitation ansatz $|\Phi_p^{(A)}(B_s)\rangle$, for $s = 1, 2, \dots, s_{\max}$, which only allows for variations with respect to an interval $[s, s_{\max}]$ of tensors in the Wilson MPO description of the full excitation ansatz. The restricted tensor $B_s^i(x) \equiv \Xi_s^i(x)$

is defined in terms of a linear mapping

$$\Xi_s : \mathbb{C}^{\prod_{s'=s}^{s_{\max}} \chi_{s'} \times d_s \times \prod_{s'=s}^{s_{\max}} \chi_{s'}} \rightarrow \mathbb{C}^{D \times d \times D}, \quad (4.16)$$

which glues the variational parameters x to the surrounding MPS ground state tensors $A^i \in \mathbb{C}^{D \times d \times D}$. For different layers s , this tensor parametrizes different subspaces of the full variational space⁴ spanned by the states $|\Phi_p^{(A)}(B)\rangle$ with unrestricted B^i . Starting from $B_{s_{\max}}^i$, where only the variational degrees of freedom in the top tensor are considered, we can gradually take all layers $[1, \dots, s_{\max}]$ into account until the ansatz culminates into the full $B^i \equiv B_1^i$, incorporating all length scales.

Note that the role of our restricted ansatz is not so much in improving the efficiency of numerically calculating excitations within the framework established in Ref. [61], but in providing a novel and conceptually intriguing interpretation of excitations within MPS in a way that explicitly tries to resolve the different energy scales present in the MPS ground state tensor. In Sec. 4.7.2, we will verify that the number of null-modes as function of layer index s and momentum p is intimately tied to the effective reduction of the Hilbert space at higher renormalization scales.

4.7 Numerical results

To assess the validity of our ansatz, we performed numerical simulations using the MPS ansatz introduced in Sec. 4.4 to discuss the transfer matrix and Schmidt spectra of the resulting MPS ground states. We have also calculated dispersion relations using the setup of Sec. 4.6 to illustrate that variational subspaces corresponding to the upper layers of our MPS ansatz are effectively restricted to the low-energy part of the spectrum. Additionally, we translate our method for compressing transfer matrices to the setting of free fermions, where the additionally imposed structure on the numerics allows us to highlight and further corroborate our findings.

4.7.1 MPS ansatz from Wilson MPO

Consider the quantum Ising model in a transverse field, which can be defined in terms of the Hamiltonian

$$H = - \sum_i \sigma_i^x \sigma_{i+1}^x - \lambda \sum_i \sigma_i^z, \quad (4.17)$$

where λ determines the strength of the applied magnetic field. One can easily show how to construct a translation invariant MPO representation[137] of the Trotter-Suzuki decomposition of $e^{-\delta H}$, to which we apply our ansatz along the imaginary time direction. Comparing the ground state energy density of the MPS resulting from our ansatz with the exact solution, we find relative energy errors

⁴Note that the restricted generalized eigenvalue problem is variational with respect to using the full B^i , but not necessarily with respect to the exact problem. Although the reduced $B^i(x)$ will always yield excitation energies higher than those obtained by varying the full B^i , these energies might still be lower than the exact excitation energies due to errors in the ground state MPS approximation [61].

$\Delta E = (E - E_0)/E_0 \sim 10^{-6}$ both for the gapped ($\lambda \neq 1$) and gapless ($\lambda = 1$) phases. Having obtained a uniform MPS from the Wilson MPO, we can further quantify the accuracy of our ansatz by studying the spectrum of the transfer matrix Eq. (4.2), and the Schmidt values of the MPS, which can be retrieved from the spectrum of the dominant eigenvector of the transfer matrix Eq. (4.2). In Fig. 4.4 and Fig. 4.5, we show a comparison of low-lying transfer matrix spectra obtained with respectively our coarse-graining method and a MPS that was variationally optimized using the time-dependent variational principle [75].

For the gapped case depicted in Fig. 4.4, an excellent match is found for both the TM eigenvalues λ_n and the Schmidt coefficients λ_α as soon as the number of coarse-graining layers is chosen sufficiently large, which demonstrates the behavior of the infrared cutoff as explained in Sec. 4.4.

For the gapless case in Fig. 4.5, the infrared cutoff can be recognized as a very particular initial state in the effective imaginary time evolution induced by the Wilson MPO, spoiling the relevant infrared data for critical models. From the impurity point of view, there is a strong interaction between the different sites in the Wilson chain \mathcal{L}^W , corresponding to degrees of freedom living at different energy scales. Indeed, the infrared cutoff introduced after a finite number of layers at one end of the Wilson chain, has a strong feedback on the physics of the impurity, which is living at the other end of the Wilson chain. As argued in Sec. 4.4, different implementations of the implicit infrared cutoff for gapless states, yield different variational MPS approximations, which has recently been discussed in Ref. [132].

To illustrate this explicitly, we also studied the effect of further truncating the Wilson based MPS to some specific bond dimensions using the standard MPS recipe (i.e. throwing away the smallest Schmidt coefficients). While this has no distinguishable effect on the remaining Schmidt coefficients of Fig. 4.5(b), the effect

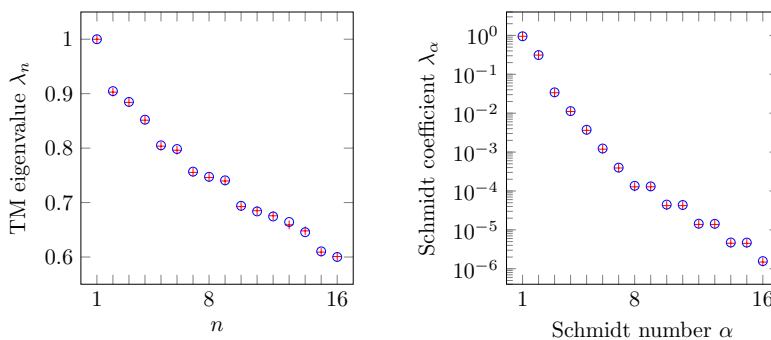


FIGURE 4.4: Comparison of transfer matrix (TM) spectra (left) and Schmidt spectra (right) of the transverse Ising model Eq. (4.17) between our MPS ansatz $|\Psi[\tilde{A}]\rangle$ based on the Wilson MPO (blue circles) and a variational MPS ground state $|\Psi[A]\rangle$ (red crosses) for $\lambda = 1.1$ (gapped) and $D = 16$. All MPO simulations were performed using a Trotter step $\delta = 0.001$ and local dimensions $d_s, \chi_s, d'_s \in \{2, 4\}$ of the coarse-graining tensors with $s_{\max} = 14$ layers.

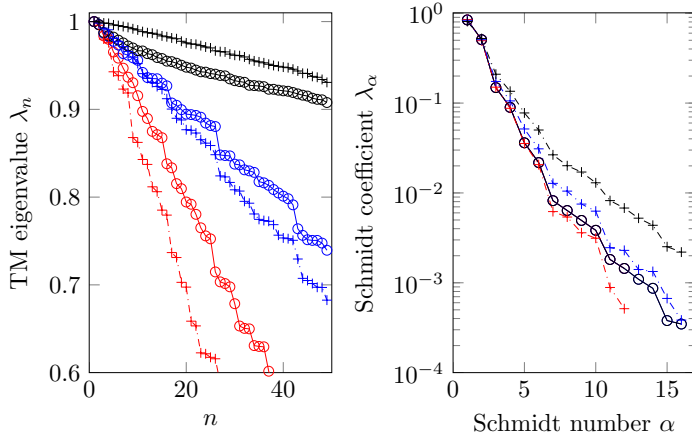


FIGURE 4.5: Comparison of transfer matrix (TM) spectra and Schmidt spectra of the transverse Ising model Eq. (4.17) between our MPS ansatz $|\Psi[\hat{A}]$ based on the Wilson MPO (black circles) and a variational MPS ground state $|\Psi[A]\rangle$ (crosses) with bond dimension $D = 12$ (red), $D = 24$ (blue) and $D = 50$ (black) for $\lambda = 1$ (gapless). All MPO simulations were performed using a Trotter step $\delta = 0.001$ and local dimensions $d_s, \chi_s, d'_s \in \{2, 4\}$ of the coarse-graining tensors with $s_{\max} = 17$ layers, and we also investigated the effect of further truncating the MPO based ansatz to specific bond dimensions $D = 12$ (red circles) and $D = 24$ (blue circles) based on the Schmidt coefficients.

on the nondominant part of the spectrum of the transfer matrix itself is significant, as can be observed in Fig. 4.5(a). Nevertheless, when comparing to a variational MPS with a particular bond dimension, we obtain a qualitative agreement that matches the first few dominant Schmidt coefficients (see also Fig. 4.9b for analogous entanglement spectra obtained for critical free fermions).

4.7.2 MPS excitation ansatz from Wilson MPO

Using the restricted variational subspace ansatz defined in Fig. 4.3, we have calculated variational approximations to the dispersion relation of the transverse Ising model Eq. (4.17) for all layers intervals $[s, s_{\max}]$, for $s = 1, 2, \dots, s_{\max}$, of the Wilson MPO. As depicted in Fig. 4.6, sweeping across layer intervals gradually allows less layers to contribute to the variational optimization. We observe that restricting the variational degrees of freedom to the top layers limits the momentum range of the ansatz to such an extent that, within the accuracy of the ground state approximation itself, momentum states corresponding to high-energy excitations can no longer be captured. Diluting exponentially on their way down the network, momentum states corresponding to high-energy excitations are seen to yield states with a norm that effectively approaches zero, leading to ill-defined generalized eigenvalue problems Eq. (4.15) as a function of layer index s and momentum p . This observation of null-modes suggests an effective reduction of the Hilbert space of the momentum

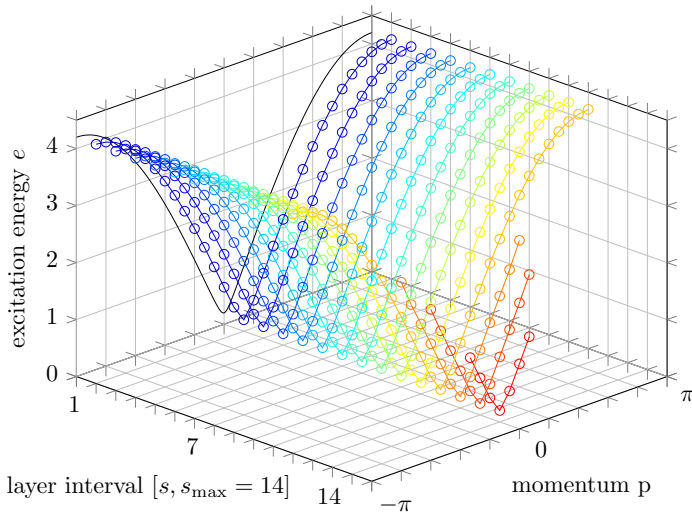


FIGURE 4.6: Variational approximations to the quantum Ising dispersion relation $e(p) = 2\sqrt{1 + \lambda^2} - 2\lambda \cos p$ (solid black line) in function of the layer index s for $\lambda = 1.1$, $s_{\max} = 14$ layers and bond dimension $D = 16$ using the restricted variational MPS excitation ansatz of Fig. 4.3. Momenta near the minimum $p = 0$ of the dispersion relation are seen to be fully captured by restricting the variational ansatz to the top tensor(s) of the Wilson MPO, in contrast to momenta corresponding to high-energy excitations, which are observed to correspond to null states with a norm effectively approaching zero. By varying the range of the variational degrees of freedom in scale space from infrared towards the ultraviolet, we recover the high-energy excitations.

states corresponding to high-energy excitations at coarser renormalization group scales.

4.7.3 Free fermion ansatz

We now develop a very similar approach to coarse-graining transfer matrices using free fermions. For the Ising model in Eq. (4.17), we can exploit the fact that it is solvable by mapping it onto a system of free fermions to gain independent evidence in support of our ansatz⁵. The additional free fermionic structure will furthermore allow us to study explicitly what happens to the transfer matrix on every coarse-graining level at the level of the fermionic modes, which is impossible to extract from the MPO construction. To that end, we employ the modified version of the free fermionic MERA [145, 146] to effectively construct the network of coarse-graining MPOs appearing in Eq. (4.4).

⁵For the free fermionic examples we used a relatively large time-step $\delta = 0.1$. We can, however, precisely quantify the resulting Trotter error. For $\lambda = 1.1$ we actually describe the ground state of the XY model [132] with magnetic field $g \simeq 1.0970$ and anisotropy $\gamma \simeq 0.9763$. For $\lambda = 1$ we approach the critical point with $g = 1$ and $\gamma \simeq 0.9803$.

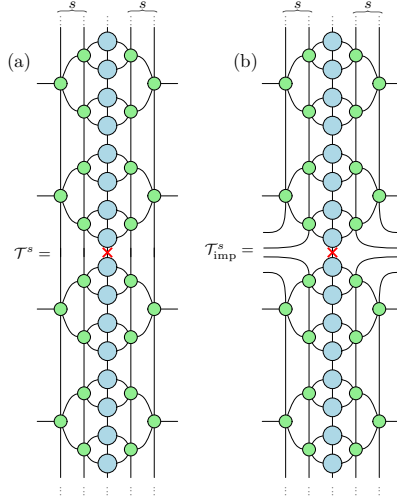


FIGURE 4.7: (a) Coarse-grained transfer matrix and (b) partially compressed transfer matrix, obtained by application of s layers of coarse-graining MPO. The same isometry is used here for the top part (i.e. ket) and the bottom part (i.e. bra) of the original MPS.

The renormalized transfer matrix \mathcal{T}^s is depicted in Fig. 4.7(a). At each renormalization scale s it can be diagonalized as

$$\mathcal{T}^s = \exp \left[- \sum_m \epsilon_m^s c_m^\dagger c_m \right], \quad (4.18)$$

where c_m are free fermionic annihilation operators, and the spectrum is fully determined by the single particle “energies” ϵ_m^s . The coarse-graining MPOs are constructed layer by layer so as to properly describe the dominant low-energy part of the spectrum of the virtual Hamiltonian \tilde{H} . As such, the free fermionic nature of the problem allows us to keep track of the spectrum of the transfer matrix at each coarse-graining step, as presented in Fig. 4.8(a,b) for non-critical and critical systems respectively. For technical details regarding the construction, as well as further details, we refer to Appendix 4.9.2.

We then use the coarse-grained MPOs obtained above to sequentially compress the transfer matrix, as depicted in Fig. 4.7(b). This allows us to observe how the spectrum of the compressed transfer matrix $\mathcal{T}_{\text{imp}}^s$ is gradually emerging with growing s , where $s = 0$ marks the original transfer matrix and $s = s_{\text{max}}$ is a fully compressed one, see Fig. 4.2(a) for comparison. We plot the single particle energies $\epsilon_m^{\text{imp},s}$, equivalent to Eq. (4.18), in Fig. 4.8(c,d) both for non-critical and critical systems. The spectra consist of a continuous part which can be attributed to the still-to-be-renormalized low-energy part of the spectrum, and discrete high-energy modes corresponding to the impurity degrees of freedom. There are two such modes emerging at each new layer (for $\chi_s = 2^1$, one comes from the ket and the other one from the bra). We can therefore argue that each fermionic mode, supported on the

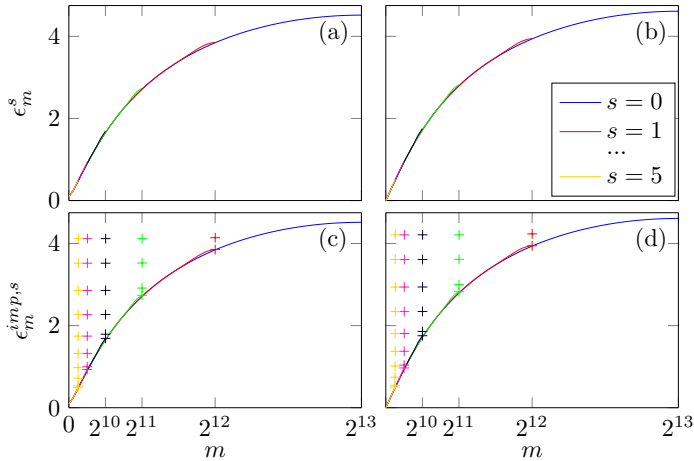


FIGURE 4.8: Single particle spectrum of (a,b) the coarse-grained transfer matrix \mathcal{T}^s in Fig. 4.7(a), and of (c,d) the impurity transfer matrix $\mathcal{T}_{\text{imp}}^s$ in Fig. 4.7(b), at different layers s . In (c,d) the approximately continuous part of the spectrum is drawn with a solid line, while pluses mark the discrete high-energy modes which are localized at, and can be associated with, the impurity degrees of freedom. Results for non-critical $\lambda = 1.1$ (a,c) and critical $\lambda = 1$ (b,d). The initial transfer matrix was obtained by applying 4096 layers of MPOs with bond dimensions equivalent to $\chi_s = 2^1$ and $d_s = d'_s = 2^4$.

Wilson chain, represents a different, exponentially shrinking momentum-window (recall that the original problem was translationally invariant), analogous to Wilson's renormalization group picture of the impurity problem.

The spectrum of the compressed transfer matrix is then effectively given by

$$\epsilon_m^{\text{imp},s_{\text{max}}} \approx \epsilon(k_m^{\text{imp}}), \quad (4.19)$$

where $\epsilon(k)$ is the dispersion relation of the original transfer matrix \mathcal{T}_A , and $k_m^{\text{imp}} \sim \lambda^m$ is a logarithmic discretization of momenta resulting from the RG scheme, at least up to some infrared cutoff related to the finite length-scale inevitably appearing in the problem. Most importantly, exactly the same structure of the transfer matrix spectrum was observed resulting from the conventional MPS truncation procedure [132]. Note, however, that here the parameter λ ($\lambda = \sqrt{2}$ in Fig. 4.8) is a constant which depends on the geometry of the tensor network through the bond dimensions d_s, χ_s, d'_s , while for the standard truncation [132] it depends non-trivially both on the bond dimension of the MPS and correlation length appearing in the problem (possibly as the result of finite entanglement scaling for the critical system). We can thus expect that the geometry of the tensor networks limits the precision of the ansatz in a similar way to using a finite bond dimension in MPS, which we discuss in more detail in Appendix 4.9.2.

Finally, in order to provide direct evidence that our ansatz allows for effective

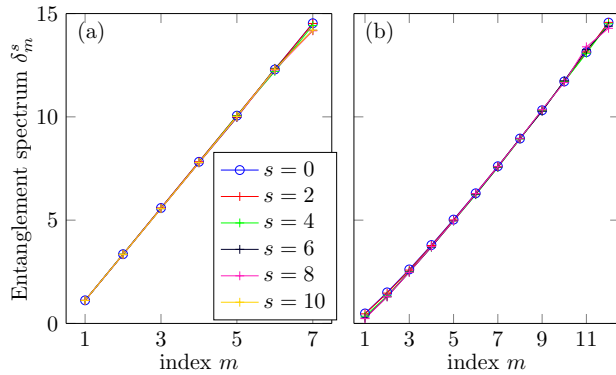


FIGURE 4.9: Dominant part of the entanglement spectrum for increasing scale s . The spectrum is preserved with good accuracy. Results for (a) $\lambda = 1.1$ and (b) $\lambda = 1$. Bond dimensions equivalent to $\chi_s = 2^1$ and (a) $d_s = d'_s = 2^4$, (b) $d_s = d'_s = 2^8$. The initial transfer matrix was obtained by applying 4096 layers of MPOs. See the text for further discussion.

compression of the transfer matrix, we show that it is reproducing the entanglement spectrum with good accuracy. To that end, the reduced density matrix of the dominant eigenvector of $\mathcal{T}_{\text{imp}}^s$ can be expressed as [147]

$$\rho^s = \frac{1}{Z} \exp \left[-2 \sum_m \delta_m^s f_m^\dagger f_m \right], \quad (4.20)$$

where f_m are fermionic annihilation operators, Z is the normalization factor, and the entanglement spectrum is determined by δ_m^s . Consequently, the Schmidt coefficients, up to normalization, are given by $1, e^{-\delta_1^s}, e^{-\delta_2^s}, e^{-(\delta_1^s + \delta_2^s)}, \dots$. In Fig. 4.9 we plot the dominant part of the spectrum for growing s , both (a) for the non-critical system $\lambda = 1.1$ and (b) the critical one $\lambda = 1$. Notice that for the non-critical case $s = s_{\text{max}} = 10$ corresponds to truncating down to 10 fermionic modes, and the plot shows 7 dominant modes in the entanglement spectrum, proving that the compression is quite effective. For the critical case we stop at $s = 8$, just before applying the top tensor. As mentioned in Sec. 4.7.1, simple top tensors limit the number of modes describing the state too quickly, which can significantly affect the resulting spectrum. We can further increase the precision by changing the geometry of the tensor network, either by increasing χ , or equivalently, by compressing slower, which amounts to increasing d' for fixed d .

4.8 Conclusion

In this chapter, we have shown how the state compression inherent to variational MPS techniques can be interpreted as resulting from a renormalization group procedure

applied to the Euclidean path integral description of a quantum system. By treating the location of the physical spin as an impurity, we were able to construct a uniform MPS representation that takes into account the degrees of freedom relevant to the impurity. The MPO structure of the coarse-graining ansatz led to a natural proposal for the structure of the MPS fixed point reduced density matrices. Furthermore, we explicitly related the different layers in the decomposition with energy scales by studying a restricted variational ansatz for excitations, which shows that perturbations at the high layers only give access to elementary excitations with a momentum near the minimum of the dispersion relation, whereas perturbations with other momenta get washed out by the subsequent layers below it. We also formulated a free fermion version of our coarse-graining ansatz that is in agreement with the results of the MPO ansatz.

Having arrived at a conceptually suggestive picture of the renormalization group structure inherent to matrix product states, we can look at the possibility of conceptual advantages in calculating correlation functions, scattering matrices, and other quantities. Further study of the behavior of excitations at this boundary between MPS and entanglement renormalization might yield insight into how to develop a proper excitation ansatz for MERA. Finally, as our Wilson-based MPS furthermore suggests that the burden of entanglement can be shifted to manageable correlations between energy scales, it would be interesting to explore the possibility of continuum generalizations of our ansatz in terms of the continuous MERA [105], and to study its applicability to the numerical optimization of two-dimensional quantum lattice systems using projected entangled pair states [80, 148].

4.9 Appendices

In these appendices, we discuss some basic notions of path integrals and their relation to wave functions in Sec. 4.9.1, details on the free fermion construction in Sec. 4.9.2, and the relation between the MPO ansatz and MERA in Sec. 4.9.3.

4.9.1 Path integrals, wave functions, and quantum states

The boundary data of Euclidean path integrals define transition amplitudes under evolution by $e^{-\beta H}$ as

$$\langle \phi_2 | e^{-\beta H} | \phi_1 \rangle = \int_{\phi(\tau=0)=\phi_1}^{\phi(\tau=\beta)=\phi_2} \mathcal{D}\phi e^{-S_E[\phi]}. \quad (4.21)$$

The interpretation of this path integral depends on the topology of space, with fixed boundary data in imaginary time. The transition amplitude defines a wavefunction in the Schrödinger picture, which for some state

$$|\Psi\rangle = |\phi_1(\tau)\rangle = e^{-\tau H} |\phi_1\rangle \quad (4.22)$$

is equal to the overlap

$$\Psi[\phi_2] = \langle \phi_2 | \Psi \rangle = \langle \phi_2 | e^{-\tau H} | \phi_1 \rangle. \quad (4.23)$$

The above implies that we can formally think of a path integral with one set of boundary conditions as a quantum state, where we leave the spatial slice associated to one cut unspecified. Put differently, the quantum state

$$|\Psi\rangle = e^{-\beta H} |\phi_1\rangle \quad (4.24)$$

can be interpreted as the path integral

$$|\Psi\rangle = \int_{\phi(\tau=0)=\phi_1}^{\phi(\tau=\beta)=?} \mathcal{D}\phi e^{-S_E[\phi]}, \quad (4.25)$$

which is a functional mapping field data $\langle \phi_2 |$ into complex numbers $\langle \phi_2 | \Psi \rangle$. More generally, any path integral with an open cut Σ defines a quantum state on Σ , with density matrices having two open cuts.

States defined by an Euclidean path integral are of course also states in the Hilbert space of the Lorentzian theory. Thus forward time evolution on some state $|X\rangle = |X(0)\rangle$ will result in a state $|X(t)\rangle = e^{-iHt} |X\rangle$ that is part Euclidean and part Lorentzian. Unnormalized ground states $|0\rangle$ can be obtained by doing an Euclidean path integral that extends to infinity in one direction. The vacuum-to-vacuum amplitude $\langle 0|0\rangle$ is then obtained by gluing upper and lower parts together at $\tau = 0$.

4.9.2 Free fermion construction

4.9.2.1 Transfer matrix

In order to construct the tensor network representation of the ground state of the quantum Ising model in Eq. (4.17), as depicted in Fig. 4.1, we start with the second-order Suzuki-Trotter decomposition of an operator $e^{-\delta H}$,

$$V = V_1^{1/2} V_2 V_1^{1/2}, \quad (4.26)$$

$$V_1 = \exp\left(\delta\lambda \sum_i \sigma_i^z\right) \quad (4.27)$$

$$V_2 = \exp\left(\delta \sum_i \sigma_i^x \sigma_{i+1}^x\right), \quad (4.28)$$

for some small⁶ time-step δ . Here, V represents a single row in the two-dimensional network in Fig. 4.1. It appears naturally as the transfer matrix operator in the solution of the two-dimensional classical Ising model and as such was extensively studied, see e.g. the Review [149]. Relevant for us, V has a simple representation in

⁶See footnote 5.

terms of a MPO with bond-dimension 2 (see e.g. Ref. [137]), which allows us to directly obtain the full transfer matrix \mathcal{T}_A [132] (a single column in Fig. 4.1), of the same form as the V above,

$$\mathcal{T}_A = W_1^{1/2} W_2 W_1^{1/2}, \quad (4.29)$$

$$W_1 = \exp \left(K_1 \sum_{l=1}^{2L} \tau_l^z \right) \quad (4.30)$$

$$W_2 = \exp \left(K_2 \sum_{l=1}^{2L-1} \tau_l^x \tau_{l+1}^x \right), \quad (4.31)$$

where $\tau_l^{x,z}$ are standard Pauli matrices acting on the virtual degrees of freedom labeled with $l = 1, 2, \dots, 2L$, where L is the number of times V was applied onto the initial state (the ground state is obtained in the limit of $L \rightarrow \infty$). The physical degree of freedom is localized at the bond between sites L and $L+1$. Finally, the parameters $K_{1,2}$ can be found as $K_1 = -\frac{1}{2} \log \tanh(\delta)$ and $K_2 = -\frac{1}{2} \log \tanh(\delta\lambda)$.

The transfer matrix \mathcal{T}_A can be diagonalized in a standard way [149] by mapping onto a system of free fermions with the Jordan-Wigner transformation $\tau_n^z = i a_{2n-1} a_{2n}$, $\tau_n^x = a_{2n-1} \prod_{m < n} \tau_m^z$. For convenience, we introduce Majorana fermions a_n , $n = 1, 2, 3, \dots, 4L$, which are Hermitian by construction and satisfy the canonical anti-commutation relations $\{a_n, a_m\} = 2\delta_{n,m}$. The transfer matrix can then be diagonalized

$$\mathcal{T}_A = \exp \left(- \sum_{m=1}^{2L} \epsilon_m i b_{2m-1} b_{2m} \right), \quad (4.32)$$

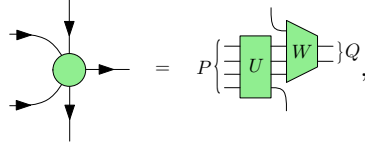
where the index m can be identified with momentum and ϵ_m is the dispersion relation. The Majorana fermions $b_m = O_{m,n}^{\mathcal{T}_A} a_n$ are described by the orthogonal matrix $O^{\mathcal{T}_A}$. Since the transfer matrix has effectively open boundary conditions, some care is needed during diagonalization. To that end, we follow the procedure outlined in Ref. [150], obtaining $O^{\mathcal{T}_A}$ and ϵ_m numerically for some large, fixed value of L .

4.9.2.2 Coarse-graining procedure

Our main goal is the construction of (the equivalent of) the coarse-graining MPO in Eq. (4.4). To that end, the transfer matrix, which is a Hermitian, positively defined and Gaussian operator, can be described uniquely (up to a normalization) using the correlation matrix

$$C_{m,n}^{\mathcal{T}_A} = \frac{\text{Tr}(a_m a_n \mathcal{T}_A)}{\text{Tr} \mathcal{T}_A}. \quad (4.33)$$

We use the free fermionic MERA ansatz, adapting the construction described in [145] to our problem. The coarse-graining MPO is decomposed here as



$$= P \left(\begin{array}{c} \text{---} \\ \text{---} \\ \text{---} \\ \text{---} \end{array} \begin{array}{c} U \\ \text{---} \\ \text{---} \\ \text{---} \end{array} \begin{array}{c} \text{---} \\ \text{---} \\ \text{---} \\ \text{---} \end{array} \begin{array}{c} W \\ \text{---} \\ \text{---} \\ \text{---} \end{array} \right) Q, \quad (4.34)$$

consisting of one disentangler U and one isometry W in the language of MERA. The gates U and W , which are in principle position and layer dependent (we skip the indices to simplify notation), are parametrized in terms of $\text{SO}(2P)$ matrices describing the local canonical transformation of Majorana fermions. They are shifted with respect to each other by one site (two Majorana modes), fixing the equivalent of the bond dimension in the coarse-graining MPO to $\chi = 2^l$, with suitable boundary conditions for the tensors at the ends of the chain. The isometries $W^\pm = W^0 Y^\pm$, where

$$Y^- = \text{diag}(\overbrace{1, 1, \dots, 1}^{2Q}, \overbrace{0, 0, \dots, 0}^{2P-2Q}), \quad (4.35)$$

and $Y^+ = \mathbb{I} - Y^-$ are diagonal $2P \times 2P$ matrices selecting the first $2Q$ and the last $2P - 2Q$ Majorana fermions, respectively. A single layer of the coarse-graining MPOs in Eq. (4.4) is in this picture a direct sum of disentanglers and isometries in that layer, and we will mark it as \mathbb{W}_s^\pm . The coarse-grained correlation matrix is obtained from the previous one as

$$C^s = \mathbb{W}_s^{-\dagger} C^{s-1} \mathbb{W}_s^-, \quad (4.36)$$

with $C^{s=0} = C^{\mathcal{T}A}$ representing the coarse-grained transfer matrix \mathcal{T}^s depicted in Fig. 4.7(a).

We optimize the orthogonal matrices U and W in each layer, starting with the bottom layer and progressing to the top, using the standard optimization strategy for MERA [142]. The cost function is given by

$$f_s(U, W) = \text{Tr} (\mathbb{W}_s^{+\dagger} C^{s-1} \mathbb{W}_s^+ Y^C), \quad (4.37)$$

which allows for a local optimization. In the above,

$$Y^C = \bigoplus_l \begin{pmatrix} 0 & -i \\ i & 0 \end{pmatrix}. \quad (4.38)$$

Notice that the canonical form of the correlation matrix, following a suitable canonical transformation, is

$$C = \bigoplus_l \begin{pmatrix} 1 & -i \tanh \epsilon_l / 2 \\ i \tanh \epsilon_l / 2 & 1 \end{pmatrix}, \quad (4.39)$$

where ϵ_l are single particle energies of the corresponding transfer matrix. Optimizing

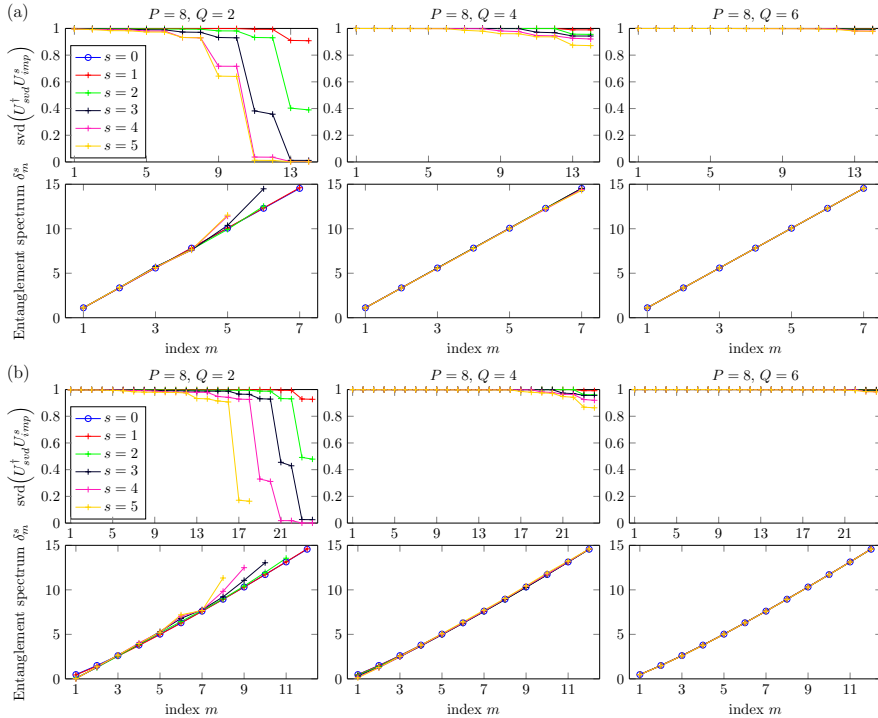


FIGURE 4.10: Dominant part of the entanglement spectrum and the overlap between the isometries U_{svd} and U_{imp}^s (see the text) for the first couple of coarse-graining layers s . Results for (a) $\lambda = 1.1$ and (b) $\lambda = 1$. The initial transfer matrix was obtained by applying 4096 layers of MPOs. Comparison of different rates of compression in one layer, set by the ratio of Q/P , see Eq. (4.34). This corresponds to the bond dimensions $\chi_s = 2^1$, $d_s = 2^{P/2}$ and $d'_s = 2^Q$ of the coarse-graining MPO.

the MERA then boils down to bringing the $\mathbb{W}_s^{+\dagger} C^{s-1} \mathbb{W}_s^+$ correlation matrix as close as possible to the canonical form, which allows for the identification of the high-energy modes that need to be truncated during the coarse-graining. We note that the truncation procedure is equivalent to *tracing out* the high-energy modes in the transfer matrix, which could, in principle, introduce some bias when compared to the (more correct) *projection* on their ground state. We observe however that the procedure is working well, see Fig. 4.8(a,b).

4.9.2.3 Compressing the transfer matrix

As indicated in the main text, we use the MERA generated above to construct the isometry used to compress the transfer matrix. We argue that the impurity (physical spin) can be well described using the degrees of freedom living on the boundary of its light cone, see Fig. 4.2. To that end, we construct the isometry U_{imp}^s which

partially compresses the transfer matrix up to the scale s ,

$$U_{\text{imp}}^s = s \left\{ \begin{array}{c} \dots \\ \dots \end{array} \right. \text{Diagram} \dots \left. \right\}, \quad (4.40)$$

where full compression is achieved for $s = s_{max}$. The partially compressed $\mathcal{T}_{\text{imp}}^s$, described by the correlation matrix C_{imp}^s , is obtained by acting with U_{imp}^s on the correlation matrix $C^{\mathcal{T}^A}$ as indicated in Fig. 4.7(b). The same U_{imp}^s is used for ket and bra of the original MPS matrix, so only about half of the tensors generated with MERA are used here in the end.

By bringing the correlation matrix C_{imp}^s into its canonical form, we can find the spectrum of the corresponding transfer matrix as

$$\mathcal{T}_{\text{imp}}^s = \exp \left[- \sum_m \epsilon_m^{\text{imp},s} c_m^\dagger c_m \right], \quad (4.41)$$

in its diagonal base of Dirac fermions c_m . The spectrum is plotted in Fig. 4.8(c,d) and discussed further in the main text. The entanglement spectrum, Eq. (4.20), which is given by the reduced density matrix of the dominant eigenvector of $\mathcal{T}_{\text{imp}}^s$, can be calculated from C_{imp}^s as well, see e.g. Ref. [147].

4.9.2.4 Comparison of impurity picture with standard truncation

Finally, we can now directly compare the isometry U_{imp}^s obtained with MERA, with the standard truncation procedure described by the isometry U_{svd} , a $2L \times 2\chi$ matrix where 2χ is the bond dimension of the truncated MPS. The matrix U_{svd} is obtained by calculating the reduced density operator of the MPS on a half-infinite chain (our initial A^i in Fig. 4.1) and finding dominant modes in its diagonal basis [132]. To that end, we look at the singular values of $U_{\text{svd}}^\dagger U_{\text{imp}}^s$, which directly show how well the dominant modes in the entanglement spectrum are preserved during the compression.

The results for the gapped and critical cases are plotted in Figs. 4.10 (a) and (b) respectively, together with the resulting entanglement spectra. Notice that each mode in the entanglement spectrum corresponds to two Majorana modes in term of the isometries U . We show the results for the first couple of layers, up to $s = 5$, and various ratios of Q/P , see Eq. (4.34). This ratio sets an effective light cone, and determines what fraction of the large energy modes of the original transfer matrix is renormalized during each coarse-graining step. Notice that from that perspective, one step for $Q/P = 2/8$ is equivalent to two steps for $Q/P = 4/8$ and almost five steps for $Q/P = 6/8$. At the same time, the number of modes describing the impurity resulting from each step is the same. The trade-off between the rate of compression and the accuracy can be readily seen. As already described in the main text, we expect that this is directly equivalent to obtaining MPS with given bond dimension D using the standard procedure. For instance, for $Q/P = 2/8$ only

the first few modes are described accurately corresponding to smaller D , while for $Q/P = 6/8$ all the dominant (as plotted) modes are reproduced corresponding to large D (we should be able to obtain the same result by increasing χ). The choice of $Q/P = 4/8$ (i.e., $d = d'$) seems to be a good compromise.

4.9.3 Isometric MPO versus MERA

In the main text, we have proposed to characterize an isometric MPO locally by introducing a five-legged tensor g , which can be interpreted as a map $g : \mathbb{I} \otimes \mathbb{I} \otimes \mathbb{V} \rightarrow \mathbb{O} \otimes \mathbb{V}$, where \mathbb{I} , \mathbb{V} , and \mathbb{O} , respectively, refer to the vector spaces of the incoming indices, the virtual indices and the outgoing indices. As a variational set of states, the ansatz Eq. (4.6), constructed of layers of isometric MPOs, includes the MERA. Explicitly, the ansatz Eq. (4.6) encompasses MERA in the sense that when the local isometry g is, for example, interpreted as a disentangler u and an isometry w of a binary MERA,

$$\begin{array}{c} \text{Diagram 1} \end{array} = \begin{array}{c} \text{Diagram 2} \end{array} = \begin{array}{c} \text{Diagram 3} \end{array}, \quad \begin{array}{c} \text{Diagram 4} \end{array} = \begin{array}{c} \text{Diagram 5} \end{array} = \begin{array}{c} \text{Diagram 6} \end{array} \quad (4.42)$$

the internal bond connecting the disentangler and the isometry is in no way restricted by $d = \dim(\mathbb{I})$. There is however no local gauge transformation, acting purely on the virtual level of the coarse-graining MPO, which can transform between Eq. (4.42). Intuitively, we expect that the virtual dimensions of the MPO structure within every layer result in a coarse graining scheme that is quasi-local rather than strictly local as in the MERA. This difference is due to the different causal cone structures. The causal region of the MPO ansatz is potentially larger than that of MERA as it, at most, extends towards infinity in one of both directions. The MERA causal cone, which is strictly local, is included in this extended causal cone. Crucially, the more general MPO ansatz enables us to renormalize translation invariant MPOs into translation invariant MPOs and renders the identification of the Wilson chain very straightforward.

Renormalization group flows of Hamiltonians

In this chapter¹, we rephrase tensor network renormalization for two-dimensional classical lattice models in a manifestly nonnegative way, leading to a TNR_+ algorithm based on nonnegative matrix factorization instead of singular-value decomposition. The resulting real-space renormalization group flow preserves positivity and hence yields an interpretation in terms of Hamiltonian flows, reconciling modern real-space tensor network renormalization methods with traditional block-spin approaches.

5.1 Background and motivation

As we have seen in Chapter 2, the study of phase transitions and critical properties of lattice models has long been at the center of statistical physics. Universal properties of critical systems can be captured by conformal field theories (CFTs), which act as low-energy effective descriptions of critical models, and whose scaling dimensions can be related to the critical exponents of asymptotic correlation functions. One way to gain insight into these phenomena is through real-space renormalization group (RG) methods, which predate the development of the modern renormalization group and can be traced back to Kadanoff's block spin procedure [19].

In his treatment of block spin methods on the lattice, Wilson emphasized that one should be able to do precise numerical calculations using pure RG methods combined with approximations based only on locality [5]. For real-space RG to work, the effective Hamiltonian at every step should be dominated by short-range interactions as interactions of arbitrary complexity are generated in subsequent iterations. Additionally, the calculation of any particular term in the coarse-grained Hamiltonian should involve but a small number of fine-grained spins.

Tensor networks are efficient, local, real-space variational ansätze for many-body wavefunctions, which are constructed by mimicking the spatial distribution of entanglement and correlations. Renormalization group methods based on tensor networks satisfy Wilson's requirements insofar as their inherent real-space locality and finite bond dimension restrict the range of newly generated effective interactions and provide a controlled approximation that can be systematically improved.

¹The work presented here has been published in Ref. [2] in collaboration with Michaël Mariën, Jutho Haegeman, and Frank Verstraete.

For two-dimensional lattice systems, the tensor renormalization group (TRG) algorithm [111, 151] put the idea of tensor network renormalization (TNR) into practice in a most explicit way. Wholly based on truncation using singular value decomposition (SVD), this algorithm works extremely well for gapped systems because of the same entanglement reasons that explain the success of the density matrix renormalization group (DMRG) for quantum spin chains [111]. Despite remarkable accuracy in determining critical exponents for finite systems, none of the methods based on TRG [113, 114, 152] is sustainable in the sense that it is capable of yielding true (approximate) fixed point tensors at criticality [115]. Recently, novel TNR algorithms respectively based on the multi-scale entanglement renormalization ansatz (MERA-TNR) [115, 116, 130, 153] and matrix product states (LOOP-TNR) [117] have been developed which do manage to flow to approximate fixed point tensors, even at criticality. Our work has been inspired by the latter proposal which formulates TNR in terms of periodic matrix product states (MPS). For the 2D classical Ising model, impressive numerical results have been obtained that seem to defy the breakdown of TRG at criticality.

In this chapter, we demonstrate how tensor networks can be used to achieve explicit real-space RG flows in the space of classical Hamiltonians. To this end, we have developed a sustainable and manifestly nonnegative TNR method (TNR₊) to coarse-grain classical partition functions. By virtue of the element-wise nonnegativity of all tensors involved, we can explicitly associate a Hamiltonian to the fixed point tensors of the RG flow generated by our algorithm. We thus believe our work opens up the possibility to begin to address one of the main concerns raised by the traditional real-space RG community about all TNR schemes: the lack of an insightful RG interpretation of what are essentially supposed to be real-space RG methods:

“[...] the more recent tensor-style work often employs indices which are summed over hundreds of values, each representing a sum of configurations of multiple spinlike variables. All these indices are generated and picked by the computer. The analyst does not and cannot keep track of the meaning of all these variables. Therefore, even if a fixed point were generated, it would not be very meaningful to the analyst. In fact, the literature does not seem to contain much information about the values and consequences of fixed points for the new style of renormalization.”

Efi Efrati, Zhe Wang, Amy Kolan, and Leo P. Kadanoff, 2014 [154]

5.2 Tensor network renormalization

The salient features shared by all TNR algorithms developed up to now are twofold. First, the breaking apart of the tensor product structure, which was introduced in TRG by splitting tensors using SVD, is crucial to the construction of new effective degrees of freedom and the removal of correlations. The reason why Kadanoff’s spin blocking fails can be traced back to the bounds on correlations imposed by the mutual information between a block and its environment (see Sec. 3.5). In order to overcome this barrier, it is essential to reorganize degrees of freedom by doing a

local basis transformation. Secondly, both MERA-TNR and LOOP-TNR address the additional need to extend the domain of the coarse-graining step to act on a block of sites in order to remove intra-block correlations. The disentangling power of both MERA-TNR and LOOP-TNR can be found in surrounding a block of sites with a coarse-graining operator. As mentioned in Sec. 3.5, this explains, for instance, why there is no way for TRG, which acts locally on each site, to detect the short-range correlations it sets out to remove at criticality.

5.3 Coarse-graining nonnegative tensor networks

Consider a two-dimensional bipartite square lattice of N classical spins $\{s_i\}$ described by an energy functional $H(s_1, s_2, \dots)$. The classical statistical partition function is then

$$Z = e^{-\beta F} = \text{Tr}_{\{s_1, s_2, \dots\}} e^{-\beta H(s_1, s_2, \dots)}, \quad (5.1)$$

where $F = E - TS$ denotes the free energy. If we imagine the spins living on the vertices of the lattice, the Boltzmann weight of a site depends on the configuration of the bonds connected to the site. We can write these probabilities as a rank-four tensor A_{ijkl} , so that the sum over all configurations in the partition function boils down to contracting a nonnegative tensor network,

$$Z[A] = \text{tTr} \bigotimes A_{ijkl}, \quad (5.2)$$

where tTr denotes the tensor-trace, i.e. the contraction of all connected indices). By coarse-graining tensor networks, we then refer to a real-space RG procedure constructing a sequence of partition functions $Z[A^0] \rightarrow Z[A^1] \rightarrow \dots \rightarrow Z[A^s]$, where each effective partition function is defined on a coarser lattice than the one before, until we are left with a single effective site after $s \approx \log_2(N)$ iterations. If we now want to additionally retain element-wise nonnegativity of all involved tensors at every step, we cannot resort to using SVD, which is the backbone of all other TNR approaches. Instead, we are led to nonnegative matrix factorization (NMF) algorithms (see Appendix 5.8.1) to approximate the following matrix factorization problem: given an element-wise nonnegative matrix $A \in \mathbb{R}_+^{m \times n}$ and a rank $k \leq \min(m, n)$, find the matrices $X \in \mathbb{R}_+^{m \times k}$ and $Y \in \mathbb{R}_+^{k \times n}$ minimizing the Frobenius² norm $\|A - XY\|_F^2$.

Now let us focus on a block of four adjacent sites (Fig. 5.1(a)), which we, following Yang *et al.* [117], interpret as a periodic four-site matrix product state (MPS) with respective physical and virtual dimensions. The local coarse-graining procedure then proceeds according to the canonical real space RG steps by (i) *introducing new effective degrees of freedom*, which here involves approximating the local block with an ansatz that has a different tensor product structure in order to

²Given the nature of the problem, one might expect an l_1 -norm. In practice, tackling the l_1 -norm optimization problem is often not economical due to the large number of constraints, hence the relaxation to a smooth optimization in practice.

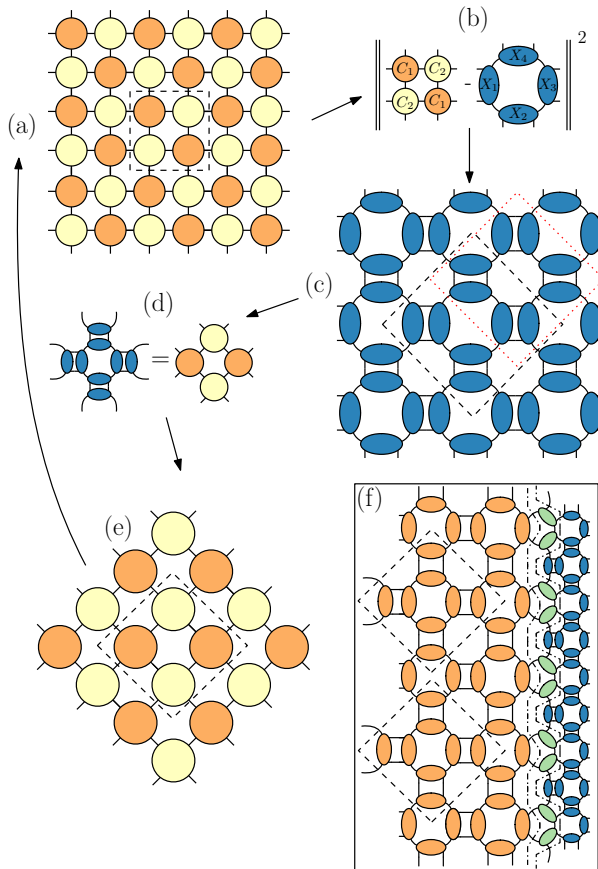


FIGURE 5.1: (a-e) Illustration of a single step of the TNR_+ algorithm. (a) Starting from a bipartite square lattice, (b) we approximate the periodic MPS representing a block of four sites by a rotated version (c) with a different tensor product structure, and (d) contract these numerically optimized tensors exactly to (e) arrive at a coarse-grained tilted lattice. (f) Iterating the TNR_+ procedure in the presence of an open boundary generates a stochastic MERA.

remove short-range correlations (Fig. 5.1(b)), (ii) *summing over old degrees of freedom* by recombining the optimized tensors into new coarse-grained tensors C_1 and C_2 (Fig. 5.1(d)). The virtual dimension in step (i) can be increased at will, which in turn determines the local dimension of the degrees of freedom living on the new lattice. While step (ii) explicitly sums over the old outer (physical) degrees of freedom to construct the coarse-grained tensors, step (i) also contains an implicit summation over the old inner (virtual) degrees of freedom. After a single RG step, the roles of the physical and virtual MPS dimensions have interchanged and the linear dimension of the lattice is reduced by $\sqrt{2}$. The tensors in Fig. 5.1(e) then serve as input to the next step, where we take into account that we have to break up the tensor product

structure again. Notice that in Fig. 5.1(c) we identify the coarse-grained lattice with the “vertex” configuration inside the dashed bounding box and not the “plaquette” configuration inside the dotted one. Even though a priori they look similar, the latter configuration leads to worse numerics which can be understood by it not being able to remove short-range correlations of the corner double-line (CDL) form (see Appendix 5.8.3).

5.4 Renormalization group flow

In Fig. 5.1(f) we have depicted the tensor network generated by the action of TNR_+ on an open boundary of the lattice. In much the same way as TRG produces a tree tensor network and MERA-TNR a multi-scale entanglement renormalization ansatz [116], our TNR_+ algorithm builds up a nonnegative tensor network approximation to the leading eigenvector of the transfer matrix. Given the nonnegativity and the alternating pattern of one iteration “disentangling” (blue tensors) and the next one reducing the degrees of freedom (green tensors), TNR_+ can be said to generate a stochastic MERA³. If we instead track the action of TNR_+ around an open impurity, we end up with the following MPO after two iterations (see Appendix 5.8.6.2),

$$R = \begin{array}{c} \begin{array}{ccc} \text{green } X_2 & \text{blue } X_2 & \text{green } X_1 \\ | & | & | \\ \text{blue } X_3 & \text{blue } X_1 & \text{blue } X_1 \\ | & | & | \\ \text{green } X_3 & \text{blue } X_1 & \text{green } X_1 \end{array} \\ \cdot \end{array} \quad (5.3)$$

In the scale invariant regime of the RG flow, this MPO is identified with the radial transfer matrix [130], which can be diagonalized to give $R = \sum_{\alpha} 2^{-\Delta_{\alpha}} |\alpha\rangle \langle \alpha|$. Here, the scaling dimensions Δ_{α} and approximate lattice representations $|\alpha\rangle$ of the primary fields and descendants of the underlying CFT description are found only if the relative gauge freedom of the coarse-grained partition functions has been fixed, i.e. if the degrees of freedom we deem equivalent after two iterations do indeed match (see Appendix 5.8.5). For critical systems, we thus end up with a window of an approximately invariant alternating sequence of partition functions $Z[C_{1,A}^*, C_{2,A}^*] \rightarrow Z[C_{1,B}^*, C_{2,B}^*]$ after the initial part of the flow has sufficiently suppressed irrelevant lattice details and up until the accumulated truncation errors eventually prevail.

We can furthermore consider the fixed point equations of TNR_+ as an algebraic

³Note that all these boundary tensor networks are but different low-rank tensor network approximations of the leading eigenvector of the transfer matrix written as an MPO [63].

set of equations in their own right by finding tensors which (approximately) satisfy

$$\text{Diagram 1} \approx \text{Diagram 2} \quad \text{and} \quad \text{Diagram 3} \approx \text{Diagram 4} \quad (5.4)$$

Exact solutions of these equations include trivial product states and Greenberger-Horne-Zeilinger states corresponding to gapped infrared fixed points, potentially with symmetry breaking. Including additional symmetry constraints, there might exist non-trivial solutions which approximately yet accurately satisfy the RG fixed point equations. The sets of these solutions and their stability under perturbations could then point towards the conditions required for a classification of all possible (approximate) RG fixed points of TNR schemes. Note that by working with symmetric tensor networks, we can also extract CFT data of non-local fields if we modify Eq. (5.3) to include a matrix product operator (MPO) threading through the transfer matrix (which encodes the anti-periodic boundary conditions and reduces to just a string of matrices for the tensor product symmetry considered in Ref.[103]). Similarly, the algebraic fixed point equations Eq. (5.4) can be modified to include an additional MPO symmetry string.

5.5 Application to classical partition functions

We have benchmarked our algorithm on the classical Ising model and the six-vertex model. As we have seen in Sec. 3.5.1, the partition function of the ferromagnetic

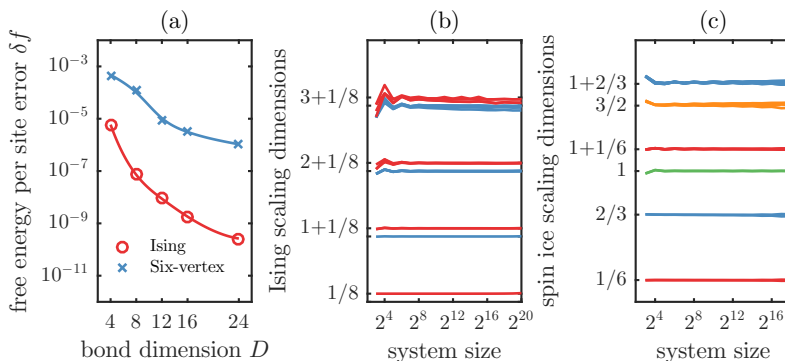


FIGURE 5.2: TNR₊ simulations for the critical Ising model and spin ice. (a) Relative error of the free energy per site in function of TNR₊ bond dimension ($N = 2^{32}$ sites). (b,c) Scaling dimensions extracted from the linear transfer matrix MPO Eq. (5.6) in function of RG step (Ising $D = 16$, spin ice $D = 12$).

Ising model can be encoded by associating a tensor

$$A_{ijkl} = \sum_s (\sqrt{a})_{is} (\sqrt{a})_{js} (\sqrt{a})_{ks} (\sqrt{a})_{ls} \quad (5.5)$$

to each vertex, where $a_{mn} = [e^\beta 1 + e^{-\beta} X]_{mn}$ denotes the contribution of the interaction between spins m and n . The Ising model exhibits a phase transition at the critical temperature $T_c = 2/\ln(1 + \sqrt{2})$ described by the free fermion $c = 1/2$ CFT introduced in Sec. 2.8.3, separating the \mathbb{Z}_2 symmetry breaking phase for $T < T_c$ from a trivial disordered phase for $T > T_c$. The partition function of the zero-field six-vertex model can be written in terms of the non-vanishing tensor elements $A_{1111} = A_{2222} = a$, $A_{2112} = A_{1222} = b$, and $A_{2121} = A_{1212} = c$, where a, b, c denote the Boltzmann weights of the allowed bond configurations. In terms of the parameter $\Delta = (a^2 + b^2 - c^2)/(2ab)$, the six-vertex model has a phase boundary determined by $|\Delta| = 1$ which separates four phases: two ferroelectric phases for $\Delta > 1$, an antiferroelectric phase for $\Delta < -1$, and a gapless disordered phase for $-1 < \Delta < 1$. The six-vertex model belongs to special classes of Hamiltonians which violate the universality hypothesis in that its phase diagram contains a continuum of critical points with continuously varying critical exponents captured by a free boson $c = 1$ CFT. In what follows, we will consider the example of spin ice, i.e. $a = b = c = 1$ and $\Delta = 0.5$.

In Fig. 5.2(a), the relative error of the free energy per site $f = -\log(Z)/N$ is plotted at criticality in function of the bond dimension. We observe very accurate free energies, with the difference in accuracy between the simulations of the two models reflecting the less trivial nature of the six-vertex model. To study the implicit approximate scale invariance of the RG flow, we calculate the smallest scaling dimensions from the linear transfer matrix MPO constructed from 4×2 effective partition function tensors,

$$M = \begin{array}{c} \text{---} \\ \text{---} \\ \text{---} \\ \text{---} \\ \text{---} \\ \text{---} \end{array} \begin{array}{cccc} \text{C}_1 & \text{C}_2 & \text{C}_1 & \text{C}_2 \\ \text{C}_2 & \text{C}_1 & \text{C}_2 & \text{C}_1 \end{array} \text{---} \quad (5.6)$$

in function of system size (or, equivalently, iteration step) in Fig. 5.2(c,d) (see Appendix 5.8.6.1). We observe that the numerically obtained implicit fixed point is stable under subsequent coarse-graining and remains so for a prolonged number of steps, in agreement with other TNR approaches [115, 117]⁴. To verify that the implicitly scale invariant tensors are also explicitly approximately scale invariant after gauge fixing, we have constructed the radial transfer matrix MPO Eq. (5.3) and calculated its smallest scaling dimensions (see Table 5.1). Together with the coarse-graining procedure described in Fig. 5.1, Eq. (5.3) can be used to study fusion of primary fields and to calculate the operator product expansion coefficients of

⁴Eventually though, the accumulated truncation errors act as a relevant perturbation steering the flow away from criticality. See also the discussion on tensor networks and real-space RG in Sec. 3.5.4.

Table 5.1: Smallest scaling dimensions extracted from the eigenvalues of the radial transfer matrix MPO Eq. (5.3) for the critical Ising model (left) and spin ice (right).

exact	Ising TNR ₊ ($D = 6$)	exact	Spin ice TNR ₊ ($D = 10$)
0.125	0.125236	1/6	0.163117
1	0.999282	1/6	0.167204
1.125	1.123883	2/3	0.659684
1.125	1.123883	2/3	0.662008
2	1.998575	1	0.997413
2	1.992823	1	0.997286
2	1.996882	7/6	1.163503
2	1.994090	7/6	1.163503

the underlying CFT, as has previously only been done using MERA-TNR for the Ising model [103]. More importantly, our results suggest that the characteristic information of the underlying CFT can also be obtained from the fixed point MPS tensors Eq. (5.4), which in our formalism act as transparent building blocks for *both* the linear and radial transfer matrix MPOs.

5.6 Effective Hamiltonians

In Fig. 5.3, we have plotted nonnegative fixed point tensors⁵ for the Ising model at $T < T_c$, $T = T_c$, and $T > T_c$. Due to the element-wise nonnegativity, it is possible to equivalently consider the element-wise logarithm, so that we can interpret the tensor elements as energies of the configurations of the bonds connected to the site. The trivial tensor C^{triv} for $T > T_c$ has one dominant element, and all other arbitrarily small elements can be regarded as penalty terms in the effective Hamiltonian, signifying the use of a superfluous bond dimension in the description of the numerical fixed point. Similarly, for $T < T_c$, the Z_2 symmetry breaking tensor $C^{Z_2} = C^{\text{triv}} \oplus C^{\text{triv}}$ is given by two equal dominant values with all other elements effectively zero. Both of these fixed points satisfy the algebraic relations Eq. (5.4) since they are exact fixed points of the RG flow. Off-criticality we thus recover the fixed points previously found by Gu and Wen [112]. The critical fixed point tensor for $T = T_c$ however is highly non-trivial, implying that the MPS optimization explores the full parameter space to approximate the exact fixed point which has infinite bond dimension. Due to the lattice geometry and the choice of the local coarse-graining transformation, the effective Hamiltonian encoded in the critical fixed point is given by local interactions between at most four effective D -dimensional degrees of freedom⁶. Note that the MPS tensors encoded in the

⁵We have only plotted $C_{1,A}^*$, but the behavior of the other tensors $C_{2,A}^*$, $C_{1,B}^*$, $C_{2,B}^*$ is very similar.

⁶Although one might be tempted to extend the domain of the coarse-graining operation to even bigger blocks, there is of course a numerical trade-off between the locality of a coarse-graining scheme and the bond dimension that can be attained in practice.

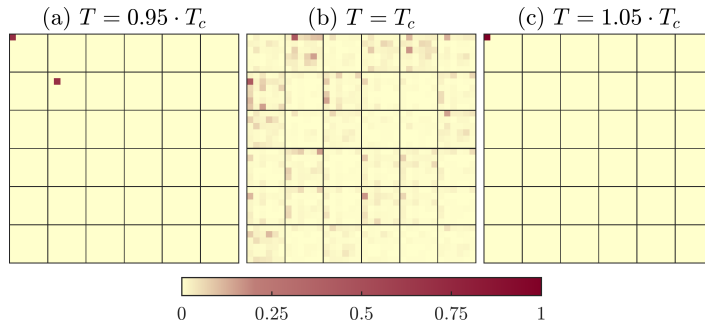


FIGURE 5.3: Nonnegative tensor elements of normalized fixed point tensors $C_{1,A}^*$ obtained from $D = 6$ TNR₊ simulations of the Ising model at (a) $T < T_c$, (b) $T = T_c$, and (c) $T > T_c$.

critical fixed point, part of which is shown in Fig. 5.3(b), provide an explicit and non-trivial example of numerically optimized solutions which *approximately* satisfy the algebraic fixed point equations Eq. (5.4) of the TNR₊ flow.

5.7 Conclusion

We have proposed a manifestly nonnegative tensor network renormalization algorithm to coarse-grain classical partition functions in real space, and provided additional evidence that tensor network renormalization techniques provide an approximation that behaves in a controlled way, introducing the required freedom to approximate the relevant physics at larger length-scales using effective interactions among effective degrees of freedom that are determined variationally. By restricting to nonnegative tensors, our work provides a bridge between heuristic block-spin prescriptions and modern tensor network approaches to coarse-graining in real space.

From an algorithmic⁷ point of view, further improvement of our numerical results is definitely possible by implementing more advanced, high performance convex NMF algorithms which should speed up convergence by reformulating the optimization problem as a linear program [155]. From a physical perspective, we can take lattice and internal symmetries into account and can try to improve the control on the gauge freedom. Due to the algorithm's formulation in terms of periodic MPS, we expect that the interplay with well-established theoretical and numerical MPS and MPO results will be of great importance in this regard.

It would be interesting to study the possibility of extracting CFT content semi-analytically directly from the fixed point TNR conditions Eq. (5.4). Or, if that turns out to be too hard, pinpoint exactly what is special about the structure of numerically obtained non-trivial TNR fixed points such that they approximately satisfy Eq. (5.4). A generalization of our scheme to the quantum case is possible by constructing

⁷Because of advances in computational power, machine learning applications are slowly but surely creeping into physics as well. See <https://physicsml.github.io/pages/papers.html> for a list of recent papers.

sequences of completely positive maps acting on projected-entangled pair states (PEPS) wave functions [80]. Another important extension, which we will come back to in detail in Chapter 6, is to incorporate the formalism of MPO algebras Refs. [82–84, 156] in order to put topological restrictions on the CFT data extracted from tensor network renormalization and derive all Ising CFT data from the lattice [50, 157].

5.8 Appendices

5.8.1 Nonnegative matrix factorization

5.8.1.1 Statement of the problem

A nonnegative matrix $A \geq 0$ is a matrix in which all elements are equal to or greater than zero. Given a nonnegative matrix $A \in \mathbb{R}_+^{m \times n}$ and a factorization rank k , the problem of *nonnegative matrix factorization* (NMF) is then to find a matrix decomposition $A \approx XY$, where $X \in \mathbb{R}_+^{m \times k}$ and $Y \in \mathbb{R}_+^{k \times n}$ are both nonnegative matrices as well. We can reformulate this problem as the following optimization problem:

$$\operatorname{argmin}_{X,Y} \|A - XY\|_F^2, \quad X \geq 0, \quad Y \geq 0, \quad (5.7)$$

where $\|\cdot\|_F$ denotes the Frobenius norm. Note that, without the nonnegativity constraints, the optimal solution to Eq. (5.7) is obtained via the singular value decomposition (SVD) of A . It is clear that NMF is not unique in general because we can always insert a matrix G and its inverse G^{-1} such that the matrix product remains invariant,

$$XY = XGG^{-1}Y = \tilde{X}\tilde{Y}. \quad (5.8)$$

If the two matrices $\tilde{X} = XG$ and $\tilde{Y} = G^{-1}Y$ are again nonnegative, they represent an equivalent parametrization (\tilde{X}, \tilde{Y}) of the same factorization (X, Y) . The requirements $\tilde{X} \geq 0$ and $\tilde{Y} \geq 0$ are surely satisfied if G is a nonnegative monomial matrix $G = PD$, where P is a permutation matrix and D an invertible diagonal matrix containing only positive diagonal elements. More generally, there might also exist equivalent parametrizations $(XG, G^{-1}Y)$ with $XG \geq 0$ and $G^{-1}Y \geq 0$ where G is not a monomial matrix, which can potentially spoil the uniqueness in a more severe way. Note that the smallest possible rank k for which an *exact* factorization $A = XY$ exists is the nonnegative rank of A , denoted with $\operatorname{rank}_+(A)$. It satisfies $\operatorname{rank}(A) \leq \operatorname{rank}_+(A) \leq \min(m, n)$, and is defined as the smallest number of nonnegative vectors such that every column of A can be written as a nonnegative linear combination of those vectors. When assuming $\operatorname{rank}(A) = \operatorname{rank}_+(A) = \operatorname{rank}(X) = k$, a given exact factorization (X, Y) of A can be said to be unique if $A = \tilde{X}\tilde{Y}$ implies $\tilde{X} = XPD$ and $\tilde{Y} = (PD)^{-1}Y$, i.e. if the only ambiguity of the factorization can be completely captured in terms of permutation and scaling matrices as defined above [158].

5.8.1.2 Intuition

To understand why NMF is an integral part of any machine learning toolbox, assume for instance that each m -dimensional column vector A_i of $A \in \mathbb{R}_+^{m \times n}$ contains an element of a set of data. Finding $X \in \mathbb{R}_+^{m \times k}$ and $Y \in \mathbb{R}_+^{k \times n}$ so that XY approximates A as accurately as possible then corresponds to extracting k features that capture latent properties of the dataset. Indeed, given the nonnegativity constraints, each element of the dataset is approximately reconstructed by summing over the k basis elements in the columns of X with coefficients given by the columns of Y , yielding a representation of the data which is a sum of distinctive parts. Applications include, but are not limited to, image processing, facial feature extraction, text mining and document classification, bioinformatics, recommender systems, clustering problems and spectral data analysis. Note however that, in general, the lack of uniqueness alluded to in Eq. (5.8) can be troublesome when the goal is to actually attribute significance to these emerging basis elements. For this reason, the uniqueness of NMF is closely linked to whether the numerically found features are really the only sensible interpretation of the data [159, 160].

5.8.1.3 Algorithms

In practice, the optimization problem Eq. (5.7) has been shown to be NP-hard [161], and all available algorithms are only guaranteed to converge to a local optimum. The algorithm that kickstarted NMF was Lee and Seung's multiplicative update rule [162],

$$X \leftarrow X \odot ((AY^T) \oslash (XY Y^T)), \quad (5.9)$$

$$Y \leftarrow Y \odot ((X^T A) \oslash (X^T X Y)), \quad (5.10)$$

where \odot and \oslash denote Hadamard product and division respectively. It is an extremely simple alternating algorithm that updates the matrices element-wise, but has a rather slow convergence rate. Numerous variations and extensions have since been developed, and we refer the interested reader to Refs. [163, 164]. In practice, we supplemented these algorithms by implementing a projected conjugate gradient approach (see Algorithm 1) to improve solutions or convergence if required. Note that there is no agreed upon convergence criterion for NMF optimization, so in practice one is free to implement a strategy that takes into account cost function values, gradient norms, projected gradient norms, local tolerances, global tolerances, and maximum number of iterations.

Another important aspect of NMF optimization is the choice of initialization (X_0, Y_0) . Starting from random nonnegative matrices surely is an option, but as NMF algorithms are local minimization algorithms, the choice of initial conditions can be crucial to the quality of the resulting local minimum and the speed of convergence. For our purposes, we favoured a semi-deterministic NNDSVD initialization based on the best rank- k approximation of A given by the SVD [165]. The initialization works by first calculating the subset of the k largest singular values and vectors of A , i.e. $U \Sigma V^T = \sum_{i=1}^k u_i \otimes v_i^T$, where the k singular values Σ appear in descending

Algorithm 1 Projected conjugate gradient algorithm for NMF

```

1: procedure PCGNMF( $A, r, \dots$ )           ▷ Input a nonnegative matrix  $A$  and a target rank  $r$  (and
   convergence tolerances)
2:    $X_0, Y_0 \leftarrow \text{NNSVD}(A, r)$                                      ▷ Initialize  $X_0$  and  $Y_0$ 
3:   while true do                                                       ▷ Repeat until globally converged
4:      $G_0 \leftarrow X_0 Y_0 Y_0^T - A Y_0^T, D_0 \leftarrow -G_0$ 
5:     while true do                                                     ▷ Repeat until locally converged for  $X$ 
6:        $\alpha \leftarrow \text{LINESEARCH}(\dots)$                                ▷ Line search
7:        $X_1 = \max(0, X_0 + \alpha D_0)$                                      ▷ Take step by projecting out all negative values
8:        $G_1 = X_1 Y_0 Y_0^T - A Y_0^T$                                    ▷ Compute new gradient
9:        $\beta^{FR} \leftarrow \|G_1\|^2 / \|G_0\|^2$                          ▷ Calculate  $\beta$  using your favourite formula
   (e.g. Fletcher-Reeves)
10:       $D_1 \leftarrow -G_1 + \beta^{FR} D_0$  ▷ Update search direction (with  $\beta^{FR} = 0$  for first iteration)
11:       $D_0 \leftarrow D_1, G_0 \leftarrow G_1, X_0 \leftarrow X_1$        ▷ Prepare for next iteration
12:      if ISLOCALCONVERGED( $A, X_0, Y_0, \dots$ ) then                 ▷ Check local convergence (or
   maximum number of iterations)
13:        break
14:      end if
15:    end while
16:     $G_0 \leftarrow X_0^T X_0 Y_0 - X_0^T A, D_0 \leftarrow -G_0$ 
17:    while true do                                                     ▷ Repeat until locally converged for  $Y$ 
18:       $\alpha \leftarrow \text{LINESEARCH}(\dots)$                                ▷ Line search
19:       $Y_1 = \max(0, Y_0 + \alpha D_0)$                                      ▷ Take step by projecting out all negative values
20:       $G_1 = X_0^T X_0 Y_1 - X_0^T A$                                    ▷ Compute new gradient
21:       $\beta^{FR} \leftarrow \|G_1\|^2 / \|G_0\|^2$                          ▷ Calculate  $\beta$  using your favourite formula
   (e.g. Fletcher-Reeves)
22:       $D_1 \leftarrow -G_1 + \beta^{FR} D_0$  ▷ Update search direction (with  $\beta^{FR} = 0$  for first iteration)
23:       $D_0 \leftarrow D_1, G_0 \leftarrow G_1, Y_0 \leftarrow Y_1$        ▷ Prepare for next iteration
24:      if ISLOCALCONVERGED( $A, X_0, Y_0, \dots$ ) then                 ▷ Check local convergence (or
   maximum number of iterations)
25:        break
26:      end if
27:    end while
28:    if ISCONVERGED( $A, X, Y, \dots$ ) then                               ▷ Check convergence of  $X$  and  $Y$  together (or
   maximum number of iterations)
29:      break
30:    else ▷ Update local tolerances based on previous local tolerances, cost function values, and
   gradient norms
31:       $\dots \leftarrow \text{UPDATETOLERANCES}(\dots)$ 
32:    end if
33:  end while
34:  return  $X_1, Y_1$ 
35: end procedure
    
```

order and have been absorbed in the vectors u_i and v_i^T . Each rank-one term $u_i \otimes v_i^T$ generally contains positive and negative values (apart from the dominant term due to Perron-Frobenius if the largest singular value is non-degenerate). A sensible nonnegative initialization is then obtained by replacing each $u_i \otimes v_i^T$, for $i = 1, \dots, k$, with the nonnegative outer products $\max(0, u_i) \otimes \max(0, v_i^T)$ or $\max(0, -u_i) \otimes \max(0, -v_i^T)$, depending on whichever has larger norm. The zero elements can be filled with small random values if need be.

Additionally, it can be convenient to fix the monomial gauge freedom Eq. (5.8).

This can be done by calculating the row vector d_X containing the sum of each column of X and column vector d_Y containing the sum of each row of Y . We then insert the identity twice so that $XY = X \text{diag}(d_X)^{-1} \text{diag}(d_X) \text{diag}(d_Y) \text{diag}(d_Y)^{-1} Y$. After sorting the values on the diagonal of $\text{diag}(d_X) \text{diag}(d_Y)$ in descending order, we permute the columns of X and the rows of Y accordingly.

5.8.2 Details on the TNR₊ implementation

5.8.2.1 Nonnegative tensor factorization

To coarse-grain a 2D bipartite lattice made up of rank-four tensors $[C_1]_{ijkl} \in \mathbb{R}_+^{d \times d \times d \times d}$ and $[C_2]_{ijkl} \in \mathbb{R}_+^{d \times d \times d \times d}$ in a manifestly nonnegative way, we will need to extend the nonnegative matrix factorization described above to nonnegative tensor factorization (NTF). Indeed, as pointed out in the main text and previously in Ref. [117], we can interpret a block of four adjacent sites as a four-site periodic matrix product state (MPS) by reinterpreting C_1 and C_2 rank-three tensors after grouping the d -dimensional “physical indices” as follows

$$\begin{array}{c}
 \begin{array}{ccc}
 & l_1 & l_2 \\
 i_1 - & C_1(1) & C_2(4) - k_4 \\
 & \circ & \circ \\
 i_2 - & C_2(2) & C_1(3) - k_3 \\
 & \circ & \circ \\
 & j_2 & j_3
 \end{array}
 & = &
 \sum_{\substack{\{i_1, i_2, j_2, j_3, \} \\ \{k_4, k_3, l_1, l_4 \}}}
 |l_1 i_1\rangle |i_2 j_2\rangle |j_3 k_3\rangle |k_4 l_4\rangle \\
 & &
 \text{Tr} \left(C_1(1)^{(l_1 i_1)} C_2(2)^{(i_2 j_2)} C_1(3)^{(j_3 k_3)} C_2(4)^{(k_4 l_4)} \right),
 \end{array}$$

where the remaining d -dimensional indices have become “virtual indices”, and are summed over in the matrix products. In the first step of the coarse-graining process, we construct an ansatz to approximate this block with a “rotated block” represented again by a ring of four sites with different rank-four tensors $[X_n]_{\alpha_n \beta_n}^{i_n j_n} \in \mathbb{R}_+^{D \times D \times d \times d}$, where $i_n, j_n = 1, \dots, d$ (physical MPS dimension), and $\alpha_n, \beta_n = 1, \dots, D \geq d$ (virtual MPS dimension). After grouping the physical dimension, we again obtain a periodic MPS representation of the block of sites. The cost function for the local approximation is then given by the constrained MPS overlap,

$$\text{argmin}_{X_1, X_2, X_3, X_4} \left\| \begin{array}{ccc}
 & C_1(1) & C_2(4) \\
 \circ & & \circ \\
 & C_2(2) & C_1(3) \\
 \circ & & \circ
 \end{array} - \begin{array}{ccc}
 & X_1 & \\
 \circ & & \circ \\
 & X_2 & \\
 \circ & & \circ
 \end{array} \right\|^2, \quad (5.11)$$

where $X_1, X_2, X_3, X_4 \geq 0$, or, after matching indices explicitly,

$$\begin{aligned}
 & \sum \text{Tr} \left(C_1(1)^{(l_1 i_1)} C_2(2)^{(i_2 j_2)} C_1(3)^{(j_3 k_3)} C_2(4)^{(k_4 l_4)} \right) |l_1 i_1\rangle |i_2 j_2\rangle |j_3 k_3\rangle |k_4 l_4\rangle \\
 & \approx \sum \text{Tr} \left([X_1]^{(i_1 i_2)} [X_2]^{(j_2 j_3)} [X_3]^{(k_3 k_4)} [X_4]^{(l_4 l_1)} \right) |i_1 i_2\rangle |j_2 j_3\rangle |k_3 k_4\rangle |l_4 l_1\rangle.
 \end{aligned}$$

Note that the original C -block and the “rotated” X -block have different tensor product structures. It is this breaking apart of the tensor product structure at each step which we believe to be a crucial feature of the success of all TRG-inspired methods.

5.8.2.2 Sweeping projected conjugate gradient

The cost function Eq. (5.11) can be optimized using a generalization of the alternating inner loops of the PCGMF procedure explained in Appendix 5.8.1 by reformulating the problem in terms of matrices. This is possible, as the cost function is equal to

$$\text{Cost} = \text{Diagram 1} - 2 \text{Diagram 2} + \text{Diagram 3} \quad (5.12)$$

Now assume we want to optimize X_1 , keeping X_2, X_3 , and X_4 fixed. Reshaping X_1 to a $D^2 \times d^2$ matrix and writing the gradient with respect to X_1 as the following $D^2 \times d^2$ matrix,

$$\text{grad}_{X_1}(x_1) = 2 \text{Diagram 1} - 2 \text{Diagram 2}, \quad (5.13)$$

we have all ingredients to implement an alternating projecting conjugate gradient method to sweep over all X tensors.

One way to initialize the X tensors is by constructing a tensor renormalization group (TRG) [111] solution. If we use PCGMF to find the rank- D nonnegative decompositions of the $d^2 \times d^2$ matrices C_1 and C_2 ,

$$C_1 \approx C_1^{\text{TR}} C_1^{\text{BR}} \quad \text{and} \quad C_2 \approx C_2^{\text{TL}} C_2^{\text{BR}}, \quad (5.14)$$

our initialization looks like

$$\text{Diagram 1} = \text{Diagram 2}. \quad (5.15)$$

If we regard this particular initialization as a nonnegative TRG solution, we observe numerically that the local approximation error can be made significantly smaller than the initial solution. Just as MERA-TNR [115] and LOOP-TNR [117],

our TNR_+ algorithm is capable of systematically improving upon TRG. We also observed that the error does not keep on increasing at criticality, but remains approximately constant for a prolonged number of iterations. Off criticality, the error decreases quickly because the tensors flows to a simple fixed point encoding a trivial Hamiltonian.

5.8.2.3 Coarse-graining

From the optimized X tensors, we can immediately construct the C tensors of the coarse-grained lattice. For the general case under consideration where we impose neither lattice nor reflection symmetries, there is an ambiguity in constructing the new C tensors of the next layer. We refer to Appendix 5.8.3 for an explanation as to why the “plaquette” grouping of the tensors mentioned in the main text is flawed. The “vertex” grouping, depicted below,

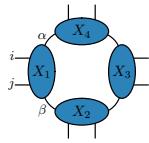
can either be done by identifying the new C tensors (and in this way choosing the orientation of the tilted lattice) counter-clockwise (a) clockwise (b), which is relevant for the construction of the radial transfer matrix MPO in Sec. 5.8.6.2.

5.8.2.4 A natural gauge choice for periodic nonnegative matrix product states

When implementing MPS optimization algorithms, choosing a canonical gauge is important both for manifestly revealing the entanglement content of a state as well as stabilizing the optimization through better conditioning of the matrices involved. Our TNR_+ algorithm can also benefit from fixing the nonnegative monomial gauge freedom Eq. (5.8) by providing a sensible basis for truncation purposes (see Appendix 5.8.3), and by aiding in the recovery of explicit scale invariance (see Appendix 5.8.5). We we will now describe a constructive way to fix the gauge freedom for a ring of nonnegative MPS tensors.

Without loss of generalization, consider a ring of four sites with rank-four tensors $[X_n]_{(\alpha\beta)}^{(ij)} \in \mathbb{R}_+^{D \times D \times d \times d}$, for $n = 1, \dots, 4$, $i, j = 1, \dots, d$ (physical MPS dimension), and $\alpha, \beta = 1, \dots, D$ (virtual MPS dimension), so that the periodic

nonnegative MPS is given by

$$\sum_{\{i_n j_n\}} \text{Tr} \left(X_1^{i_1 j_1} X_2^{i_2 j_2} X_3^{i_3 j_3} X_4^{i_4 j_4} \right) |i_1 j_1\rangle |i_2 j_2\rangle |i_3 j_3\rangle |i_4 j_4\rangle =$$


$$(5.17)$$

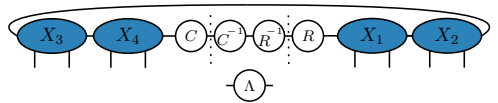
Let us now cut the bond connecting X_1 and X_4 , and sum over all physical indices of the resulting tensor,

$$E_{\gamma\delta} = \begin{array}{c} \gamma \\ \text{---} X_1 \text{---} X_2 \text{---} X_3 \text{---} X_4 \text{---} \delta \\ \text{+ +} \quad \text{+ +} \quad \text{+ +} \quad \text{+ +} \end{array},$$

where $+$ denotes a vector of ones. We then find the diagonal matrices R and C such that the matrix $M = REC$ becomes doubly stochastic, i.e. $\sum_i M_{ij} = \sum_j M_{ij} = 1$. Denoting the diagonals of R and C respectively as vectors r and c , we can find these fixed point solutions by iterating

$$c = 1./ (A^T r), \quad r = 1./ (A c),$$

which converges quickly as long as E contains sufficiently many nonzero elements [166]. We then substitute the identity twice on the bond that was cut, absorb R and C into X_1 and X_4 respectively, and obtain a central diagonal matrix,



After sorting the diagonal elements of Λ in descending order (which yields a permutation P), we can check for small values relative to the largest value and truncate up to some tolerance ε (by means of an isometry W). In the end, we arrive at the following matrices to be absorbed into X_4 and X_1 respectively,

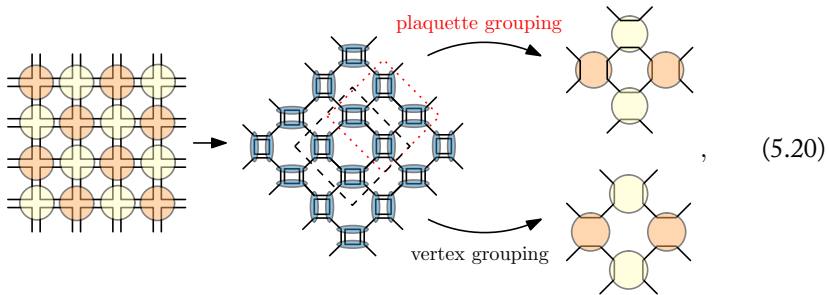
$$G_4^R = C P^T W W^T P \sqrt{\Lambda}, \quad (5.18)$$

$$G_1^L = \sqrt{\Lambda} P^T W W^T P R, \quad (5.19)$$

where the matrix W is just the identity if there is no truncation or implicit truncation by setting the small singular values to zero, and an isometry onto the subspace that is retained if there is explicit truncation. Notice how Λ gives us a nonnegative analogue of Schmidt values in the MPS case. The above gauge fixing can be repeated independently for all other bonds by permuting the tensors accordingly.

5.8.3 CDL tensors and entanglement filtering

Corner double line (CDL) tensors are a pathological case of non-critical fixed points of the TRG flow in the space of tensors. As argued in the main text, all TNR approaches (including the TEFR thanks to its entanglement filtering pre-processing step [112]) are capable of removing CDL tensors because they surround a block of sites with a coarse-graining operation that can in principle detect correlations inside the block. Indeed, one can judiciously construct coarse-graining tensors that eliminate short-range correlations with a particular CDL structure [115], which for TNR_+ proceeds as follows,



The vertex grouping groups the plaquettes which *do not* contain a loop, which results in a product state that can be approximated in the next iteration with a $D = 1$ MPS. In contrast, grouping the plaquettes that contain loops reinstates corner double line tensors.

The above considerations however do not imply that numerical algorithms built on this premise will act accordingly, since CDL configurations are still local minima of the cost function and fixed points of the RG flow. It is important to mention that, in the ideal case above, the presence of CDL correlations is reflected in the degeneracies of the Schmidt values of the MPS. In practice however, there is no obvious way to detect these (approximate) tensor product structures inside the virtual bond and, numerically, there is often no structure to be inferred at all if local corner tensors contain non-degenerate eigenvalues. One way to deal with this is by monitoring the Schmidt values on the bonds of the ring Eq. (5.17) using the gauge fixing described in Appendix 5.8.2.4 to filter local correlations in a similar way to the tensor entanglement filtering step for TEFR and LOOP-TNR discussed in Refs. [112, 117]. Reformulated in conventional MPS language: what entanglement filtering does is truncating a periodic MPS (which here describes a block of sites of a classical 2D lattice model) by truncating its virtual dimension (which here contains short-range correlations “inside” the block of sites). Note that a similar kind of truncation in MERA-TNR corresponds to alternating bond dimensions every step and inserting multiple optimized isometries at different stages in the actual implementation of the algorithm to reduce the intermediate bond dimensions and steer the optimization towards a preferred local minimum [153]. Another possible strategy, which requires no gauging, would be to maximize the overlap of a four-site periodic MPS containing irrelevant local details with a different MPS with a lower bond dimension and accept

the lower-dimensional one if the fidelity is high enough. This can be done for nonnegative MPS with the algorithm described in Appendix 5.8.2.1. Note that entanglement filtering has no effect for critical systems as there is in general no truncation possible due to the slowly decaying distribution of the Schmidt values (recall that the exact critical fixed point would require an infinite bond dimension), but by sorting diagonal values the permutations on the virtual indices can still be fixed.

5.8.4 Symmetries and tensor network renormalization

A straightforward application of Yang et al.'s [117] insight that it is worthwhile to model blocks of sites with periodic MPS, is the fundamental theorem of MPS [72, 167] and its use in relating symmetries on the physical level to those on the virtual level. Consider an on-site symmetry operator acting on all sites, e.g. the spin flip operator

$$X = \begin{pmatrix} 0 & 1 \\ 1 & 0 \end{pmatrix}, \quad (5.21)$$

for the Z_2 symmetry of the Ising model. Invariance under the action of the symmetry implies that the transformed MPS should have an overlap with the original state that has modulus one. As such, the mixed transfer matrix of the original and the transformed state must have a dominant eigenvector with eigenvalue $|\lambda| = 1$. It can then be shown that the effect of this statement is that the action of the symmetry on the physical level can be pushed through to the virtual level, up to a phase, which amounts to having a projective representation of the symmetry on the virtual level in the Schmidt basis.

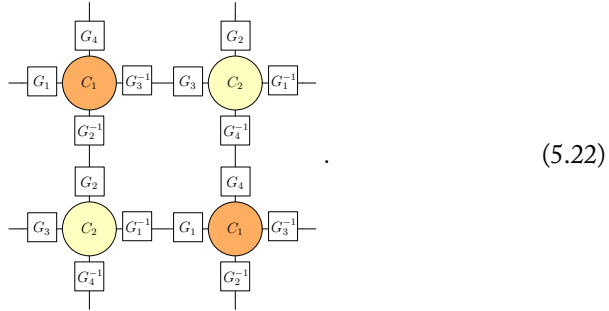
Now recall from the main text that the physical and virtual dimensions switch roles every RG iteration. This implies that the symmetry action on the virtual level becomes the action on the physical level of the next iteration, which in turn can be pushed through. In this way, the representation of the symmetry operator can be tracked throughout the entire coarse-graining network.

5.8.5 Approximate scale invariance

As demonstrated in the main text, the TNR₊ algorithm yields tensors which correspond to approximate fixed points of the RG equations, and are approximately scale invariant at criticality. By observing gauge-invariant quantities, such as the eigenvalues of the linear transfer matrix (see Appendix 5.8.6.1), it is clear that the fixed point tensors are implicitly approximately scale invariant and remain so for a large number of iterations.

To recover explicit approximate scale invariance at the level of the individual tensor elements however, we need to fix the gauge freedom of the partition function across different scales. Note that the partition function written in terms of C_1 and

C_2 remains invariant under the following transformations,



One simple way to achieve approximate scale invariance during the optimization itself is by adding additional constraints to the cost function Eq. (5.12). We can introduce a small penalty term λ_i for each individual X_i by adding

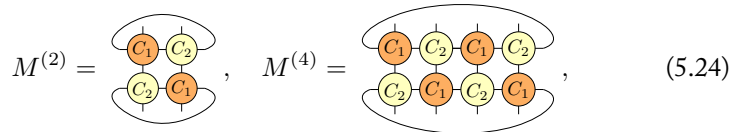
$$\sum_{i=1}^4 \lambda_i \left\| X_i^{(s-2)} - X_i^{(s)} \right\|^2 \tag{5.23}$$

to the cost function. This modified cost function will favor solutions which stay close to the previous equivalent solutions, i.e. those of the even or odd iterations connecting lattices of the same orientation, which in turn renders the respective C_1 and C_2 tensors of the even and odd iterations approximately explicitly scale invariant as well.

5.8.6 Conformal data from tensor networks

5.8.6.1 Linear transfer matrix

Scaling dimensions of the conformal field theory (see Sec. 2.8) underlying a critical partition function can be extracted directly from its tensor network representation by constructing the linear transfer matrix [112]. At every iteration step, we can construct the effective 2×2 and 4×2 row-to-row transfer matrices,



whose gauge invariant eigenvalues can be directly related to the scaling dimensions of the primary operators and descendants of the CFT. The leading contribution to the partition function (ignoring non-universal finite-size corrections) on a torus of size $L_x \times L_y$ is given by

$$Z \approx e^{aL_x L_y} \sum_{\alpha} e^{-2\pi \frac{L_y}{L_x} (\Delta_{\alpha} - \frac{c}{12})}, \tag{5.25}$$

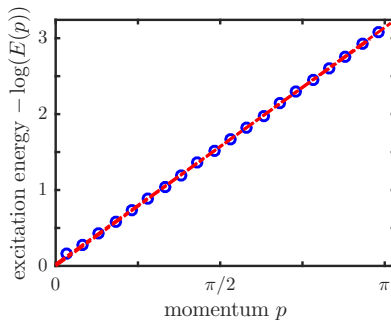


FIGURE 5.4: Linear energy-momentum spectrum of the critical Ising Hamiltonian encoded in the infinite row-to-row transfer matrix Eq. (5.27) obtained from a TNR₊ simulation with $D = 6$ in the scale invariant regime. For the MPO fixed point calculations, a boundary MPS with bond dimension $\chi = 18$ was used.

where the non-universal contribution $e^{\alpha L_x L_y}$ can be taken care of in the tensor network representation by properly normalizing the tensors, and Δ_α and c are respectively the scaling dimensions the central charge. We can then write the partition function $Z = \text{Tr}(M^{L_y})$ in terms the row-to-row transfer matrix M , whose eigenvalue decomposition can be shown to be given by

$$M = \sum_{\alpha} e^{-\frac{2\pi}{L_x}(\Delta_\alpha - \frac{c}{12})} |\alpha\rangle \langle \alpha|, \quad (5.26)$$

which immediately yields numerical estimates for the scaling dimensions and the central charge given that $\Delta_0 = 0$. Note that we have assumed M to be Hermitian, yet small deviations are to be expected numerically if no symmetries are enforced, resulting in distinct left and right eigenvectors.

As an aside, we can interpret the row-to-row transfer matrix of Eq. (5.24) as an infinite MPO

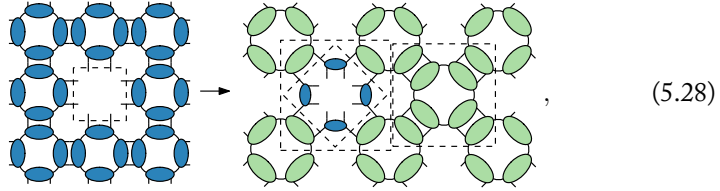
$$(5.27)$$

by blocking the tensors inside the dashed squares. Using the numerical MPO techniques recently developed in Ref. [63], we can then calculate the low-lying excitation spectrum of this operator directly in the thermodynamic limit in terms of MPS excitation ansätze. As is to be expected, Fig. 5.4 reveals a linear dispersion relation reflecting the continuum collapse of the CFT finite-size scaling results.

5.8.6.2 Radial transfer matrix

Alternatively, we can extract conformal data from the radial transfer matrix, which can be obtained by tracking the RG flow around an open impurity [103]. For the

RG flow of TNR_+ , we obtain after two iterations,



where, for scale invariant systems, doing the next iteration everywhere on the block of tensors inside the rightmost bounding box gives rise to the same tensors as those obtained from the first iteration. Note that (see Appendix 5.8.2.3), we used different combinations of X-tensors in constructing the new C-tensors for even and odd iterations to arrive again at the same orientation after two iterations (“rotate back-and-forth”). If we would use the same contraction each iteration it would take eight iterations to again arrive at the original orientation (“rotate clockwise or counter-clockwise”), which would lead to a rather impractical superoperator. For scale invariant systems, we thus end up with repeated applications of the following MPO,

(5.29)

which, after proper normalization, can be diagonalized to give [130]

$$R = \sum_{\alpha} 2^{-\Delta_{\alpha}} |\alpha\rangle \langle \alpha|. \quad (5.30)$$

Note that here again we have assumed R to be Hermitian, yet small deviations are to be expected numerically if no symmetries are enforced, resulting in distinct left and right eigenvectors. If the gauge freedom has been fixed across RG steps, Δ_{α} and $|\alpha\rangle$ are found to be respectively the scaling dimensions and approximate lattice representations of the primary fields and descendants. Indeed, for this construction to work, it is crucial to fix the gauge (see Appendix 5.8.5), or else the degrees of freedom we deem equivalent do not match due to the different local gauges Eq. (5.22).

Mapping topological to conformal field theories through strange correlators

In this chapter¹, we study non-local symmetries in tensor networks by expressing two-dimensional classical partition functions in terms of strange correlators of judiciously chosen product states and topological string-net wave functions. When tuning the partition function to criticality, non-local matrix product operator (MPO) symmetries emerge which highlight the parallels between topological sectors and conformal primary fields in the shared framework of MPO algebras. In particular, we numerically identify the topological sectors of the Ising model in finite-size conformal field theory spectra of twisted partition functions on the torus. Additionally, we provide a complementary perspective on real-space renormalization by showing how known tensor network renormalization methods can be understood as the approximate truncation of an exactly coarse-grained strange correlator.

6.1 Background and motivation

This chapter touches on a lot of different topics, so let us first of all provide a superficial, high-level overview to guide our thoughts. Central to the framework of topologically ordered phases (see Sec. 2.7.5 and Sec. 3.3.2) is the concept of tensor fusion categories, which naturally appear in the context of both conformal field theories (CFTs) [39] and topological quantum field theories (TQFTs) [38]. Tensor fusion categories have been proposed to characterize and classify topological phases, capturing the universal behavior of topological phases much like group theory does for symmetry-breaking phases. Since it is our intention to do numerics using tensor networks, we are interested in lattice realizations of CFTs and TQFTs. As mentioned in Sec. 3.3.2, nonchiral (2+1)-dimensional TQFTs can be realized on the lattice using Turaev-Viro state sum constructions [90], with Levin and Wen’s string-net models offering a concrete condensed matter realization of these mathematical ideas [89]. String-nets additionally provide a physical mechanism which clarifies how topological phases can emerge from microscopic degrees of freedom through the condensation of extended “string-like” objects [89]. In Chapter 2, we have discussed

¹An updated and condensed version of the work presented here has appeared in an arXiv pre-print [3] and has been done in collaboration with Dominic Williamson, Robijn Vanhove, Nick Bultinck, Jutho Haegeman, and Frank Verstraete.

how rational CFTs in two dimensions can be realized on the lattice as the scaling limit of critical statistical-mechanical models, the most famous example being the classical Ising model. The properties and fusion algebra of conformal defects² in CFTs are very much related to those of topological sectors in string-nets, and have been analyzed in great detail in a series of TQFT-infused CFT papers by Fröhlich, Fuchs, Runkel, and Schweigert [168–170].

In this chapter, we provide a first step towards a constructive tensor network realization of this correspondence. To do this, we make use of three ideas.

First, we use the fact that there exist natural PEPS representations of string-net wave functions [112, 171], and that their topological features are completely characterized by symmetries of local tensors in the form of MPOs [82–84, 156]. In Sec. 6.3.3, we will sketch how the MPO algebra representation of these symmetries naturally leads to a second algebra, a so-called Ocneanu’s tube algebra, whose central idempotents are identified with the different topological sectors [84, 156]. Secondly, we focus on classical partition functions on the lattice and make use of the concept of a *strange correlator* introduced in Ref. [172] to write a classical partition function Z as the overlap $\langle \Omega | \Psi_{\text{SN}} \rangle$ of a string-net $|\Psi_{\text{SN}}\rangle$ and a product state $|\Omega\rangle$. Even though both of these wave functions are gapped and have zero correlation length, their overlap is highly nontrivial since the partition function obtained in this way actually represents the physics at the interface between a topological phase and a trivial phase. Indeed, we will confirm that the strange correlator is able to capture the critical correlations of the classical model. Looking ahead, the topological properties of the string-net will ensure that (part of) the emerging non-local symmetries of the scaling limit of the classical partition function at criticality are already enforced at the ultraviolet level. Thirdly, we rely on a folklore structure theorem for MPO algebras, which states that any one-dimensional quantum Hamiltonian or transfer matrix on a spin chain which commutes with all elements of this algebra has to be either gapless/critical or symmetry broken. For our purposes, this implies that the partition function with a given MPO symmetry obtained from the strange correlator will be critical or symmetry broken. Note that even if the partition function turns out to be critical/gapless, we are not necessarily guaranteed to obtain a CFT.

We believe our tensor network construction is useful because it provides explicit lattice representations of topological conformal defects³. As shown by Petkova and Zuber [173, 174], these defects can be interpreted as generalized twisted boundary conditions obtained by inserting a (non-local) defect operator X into the partition function on a torus $Z_X = \text{Tr}(X e^{-\text{Im}(\tau)H})$. The effect of this operator is to twist the boundary conditions, similar to defect lines in statistical mechanics. For the Ising model, inserting the spin-flip operator along a non-contractible cycle of the cylinder results in anti-periodic boundary conditions. The spin-flip operator is a topological conformal defect since it can be shown to commute with the action of

²A conformal defect is obtained by cutting space-time along a defect line and rejoining the two sides in the presence of an appropriate boundary condition, which describes how the bulk fields behave when crossing the cut. Conformal defects which respect the conformal symmetry can be labelled by the primary fields.

³A topological conformal defect is a conformal defect which can be deformed at will as long as it does not cross another field insertion.

two copies of the Virasoro algebra $[L_n, X] = [\bar{L}_n, X] = 0$ so that the closed defect line of string operators can be moved around.

Related work has been done recently in Ref. [157], where the twisted partitions Z_1 , Z_ψ , and Z_σ of the Ising model have been studied numerically using \mathbb{Z}_2 -invariant tensor networks. The σ -duality defect is constructed from its action at the level of the Hamiltonian of the quantum Ising spin chain instead of finding the explicit realization for the classical partition function. As will become clear in Sec. 6.3, the MPO algebra readily gives the correct non-local symmetry operators and demonstrates that truly identifying the topological sectors requires two defect lines and a way of constructing projectors onto the topological sectors. An analytic description of topological defects on the lattice was recently achieved in Ref. [50] based on defect commutation relations. This approach is inspired by the previously mentioned generalized twisted CFT partition function approach by Petkova and Zuber applied to a special class of integrable lattice models (RSOS models [175, 176]) [174], and is hence very much related to our work. Our SC construction leads to a very similar picture reformulated in terms of MPO algebras, but introduces numerics into the picture. In this sense, our work unifies the numeric and algebraic approaches of respectively Ref. [157] and Ref. [50] and sheds light on the difficulties encountered when trying to achieve a full identification of the topological sectors in finite-size spectra of twisted partition functions on the lattice. In case of getting lost, the reader should take a step back and remember that all we are doing is studying the Ising model.

6.2 Partition functions from strange correlators

Let us first of all show how to relate the strange correlator overlap of two quantum wave functions to the classical partition function of the Ising model. To implement the Kramers-Wannier duality (see Appendix 6.6.1) on the lattice, we make use of symmetry-enriched (SET) string-nets [177–179] to encode both the primal and the dual lattice. We show how the partition function tensors satisfy SET pulling-through conditions which allow duality defects to be moved around and extract the critical temperature from demanding that the product state inserted into the strange correlator is the same on both sides of the duality. In Sec. 6.2.4 we will comment on possible extensions to other minimal models.

6.2.1 Symmetry-enriched string-net models

The string-net construction is based on the algebraic data of an input unitary fusion category \mathcal{C} associated to a finite set of simple objects $\{a\}$ with respective quantum dimensions d_a . Let N_{ab}^c denote a rank-three tensor which encodes the allowed fusion channels of the objects labelled by a , where $N_{ab}^c = 1$ if $a \times b$ contains c and $N_{ab}^c = 0$ otherwise. These objects can be represented by lines obeying the following

diagrammatic rules⁴

$$\begin{array}{c} a \\ \circlearrowleft \\ \end{array} = d_a, \quad \begin{array}{c} j \\ \circlearrowleft \\ k \\ \circlearrowleft \\ i \\ \end{array} = \delta_{ij} \sqrt{\frac{d_k d_l}{d_i}}, \quad (6.1)$$

$$\begin{array}{c} i \\ \circlearrowleft \\ \end{array} \cdots \begin{array}{c} j \\ \circlearrowleft \\ \end{array} = \sum_k N_{ij}^k \sqrt{\frac{d_k}{d_i d_j}} \begin{array}{c} i \quad j \\ \diagdown \quad / \\ k \\ \diagup \quad \diagdown \\ i \quad j \end{array} \quad (6.2)$$

Closed loops of label a yield a quantum dimension d_a , bubbles pop and leave behind quantum dimensions, and a vacuum line can be replaced by a summation over other labels which are compatible. For the Ising fusion category, we have the objects $a \in \{1, \psi, \sigma\}$ with non-zero fusion coefficients

$$N_{11}^1 = 1, \quad N_{1\sigma}^\sigma = 1, \quad N_{1\psi}^\psi = 1, \quad N_{\sigma\sigma}^1 = 1, \quad (6.3)$$

up to allowed permutations, so that the non-trivial fusion rules are given by

$$\psi \times \psi = 1 \quad (6.4)$$

$$\sigma \times \psi = \sigma \quad (6.5)$$

$$\sigma \times \sigma = 1 + \psi. \quad (6.6)$$

Pictorially, this means that only the following vertices (up to permutations) are allowed in trivalent graphs,

$$\begin{array}{c} 1 \\ \diagdown \quad / \\ 1 \end{array} \quad \begin{array}{c} \psi \\ \diagdown \quad / \\ 1 \end{array} \quad \begin{array}{c} \sigma \\ \diagdown \quad / \\ 1 \end{array} \quad \begin{array}{c} \sigma \\ \diagdown \quad / \\ \psi \end{array} \quad (6.7)$$

For the Ising case, the quantum dimensions d_a associated to the labels are respectively $d_1 = d_\psi = 1$ and $d_\sigma = \sqrt{2}$.

Another diagrammatic rule involves the F -symbols

$$F_{def}^{abc} = [F_d^{abc}]_e^f = N_{ab}^e N_{ec}^d [F_d^{abc}]_e^f N_{bc}^f N_{af}^d, \quad (6.8)$$

which satisfy the “ F -move” equation,

$$\begin{array}{c} a \\ \diagdown \\ b \quad e \\ \diagup \\ c \end{array} \quad \begin{array}{c} \diagdown \\ \diagup \\ d \end{array} = [F_d^{abc}]_e^f \begin{array}{c} a \\ \diagdown \\ b \quad f \\ \diagup \\ c \end{array} \quad \begin{array}{c} \diagdown \\ \diagup \\ d \end{array} \quad (6.9)$$

When interpreted as matrices, the F -symbols are unitary in the subspaces where

⁴Actually, these lines are oriented and we should include arrows. We will suppress the arrows in most diagrams because the orientation of the lines plays no role for the fusion categories we consider explicitly.

they are defined,

$$[(F_d^{abc})^{-1}]_f^e = [(F_d^{abc})^\dagger]_f^e = (F_{def}^{abc})^*, \quad (6.10)$$

so that $\sum_f F_{def}^{abc} (F_{def}^{abc})^* = \delta_{e\bar{e}} N_{ab}^e N_{ec}^d$ and $\sum_e (F_{def}^{abc})^* F_{def}^{abc} = \delta_{\bar{f}f} N_{bc}^f N_{af}^d$. The non-trivial F -symbols for the Ising case are given by

$$[F_\sigma^{\sigma\sigma\sigma}]_{ij} = \frac{1}{\sqrt{2}} \begin{pmatrix} 1 & 1 \\ 1 & -1 \end{pmatrix}, \quad [F_\psi^{\psi\psi\sigma}]_\sigma = [F_\sigma^{\psi\psi\psi}]_\sigma = -1. \quad (6.11)$$

All other elements are either zero or one and are completely determined by the fusion constraints in Eq. (6.8).

We now have all ingredients to define the PEPS representations of the trivalent SET string-net tensors,

$$\begin{array}{c} \beta \\ \swarrow \quad \downarrow \quad \searrow \\ i \quad k \quad j \\ \swarrow \quad \downarrow \quad \searrow \\ \alpha \quad k \quad \gamma \end{array} = \frac{(d_i d_j)^{1/4}}{(d_k)^{1/4}} \frac{F_{\gamma\beta k}^{\alpha ij}}{(d_\beta)^{1/2}}, \quad \begin{array}{c} k \\ \uparrow \quad \downarrow \quad \downarrow \\ \alpha \quad i \quad j \\ \swarrow \quad \downarrow \quad \searrow \\ \beta \quad k \quad \gamma \end{array} = \frac{(d_i d_j)^{1/4}}{(d_k)^{1/4}} \frac{(F_{\gamma\beta k}^{\alpha ij})^*}{(d_\beta)^{1/2}}, \quad (6.12)$$

where we have included appropriate quantum dimensions⁵. These are identical to the usual PEPS representation of string-nets [112, 171], but sector information of the virtual loop is copied to the physical level, which we denote by additional physical indices emanating from the loops. By this we mean that, for the SET extension of string-nets, the Ising fusion category $\{1, \psi, \sigma\}$ is to be regarded as a Z_2 extension of $\{1, \psi\}$ with a Z_2 grading given by $\{1, \psi\}_{+1}$ and $\{\sigma\}_{-1}$ [85, 177], i.e. $\mathcal{C} = \{1, \psi\} \oplus \{\sigma\}$. Note that we have already anticipated the contraction of these tensors in a bigger tensor network by being sloppy with the index labeling. To avoid confusion, let us write out one of the tensors in Eq. (6.12) in full by including Kronecker δ -functions,

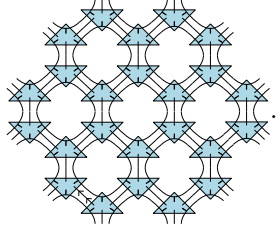
$$\begin{array}{c} \beta \quad \beta' \\ \swarrow \quad \downarrow \quad \searrow \\ i \quad k \quad j \\ \swarrow \quad \downarrow \quad \searrow \\ \alpha \quad k' \quad \gamma' \end{array} = \delta_{\alpha\alpha'} \delta_{\beta\beta'} \delta_{\gamma\gamma'} \delta_{ii'} \delta_{jj'} \delta_{kk'} \frac{(d_i d_j)^{1/4}}{(d_k)^{1/4}} \frac{F_{\gamma\beta k}^{\alpha ij}}{(d_\beta)^{1/2}}, \quad (6.13)$$

where we actually have to add three more δ -functions for the SET indices which yield the sector information $\{1, \psi\}_{+1}$ and $\{\sigma\}_{-1}$ consistent with the value of the loop. This explicit notation also clarifies that we interpret the physical indices in the PEPS representation not as living on the links, but as being doubled so as to live on the vertices, e.g. the indices ijk correspond to doubled physical indices which are identified.

States in the Hilbert space of string-net models are linear superpositions of

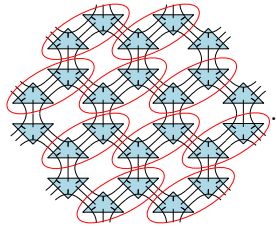
⁵Not all of these quantum dimensions are required for the construction of a consistent MPO algebra framework. Additional factors $(d_i d_j d_k)^{1/4}$ have been added which correspond to a filtering operation on the physical level but play no role in pulling-through equations and other properties that have to be satisfied by the MPO algebra tensors (see Refs. [84]).

different spatial configurations of string-nets. In this way, the triangles Eq. (6.12) define a tensor network representation of the string-net ground state wave function on the hexagonal lattice, depicted by the contraction below,


(6.14)

Rather than absorbing factors of quantum dimensions locally, we adopt the diagrammatic rule that every closed loop of label a introduces a factor d_a .

Let us now construct a tensor network representation on a bipartite square lattice by blocking the triangle tensors in Eq. (6.14) as follows


(6.15)

Explicitly, the tensor making up the bipartite square lattice is given by

$$[Q^{\square}]_{ijklm} = i \begin{array}{c} j \\ \beta \diagdown \quad \diagup \gamma \\ \alpha \quad \delta \\ l \end{array} k = \frac{(d_m)^{1/2} (d_i d_k)^{1/4}}{(d_\beta d_\delta)^{1/2} (d_l d_j)^{1/4}} (F_{\gamma\delta j}^{\beta m k})^* F_{\delta\beta l}^{\alpha i m}. \quad (6.16)$$

Using the pentagon equation⁶ for the F -symbols

$$F_{eqr}^{pcd} F_{eps}^{abr} = \sum_n F_{qpn}^{abc} F_{eqs}^{and} F_{snr}^{bcd}, \quad (6.17)$$

and tetrahedral symmetry of the F -symbols, we can locally relate every other square tensor to its 90-degrees rotated version to arrive at a genuine A-B lattice structure since

$$(F_{\gamma\delta j}^{\beta m k})^* F_{\delta\beta l}^{\alpha i m} = F_{kj\delta}^{\gamma\beta m} F_{\delta\beta l}^{\alpha i m} = F_{mj\delta}^{\beta\gamma k} F_{m\beta l}^{i\alpha\delta} = \sum_n F_{j\beta n}^{i\alpha\gamma} F_{mj l}^{ink} F_{ln\delta}^{\alpha\gamma k}, \quad (6.18)$$

⁶The pentagon equation is an extremely important consistency relation reflective of the ‘‘associativity’’ property of the F -symbols, and is actually more important than the F -symbols since valid F -symbols are those which are found to satisfy the pentagon equation.

which leads to

$$\sum_n F_{j\beta n}^{i\alpha\gamma} F_{mjl}^{ink} F_{ln\delta}^{\alpha\gamma k} = \sum_n F_{mjl}^{ink} F_{\alpha\beta n}^{\gamma j i} F_{ln\delta}^{\alpha\gamma k} \quad (6.19)$$

$$= \frac{(d_\beta d_\delta)^{1/2}}{(d_j d_\alpha d_\gamma d_l)^{1/2}} \sum_n d_n F_{mjl}^{ink} F_{nj\alpha}^{\gamma\beta i} F_{\delta\gamma l}^{\alpha\gamma k} \quad (6.20)$$

$$= \frac{(d_\beta d_\delta)^{1/2}}{(d_\alpha d_\gamma)^{1/2}} \sum_n \sqrt{\frac{d_n}{d_m}} F_{lnm}^{ijk} (F_{\gamma\alpha j}^{\beta in})^* F_{\delta\gamma l}^{\alpha\gamma k}. \quad (6.21)$$

If we now define

$$[Q^\square]_{ijklm} = i \begin{array}{c} \beta \quad j \\ \diagup \quad \diagdown \\ \alpha \quad \delta \\ \diagdown \quad \diagup \\ \alpha \quad \delta \end{array} k = \frac{(d_m)^{1/2} (d_i d_k)^{1/4}}{(d_\alpha d_\gamma)^{1/2} (d_l d_j)^{1/4}} (F_{\gamma\alpha j}^{\beta im})^* F_{\delta\gamma l}^{\alpha\gamma k}, \quad (6.22)$$

we find that Q^\square and Q^\square are interchangeable in the sense that they are related by a local operation on the physical indices

$$[Q^\square]_{i'j'k'l'm'} = \sum_m F_{l'mm'}^{i'j'k'} [Q^\square]_{i'j'k'l'm}. \quad (6.23)$$

We can interpret this as the action of a gate which is unitary on the allowed subspace

$$U_{i'j'k'l'm',ijklm} = \delta_{i'i} \delta_{j'j} \delta_{k'k} \delta_{l'l} F_{lmm'}^{ijk}, \quad (6.24)$$

satisfying

$$U_{i'j'k'l'm',ijklm} (U_{i''j''k''l''m'',ijklm})^\dagger \quad (6.25)$$

$$= \delta_{i''i'} \delta_{j''j'} \delta_{k''k'} \delta_{l''l'} \delta_{m''m'} N_{j'k'}^{m'} N_{i'm'}^{l'}, \quad (6.26)$$

$$(U_{ijklm,i''j''k''l''m''})^\dagger U_{ijklm,i'j'k'l'm'} \quad (6.27)$$

$$= \delta_{i''i'} \delta_{j''j'} \delta_{k''k'} \delta_{l''l'} \delta_{m''m'} N_{i'j'}^{m'} N_{m'k'}^{l'}, \quad (6.28)$$

so that indeed

$$[Q^\square]_{i'j'k'l'm'} = \sum_{ijklm} U_{i'j'k'l'm',ijklm} [Q^\square]_{ijklm} = \sum_m F_{l'mm'}^{i'j'k'} [Q^\square]_{i'j'k'l'm}. \quad (6.29)$$

Conversely, we find that

$$[Q^\square]_{i'j'k'l'm'} = \sum_m F_{i'mm'}^{j'k'l'} [Q^\square]_{i'j'k'l'm}. \quad (6.30)$$

A patch of the string-net wave function $|\Psi_{\text{SN}}\rangle$ on the bipartite square lattice we

consider thus looks like

$$|\Psi_{\text{SN}}\rangle = \text{Diagram} \quad (6.31)$$

6.2.2 Strange correlators

We will now describe several flavors of product states $|\Omega\rangle$, whose overlap $\langle\Omega|\Psi_{\text{SN}}\rangle$ with the PEPS representation of the string-net wave function $|\Psi_{\text{SN}}\rangle$ leads to a strange correlator (SC) representation of the classical partition function.

6.2.2.1 Product states: flavor #1

Let us now construct two product states which act on all physical indices of respectively Q_A^{\square} and Q_B^{\square} , where we have chosen the convention that the slanted A sublattice will correspond to horizontal Ising interactions with coupling constant $K = \beta J_x$ and the slanted B sublattice to vertical interactions $L = \beta J_y$,

$$\langle\Omega^{\square}[f_A]|\equiv \left\langle \begin{array}{ccc} 1 & \sigma & -1 \\ \sigma & \langle f_A | & \sigma \\ -1 & \sigma & 1 \end{array} \right| \quad \text{and} \quad \langle\Omega^{\square}[f_B]|\equiv \left\langle \begin{array}{ccc} -1 & \sigma & 1 \\ \sigma & \langle f_B | & \sigma \\ 1 & \sigma & -1 \end{array} \right|, \quad (6.32)$$

where the SET-labels are denoted by their respective sector and where $\langle f|\equiv \langle f(\alpha)|$ is a product state depending continuously on a single scalar parameter α . We will often consider the fixed σ indices and the SET indices as “dressing” of the non-trivial inputs $\langle f|$ and also ignore the difference between single or double SET-inputs along the diagonals, the latter of which we can of course just as well be replaced by a single label. The strange correlator is then taken to be the overlap of a trivial PEPS

$$|\Omega\rangle = \bigotimes_{a \in A} |\Omega^{\square}[f_A]\rangle_a \bigotimes_{b \in B} |\Omega^{\square}[f_B]\rangle_b, \quad (6.33)$$

with a PEPS string-net wave function Eq. (6.31), which gives

$$\langle\Omega|\Psi_{\text{SN}}\rangle = \text{Diagram} \quad (6.34)$$

because the product state fixes the internal labels to be σ and the loop labels to be either $\{1, \psi\}_{+1}$ or $\{\sigma\}_{-1}$. To see how the Ising partition function explicitly arises

More precisely, the Ising model arising from the strange correlator is defined on the slanted square lattice with the spins living on the $1/\psi$ plaquettes and the interactions mediated by the $\langle \Omega^{\square} | Q_A^{\square} \rangle$ and $\langle \Omega^{\square} | Q_B^{\square} \rangle$ tensors living on the A and B sublattices. The two different flavors for the SET-labels introduced above are of course related to the (self-)duality of the Ising model, as we will describe in the next section.

6.2.2.3 Equivalent strange correlator descriptions

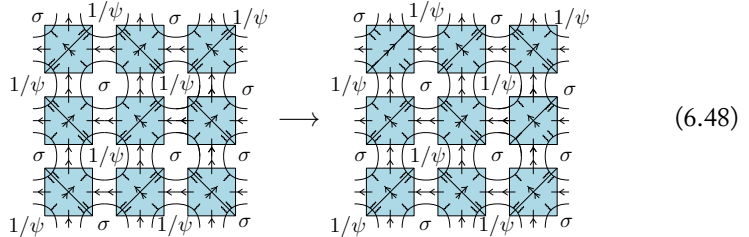
Due to its construction, different strange correlator descriptions can be unitarily equivalent. Consider the designation of A and B sublattices to be fixed. Let U denote the tensor product of all local unitaries Eq. (6.23) and Eq. (6.30) acting on the physical indices of the tensors on the A and B sublattices. Using the definitions of the product states Eq. (6.32) and Eq. (6.32), we then find

$$\langle \Omega | \Psi_{SN} \rangle = \langle \Omega | U U^\dagger | \Psi_{SN} \rangle \quad (6.45)$$

$$= \left(\bigotimes_{a \in A} \langle \Omega^{\square} [f(K)] |_a \right) \left(\bigotimes_{b \in B} \langle \Omega^{\square} [f(L)] |_b \right) U U^\dagger | \Psi_{SN} \rangle \quad (6.46)$$

$$= \left(\bigotimes_{a \in A} \langle \Omega^{\square} [g(K)] |_a \right) \left(\bigotimes_{b \in B} \langle \Omega^{\square} [g(L)] |_b \right) | \Psi_{SN}^{\square \leftrightarrow \square} \rangle, \quad (6.47)$$

and *not* in terms of $\tilde{\Omega}^{\square}$ and $\tilde{\Omega}^{\square}$ since these product states have flipped values for the SET indices, which the unitaries do not act upon. Pictorially, this means that doing F -moves in the following way to go from



leads to physically equivalent partition functions if the product states transform accordingly as well, leaving the strange correlator invariant. Indeed, the unitary acting on the product state mixes the components in just the right way to yield the correct interactions on the bonds. This is also why the factor $\sqrt{2}$ pops up in Eq. (6.42). Since the insertion of $U U^\dagger$ in the strange correlator does not touch the SET loop indices, we can regard the “filled” primal and “empty” dual lattice interpretation of the partition function as unchanged.

6.2.2.4 Strange correlator partition function perspective on duality

Starting from the last remark of the previous section, we can intuit that we will arrive at the dual description when we flip the SET loop labels while leaving alone the

physical indices. Indeed, if $\langle \Omega | \Psi_{\text{SN}} \rangle$ defines an isotropic Ising partition function at inverse temperature β , then we can equally well interpret it as the overlap $\langle \tilde{\Omega} | \Psi_{\text{SN}} \rangle$ at the dual inverse temperature

$$\tilde{\beta} = -\frac{1}{2} \log(\tanh \beta). \tag{6.49}$$

Indeed, after flipping the SET labels, we find that

$$\langle \Omega^{\boxtimes} | Q_A^{\boxtimes} \rangle_{\alpha, \gamma} = 2^{-1/2} \begin{pmatrix} 1 & 1 \\ 1 & -1 \end{pmatrix} \begin{pmatrix} e^{\beta} & 0 \\ 0 & e^{-\beta} \end{pmatrix} \begin{pmatrix} 1 & 1 \\ 1 & -1 \end{pmatrix} \tag{6.50}$$

$$= \sqrt{2} \begin{pmatrix} \cosh(\beta) & \sinh(\beta) \\ \sinh(\beta) & \cosh(\beta) \end{pmatrix} \stackrel{!}{=} \begin{pmatrix} e^{\tilde{\beta}} & e^{-\tilde{\beta}} \\ e^{-\tilde{\beta}} & e^{\tilde{\beta}} \end{pmatrix}, \tag{6.51}$$

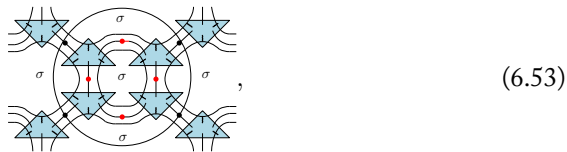
so that from $\sqrt{2} \cosh(\beta) = e^{\tilde{\beta}}$ and $\sqrt{2} \sinh(\beta) = e^{-\tilde{\beta}}$, we find

$$\tanh(\beta) = e^{-2\tilde{\beta}}. \tag{6.52}$$

One can easily check that the dual of the dual again yields the dual, as expected. For more details on the Kramers-Wannier duality in the classical Ising model, see Appendix 6.6.1. Physically, the SET string-net tensors are needed to keep track of a single additional bit of information denoting the “active” lattice.

6.2.2.5 Yet another way to encode the Ising model using SET string-nets

Note that the product state flavors defined above fixed some physical indices to σ and allowed for fluctuating loops to encode the primal and dual lattice. We can however also encode the partition function with all loops fixed to σ and all physical degrees of freedom $1/\psi$ as follows



where the black and red dots mark the $1/\psi$ degrees of freedom. The encircled tensor corresponds to a well-known PEPS representation of the toric code ground state [64],

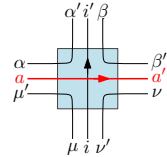
$$\begin{array}{c} l+i \\ \text{---} \\ i+j \end{array} \begin{array}{c} l \\ \text{---} \\ j+k \end{array} \begin{array}{c} k+l \\ \text{---} \\ j+k \end{array} \begin{array}{c} k \\ \text{---} \\ j+k \end{array} = 1 \tag{6.54}$$

where all degrees of freedom are \mathbb{Z}_2 variables and the summation is mod 2. By now acting with a product state spanning a slightly larger region corresponding to the

circle above, we can allocate particular weights to some configurations to arrive at the correct weights for the Ising model partition function expressed in terms of closed loops. Since applying the MPO algebra formalism is however less intuitive in this representation, we will not consider it in detail. Note however that the Ising partition function representation Eq. (6.53) will naturally appear in Sec. 6.4.3 after just a single coarse-graining step on the SC overlap, indicating that it might prove worthwhile to translate all of the findings below into this representation.

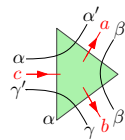
6.2.3 MPO algebra and pulling-through

By representing the classical partition function as a strange correlator, we can immediately make use of the MPO algebra formalism developed in Refs. [82–84] and its extension to the SET case [85] (see also Sec. 3.3.2). To do this, we will need the (left-handed) MPO tensors

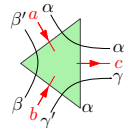


$$= \delta_{\alpha\alpha'}\delta_{\beta\beta'}\delta_{\mu\mu'}\delta_{\nu\nu'}\delta_{ii'}\delta_{aa'}\frac{F_{\beta\alpha\nu}^{a\mu i}}{\sqrt{d_\alpha d_\nu}}, \quad (6.55)$$

where a corresponds to the block label of the MPO. For the Ising case, Eq. (6.55) defines a symmetry MPO for every choice of $a \in \{1, \psi, \sigma\}$. On a periodic chain of L tensors, these MPOs are matrices which form an MPO representation of the input fusion algebra $\text{MPO}_a \text{MPO}_b = \sum_c N_{ab}^c \text{MPO}_c$. To multiply MPOs with open boundary conditions, we require the fusion and splitting tensors



$$= \delta_{\alpha\alpha'}\delta_{\beta\beta'}\delta_{\gamma\gamma'}\frac{(d_a d_b)^{1/4} F_{\alpha\beta}^{ab\gamma}}{(d_c)^{1/4} \sqrt{d_\beta}}, \quad (6.56)$$

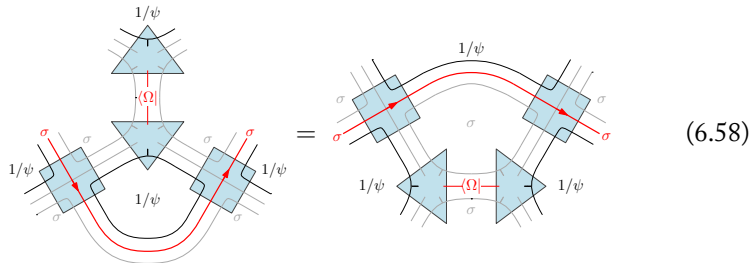


$$= \delta_{\alpha\alpha'}\delta_{\beta\beta'}\delta_{\gamma\gamma'}\frac{(d_a d_b)^{1/4} (F_{\alpha\beta}^{ab\gamma})^*}{(d_c)^{1/4} \sqrt{d_\beta}}, \quad (6.57)$$

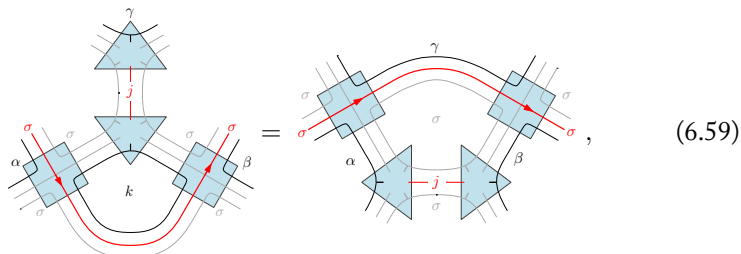
which will also be needed to construct the anyon ansatz later on in Sec. 6.3.

The symmetry-enriched MPOs are identical to those for the usual string-net Eq. (6.55), but they now induce a group action on the virtual loops when they are moved through the lattice [85]. In particular for the SC, a special case of the SET pulling-through equations encodes the action of the duality which maps primal to

dual lattice:



where we have shaded the indices fixed to σ in gray since they are effectively gone for all intents and purposes. We have also colored the indices where the product states acts on in red. Because the Ising model is self-dual at its critical point, we demand that Eq. (6.58) holds componentwise for identical product states $|\Omega(\beta)\rangle$ of the form Eq. (6.37) on the left- and right-hand side, which forces the parameter β to take on its critical value $\beta_c = \log(1 + \sqrt{2})/2$. Indeed, by labeling the indices which survive the projection as



where $\alpha, \beta, \gamma, j, k \in \{1, \psi\}$, we obtain the tensor equation

$$\sum_{jk} (d_\sigma)^{1/2} F_{\sigma\beta j}^{\sigma\sigma\sigma} (d_\sigma)^{1/2} \Omega_j (F_{\sigma k j}^{\sigma\sigma\sigma})^* \frac{F_{k\sigma\sigma}^{\sigma\alpha\sigma}}{(d_\sigma d_\sigma)^{1/2}} F_{\sigma k \beta}^{\sigma\sigma\sigma} \quad (6.60)$$

$$= d_\sigma \sum_j (d_\sigma)^{1/2} F_{\sigma\alpha j}^{\sigma\sigma\sigma} (d_\sigma)^{1/2} \Omega_j (F_{\sigma\beta j}^{\sigma\sigma\sigma})^* \frac{F_{\gamma\sigma\sigma}^{\sigma\alpha\sigma}}{(d_\sigma d_\sigma)^{1/2}} F_{\sigma k \beta}^{\sigma\sigma\sigma}, \quad (6.61)$$

where we have used the definitions for the string-net tensors Eq. (6.12) and the MPO tensors Eq. (6.55) and the fact that $d_a = 1$ for $a \in \{1, \psi\}$. The additional factor d_σ on the right-hand side appears because there is a closed σ -loop on the right-hand side of Eq. (6.58). Making use of the explicit Ising F -symbols Eq. (6.11), we find, for example, that the $(\alpha, \beta, \gamma) = (1, 1, 1)$ has to satisfy

$$\Omega_1 \left(\frac{1}{\sqrt{2}} + \frac{1}{\sqrt{2}} \right) + \Omega_\psi \left(\frac{1}{\sqrt{2}} - \frac{1}{\sqrt{2}} \right) = \sqrt{2} \left(\frac{\Omega_1}{\sqrt{2}} + \frac{\Omega_\psi}{\sqrt{2}} \right) \quad (6.62)$$

or

$$\sqrt{2}\Omega_1 = \Omega_1 + \Omega_\psi, \quad (6.63)$$

which, for the product state ansatz $|\Omega(\beta)\rangle$ of Eq. (6.42), leads to $\beta = \log(1 + \sqrt{2})/2$.

The critical temperature of the Ising model thus follows immediately from requiring that the SET pulling-through equations hold for the SC with identical product states on both sides of the duality. Away from the critical point, a product state corresponding to the dual inverse temperature $\tilde{\beta} = -\log(\tanh \beta)/2$ is required instead (see Sec. 6.2.2.4). Physically, the SET string-net tensors are needed to keep track of a single additional bit of information which signifies whether the spins $1/\psi$ live on the primal or dual lattice.

6.2.4 Extension to other minimal models

Given the results by Petkova and Zuber on generalized twisted CFT partition functions for RSOS models (see Sec. 6.1), we expect that we should at least be able to implement the SC construction for all RSOS models. On the CFT side, this corresponds to the minimal models, since the scaling limit of the critical RSOS models realizes the simplest rational CFTs, i.e. the minimal models discussed in Sec. 2.8.3 [180].

However, finding the right input unitary fusion category that leads to the correct topological sectors requires *a priori* knowledge of what MPO symmetries to consider, which is related to the problem of recognizing MPO symmetries in variationally optimized PEPS. Put differently, we can really never do more than find topological sectors for fields in the CFT since it seems to already require full knowledge of the relevant CFT to decide which MPOs one should use to have the topological sectors match the primaries. Through the strange correlator construction, our partition function representation contains the full data of the emergent CFT and hence the properties of the tube algebra we will discuss in 6.3.3, so that the topological spins and scaling dimensions are built-in and have to exactly match those of the resulting CFT.

To illustrate this, let us give an example of an extension leading to the classical partition function of the 3-state Potts model. The \mathbb{Z}_3 Tambara-Yamagami category [83] consists of two sectors $\mathcal{C}_0 \oplus \mathcal{C}_1$, where the trivial sector contains three labels $\mathcal{C}_0 = \{1, \psi, \epsilon\}$ of a \mathbb{Z}_3 anyon theory with fusion rules $N_{ab}^c = \delta_{a+b=c \pmod 3}$ and trivial F -symbols. The nontrivial sector contains a single defect $\mathcal{C}_1 = \{\sigma\}$, so that the fusion look like a slight generalization of the Ising case,

$$\sigma \times a = a \times \sigma = \sigma, \quad \sigma \times \sigma = \sum_{a \in \mathcal{C}_0} a, \quad (6.64)$$

with nontrivial F -symbols

$$[F_\sigma^{a\sigma b}]_\sigma = [F_b^{\sigma a \sigma}]_\sigma = \chi(a, b), \quad [F_\sigma^{\sigma\sigma\sigma}]_a = \frac{\kappa_\sigma}{\sqrt{3}} \chi(a, b)^* \quad (6.65)$$

where $\chi(a, b) = e^{2\pi i ab/3}$ and $\varkappa_\sigma = \pm 1$. The anyons in \mathcal{C}_0 have quantum dimension 1 and $d_\sigma = \sqrt{3}$. Taking this data as the input category and constructing an appropriate product state $|\Omega\rangle$, which is a slight generalization of the one for Ising, we immediately find a SC representation of the 3-state Potts model partition function. From the pulling-through equation Eq. (6.58), the critical temperature now follows from $\sqrt{3}\Omega_1 = \Omega_1 + \Omega_\psi + \Omega_\epsilon$. This critical SC will only contain a subset of the primaries of the unitary minimal model $m = 5$ with central charge $c = 4/5$. We have not yet checked whether this subset matches⁷ the one expected for the 3-state Potts model [13].

6.3 Exact diagonalization and topological sectors

6.3.1 Motivation

In this section we will demonstrate how to numerically identify all topological sectors in the CFT spectra associated to Ising partition functions with twisted boundary conditions. Since the SC construction exposes and enforces the topological symmetries of the scaling limit of the classical partition function already at the ultraviolet level, we should be able to go beyond the \mathbb{Z}_2 labeled twisted CFT spectra obtained for the Ising model in Ref. [157] (see Sec. 6.1).

We can introduce anti-periodic boundary conditions on the cylinder by inserting a horizontal ψ -twist which effectively flips spins across the defect line. Inserting a σ -twist implements twisted boundary conditions corresponding to the Kramers-Wannier duality and maps primal to dual lattice. Along the periodic direction of the cylinder, we can identify the dual lattice again with its self-dual primal by removing half a row of transfer matrices (see the M_1 , M_ψ , and M_σ in the top row of Fig. 6.2). All of these twists are immediately given by their respective MPO representations

$$\text{MPO}_1 = \begin{array}{c} \begin{array}{ccccccc} & \sigma & & \sigma & & \sigma & \\ \sigma & \downarrow & & \downarrow & & \downarrow & \\ \psi & \rightarrow & \rightarrow & \rightarrow & \rightarrow & \rightarrow & \\ \sigma & \uparrow & & \uparrow & & \uparrow & \\ & 1/\psi & & 1/\psi & & 1/\psi & \end{array} \end{array} \quad (6.66)$$

$$\text{MPO}_\psi = \begin{array}{c} \begin{array}{ccccccc} & \sigma & & \sigma & & \sigma & \\ \sigma & \downarrow & & \downarrow & & \downarrow & \\ \psi & \rightarrow & \rightarrow & \rightarrow & \rightarrow & \rightarrow & \\ \sigma & \uparrow & & \uparrow & & \uparrow & \\ & 1/\psi & & \psi/1 & & 1/\psi & \\ & & & & & & \psi/1 \end{array} \end{array} \quad (6.67)$$

$$\text{MPO}_\sigma = \begin{array}{c} \begin{array}{ccccccc} & \sigma & & \sigma & & \sigma & \\ 1/\psi & \downarrow & & \downarrow & & \downarrow & \\ \sigma & \rightarrow & \rightarrow & \rightarrow & \rightarrow & \rightarrow & \\ & \uparrow & & \uparrow & & \uparrow & \\ & 1/\psi & & 1/\psi & & 1/\psi & \\ & & & & & & \sigma \end{array} \end{array} \quad (6.68)$$

⁷The CFT describing the 3-state Potts model is actually not the bare $m = 5$ minimal model, but a related model whose modular invariant partition function involves only a subset of the $m = 5$ primary fields with different multiplicities. These multiplicities indicate that the 3-state Potts model is not just a subtheory of the $m = 5$ minimal model, as it contains copies of some of its fields. Similarly, the 3-state Potts fusion rules are not just a subset of those of the $m = 5$ minimal model [13].

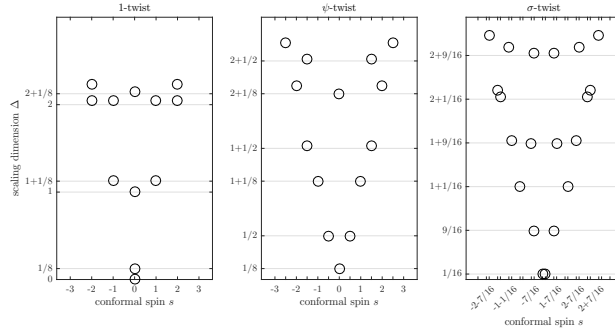


FIGURE 6.1: Finite-size CFT spectra (scaling dimension Δ versus conformal spin s) of twisted Ising partition functions on a cylinder ($L_y = 11$).

which are special cases of the more general MPOs presented in Eq. (6.55). Exact diagonalization of the SC partition function on a cylinder with an additional horizontal insertion of MPO_1 , MPO_ψ , or MPO_σ then leads to the twisted spectra shown in Fig. 6.1, from which one can identify the field content of three modular invariant partition functions built from the holomorphic primary fields of the Ising CFT.

But there are more than three modular invariant partition functions for the Ising model (or more than six if one considers the \mathbb{Z}_2 parity labeling of Ref. [157] as genuine topological sectors). As shown analytically in Ref. [50], modular transformations can be implemented exactly on the lattice without invoking the continuum by considering well-defined operations on the lattice partition function. Doing so leads to ten different possible modular invariant partition functions for the Ising model related to nine independent topological defect configurations on the torus⁸. As mentioned in Sec. 6.1, our SC construction leads to a very similar picture reformulated in terms of MPO algebras, but introduces numerics into the picture.

6.3.2 Topological corrections to the conformal spin

Let us first of all extend the results of Sec. 5.8.6.1 on extracting conformal data from the linear transfer matrix to include conformal spin. More generally, to derive the scaling dimensions and conformal spins from exact diagonalization, we write the CFT partition function result Eq. (2.153) in terms of the eigenvalues of the Virasoro operators,

$$Z = \text{Tr} e^{-\text{Im}(\tau)H + i\text{Re}(\tau)P} \quad (6.69)$$

$$\sum_{\alpha} e^{-2\pi\text{Im}(\tau)(h_{\alpha} + \bar{h}_{\alpha} - \frac{c}{12}) + 2\pi i\text{Re}(\tau)(h_{\alpha} - \bar{h}_{\alpha})}, \quad (6.70)$$

$$= \sum_{\alpha} e^{-2\pi\text{Im}(\tau)(\Delta_{\alpha} - \frac{c}{12}) + 2\pi i\text{Re}(\tau)(s_{\alpha})}, \quad (6.71)$$

⁸This ambiguity is due to the anyon Eq. (6.85) which appears in two different partition functions.

where Δ_α and s_α denote the scaling dimension and the conformal spin. Dropping all subleading, non-universal, finite-size terms, we can apply this formula to the tensor network representation

$$Z = \text{Tr}(M^{L_x}) \tag{6.72}$$

of a critical classical partition function on an $L_x \times L_y$ torus, where M denotes the column-to-column transfer matrix [112, 157]. Let us assume periodic boundary conditions and translation invariance. If the transfer matrix M commutes the translation operator

$$T = e^{\frac{2\pi i}{L_y} P}, \tag{6.73}$$

which shifts the lattice over one site, then the eigenvalues $e^{\frac{2\pi i}{L_y} p_\alpha}$ of T provide a good momentum quantum number p_α . Since $P = L_0 - \bar{L}_0$, this momentum corresponds to the conformal spin $s_\alpha = h_\alpha - \bar{h}_\alpha$. A shortcut to obtain both scaling dimensions and conformal spins at the same time is given by diagonalizing the product $T \cdot M$ instead, corresponding to a torus with modular parameter

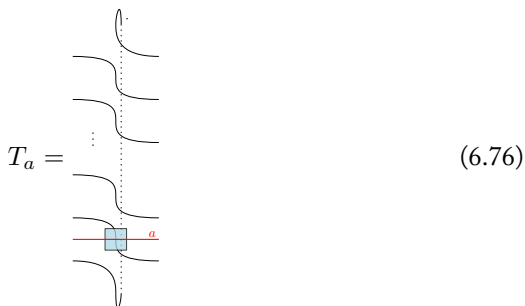
$$\tau = 1/L_y + i/L_y. \tag{6.74}$$

Indeed, the universal content of the product of the eigenvalues of T and M is then

$$\lambda_\alpha = e^{-\frac{2\pi}{L_y}(\Delta_\alpha - \frac{c}{12}) + \frac{2\pi i}{L_y} s_\alpha}, \tag{6.75}$$

where the modulus coincides with Eq. (5.26) derived previously and the phase yields the conformal spin.

The above derivation assumed periodic boundary conditions, which corresponds to the case of no horizontal defects or, equivalently, identity defects. We then have that $(T_1)^{L_y} = \mathbb{1}$ so that the momenta, which are the eigenvalues of P_1 , have to be integers. For a horizontal ψ -twist, this is no longer the case. The topological obstruction of the defect line implies the existence of a corresponding *twisted* translation operator T_a on the cylinder [181],



$$T_a = \tag{6.76}$$

which is obtained by demanding that the horizontal defect line stays put under vertical translation. The crossing of lines introduces an MPO tensor with non-trivial

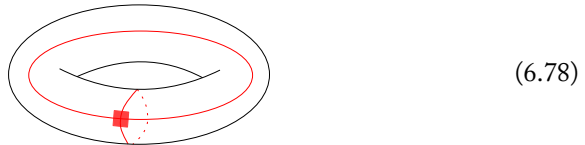
consequences for the momenta. The process of inserting the Dehn twist operator $D_\psi \equiv (T_\psi)^{L_y}$ into the partition function on a torus boils down to cutting the torus into a cylinder, fully twisting one end of the cylinder, and gluing the pieces back together. Doing this can have non-trivial effects when a horizontal defect is present. One non-trivial consequence is that the length L for which $(T_\psi)^L = \mathbb{1}_\psi$, where $\mathbb{1}_\psi$ denotes the identity on the appropriate subspace, is actually $2L_y$ for anti-periodic boundary conditions, so that the momenta, and hence the conformal spins, are given by half-integers modulo an integer. This is the origin of the topological correction to the conformal spin. The case of the duality defect MPO_σ is slightly more involved, but the action of the Dehn twist D_σ is similar in that it also adds a vertical MPO_σ to the torus. One can show that [50, 182]

$$(T_\sigma)^{2L_y-1} = D_\sigma^2, \quad (6.77)$$

which implies that the effective length L of the system with σ -twisted boundary conditions is given by $L = L_y - 1/2$. Indeed, at the level of the eigenvalues, we have that if $e^{2\pi i p_\sigma / (L_y - 1/2)}$ is an eigenvalue of the twisted translation operator T_σ , then $e^{4\pi i p_\sigma}$ is an eigenvalue of D_σ^2 . Since $D_\sigma^{16} = \mathbb{1}_\sigma$, where $\mathbb{1}_\sigma$ again denotes the identity on the appropriate subspace, the momenta are restricted to $p_\sigma = \pm 1/16, \pm 7/16$ up to an integer.

6.3.3 Ocneanu's tube algebra and the anyon ansatz

Before discussing the exact diagonalization results for the twisted Ising partition functions, let us give a short summary of the additional pieces of MPO algebra knowledge we need to go from having a single defect line to two crossing defect lines on the torus. It is intuitively clear that something interesting has to happen when two non-contractible defect lines meet,



For our pedestrian purposes, it is enough to know that the objects at the intersection are called irreducible central idempotents and that they project onto the topological sectors obtained from block diagonalizing Ocneanu's tube algebra. The irreducible central idempotents of this tube algebra correspond to Hermitian projectors onto each irreducible block. From the projectors onto these blocks (which are identified with the topological sectors), the topological data of the emergent anyonic excitations can be extracted. For details on how Ocneanu's tube algebra can be naturally derived from the MPO symmetry algebra, we refer to Refs. [84, 156]. Technically, these idempotents realize the topological superselection sectors of the emergent anyon theory, or modular tensor category, which is the Drinfeld center $\mathcal{Z}(\mathcal{C})$ of the unitary fusion category \mathcal{C} we started from in Sec. 6.2.1 [156].

To construct the anyon ansatz for string-nets, we first define a basis of tubes

\mathcal{T}_{ppp}^s which are built from the fusing and splitting tensors Eq. (6.56) and Eq. (6.57),

$$\mathcal{T}_{ppp}^s = \text{Diagram} \quad (6.79)$$

where one has to imagine this object to be connected to a closed string of MPO_s tensors going vertically around on the cylinder. The irreducible central idempotents are then expressed as linear combinations of these tube basis elements,

$$P_i = \frac{1}{\mathcal{D}^2} \sum_{pq s} t_i^{pq s} \text{Diagram} \quad (6.80)$$

where $\mathcal{D} = (\sum_{a \in \mathcal{C}} d_a^2)^{1/2}$ is the total quantum dimension and $t_i^{pq s}$ are coefficients. For the Ising case, these projectors (anyons) are given explicitly by

$$P_0 = \mathcal{T}_{111}^1 + \mathcal{T}_{1\psi 1}^\psi + \sqrt{2} \mathcal{T}_{1\sigma 1}^\sigma \quad (6.81)$$

$$P_{\psi\bar{\psi}} = \mathcal{T}_{111}^1 + \mathcal{T}_{1\psi 1}^\psi - \sqrt{2} \mathcal{T}_{1\sigma 1}^\sigma \quad (6.82)$$

$$P_\psi = \mathcal{T}_{\psi\psi\psi}^1 - \mathcal{T}_{\psi 1\psi}^\psi - i\sqrt{2} \mathcal{T}_{\psi\sigma\psi}^\sigma \quad (6.83)$$

$$P_{\bar{\psi}} = \mathcal{T}_{\psi\psi\psi}^1 - \mathcal{T}_{\psi 1\psi}^\psi + i\sqrt{2} \mathcal{T}_{\psi\sigma\psi}^\sigma \quad (6.84)$$

$$P_{\sigma\bar{\sigma}} = 2\mathcal{T}_{111}^1 - 2\mathcal{T}_{1\psi 1}^\psi + 2\mathcal{T}_{\psi\psi\psi}^1 + 2\mathcal{T}_{\psi 1\psi}^\psi \quad (6.85)$$

$$P_\sigma = \mathcal{T}_{\sigma\sigma\sigma}^1 - i\mathcal{T}_{\sigma\sigma\sigma}^\psi + e^{-\frac{i\pi}{8}} \mathcal{T}_{\sigma 1\sigma}^\sigma + e^{\frac{i3\pi}{8}} \mathcal{T}_{\sigma\psi\sigma}^\sigma \quad (6.86)$$

$$P_{\sigma\bar{\psi}} = \mathcal{T}_{\sigma\sigma\sigma}^1 - i\mathcal{T}_{\sigma\sigma\sigma}^\psi + e^{\frac{i7\pi}{8}} \mathcal{T}_{\sigma 1\sigma}^\sigma + e^{-\frac{i5\pi}{8}} \mathcal{T}_{\sigma\psi\sigma}^\sigma \quad (6.87)$$

$$P_{\bar{\sigma}} = \mathcal{T}_{\sigma\sigma\sigma}^1 + i\mathcal{T}_{\sigma\sigma\sigma}^\psi + e^{\frac{i\pi}{8}} \mathcal{T}_{\sigma 1\sigma}^\sigma + e^{-\frac{3\pi i}{8}} \mathcal{T}_{\sigma\psi\sigma}^\sigma \quad (6.88)$$

$$P_{\psi\bar{\sigma}} = \mathcal{T}_{\sigma\sigma\sigma}^1 + i\mathcal{T}_{\sigma\sigma\sigma}^\psi + e^{-\frac{i7\pi}{8}} \mathcal{T}_{\sigma 1\sigma}^\sigma + e^{\frac{i5\pi}{8}} \mathcal{T}_{\sigma\psi\sigma}^\sigma, \quad (6.89)$$

where we have left out the division by the overall normalization factor $\mathcal{D}^2 = 4$ in every projector. In Table 6.1, the Ising anyons are listed together with their corresponding topological spins h_i , which can be obtained in the MPO algebra framework from the eigenvalue $e^{2\pi i h_i}$ of a 2π -rotation (Dehn twist) of the irreducible central idempotent P_i corresponding to the anyon of type i [84].

6.3.4 Topological sectors of the Ising model

We are now in a position to study the topological sectors of the Ising model directly on the lattice through the SC construction using exact diagonalization. If we want to make use of the anyon ansatz, we better make sure our duality MPO_σ acts as a symmetry. One way of achieving this is by going back to the topological string-net. We have tried many other approaches, but there seems to be no way around

Table 6.1: Anyon table for the doubled Ising model with exact topological spins and notations used in respectively [156] and [84].

Anyon [156]	Anyon [84]	topological spin
0	$(1, 1)$	0
$\psi\bar{\psi}$	$(\psi, \bar{\psi})$	0
ψ	$(1, \psi)$	$-1/2$
$\bar{\psi}$	$(\psi, 1)$	$1/2$
$\sigma\bar{\sigma}$	$(\sigma, \bar{\sigma})$	0
σ	$(1, \bar{\sigma})$	$-1/16$
$\sigma\bar{\psi}$	$(\psi, \bar{\sigma})$	$7/16$
$\bar{\sigma}$	$(\sigma, 1)$	$1/16$
$\psi\bar{\sigma}$	$(\sigma, \bar{\psi})$	$-7/16$

introducing both primal and dual lattice if the tube algebra of Sec. 6.3.3 is to survive. In a way, introducing both lattices is inevitable since the anyons Eqs. (6.81)-(6.89) contain tubes with a vertical MPO_σ , which are exactly those which mix primal and dual lattices, i.e. some emergent anyons are inextricably made up of primal and dual objects, or, in terms of the classical Ising interpretation, of spin operators and disorder operators [51]. We found that trying to correct the MPO symmetries by including a half-shift to glue the primal and dual lattice together again on both sides of a vertical duality MPO_σ manifestly breaks the projector properties of the central idempotents. In short, there does not seem to be an obvious way to restore the tube algebra in the presence of additional half-shifts.

Having identified the product state which tunes the SC to criticality for the SET case, we apply the same product state to act on the purely topological string-net where the MPO_σ duality defect may again be freely moved around on the virtual level. From the point of view of the classical partition function, going back to the purely topological case amounts to restoring the superposition between primal and dual lattices. In doing so, we lift the action of the duality MPO_σ to a virtual symmetry which interchanges two shifted copies of the self-dual Ising partition function, which now corresponds to the direct sum of primal and dual lattices Eq. (6.90). By removing the parts of the product state Eq. (6.37) which fix the SET indices, the unit cell tensor making up a single column M of the transfer matrix T now has a block diagonal structure corresponding to the subset of the topological Ising string-net allowed by the fusion rules after fixing indices,

$$\begin{array}{c} \text{Diagram 1} \end{array} = \begin{array}{c} \text{Diagram 2} \end{array} \oplus \begin{array}{c} \text{Diagram 3} \end{array} \quad (6.90)$$

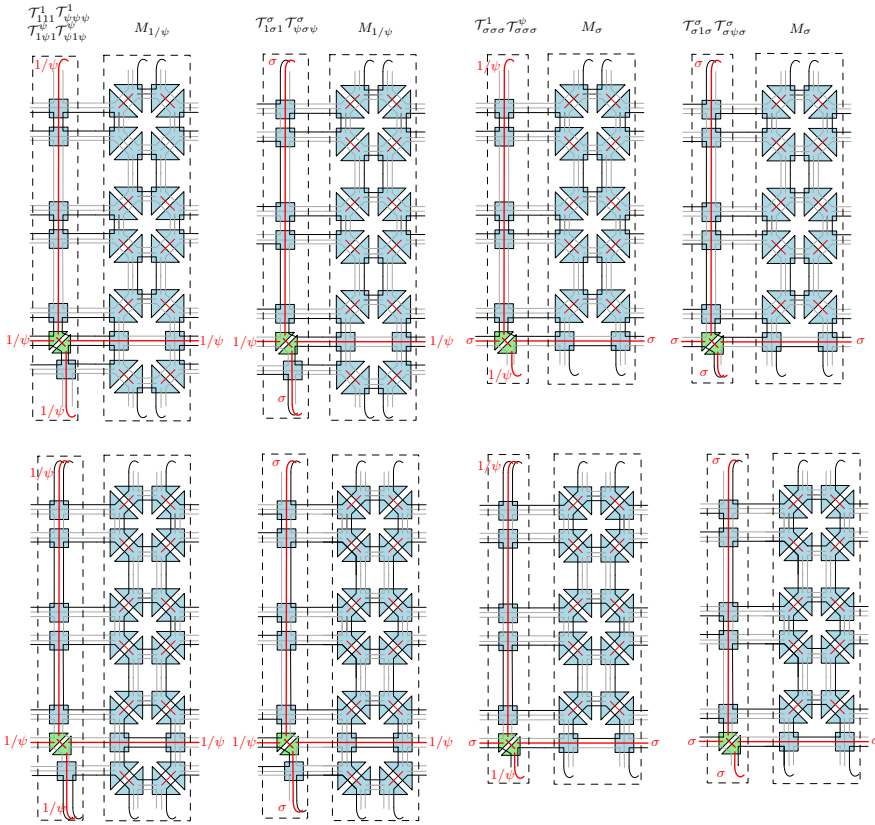


FIGURE 6.2: Tensor network diagrams for the action of the ten tubes Eq. (6.79) appearing in Eqs. (6.81)-(6.89) on a cylinder of three sites, where the top and bottom row respectively denote all possibilities on the primal and dual lattice. The central idempotents are then constructed by taking linear combinations of the tubes via Eqs. (6.81)-(6.89).

where the left-hand side should be diagrammatically interpreted⁹ as a collapse of the primal and dual parts on the right-hand side, reflecting the superposition, and where the product state acts on the red indices. The block decomposition of Eq. (6.90) carries over to all other objects required to do exact diagonalization on a cylinder. In particular, the MPOs Eq. (6.66) and Eq. (6.67) are now block-diagonal, acting independently on the primal and dual lattice, while the duality MPO Eq. (6.68) is block-off-diagonal and connects the primal and dual lattice as a symmetry. In this way, one can (numerically) check that the tube algebra, which leads to the central idempotents, is preserved and that all projectors commute with the transfer matrix. Similarly, the twisted translation operators are block-off-diagonal, since the natural translation on the string-net Eq. (6.90) is a half-shift (a shift by half a lattice spacing)

⁹As it is pictured, the configuration on the left-hand side of course looks like it is not allowed by the fusion rules.

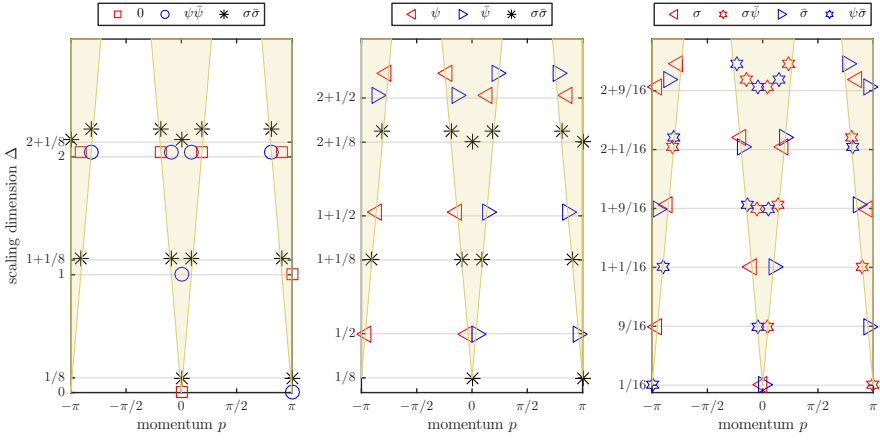


FIGURE 6.3: Topological sector labeling of finite-size CFT spectra (scaling dimension Δ versus momentum p) of twisted partition functions on a cylinder ($L_y = 11$). From left to right: the 1-twist, ψ -twist, and σ -twist spectra.

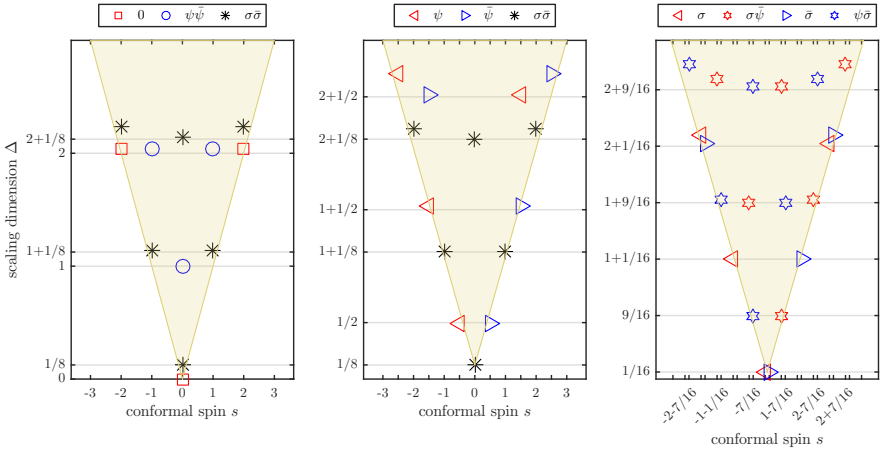


FIGURE 6.4: Central branch of Fig. 6.3. Topological sector labeling of finite-size CFT spectra (scaling dimension Δ versus conformal spin s) of twisted partition functions on a cylinder ($L_y = 11$). From left to right: the 1-twist, ψ -twist, and σ -twist spectra.

going from primal to dual lattice or vice versa, and can be shown to commute with both the transfer matrix and the central idempotents.

Let us now turn to the actual numerics. Using a Lanczos algorithm, we diagonalize the product of the twisted translation operator T_a (see Eq. (6.76)) together with the twisted transfer matrix M_a , where $a \in \{1, \psi, \sigma\}$ denotes the horizontal defect line (see Sec. 6.3.2). Additionally, we act with one of the compatible anyon projectors P_i listed in Eqs. (6.81)–(6.89) to project $T_a \cdot M_a$ onto a definite topological sector i . The relevant tensor network diagrams for implementing the action of the tubes on

the transfer matrix are shown in Fig. 6.2, where the top and bottom row respectively collect all possibilities on the primal lattice and dual lattice. Note that one has to be aware of the closed loop convention when multiplying these matrices on the cylinder by carefully inserting the correct quantum dimensions to account for the popping of closed σ -loops. For clarity, let us emphasize that we implicitly assume that the vertical and horizontal MPOs, and thus all tubes in the anyon projector, match the a -twisted partition function M_a so that all contractions are compatible on the cylinder.

The labeled twisted CFT spectra are shown in Fig. 6.3. In terms of Table 6.1, the trivially twisted transfer matrix M_1 then contains 0, $\psi\bar{\psi}$, and part of $\sigma\bar{\sigma}$, while M_ψ contains ψ , $\bar{\psi}$, and a different part of $\sigma\bar{\sigma}$. The σ -twisted transfer matrix M_σ can be broken up in σ , $\sigma\bar{\psi}$, $\bar{\sigma}$, and $\psi\bar{\sigma}$ contributions. Due to the superposition of the primal and dual lattice, the eigenvalues of the transfer matrix have an additional degeneracy, which is the origin of the spurious fields appearing around momentum $p = \pm\pi$. The labeling of these spurious fields is completely compatible with the presence of an additional $\psi\bar{\psi}$ vacuum at momentum $p = \pm\pi$. Indeed, $\psi\bar{\psi}$ appears with scaling dimension $\Delta = 0$ in the 1-twist partition function spectrum. Drawing light cones of the ground state in each twisted sector makes it clear that these unwanted, mirrored copies do not hinder the identification of the topological sectors of the branch around momentum $p = 0$. In Fig. 6.4, we plot this central branch and relate¹⁰ momentum to the conformal spin, which receives topological corrections for the ψ - and σ -twist (see Sec. 6.3.2).

6.4 Coarse-graining strange correlators

Having established the strange correlator, its properties, and its usefulness in characterizing the topological sectors appearing in CFT spectra, let us now discuss its real-space renormalization properties. Since we have decomposed the classical partition function into the overlap of two wave functions (with one of them being a product state), we can try to reinterpret the renormalization procedures on the partition function of Sec. 3.5 and Chapter 5 at the level of quantum states instead. This approach is particularly appealing since string-nets are known to be exact zero correlation length RG fixed point wave functions of a particular RG transformation.

6.4.1 Exact string-net renormalization

By construction, string-net wave functions are gapped, fixed point wave functions with zero correlation length. As demonstrated by König, Reichardt, and Vidal in Ref. [183], it is possible to construct a real-space RG transformation which maps ground-state fixed point string-net wave functions onto themselves. Essentially, the procedure yields a sequence of F -moves, which can be interpreted as an exact quantum circuit, made up of local disentanglers and isometries, preserving the

¹⁰Since a twisted half-shift translation operator was used, the conformal spins are respectively related to the momenta p via $s_{1,i} = 2L_y p_{1,i}/(2\pi)$, $s_{\psi,i} = 2L_y p_{\psi,i}/(2\pi)$, and $s_{\sigma,i} = 2(L_y - 1/2)p_{\sigma,i}/(2\pi)$.

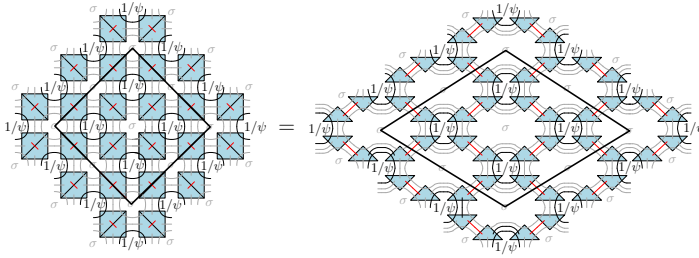


FIGURE 6.5: A patch of the lattice defined by the SC obtained from Eq. (6.38).

topological degrees of freedom. In this way, we can interpret the circuit as an exact MERA representation of the wave function since every coarse-graining step locally eliminates part of the ground-state entanglement.

The coarse-graining transformation is defined in two steps. First, we reshape the lattice using F -moves. Since our basic building blocks Eq. (6.16) and Eq. (6.22) are defined in terms of two F -symbols (triangles), we need to make use of the pentagon equation to relate the local configurations before and after reshaping. Secondly, we eliminate physical degrees of freedom by disentangling them exactly to obtain tadpoles connected to the rest of the network by a vacuum line. The loop states $\sum_a d_a |a\rangle$ can then be safely projected out, reducing the number of physical degrees of freedom. Taken together, these two steps constitute the (exact) coarse-graining transformation on the string-net wave function.

Let us now give a pictorial derivation for our square lattice structure. We refer the reader to Appendix 6.6.2 for explicit derivations of the expressions for the unitary and isometric gates, which are needed to do actual numerics. Note that all gates of the quantum circuit are defined completely in terms of F -symbols and act solely on the physical degrees of freedom. For clarity, let us first revisit the SC obtained from Eq. (6.38) where the spins $1/\psi$ live on the primal lattice defined by the virtual loops inside the squares, and the σ loops label the empty, dual lattice inside the octagons (see Fig. 6.5). Aficionados of the tensor network renormalization methods introduced in Sec. 3.5 and Chapter 5 might want to keep track of the black bounding box, which tracks a block of four Ising spins in the SC representation of the partition function. Let us now drop all loop labels since we only consider the string-net wave function and focus on a patch of the lattice containing the black bounding box and its immediate neighborhood. To implement the first step of the coarse-graining process, we act with unitary gates on the pairs of F -symbols inside the black ellipses,

(6.91)

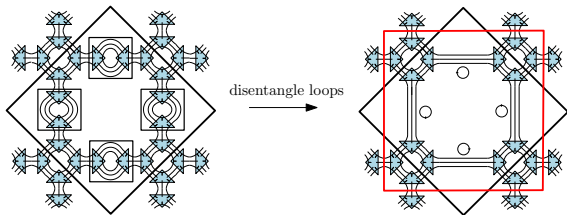
The relevant unitary gates are given by

$$\alpha \begin{array}{c} i' \beta j' \\ \swarrow \quad \searrow \\ \delta \\ \swarrow \quad \searrow \\ i' \gamma k' \end{array} = \delta_{i'i} \delta_{j'j} \delta_{k'k} \delta_{l'l} \sum_n F_{jnn'}^{kli} \begin{array}{c} i \beta j \\ \swarrow \quad \searrow \\ \alpha \\ \swarrow \quad \searrow \\ l \delta k \end{array}, \quad (6.92)$$

$$\alpha \begin{array}{c} i' \beta j' \\ \swarrow \quad \searrow \\ \delta \\ \swarrow \quad \searrow \\ i' \gamma k' \end{array} = \delta_{i'i} \delta_{j'j} \delta_{k'k} \delta_{l'l} \sum_n F_{knn'}^{lij} \begin{array}{c} i \beta j \\ \swarrow \quad \searrow \\ \alpha \\ \swarrow \quad \searrow \\ l \delta k \end{array}, \quad (6.93)$$

$$\alpha \begin{array}{c} i' \beta j' \\ \swarrow \quad \searrow \\ \delta \\ \swarrow \quad \searrow \\ i' \gamma k' \end{array} = \delta_{i'i} \delta_{j'j} \delta_{k'k} \delta_{l'l} \sum_n F_{knn'}^{lij} \begin{array}{c} i \beta j \\ \swarrow \quad \searrow \\ \alpha \\ \swarrow \quad \searrow \\ l \delta k \end{array}. \quad (6.94)$$

Next, we act with a different unitary operator on the degrees of freedom inside the black squares below to get rid of physical degrees of freedom,



$$(6.95)$$

with the gate given by

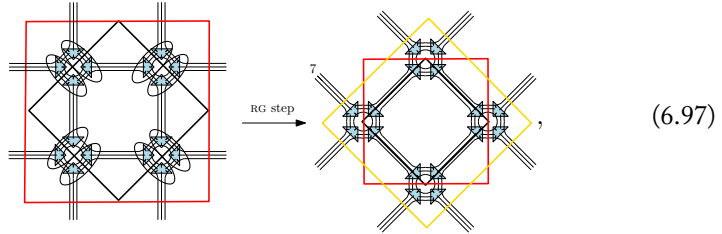
$$\begin{array}{c} \gamma \\ \alpha \\ \gamma \\ \alpha \end{array} \begin{array}{c} \equiv \\ \equiv \\ \equiv \\ \equiv \end{array} \begin{array}{c} \gamma \\ \alpha \\ \gamma \\ \alpha \end{array} = d_i \delta_{k'k} N_{\alpha k}^\gamma = \sum_j F_{kj0}^{k'ii} \left(\begin{array}{c} j \\ \gamma \\ \swarrow \quad \searrow \\ \alpha \\ \swarrow \quad \searrow \\ k' \beta k \end{array} \right). \quad (6.96)$$

By explicitly projecting j onto the vacuum and i onto the loop state $\sum_a d_a |a\rangle$ and identifying the degrees of freedom k' and k , we can interpret the unitary as an isometry. No information is lost because we know the exact states we have projected onto: the whole procedure in terms of its quantum circuit is an example of an *exact* unitary circuit.

After this single RG step, we end up with a string-net defined on a coarser lattice¹¹. Iterating the coarse-graining procedure again will lead us back to the original lattice orientation and will have reduced the number of Ising spins by a

¹¹As we will see later on, we can relate the coarse-grained string-net back to the partition function by identifying the tensors inside the red bounding box in Eq. (6.95) with a block of four coarse-grained partition function tensors defined on half the number of Ising spins. Note the obvious similarity of the string-net coarse-graining with TRG as described in Fig. 3.5.

factor of four. Indeed, one more RG transformation yields



where the gold box represents the four coarse-grained partition function tensors defined on the effective lattice obtained after two (T)RG steps.

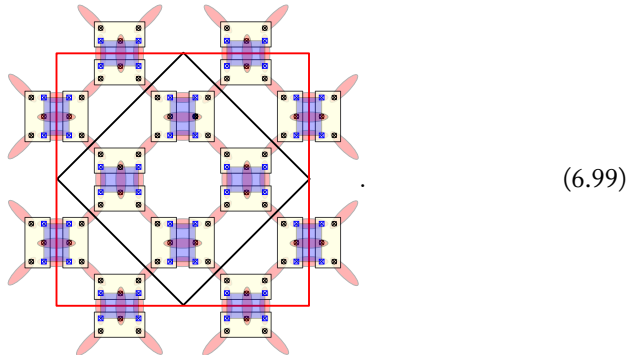
6.4.2 Coarse-graining map as a PEPO

The RG map acting on the physical indices can be written as a *projected entangled pair operator* (PEPO), the higher-dimensional generalization of a matrix product operator (MPO). To see this, let us introduce a double-GHZ tensor which takes two inputs and forces them to be equal to each other (i.e. identifies two indices):

The reason for introducing this trivial tensor is that it allows us to represent the coarse-graining PEPO using doubled physical indices, similar in spirit to the PEPS representation of the string-net ground state tensors Eq. (6.12) where physical indices are also doubled and identified across tensors. Otherwise, we would have to resort to an awkward stacking of the quantum circuit since the gates overlap, with more than one gate acting on a single physical degree of freedom.

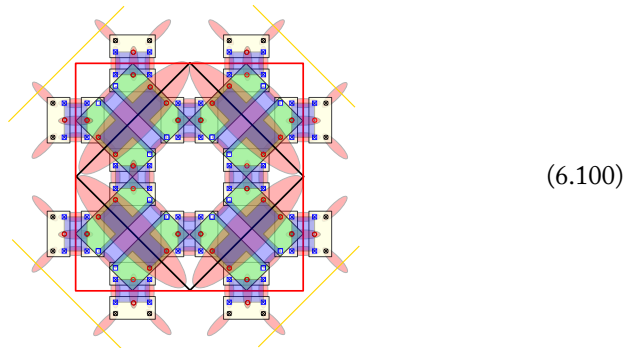
Let us now construct the PEPO representation of the first coarse-graining layer Eq. (6.97). In the top-view below, the yellow rectangles are understood to denote the appropriate disentangling gates Eqs. (6.92), (6.93), and (6.94), and the transparent blue rectangles denotes the disentangling gate Eq. (6.96) prior to the isometry. The output indices colored in blue correspond to the j and i indices in Eq. (6.96) which are either summed over or projected out onto a closed loop state, while the two central output degrees of freedom inside the central ellipses are identified using

Eq. (6.98) tensors.



This configuration of gates implements the F -moves which go from the left-hand side of Eq. (6.91) to the right-hand side of Eq. (6.95). To guide the eye, we have added black and red bounding boxes matching those of the figures in the previous section.

Grouping the tensors in squares, the bond dimension of the PEPO is equal to the number of labels in the string-net (i.e. $D = 3$ for the Ising model $\{1, \psi, \sigma\}$) because we cut along the double-GHZ tensors Eq. (6.98). By adding another iteration on top, we return to the initial orientation of the lattice,



Note that we have left all indices explicit using double-GHZ tensors Eq. (6.98), many of them are actually identified. The output indices after two layers are the indices denoted with red circles, which are again identified. The output of the first layer is also left explicitly so that one actually has to imagine the insertion of additional GHZs inbetween the first and second layer so that the indices “fit” the gates, which is of course a completely trivial operation.

Looking ahead, we can already appreciate that the way in which the layers of the string-net coarse-graining PEPO overlap and stack very much resembles tensor network renormalization methods. Indeed, focusing on the black, red, and gold bounding boxes already reveals that if we apply the conjugate of this coarse-graining PEPO to a PEPS, the action of the gates on the physical level will block physical

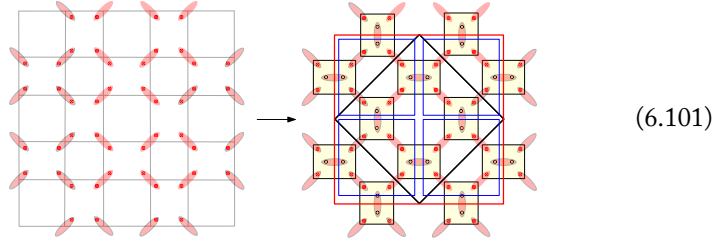
indices so that we will have to truncate the virtual level accordingly if we want to preserve the PEPS representation of the wave function.

6.4.3 Real-space RG and SC renormalization

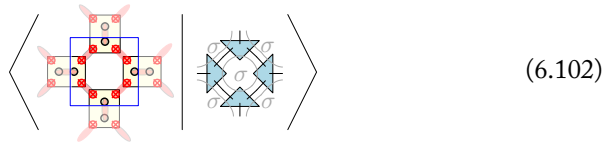
Inserting the coarse-graining PEPO Eq. (6.99) and its conjugate inbetween the SC overlap $\langle \Omega | \Psi_{\text{SN}} \rangle$, we immediately obtain a sequence of effective partition function tensors induced by the exact renormalizability of the string-net part,

$$\langle \Omega | \Psi_{\text{SN}} \rangle \xrightarrow{\text{RG step}} \langle \Omega^{(i)} | U^\dagger U | \Psi_{\text{SN}}^{(i)} \rangle = \langle \Omega^{(i)} | U^\dagger | \Psi_{\text{SN}}^{(i+1)} \rangle \simeq \langle \Omega^{(i+1)} | \Psi_{\text{SN}}^{(i+1)} \rangle,$$

where $\langle \Omega^{(i+1)} |$ is a truncation of the PEPS $\langle \Omega^{(i)} | U^\dagger$ and $|\Psi_{\text{SN}}^{(i+1)}\rangle$ is a string-net on a coarse-grained lattice. The first blocking steps can generally be done exactly up to a certain bond dimension and turn the initial product state $|\Omega\rangle$ into an entangled PEPS. If we want the bond dimension of the input PEPS to remain constant¹², subsequent iterations will require truncation. To see this, consider the action of the coarse-graining PEPO on the initial product state,



where at each site we have used Eq. (6.98) to distribute the square roots of the nonnegative weights in the product state evenly across the gates. Apart from the familiar black and red bounding boxes, we have also drawn blue bounding boxes which indicate the location of the corresponding tensors in the coarse-grained string-net part of the SC overlap. Indeed, one can easily verify that, for the product states constructed in Sec. 6.2.2, the effective SC overlap $\langle \Omega^{i+1} | \Psi_{\text{SN}}^{i+1} \rangle$ defines a coarse-grained partition function in terms of the partition function tensor



In Fig. 6.6, we show how, at every layer, the coarse-grained PEPS has an internal substructure in terms of four tensors which can be derived from those of the previous layer. Some of the disentangling gates can be done on each of these four tensors individually, but the isometric gates connect the coarse-grained PEPS with its nearest

¹²Or have it alternating every other layer as in MERA-TNR [153]. The point is that we want to keep it from growing with every application of the coarse-graining step.

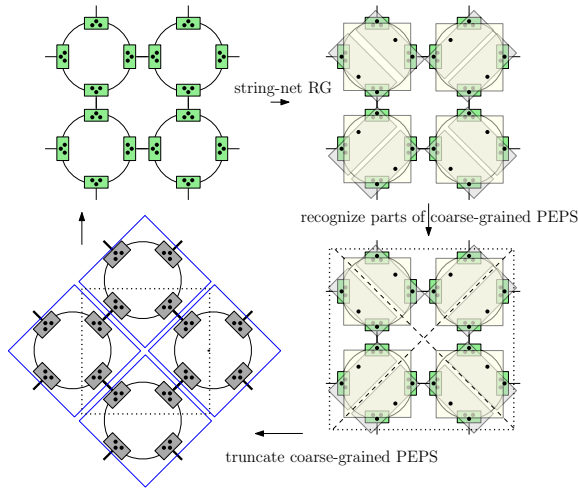


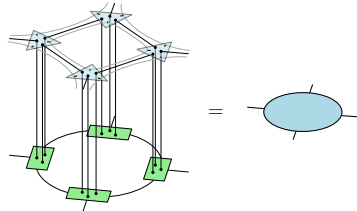
FIGURE 6.6: Every RG step, the gates of the coarse-graining map Eq. (6.99) block the PEPS tensors in such a way that preserving the PEPS structure leads to an increased bond dimension, so that we have to truncate the coarse-grained PEPS if we want a sustainable RG transformation.

neighbor tensors. Rewriting the PEPS after applying the isometric gates again as a PEPS requires truncation (see Sec. 3.3.3). Crucially, it is the way in which this truncation step is carried out which differentiates between the different tensor network renormalization schemes of Sec. 3.5.

At this point, we would like to stress that the string-net gates of the coarse-graining circuit Eq. (6.99) do *not* implement a real-space renormalization procedure on their own. Indeed, looking at Eqs. 6.92, 6.93, and 6.94 should convince us of the fact that these gates are in fact very simple, sparse objects. Their action on the physical level of the PEPS input state amounts to blocking sites, which increases the virtual bond dimension, projecting out half of the physical indices, and constraining the surviving physical indices of the PEPS to match the configurations of the physical indices allowed by the string-net fusion rules. More generally, the SC construction exposes and enforces (part of) the topological symmetries of the scaling limit of the classical partition function already at the ultraviolet level. In this sense, it extends the usual applications of symmetries in tensor networks to include MPO symmetries, which was exactly what enabled us to go beyond the \mathbb{Z}_2 parity labeling of the twisted Ising spectra in Sec. 6.3. The actual renormalization step, which gets rid of local, short-range correlations, depends on the choice of PEPS truncation on the virtual level, as we will elaborate upon below.

In terms of the frog-bird analogy of Sec. 1.2, the gapped, RG invariant string-net part $|\Psi_{\text{SN}}\rangle$ of the SC corresponds to a *bird state* containing (part of) the universal topological data of the RG fixed point model. The (coarse-grained) input state can be interpreted as a *frog state* pertaining to the muddy ultraviolet physics of the critical lattice model, i.e. the Boltzmann weights which tune the lattice model to

criticality. By acting with the string-net RG circuit and its conjugate inside the SC $\langle \Omega | \Psi_{\text{SN}} \rangle$, we are able to gradually shift the renormalization group scale, which introduces correlations into the the input state $\langle \Omega |$ but leaves the universal part $|\Psi_{\text{SN}}\rangle$ invariant. After the first layer which turns the product state into a PEPS, the effective partition function tensor at every subsequent layer is given in terms of an approximate, renormalized SC, given by

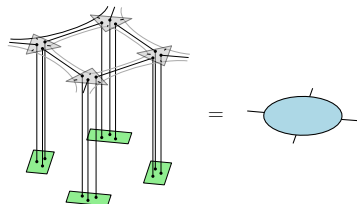


$$(6.103)$$

Consequently, the bond dimension $\chi = \chi_{\Omega} \chi_{\text{SN}}$ of the effective partition function completely results from the truncation of the PEPS to χ_{Ω} , since the physical dimension of the string-net χ_{SN} is fixed. For the Ising model, this fixed dimension is $\chi_{\text{SN}} = 2$, corresponding to the spin as represented by the labels $\{1, \psi\}$.

6.4.4 Kadanoff's block-spin truncation

One way to stay in the Ising phase diagram is to enforce that the input state remains a product state, i.e. approximate the coarse-grained PEPS as good as possible with a product state. Doing this yields a flow in terms of partition function tensors with a bond dimension that remains equal to $\chi = \chi_{\text{SN}}$, since the bond dimension of the partition function is now solely determined by the (doubled) physical indices of the string-net,



$$(6.104)$$

This flow is reminiscent of Kadanoff's block spin method (see Sec. 2.10) where the effective Hamiltonian is truncated to the nearest-neighbor term [154]. We have already amply commented upon the reasons for the breakdown of the Kadanoff picture in Chapter 2. Here, we interpret the failure as following from the restriction the frog state to a product state instead of allowing a full PEPS ansatz to explore higher-order interactions in a larger parameter space of the generalized Ising model Eq. (2.71).

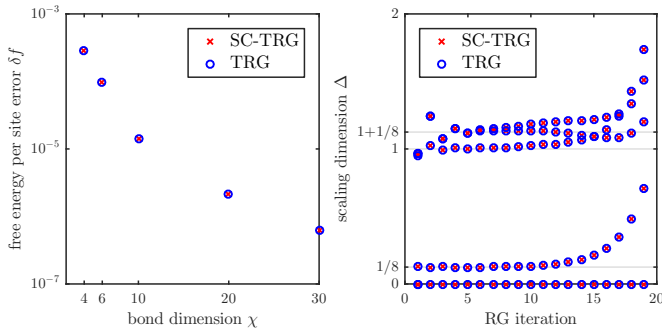


FIGURE 6.7: Comparison between SC-TRG and TRG: (left) free energy density error at criticality in function of bond dimension, (right) flow of scaling dimensions for $\chi = 10$ from the linear transfer matrix defined in Eq. (5.24).

6.4.5 Tensor renormalization group (TRG)

The simplest non-trivial way to truncate the coarse-grained PEPS in Eq. (6.102) is by doing independent singular value decompositions to pull the coarse-grained tensors apart, which is closely related to the simple update method for PEPS optimization (see Sec. 3.3.3). We end up with a sequence of effective partition function tensors of the form

$$\begin{array}{c} \circ \\ | \\ A' \\ | \\ \circ \end{array} \approx \left\langle \begin{array}{c} \text{---} \text{---} \text{---} \\ \text{---} \text{---} \text{---} \\ \text{---} \text{---} \text{---} \\ \text{---} \text{---} \text{---} \\ \text{---} \text{---} \text{---} \end{array} \right\rangle \left| \begin{array}{c} \text{---} \text{---} \text{---} \\ \text{---} \text{---} \text{---} \\ \text{---} \text{---} \text{---} \\ \text{---} \text{---} \text{---} \\ \text{---} \text{---} \text{---} \end{array} \right\rangle \quad (6.105)$$

where the fat indices correspond to the truncated indices, which will become the inner indices in the substructure of PEPS of the next layer. Numerically, we observe that this SC-TRG real-space scheme yields results which are indistinguishable from TRG (see Fig. 6.7). Even though the numerical results are identical, we would like to stress that the partition function tensors obtained from SC-TRG have a more insightful interpretation. Given that the SC-TRG tensors are gradually built up from extremely sparse F -symbol objects and that the blocking operation is done using gates which themselves are nothing but F -symbols, the effective partition function tensors remain extremely sparse all along the RG flow. Indeed, even if the PEPS truncation were to introduce “forbidden”¹³ non-zero values in the truncated PEPS, the eventual contraction with the string-net would remove all values which violate the inherent symmetries of the string-net.

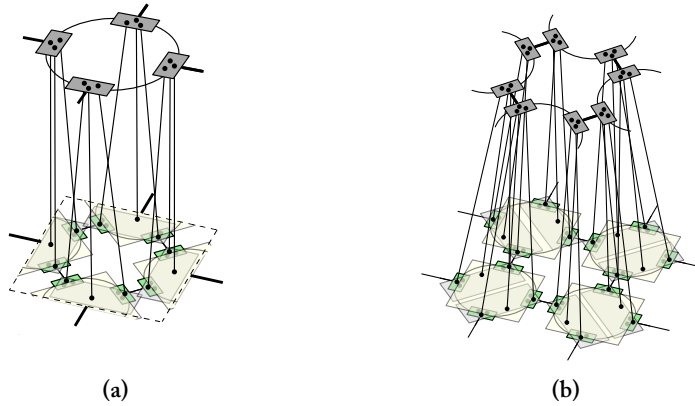


FIGURE 6.8: Coarse-grained strange correlators for two kinds of translation invariant unit cells, where the PEPS tensor has an internal substructure given by (a) four tensors, (b) eight tensors. Truncating the PEPS using full update is one possible implementation of the truncation step alluded to in Fig. 6.6.

6.4.6 Beyond tensor network renormalization (TNR)

Thinking in terms of PEPS optimization, the most straightforward way to improve SC-TRG is to include the full environment and set up a variational PEPS optimization which maximizes the overlap between the coarse-grained PEPS with an increased bond dimension and a truncated one. The idea is that this could provide an optimal approximation of the exact contraction Eq. (6.102). The resulting coarse-grained strange correlators are depicted in Fig. 6.8 for two kinds of PEPS unit cells. Using a customized implementation of the variational method sketched in Sec. 3.3.3, we implemented the PEPS overlap maximization using a full environment both for the translation invariant unit cell containing four tensors (Fig. 6.8(a)) and a larger translation invariant unit cell with an A-B structure containing eight tensors (Fig. 6.8(b)). We were able to significantly improve the value of the cost function compared to the initial SC-TRG solution, similar to how TNR improves upon the TRG solution. However, despite the better overlap of the PEPS, we numerically observed free energy densities and scaling dimensions which were only marginally better than SC-TRG, resembling the improvements of TRG which include approximations of the environment of the partition function (see Sec. 3.5.2).

In hindsight, the reason for this behavior is obvious: the conventional overlap maximization has no way of knowing that it is actually part of a coarse-graining algorithm. Put differently, the optimal environment for truncating local, short-range correlations has a lot less to do with the full environment required for ground state optimizations than one might intuitively anticipate. Indeed, we know from Sec. 3.5

¹³This could happen since the truncation on the virtual level is done on the input $\langle \Omega |$ PEPS in isolation, irrespective of the eventual contraction with the string-net part $|\Psi_{\text{SN}}\rangle$ in the SC.

and Chapter 5 that the success of TNR methods can be attributed to the removal of local correlations in a highly asymmetric way.

Our results confirm that using the full environment for real-space RG purposes is inadequate since it is in a sense too “globally” optimal. One solution would be to come up with a different cost function to maximize PEPS overlaps which uses an environment attuned to the removal of short-range correlations. We want our approximate environment to be less local than SC-TRG, which is blind to important short-range correlations, but less global than a conventional PEPS optimization, which overlooks the very same short-range correlations. We leave the design of such a TNR-like PEPS truncation procedure for future work but already note the relevance of the recently developed implicitly disentangled renormalization [184]. Another approach would be to insert a different coarse-graining map into the strange correlator instead of the one given by the exact string-net RG of Sec. 6.4.1, which we know is based on TRG and basically just blocks sites. There might exist more general exact coarse-graining maps which still also have string-nets as their fixed point¹⁴. For example, in Ref. [48] the Virasoro algebra is rigorously identified as a limit of spin operators using intricate coarse-graining operators, which could give a much better representation of the CFT coarse-graining operator than simply blocking sites.

6.5 Conclusion

We have shown how the strange correlator provides access to the non-local symmetries of the scaling limit of critical partition functions on the lattice by enabling the identification of the topological sectors appearing in finite-size CFT spectra of generalized twisted partition functions. The MPO algebra approach starts from defects, which we can immediately relate to conformal primary fields for diagonal CFT partition functions such as Ising. For non-diagonal partition functions, the interpretation is more subtle and has been considered in Ref. [3] for the Fibonacci string-net/hard hexagon case. We have also revealed an elegant perspective on the tensor network approach to real-space renormalization.

For future work, it would be interesting to properly relate our work to the literature introduced in Sec. 6.1. In particular, the connection to the work on dualities by Fröhlich *et al.* [169] is unclear since we start from the defects whereas these defects are the final results of the TQFT/CFT construction. It might be worthwhile to work out the extension to other models to obtain a better understanding of the limitations of the strange correlator construction (Sec. 6.2.4). A possible solution to the appearance of the spurious fields in Sec. 6.3.4 might be to consider half a transfer matrix, since we are already considering translations over half a lattice site. Neither of these approaches may be particularly elegant, but nobody promised a rose garden.

Lots of open questions remain. As we have stated before, the RG invariant string-net part of the SC corresponds in many ways to the *bird state* containing the universal topological data of the RG fixed point model. The (coarse-grained) input state can be referred to as the *frog state* pertaining to the muddy ultraviolet physics of the critical lattice model. The strange correlator is thus not an RG fixed

¹⁴We thank Dominic Williamson for making this point (and many others).

point and is totally ultraviolet from an RG point of view. Yet it captures the most important (non-local) symmetries of the resulting CFT despite its ultraviolet nature. For the Ising model we have seen that knowing the topological sectors tells us almost everything there is to know about the primary fields of the CFT, even though we cannot construct their exact representations at the ultraviolet scale. The primary fields themselves might correspond to the leading eigenvectors of a coarse-graining map within each sector of the tube algebra. So in a sense they are not MPOs but rather vectors in the irreducible representations of the MPO tube algebra. It would be very interesting to combine the results of Sec. 6.3 and Sec. 6.4 and study what happens to the MPO algebra when coarse-graining the strange correlator. We believe that a deeper understanding of how to approach conformal field theories using tensor networks is right around the corner and that MPOs will play a central role. In this light, the results of this chapter constitute a significant first step.

6.6 Appendices

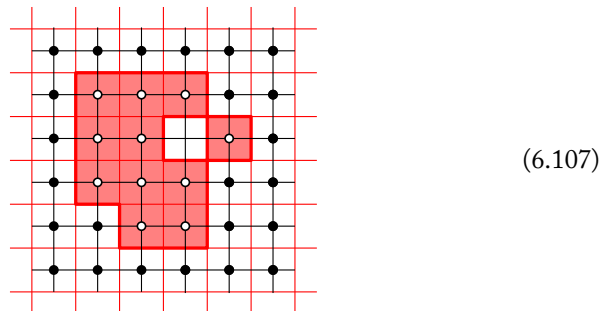
6.6.1 Kramers-Wannier duality

Since it is our intention to include duality defects into tensor network descriptions of classical partition functions, let us remind ourselves of the hidden duality discovered by Kramers and Wannier in the two-dimensional Ising model [185].

Consider yet again the two-dimensional ferromagnetic Ising model on the square lattice having N sites and $2N$ links. At each site there is a classical spin $\sigma_i = \pm 1$, with the energy of a configuration of spins given by $\mathcal{H}[\sigma] = -J \sum_{\langle i,j \rangle} \sigma_i \sigma_j$. The partition function at inverse temperature β is given by

$$Z = \sum_{\{\sigma\}=\pm 1} \exp \left(\beta J \sum_{\langle i,j \rangle} \sigma_i \sigma_j \right) = \sum_{\{\sigma\}=\pm 1} \prod_{\langle i,j \rangle} e^{\beta J \sigma_i \sigma_j}, \quad (6.106)$$

where the sum/product runs over nearest-neighbor sites of the lattice. In addition to the \mathbb{Z}_2 symmetry under global spin flips, the Ising model also has a more subtle duality property. For later purposes, let us already introduce the sites of the dual lattice at the center of the plaquettes of the original lattice, as shown below



where a particular spin configuration is shown on the primal lattice (black) and the

dual lattice (red). Islands of spin-down (\circ) in a spin-up (\bullet) sea are marked red and surrounded by domain walls.

The *Kramers-Wannier duality* is then a mapping between the low-temperature and high-temperature series expansions of the partition function. At low temperature the expansion is done in terms of configurations of closed domain walls, or polygon configurations [176], at high temperature in terms of closed loops of spin configurations. As we will show in the next section, these expansions can be mapped into each other if the coupling $K = \beta J$ is related to the dual coupling K^* by

$$e^{-2K^*} = \tanh(K). \quad (6.108)$$

This duality is an exact identity *only in the thermodynamic limit* as boundary conditions change under the action of the duality for finite systems. A duality transformation can thus only be considered a “symmetry” of local observables asymptotically in the thermodynamic limit. Because of the self-duality of the square lattice, the Kramers-Wannier duality on the square lattice relates a low-temperature Ising model to a high-temperature Ising model *on the same lattice geometry*. For honeycomb or triangle lattices, additional star-triangle relations are required on top of the duality to match the lattice geometries.

6.6.1.1 Low-temperature series expansion

At low temperatures, the energy of the system is minimized by spin-aligned configurations which have a larger statistical weight than the misaligned configurations. This suggests to expand the partition function in terms of *domain walls*, which are lines on the bonds of the dual lattice that separate regions of spin up and down. The Boltzmann weight associated to a dual bond with a domain wall present relative to no domain wall present is e^{-2K} , so that we can rewrite the partition function as

$$Z = 2e^{2NK} \sum_{\{\sigma\}=\pm 1} e^{-2KN_l}, \quad (6.109)$$

where N is the total number of sites and N_l the number of domain walls (dual bonds), which boils down to the length of the domain walls. The sum is still over the spin configurations, and the translation to a summation over domain walls depends on the boundary conditions. We will be cavalier about boundary conditions by implying the thermodynamic limit, and immediately write down the partition function in terms of a sum over domain wall loops of length n as

$$Z = 2e^{2NK} \sum_n C_N^{(n)} (e^{-2K})^n = 2e^{NK} \left(1 + N(e^{-2K})^4 + \dots \right), \quad (6.110)$$

where $C_N^{(n)}$ denotes the number of closed domain walls of length n on the *dual square lattice* of N sites (which is again the square lattice). Note that even though this expansion is exact, it is called a low-temperature expansion because as $\beta \rightarrow \infty$, the term without any loops dominates (two configurations: all spins up or all spins

down). The first correction has one flipped spin, so four domain walls surrounding the flipped spin. The partition function can thus be interpreted as a sum over domain walls/polygon configurations on the dual lattice.

6.6.1.2 High-temperature series expansion

Let us now write down a high-temperature expansion, starting from the identity

$$e^{K\sigma_i\sigma_j} = \cosh(K) + \sinh(K)\sigma_i\sigma_j, \quad (6.111)$$

leading to

$$Z = \sum_{\{\sigma\}=\pm 1} \prod_{\langle i,j \rangle} (\cosh(K) + \sinh(K)\sigma_i\sigma_j). \quad (6.112)$$

The product can be expanded into a sum of 2^{N_l} terms, where N_l is the number of bonds. This can be done by introducing a new \mathbb{Z}_2 variable $b_{(i,j)}$ for every bond between site i and j , where $b_{(i,j)} = 0$ if the bond contains a $\cosh(K)$ term and $b_{(i,j)} = 1$ if the bond contains $\sinh(K)\sigma_i\sigma_j$, so that

$$Z = (\cosh(K))^{N_l} \sum_{\{\sigma\}=\pm 1} \sum_{\{b_{(i,j)}\}=0,1} \prod_{\langle i,j \rangle} (\tanh(K)\sigma_i\sigma_j)^{b_{(i,j)}}. \quad (6.113)$$

This gives a one-to-one correspondence between the terms in the expansion and line configurations on the bonds of the original lattice. Now switch the order of the sums over the independent variables b and σ to first fix bond configurations before summing over all spins,

$$Z = (\cosh(\beta J))^{N_l} \sum_{\{b_{(i,j)}\}=0,1} \tanh(\beta J)^{\sum_{\langle i,j \rangle} b_{(i,j)}} \left(\sum_{\{\sigma\}=\pm 1} \prod_{\langle i,j \rangle} (\sigma_i\sigma_j)^{b_{(i,j)}} \right). \quad (6.114)$$

Since $\sigma_i = \pm 1$, each term

$$\sum_{\{\sigma\}=\pm 1} \prod_{\langle i,j \rangle} (\sigma_i\sigma_j)^{b_{(i,j)}} = \sum_{\{\sigma\}=\pm 1} \prod_i (\sigma_i)^{\sum_j b_{(i,j)}} \quad (6.115)$$

where the sum over sites j is restricted to the nearest-neighbors of site i , is actually only non-zero for a particular $b_{(i,j)}$ configuration if the exponents of all the σ_i 's are even. In this case, the contribution is 2^N , otherwise it is zero:

$$Z = 2^N (\cosh(\beta J))^{N_l} \sum_{\substack{\{b_{(i,j)}\}=0,1 \\ \sum_{\langle i,j \rangle} b_{(i,j)}=0,2,4,\dots}} (\tanh(\beta J))^{\sum_{\langle i,j \rangle} b_{(i,j)}}. \quad (6.116)$$

The sum over all spin configurations thus forces only closed loops to contribute (as there can be no lines ending or branching),

$$Z = 2^N (\cosh(\beta J))^{Nl} \sum_n C_N^{(n)} (\tanh(\beta J))^n \quad (6.117)$$

$$= (\cosh(\beta J))^{Nl} 2^N (1 + N(\tanh(\beta J))^4 + \dots), \quad (6.118)$$

where we have introduced the same counting function $C_N^{(n)}$ to denote the number of distinct closed loops of length n on the *primal square lattice* of N sites. Indeed, because of the self-duality of the square lattice, counting the number of closed loops on either the dual or the primal lattice is identical.

6.6.1.3 Kramers-Wannier duality

The duality now arises because both the low-temperature expansion in terms of domain walls and the high-temperature expansion in terms of closed loops are actually identical on the square lattice, albeit one being on the dual lattice and the other one on the original lattice. From equating the free energy per site of the partition function series expansions Eq. (6.110) and Eq. (6.117) in the thermodynamic limit, we find the constraint

$$\frac{\ln Z}{N} = 2K + g(e^{-2K}) = \ln 2 + 2 \ln \cosh K + g(\tanh K), \quad (6.119)$$

where the function g denotes the logarithm of the series expansion. The low- and high-temperature arguments of g are related by the duality condition

$$g(e^{-2\tilde{K}}) \leftrightarrow g(\tanh(K)) \quad \rightarrow \quad \tilde{K} \equiv -\frac{1}{2} \ln(\tanh(K)). \quad (6.120)$$

Note that the dual of the dual is again the primal, since

$$\sinh(2K) \sinh(2\tilde{K}) = 1. \quad (6.121)$$

If the free energy Eq. (6.119) is singular at a critical point K_c , this must be reflected in non-analytic behavior of the function $g(K)$. But because of the duality, the function $g(K)$ also has a singularity at \tilde{K}_c . Since the free energy should be analytic everywhere except at the critical point, the model must be self-dual, which means that

$$e^{-2\tilde{K}_c} = \tanh(K_c) = \frac{1 - e^{-2K_c}}{1 + e^{-2K_c}}, \quad (6.122)$$

so that, $e^{-2K_c} = -1 \pm \sqrt{2}$. Discarding the negative solution, we obtain the critical coupling of the square lattice Ising model immediately from its duality property

$$K_c = \frac{\ln(1 + \sqrt{2})}{2} = 0.441 \dots \quad (6.123)$$

6.6.2 Explicit string-net coarse-graining gates

In this Appendix, we provide the tedious F -symbol manipulations required to arrive at the expressions for the exact string-net coarse-graining gates given in Eqs. (6.92), (6.93), (6.94), and (6.96).

6.6.2.1 Disentangler

Using Eq. (6.12), properties of F -symbols, and the pentagon equation, we start from

$$\begin{array}{c} i \\ \beta \\ \alpha \\ \gamma \\ l \\ \delta \\ k \end{array} \begin{array}{c} j \\ \beta \\ \alpha \\ \gamma \\ l \\ \delta \\ k \end{array} = \frac{(d_i d_j d_k d_l)^{1/4}}{(d_\beta d_\delta d_n)^{1/2}} F_{\gamma\beta n}^{\alpha i j} (F_{\gamma\delta n}^{\alpha l k})^*, \quad (6.124)$$

so that

$$F_{\gamma\beta n}^{\alpha i j} (F_{\gamma\delta n}^{\alpha l k})^* = d_n \frac{(d_\beta d_\delta)^{1/2}}{(d_\alpha d_\gamma d_i d_k)^{1/2}} \sum_{n'} F_{i\alpha n'}^{l\delta\beta} F_{n i k}^{l n' j} F_{k n' \gamma}^{\delta\beta j} \quad (6.125)$$

$$= d_n \frac{(d_\beta d_\delta)^{1/2}}{(d_\alpha d_\gamma d_i d_k)^{1/2}} \sum_{n'} F_{n i k}^{l n' j} F_{i\alpha n'}^{l\delta\beta} (F_{\delta\gamma n'}^{\beta j k})^* \quad (6.126)$$

$$= \frac{(d_\beta d_\delta)^{1/2}}{(d_\alpha d_\gamma)^{1/2}} \sum_{n'} \sqrt{\frac{d_n}{d_{n'}}} F_{k n' n}^{l i j} F_{\beta\alpha n'}^{\delta l i} (F_{\beta\gamma n'}^{\delta k j})^*. \quad (6.127)$$

Defining

$$\begin{array}{c} i' \\ \beta \\ \alpha \\ \gamma \\ l' \\ \delta \\ k' \end{array} \begin{array}{c} j' \\ \beta \\ \alpha \\ \gamma \\ l' \\ \delta \\ k' \end{array} = \frac{(d_{i'} d_{j'} d_{k'} d_{l'})^{1/4}}{(d_\alpha d_\gamma d_{n'})^{1/2}} F_{\beta\alpha n'}^{\delta l' i'} (F_{\beta\gamma n'}^{\delta k' j'})^*, \quad (6.128)$$

it follows that

$$\begin{array}{c} i \\ \beta \\ \alpha \\ \gamma \\ l \\ \delta \\ k \end{array} \begin{array}{c} j \\ \beta \\ \alpha \\ \gamma \\ l \\ \delta \\ k \end{array} = \delta_{i i'} \delta_{j j'} \delta_{k k'} \delta_{l l'} \sum_{n'} F_{k' n' n}^{l' i' j'} \begin{array}{c} i' \\ \beta \\ \alpha \\ \gamma \\ l' \\ \delta \\ k' \end{array} \begin{array}{c} j' \\ \beta \\ \alpha \\ \gamma \\ l' \\ \delta \\ k' \end{array} \quad (6.129)$$

Conversely,

$$\begin{array}{c} i' \\ \beta \\ \alpha \\ \gamma \\ l' \\ \delta \\ k' \end{array} \begin{array}{c} j' \\ \beta \\ \alpha \\ \gamma \\ l' \\ \delta \\ k' \end{array} = \delta_{i' i} \delta_{j' j} \delta_{k' k} \delta_{l' l} \sum_n F_{j n n'}^{k l i} \begin{array}{c} i \\ \beta \\ \alpha \\ \gamma \\ l \\ \delta \\ k \end{array} \begin{array}{c} j \\ \beta \\ \alpha \\ \gamma \\ l \\ \delta \\ k \end{array} \quad (6.130)$$

with the unitary gate

$$[U_V]_{i'j'k'l'n',ijkln} = \delta_{i'i}\delta_{j'j}\delta_{k'k}\delta_{l'l} \sum_n F_{jnn'}^{kli} \quad (6.131)$$

so that

$$\begin{array}{c} i' \quad \beta \quad j' \\ \alpha \quad n \quad \gamma \\ l' \quad \delta \quad k' \end{array} = \sum_{ijkln} [U_V]_{i'j'k'l'n',ijkln} \begin{array}{c} i \quad \beta \quad j \\ \alpha \quad n \quad \gamma \\ l \quad \delta \quad k \end{array}. \quad (6.132)$$

For U_H^∇ , we start from

$$\begin{array}{c} i' \quad \beta \quad j' \\ \alpha \quad n \quad \gamma \\ l' \quad \delta \quad k' \end{array} = \frac{(d_{i'}d_{j'}d_{k'}d_{l'})^{1/4}}{(d_\beta d_\delta d_{n'})^{1/2}} F_{\gamma\beta n'}^{\alpha i' j'} (F_{\gamma\delta n'}^{\alpha l' k'})^*, \quad (6.133)$$

yielding

$$F_{\gamma\beta n'}^{\alpha i' j'} (F_{\gamma\delta n'}^{\alpha l' k'})^* = \frac{(d_{n'}d_\delta)^{1/2}}{(d_\alpha d_{k'})^{1/2}} \sum_n F_{\beta\alpha n}^{\delta l' i'} F_{\gamma\beta k'}^{\delta n j'} F_{k'nn'}^{l' i' j'}. \quad (6.134)$$

$$= \frac{(d_{n'}d_\beta)^{1/2}}{(d_\delta d_{i'}d_{j'})^{1/2}} \sum_n (d_n)^{1/2} F_{k'nn'}^{l' i' j'} F_{\beta\delta i'}^{\alpha l' n} F_{\gamma\delta j'}^{\beta n k'}. \quad (6.135)$$

We define

$$\begin{array}{c} i \quad \beta \quad j \\ \alpha \quad n \quad \gamma \\ l \quad \delta \quad k \end{array} = \frac{(d_n)^{1/2}(d_k d_l)^{1/4}}{d_\delta (d_i d_j)^{1/4}} (F_{\beta\delta i}^{\alpha l n})^* (F_{\gamma\delta j}^{\beta n k})^*, \quad (6.136)$$

to find

$$\begin{array}{c} i' \quad \beta \quad j' \\ \alpha \quad n \quad \gamma \\ l' \quad \delta \quad k' \end{array} = \delta_{i'i}\delta_{j'j}\delta_{k'k}\delta_{l'l} \sum_n F_{knn'}^{lij} \begin{array}{c} i \quad \beta \quad j \\ \alpha \quad n \quad \gamma \\ l \quad \delta \quad k \end{array} \quad (6.137)$$

For U_H^Δ , we analogously start from

$$\begin{array}{c} i' \quad \beta \quad j' \\ \alpha \quad n \quad \gamma \\ l' \quad \delta \quad k' \end{array} = \frac{(d_{i'}d_{j'}d_{k'}d_{l'})^{1/4}}{(d_\beta d_\delta d_{n'})^{1/2}} F_{\gamma\beta n'}^{\alpha i' j'} (F_{\gamma\delta n'}^{\alpha l' k'})^*, \quad (6.138)$$

Define

$$\begin{array}{c} \beta \\ \diagup \quad \diagdown \\ i \quad n \quad j \\ \diagdown \quad \diagup \\ \alpha \quad l \quad \delta \quad k \quad \gamma \end{array} = \frac{(d_n)^{1/2} (d_i d_j)^{1/4}}{d_\beta (d_k d_l)^{1/4}} F_{\delta\beta l}^{\alpha i n} F_{\gamma\beta k}^{\delta n j}, \quad (6.139)$$

which we can match with the previous solution

$$F_{\gamma\beta n'}^{\alpha i' j'} (F_{\gamma\delta n'}^{\alpha l' k'})^* = \frac{(d_{n'} d_\beta)^{1/2}}{(d_\delta d_{i'} d_{j'})^{1/2}} \sum_n (d_n)^{1/2} F_{k' n n'}^{l' i' j'} F_{\beta\delta i' n}^{\alpha l' n} F_{\gamma\delta j'}^{\beta n k'} \quad (6.140)$$

$$= \frac{(d_{n'} d_\delta)^{1/2}}{(d_\beta d_{k'} d_{l'})^{1/2}} \sum_n (d_n)^{1/2} F_{k' n n'}^{l' i' j'} F_{\delta\beta l'}^{\alpha i' n} F_{\gamma\beta k'}^{\delta n j'} \quad (6.141)$$

to find the same unitary

$$\begin{array}{c} \beta \\ \diagup \quad \diagdown \\ i' \quad n \quad j' \\ \diagdown \quad \diagup \\ \alpha \quad m \quad \gamma \\ \diagdown \quad \diagup \\ l' \quad \delta \quad k' \end{array} = \delta_{i' i} \delta_{j' j} \delta_{k' k} \delta_{l' l} \sum_n F_{k n n'}^{l i j} \begin{array}{c} \beta \\ \diagup \quad \diagdown \\ i \quad n \quad j \\ \diagdown \quad \diagup \\ \alpha \quad l \quad \delta \quad k \quad \gamma \end{array} \quad (6.142)$$

6.6.2.2 Isometries

As we are interested in the gates acting on the physical indices (and the corresponding exact RG circuit), we need to disentangle degrees of freedom first. We start from

$$\sum_\beta d_\beta \frac{(d_i d_j)^{1/2}}{d_\beta (d_k d_{k'})^{1/4}} (F_{\gamma\beta k'}^{\alpha i j})^* F_{\gamma\beta k}, \quad (6.143)$$

where the additional d_β is due to the closed virtual loop convention, so that

$$\sum_\beta \frac{(d_i d_j)^{1/2}}{(d_k d_{k'})^{1/4}} (F_{\gamma\beta k'}^{\alpha i j})^* F_{\gamma\beta k} \quad (6.144)$$

$$= \sum_\beta \frac{d_\beta (d_k d_{k'})^{1/4}}{(d_\alpha d_\gamma)^{1/2}} F_{\beta\alpha j}^{\gamma k' i} F_{\beta\gamma i}^{\alpha k j} \quad (6.145)$$

$$= \sum_\beta \frac{d_\beta (d_k d_{k'})^{1/4}}{(d_\alpha d_\gamma)^{1/2}} \sum_n F_{\alpha\gamma n}^{\alpha k k'} F_{\beta\alpha i}^{\alpha n i} F_{i n j}^{k k' i} \quad (6.146)$$

$$= \sum_\beta \frac{(d_\beta d_i)^{1/2} (d_k d_{k'})^{1/4}}{(d_\gamma)^{1/2}} \sum_n \frac{1}{(d_n)^{1/2}} F_{\alpha\gamma n}^{\alpha k k'} F_{i\beta n}^{\alpha\alpha} F_{i n j}^{k k' i} \quad (6.147)$$

$$= \sum_{\beta, n} d_\beta F_{i n j}^{k k' i} \left(\frac{(d_k d_{k'} d_n)^{1/4} F_{\alpha\gamma n}^{\alpha k k'}}{(d_\gamma d_n)^{1/2}} \right) \left(\frac{(d_i)^{1/2} (d_n)^{1/4} (F_{\alpha\beta n}^{\alpha i i})^*}{(d_\beta d_n)^{1/2}} \right). \quad (6.148)$$

We now recognize a trivial symbol $F_{\alpha\beta 0}^{\alpha ii} = (d_\beta)^{1/2}(d_\alpha d_i)^{-1/2} N_{\alpha i}^\beta$,

$$\sum_\beta \frac{(d_i d_j)^{1/2}}{(d_k d_{k'})^{1/4}} (F_{\gamma\beta k'}^{\alpha ij})^* F_{\gamma\beta k}^{\alpha ij} \quad (6.149)$$

$$= \sum_{\beta, n} d_\beta F_{in j}^{kk' i} \left(\frac{(d_k d_{k'} d_n)^{1/4} F_{\alpha\gamma n}^{\alpha k' k}}{(d_\gamma d_n)^{1/2}} \right) \left(\frac{(d_i)^{1/2} (d_n)^{1/4} (F_{\alpha\beta n}^{\alpha ii})^*}{(d_\beta d_n)^{1/2}} \right) \left(\frac{(d_\alpha d_i)^{1/2}}{(d_\beta)^{1/2}} F_{\alpha\beta 0}^{\alpha ii} \right) \quad (6.150)$$

$$= \sum_n F_{in j}^{kk' i} \left(\frac{(d_k d_{k'} d_n)^{1/4} F_{\alpha\gamma n}^{\alpha k' k}}{(d_\gamma d_n)^{1/2}} \right) \delta_{n,0} \left(\frac{(d_i)^{1/2} (d_n)^{1/4}}{(d_n)^{1/2}} \right) \left((d_\alpha d_i)^{1/2} \right) \quad (6.151)$$

$$= F_{i0 j}^{kk' i} \left(\frac{(d_k d_{k'})^{1/4} F_{\alpha\gamma 0}^{\alpha k' k}}{(d_\gamma)^{1/2}} \right) d_i (d_\alpha)^{1/2} \quad (6.152)$$

$$= \delta_{k' k} \frac{(d_i d_j)^{1/2}}{(d_k)^{1/2}} N_{ij}^k N_{\alpha k}^\gamma \quad (6.153)$$

Let's now do the calculation in the other way as well to get the disentangling gate we need. We start from

$$\sum_\beta \left(\frac{(d_k d_{k'} d_n)^{1/4} F_{\alpha\gamma n}^{\alpha k' k}}{(d_\gamma d_n)^{1/2}} \right) \left(\frac{(d_i)^{1/2} (d_n)^{1/4} (F_{\alpha\beta n}^{\alpha ii})^*}{(d_\beta d_n)^{1/2}} \right) \quad (6.154)$$

and want to get to

$$\sum_\beta \frac{(d_i d_j)^{1/2}}{(d_k d_{k'})^{1/4}} (F_{\gamma\beta k'}^{\alpha ij})^* F_{\gamma\beta k}^{\alpha ij} \quad (6.155)$$

We find

$$\sum_\beta \left(\frac{(d_k d_{k'} d_n)^{1/4} F_{\alpha\gamma n}^{\alpha k' k}}{(d_\gamma d_n)^{1/2}} \right) \left(\frac{(d_i)^{1/2} (d_n)^{1/4} (F_{\alpha\beta n}^{\alpha ii})^*}{(d_\beta d_n)^{1/2}} \right) \quad (6.156)$$

$$= \sum_\beta \frac{(d_n)^{1/2} (d_{k'})^{1/4}}{d_\alpha (d_k)^{1/4}} F_{ni\alpha}^{\alpha\beta i} F_{n\alpha k}^{k'\gamma\alpha} \quad (6.157)$$

$$= \sum_{\beta, j} \frac{(d_n)^{1/2} (d_{k'})^{1/4}}{d_\alpha (d_k)^{1/4}} F_{i\alpha j}^{k'\gamma\beta} F_{nik}^{k'ji} F_{kj\alpha}^{\gamma\beta i} \quad (6.158)$$

$$= \sum_{\beta, j} F_{kjn}^{k'ii} \frac{(d_i d_j)^{1/2}}{(d_k d_{k'})^{1/4}} \frac{(F_{\gamma\beta k'}^{\alpha ij})^*}{(d_\beta)^{1/2}} \frac{F_{\gamma\beta k}^{\alpha ij}}{(d_\beta)^{1/2}}, \quad (6.159)$$

leading to

$$\sum_{\beta} d_{\beta} \left(\frac{(d_k d_{k'} d_n)^{1/4} F_{\alpha\gamma n}^{\alpha k' k}}{(d_{\gamma} d_n)^{1/2}} \right) \left(\frac{(d_i)^{1/2} (d_n)^{1/4} (F_{\alpha\beta n}^{\alpha i i})^*}{(d_{\beta} d_n)^{1/2}} \right) \quad (6.160)$$

$$= \left(\frac{(d_k d_{k'} d_n)^{1/4} F_{\alpha\gamma n}^{\alpha k' k}}{(d_{\gamma} d_n)^{1/2}} \right) \sum_{\beta} d_{\beta} \left(\frac{(d_i)^{1/2} (d_n)^{1/4} (F_{\alpha\beta n}^{\alpha i i})^*}{(d_{\beta} d_n)^{1/2}} \right) \left(\frac{(d_{\alpha} d_i)^{1/2}}{(d_{\beta})^{1/2}} F_{\alpha\beta 0}^{\alpha i i} \right) \quad (6.161)$$

$$= d_i \left(\frac{(d_k d_{k'})^{1/4} F_{\alpha\gamma n}^{\alpha k' k}}{(d_{\gamma})^{1/2}} \right) \delta_{n,0} \left(\frac{1}{(d_n)^{1/2}} \right) (d_{\alpha})^{1/2} \quad (6.162)$$

$$= d_i \delta_{k'k} N_{\alpha k}^{\gamma} \quad (6.163)$$

$$(6.164)$$

The take-home message is

$$\sum_j F_{k'j0}^{k'ii} \sum_{\beta} d_{\beta} \frac{(d_i d_j)^{1/2}}{(d_k d_{k'})^{1/4}} \frac{(F_{\gamma\beta k'}^{\alpha ij})^*}{(d_{\beta})^{1/2}} \frac{F_{\gamma\beta k}^{\alpha ij}}{(d_{\beta})^{1/2}} = d_i \delta_{k'k} N_{\alpha k}^{\gamma} \quad (6.165)$$

so that the gate on the physical indices looks like

$$\sum_j F_{k'j0}^{k'ii} \left(\begin{array}{c} j \\ \gamma \\ \beta \\ \alpha \\ i \\ k' \quad k \end{array} \right) = d_i \delta_{k'k} N_{\alpha k}^{\gamma} \quad (6.166)$$

where $\sum_{\beta} d_{\beta}$ is understood to be included in the tensor network diagram. As expected, the n label gets fixed to the vacuum, the j label gets summed over, and the i label yields a quantum dimension. In actual numerics we implement the isometry by projecting the respective indices onto the vacuum and a loop state.

Outlook

Since the end of a dissertation is a place for contemplation and reverie, we refer the reader to the separate conclusions at the end of Chapters 4, 5, and 6 for specific, technical conclusions, and would like to reserve this last page for a broader outlook.

“For all the work that has been invested in the renormalization group it may seem the results obtained so far are rather scanty. It should be kept in mind that the problems to which the method is being applied are among the hardest problems known in the physical sciences. If they were not, they would have been solved by easier methods long ago. Indeed, a substantial number of the unsolved problems in physics trace their difficulty to a multiplicity of scales. The most promising path to their solution, even if it is an arduous path, is the further refinement of renormalization group methods.”

K. G. Wilson, 1979 [21]

Even though Wilson’s quote befits the conclusion of our work, we are well aware of the fact that one would have a hard time finding a top theoretical physicist today who would agree with this sentiment. Contemporary high-flying birds revel in strings and branes, and have found different, more rewarding paths to explore. Maybe they will return to “the most promising path” some day. Most likely though, they won’t.

Throughout this dissertation, the two-dimensional classical Ising model has been our steady companion. It first appeared in Chapter 2 in early discussions on criticality and phase transitions. Then as one of the theoretical laboratories Wilson used to scrutinize his ideas on renormalization group theory and later on as the microscopic lattice model underlying the Ising conformal field theory. We used tensor network renormalization methods to coarse-grain it at criticality in Chapter 5 and discussed its duality properties in Chapter 6, where, at last, all of its properties could be distilled into relations between structures of the Ising fusion category. We find it quite remarkable that a century old model continues to evolve along with the development of our understanding of physics.

We hope that the “further refinement of renormalization group methods” will not grind to a halt soon and that the Wilsonian spirit will live on in the physics of tomorrow.

Bibliography

- [1] M. Bal, M. M. Rams, V. Zauner, J. Haegeman, and F. Verstraete, “Matrix product state renormalization”, *Physical Review B* **94**, 1 (2016), arXiv:1509.01522.
- [2] M. Bal, M. Mariën, J. Haegeman, and F. Verstraete, “Renormalization Group Flows of Hamiltonians Using Tensor Networks”, *Physical Review Letters* **118**, 250602 (2017), arXiv:1703.00365.
- [3] M. Bal, D. J. Williamson, R. Vanhove, N. Bultinck, J. Haegeman, and F. Verstraete, “Mapping topological to conformal field theories through strange correlators”, (2018), arXiv:1801.05959.
- [4] F. Dyson, “Birds and frogs”, *Notices of the AMS* **56**, 212 (2009).
- [5] K. G. Wilson, “The renormalization group: Critical phenomena and the Kondo problem”, *Reviews of Modern Physics* **47**, 773 (1975).
- [6] K. G. Wilson, “Renormalization Group and Critical Phenomena. I. Renormalization Group and the Kadanoff Scaling Picture”, *Physical Review B* **4**, 3174 (1971).
- [7] K. G. Wilson, “Renormalization group and critical phenomena. II. Phase-space cell analysis of critical behavior”, *Physical Review B* **4**, 3184 (1971), arXiv:arXiv:1011.1669v3.
- [8] M. E. Fisher, “Renormalization group theory: Its basis and formulation in statistical physics”, *Reviews of Modern Physics* **70**, 653 (1998).
- [9] A.N. Schellekens, *Conformal Field Theory*, 2016.
- [10] J. Cardy, “Conformal Field Theory and Statistical Mechanics”, *Exact Methods in Low-dimensional Statistical Physics and Quantum Computing* **89**, 65 (2008), arXiv:0807.3472.
- [11] K. Huang, *Statistical Mechanics, 2nd Edition*, 1987.
- [12] J. Cardy and D. Thouless, “Scaling and Renormalization in Statistical Physics”, *Physics Today* **50**, 74 (1997).
- [13] P. D. Francesco, P. Mathieu, and D. Senechal, *Conformal Field Theory* (Springer, 1997), p. 890.
- [14] K. Christensen and N. R. Moloney, *Complexity And Criticality*, Vol. 1, Imperial College Press Advanced Physics Texts (Oct. 2005), p. 392.

- [15] M. Kardar, *Statistical Physics of Fields* (Cambridge University Press, Cambridge, 2007), p. 359, arXiv:arXiv:1011.1669v3.
- [16] K. G. K. G. Wilson, “The Origins of Lattice Gauge Theory”, *Nuclear Physics B - Proceedings Supplements* **140**, 3 (2005), arXiv:0412043 [hep-lat].
- [17] F. J. Dyson, “The S matrix in quantum electrodynamics”, *Physical Review* **75**, 1736 (1949).
- [18] M. Gell-Mann and F. E. Low, “Quantum electrodynamics at small distances”, *Physical Review* **95**, 1300 (1954).
- [19] L. Kadanoff, “Scaling laws for Ising models near $T(c)$ ”, *Physics* **2**, 263 (1966).
- [20] R. Shankar, “Renormalization-group approach to interacting fermions”, *Reviews of Modern Physics* **66**, 129 (1994), arXiv:9307009 [cond-mat].
- [21] K. G. Wilson, “Problems in Physics with many Scales of Length”, *Scientific American* **241**, 158 (1979).
- [22] B. R. Ashrafi, K. Hall, S. S. Schweber, and A. A. Martínez, *Physics of Scale Activities Page*, 2001.
- [23] P. W. Anderson, “Theory of localized magnetic states in metals”, *Journal of Applied Physics* **37**, 1194 (1966).
- [24] K. G. Wilson, “Renormalization Group Methods”, *Advances in Mathematics* **16**, 170 (1975).
- [25] K. G. Wilson, “The renormalization group and the ϵ expansion”, *Physics Reports* **12**, 75 (1974).
- [26] L. Landau, “The Theory of Phase Transitions”, *Nature* **138**, 840 (1936).
- [27] S. El-Showk, M. F. Paulos, D. Poland, S. Rychkov, D. Simmons-Duffin, and A. Vichi, “Solving the 3d Ising Model with the Conformal Bootstrap II. c -minimization and Precise Critical Exponents”, *Journal of Statistical Physics* **157**, 869 (2014), arXiv:1403.4545.
- [28] K. G. Wilson, “Critical phenomena in 3.99 dimensions”, *Physica* **73**, 119 (1974).
- [29] K. G. Wilson, *Ken Wilson memorial volume : Renormalization, Lattice Gauge Theory, the Operator Product Expansion and Quantum Fields*, edited by B. E. Baaquie, K. Huang, M. E. Peskin, and K. K. Phua (World Scientific Publishing, 2015), p. 385.
- [30] S. D. Glazek and K. G. Wilson, “Limit Cycles in Quantum Theories”, *Physical Review Letters* **89**, 230401 (2002), arXiv:0203088 [hep-th].
- [31] D. J. Amit and L. Peliti, “On dangerous irrelevant operators”, *Annals of Physics* **140**, 207 (1982).
- [32] K. G. Wilson and M. E. Fisher, “Critical exponents in 3.99 dimensions”, *Physical Review Letters* **28**, 240 (1972).

-
- [33] E. Brézin, “Wilson’s Renormalization Group: A Paradigmatic Shift”, *Journal of Statistical Physics* **157**, 644 (2014), arXiv:1402.3437.
- [34] D. C. Tsui, H. L. Stormer, and A. C. Gossard, “Two-Dimensional Magnetotransport in the Extreme Quantum Limit”, *Physical Review Letters* **48**, 1559 (1982).
- [35] R. B. Laughlin, “Anomalous Quantum Hall Effect: An Incompressible Quantum Fluid with Fractionally Charged Excitations”, *Physical Review Letters* **50**, 1395 (1983).
- [36] M. B. Hastings and X.-G. Wen, “Quasiadiabatic continuation of quantum states: The stability of topological ground-state degeneracy and emergent gauge invariance”, *Physical Review B* **72**, 045141 (2005).
- [37] X. Chen, Z.-C. Gu, and X.-G. Wen, “Classification of gapped symmetric phases in one-dimensional spin systems”, *Physical Review B* **83**, 035107 (2011), arXiv:1008.3745.
- [38] E. Witten, “Topological quantum field theory”, *Communications in Mathematical Physics* **117**, 353 (1988).
- [39] G. Moore and N. Seiberg, “Classical and quantum conformal field theory”, *Communications in Mathematical Physics* **123**, 177 (1989).
- [40] D. Friedan, Z. Qiu, and S. Shenker, “Conformal invariance, unitarity, and critical exponents in two dimensions”, *Physical Review Letters* **52**, 1575 (1984).
- [41] A. M. Polyakov, “Non-Hamiltonian approach to conformal quantum field theory”, *USSR Academy of Sciences Zh. Eksp. Teor. Fiz* **66**, 23 (1973).
- [42] K. G. Wilson, *On products of quantum field operators at short distances*, 1965.
- [43] K. G. Wilson, “Non-Lagrangian Models of Current Algebra”, *Physical Review* **179**, 1499 (1969).
- [44] L. P. Kadanoff, “Operator Algebra and the Determination of Critical Indices”, *Physical Review Letters* **23**, 1430 (1969).
- [45] A. M. Polyakov, “Conformal Symmetry of Critical Fluctuations”, *Pisma Zh. Eksp. Teor. Fiz.* **12**, 538 (1970).
- [46] H. W. J. Blöte, J. L. Cardy, and M. P. Nightingale, “Conformal invariance, the central charge, and universal finite-size amplitudes at criticality”, *Physical Review Letters* **56**, 742 (1986).
- [47] A. Zamolodchikov, “Irreversibility of the Flux of the Renormalization Group in a 2D Field Theory”, *JETP Lett.* **43**, 565 (1986).
- [48] M. S. Zini and Z. Wang, “Conformal Field Theories as Scaling Limit of Anyonic Chains”, arXiv:1706.08497 (2017), arXiv:1706.08497.
- [49] R. S. K. Mong, D. J. Clarke, J. Alicea, N. H. Lindner, and P. Fendley, “Parafermionic conformal field theory on the lattice”, *Journal of Physics A: Mathematical and Theoretical* **47**, 452001 (2014), arXiv:1406.0846.

- [50] D. Aasen, R. S. K. Mong, and P. Fendley, “Topological defects on the lattice: I. The Ising model”, *Journal of Physics A: Mathematical and Theoretical* **49**, 354001 (2016), arXiv:1601.07185.
- [51] L. P. Kadanoff and H. Ceva, “Determination of an Operator Algebra for the Two-Dimensional Ising Model”, *Physical Review B* **3**, 3918 (1971).
- [52] R. Bulla, T. A. Costi, and T. Pruschke, “Numerical renormalization group method for quantum impurity systems”, *Reviews of Modern Physics* **80**, 395 (2008), arXiv:0701105 [cond-mat].
- [53] S. R. White, “Density matrix formulation for quantum renormalization groups”, *Physical Review Letters* **69**, 2863 (1992).
- [54] H. J. Maris and L. P. Kadanoff, “Teaching the renormalization group”, *American Journal of Physics* **46**, 652 (1978).
- [55] L. P. Kadanoff, A. Houghton, and M. C. Yalabik, “Variational approximations for renormalization group transformations”, *Journal of Statistical Physics* **14**, 171 (1976).
- [56] T. Niemeijer and J. M. J. Van Leeuwen, “Wilson Theory for Spin Systems on a Triangular Lattice”, *Physical Review Letters* **31**, 1411 (1973).
- [57] F. Verstraete, V. Murg, and J. Cirac, “Matrix product states, projected entangled pair states, and variational renormalization group methods for quantum spin systems”, *Advances in Physics* **57**, 143 (2008).
- [58] J. I. Cirac and F. Verstraete, “Renormalization and tensor product states in spin chains and lattices”, *Journal of Physics A: Mathematical and Theoretical* **42**, 504004 (2009), arXiv:0910.1130.
- [59] N. Schuch, “Condensed Matter Applications of Entanglement Theory”, arXiv:1306.5551 (2013), arXiv:1306.5551.
- [60] R. Orús, “A practical introduction to tensor networks: Matrix product states and projected entangled pair states”, *Annals of Physics* **349**, 117 (2014), arXiv:1306.2164.
- [61] J. Haegeman, T. J. Osborne, and F. Verstraete, “Post-matrix product state methods: To tangent space and beyond”, *Physical Review B* **88**, 075133 (2013), arXiv:1305.1894.
- [62] B. Zeng, X. Chen, D.-L. Zhou, and X.-G. Wen, “Quantum Information Meets Quantum Matter – From Quantum Entanglement to Topological Phase in Many-Body Systems”, arXiv:1508.02595 (2015), arXiv:1508.02595.
- [63] J. Haegeman and F. Verstraete, “Diagonalizing transfer matrices and matrix product operators: a medley of exact and computational methods”, *Annual Review of Condensed Matter Physics* **8**, 355 (2016), arXiv:1611.08519.
- [64] J. C. Bridgeman and C. T. Chubb, “Hand-waving and interpretive dance: An introductory course on tensor networks”, *Journal of Physics A: Mathematical and Theoretical* **50** (2017) 10.1088/1751-8121/aa6dc3, arXiv:1603.03039.

-
- [65] D. Poulin, A. Qarry, R. Somma, and F. Verstraete, “Quantum simulation of time-dependent hamiltonians and the convenient illusion of hilbert space”, *Physical Review Letters* **106**, 170501 (2011), arXiv:1102.1360.
- [66] J. Eisert, M. Cramer, and M. B. Plenio, “Colloquium : Area laws for the entanglement entropy”, *Reviews of Modern Physics* **82**, 277 (2010).
- [67] F. Verstraete and J. I. Cirac, “Matrix product states represent ground states faithfully”, *Physical Review B* **73**, 094423 (2006).
- [68] Y. H. Su, S. Y. Cho, B. Li, H. L. Wang, and H. Q. Zhou, “Non-local correlations in the Haldane phase for an XXZ spin-1 chain: A perspective from infinite matrix product state representation”, *Journal of the Physical Society of Japan* **81**, 401 (2012), arXiv:1202.6147.
- [69] D. Pérez-García, M. M. Wolf, M. Sanz, F. Verstraete, and J. I. Cirac, “String Order and Symmetries in Quantum Spin Lattices”, *Physical Review Letters* **100**, 167202 (2008), arXiv:0802.0447.
- [70] N. Schuch, D. Pérez-García, and I. Cirac, “Classifying quantum phases using matrix product states and projected entangled pair states”, *Physical Review B* **84**, 165139 (2011), arXiv:1010.3732.
- [71] F. Verstraete, J. I. Cirac, J. I. Latorre, E. Rico, and M. M. Wolf, “Renormalization-group transformations on quantum states”, *Physical Review Letters* **94**, 1 (2005), arXiv:0410227 [quant-ph].
- [72] J. I. Cirac, D. Pérez-García, N. Schuch, F. Verstraete, D. Perez-Garcia, N. Schuch, and F. Verstraete, “Matrix product density operators: Renormalization fixed points and boundary theories”, *Annals of Physics* **378**, 100 (2017), arXiv:1606.00608.
- [73] F. Verstraete, J. J. García-Ripoll, and J. I. Cirac, “Matrix product density operators: Simulation of finite-temperature and dissipative systems”, *Physical Review Letters* **93**, 12 (2004), arXiv:0406426 [cond-mat].
- [74] U. Schollwöck, “The density-matrix renormalization group in the age of matrix product states”, *Annals of Physics* **326**, 96 (2011), arXiv:1008.3477.
- [75] J. Haegeman, J. I. Cirac, T. J. Osborne, I. Pižorn, H. Verschelde, and F. Verstraete, “Time-Dependent Variational Principle for Quantum Lattices”, *Physical Review Letters* **107**, 070601 (2011), arXiv:1103.0936.
- [76] J. Haegeman, C. Lubich, I. Oseledets, B. Vandereycken, and F. Verstraete, “Unifying time evolution and optimization with matrix product states”, *Physical Review B* **94**, 165116 (2016), arXiv:1408.5056.
- [77] V. Zauner-Stauber, L. Vanderstraeten, M. T. Fishman, F. Verstraete, and J. Haegeman, “Variational optimization algorithms for uniform matrix product states”, (2017), arXiv:1701.07035.
- [78] J. Haegeman, B. Pirvu, D. J. Weir, J. I. Cirac, T. J. Osborne, H. Verschelde, and F. Verstraete, “Variational matrix product ansatz for dispersion relations”, *Physical Review B* **85**, 100408 (2012).

- [79] L. Vanderstraeten, F. Verstraete, and J. Haegeman, “Scattering particles in quantum spin chains”, *Physical Review B* **92**, 125136 (2015), arXiv:1506.01008.
- [80] F. Verstraete and J. I. Cirac, “Renormalization algorithms for quantum-many body systems in two and higher dimensions”, (2004), arXiv:cond-mat/0407066.
- [81] F. Verstraete, M. M. Wolf, D. Perez-Garcia, and J. I. Cirac, “Criticality, the area law, and the computational power of projected entangled pair states”, *Physical Review Letters* **96**, 1 (2006), arXiv:0601075 [quant-ph].
- [82] M. B. Şahinoğlu, D. Williamson, N. Bultinck, M. Mariën, J. Haegeman, N. Schuch, and F. Verstraete, “Characterizing Topological Order with Matrix Product Operators”, arXiv:1409.2150, 1 (2014), arXiv:1409.2150.
- [83] D. J. Williamson, N. Bultinck, M. Mariën, M. B. Şahinoğlu, J. Haegeman, and F. Verstraete, “Matrix product operators for symmetry-protected topological phases: Gauging and edge theories”, *Physical Review B* **94**, 1 (2016), arXiv:1412.5604.
- [84] N. Bultinck, M. Mariën, D. J. Williamson, M. B. Şahinoğlu, J. Haegeman, and F. Verstraete, “Anyons and matrix product operator algebras”, *Annals of Physics* **378**, 183 (2017), arXiv:1511.08090.
- [85] D. J. Williamson and Z. Wang, “Hamiltonian models for topological phases of matter in three spatial dimensions”, *Annals of Physics* **377**, 311 (2017), arXiv:1606.07144.
- [86] M. Mariën, J. Haegeman, P. Fendley, and F. Verstraete, “Condensation-driven phase transitions in perturbed string nets”, *Physical Review B* **96**, 155127 (2017).
- [87] N. Bultinck, D. J. Williamson, J. Haegeman, and F. Verstraete, “Fermionic projected entangled-pair states and topological phases”, *Journal of Physics A: Mathematical and Theoretical* **51**, 025202 (2018), arXiv:1707.00470.
- [88] A. Kitaev, “Fault-tolerant quantum computation by anyons”, *Annals of Physics* **303**, 2 (2003).
- [89] M. A. Levin and X.-G. G. Wen, “String-net condensation: A physical mechanism for topological phases”, *Physical Review B* **71**, 045110 (2005), arXiv:0404617 [cond-mat].
- [90] V. G. Turaev and O. Y. Viro, “State sum invariants of 3-manifolds and quantum 6j-symbols”, *Topology* **31**, 865 (1992).
- [91] N. Schuch, M. M. Wolf, F. Verstraete, and J. I. Cirac, “Computational complexity of projected entangled pair states”, *Physical Review Letters* **98**, 1 (2007), arXiv:0708.1567.
- [92] R. J. Baxter, “Corner transfer matrices”, *Physica A: Statistical Mechanics and its Applications* **106**, 18 (1981).
- [93] T. Nishino and K. Okunishi, “Corner Transfer Matrix Renormalization Group Method”, *Journal of the Physical Society of Japan* **65**, 891 (1996).

-
- [94] R. Orús and G. Vidal, “Infinite time-evolving block decimation algorithm beyond unitary evolution”, *Physical Review B - Condensed Matter and Materials Physics* **78**, 155117 (2008), arXiv:0711.3960.
- [95] R. Orús and G. Vidal, “Simulation of two-dimensional quantum systems on an infinite lattice revisited: Corner transfer matrix for tensor contraction”, *Physical Review B* **80**, 094403 (2009), arXiv:0905.3225.
- [96] H. C. Jiang, Z. Y. Weng, and T. Xiang, “Accurate Determination of Tensor Network State of Quantum Lattice Models in Two Dimensions”, *Physical Review Letters* **101**, 090603 (2008).
- [97] J. Jordan, R. Orús, G. Vidal, F. Verstraete, and J. I. Cirac, “Classical Simulation of Infinite-Size Quantum Lattice Systems in Two Spatial Dimensions”, *Physical Review Letters* **101**, 250602 (2008), arXiv:0605597 [cond-mat].
- [98] H. N. Phien, J. A. Bengua, H. D. Tuan, P. Corboz, and R. Orús, “Infinite projected entangled pair states algorithm improved: Fast full update and gauge fixing”, *Physical Review B* **92**, 035142 (2015).
- [99] L. Vanderstraeten, J. Haegeman, P. Corboz, and F. Verstraete, “Gradient methods for variational optimization of projected entangled-pair states”, *Physical Review B* **94** (2016) 10.1103/PhysRevB.94.155123, arXiv:1606.09170.
- [100] G. Vidal, “Entanglement renormalization”, *Physical Review Letters* **99**, 220405 (2007), arXiv:0512165 [cond-mat].
- [101] G. Evenbly and G. Vidal, “Entanglement Renormalization in Two Spatial Dimensions”, *Physical Review Letters* **102**, 180406 (2009).
- [102] J. C. Bridgeman and D. J. Williamson, “Anomalies and entanglement renormalization”, *Physical Review B* **96**, 125104 (2017), arXiv:arXiv:1703.07782v1.
- [103] G. Evenbly and S. R. White, “Entanglement Renormalization and Wavelets”, *Physical Review Letters* **116**, 140403 (2016), arXiv:1602.01166.
- [104] J. Haegeman, B. Swingle, M. Walter, J. Cotler, G. Evenbly, and V. B. Scholz, “Rigorous free fermion entanglement renormalization from wavelet theory”, arXiv:1707.06243 (2017), arXiv:1707.06243.
- [105] J. Haegeman, T. J. Osborne, H. Verschelde, and F. Verstraete, “Entanglement Renormalization for Quantum Fields in Real Space”, *Physical Review Letters* **110**, 100402 (2013), arXiv:1102.5524.
- [106] S. Bravyi, M. B. Hastings, and S. Michalakis, “Topological quantum order: Stability under local perturbations”, *Journal of Mathematical Physics* **51**, 093512 (2010).
- [107] V. Giovannetti, S. Montangero, and R. Fazio, “Quantum multiscale entanglement renormalization ansatz channels”, *Physical Review Letters* **101**, 180503 (2008), arXiv:0804.0520.
- [108] G. Evenbly and G. Vidal, “Algorithms for entanglement renormalization”, *Physical Review B* **79**, 144108 (2009).

- [109] G. Evenbly and G. Vidal, “Algorithms for Entanglement Renormalization: Boundaries, Impurities and Interfaces”, *Journal of Statistical Physics* **157**, 931 (2014), arXiv:1312.0303.
- [110] M. M. Wolf, F. Verstraete, M. B. Hastings, and J. I. Cirac, “Area laws in quantum systems: Mutual information and correlations”, *Physical Review Letters* **100**, 1 (2008), arXiv:0704.3906.
- [111] M. Levin and C. P. Nave, “Tensor renormalization group approach to two-dimensional classical lattice models”, *Physical Review Letters* **99**, 120601 (2007).
- [112] Z.-C. Gu, M. Levin, B. Swingle, and X.-G. Wen, “Tensor-product representations for string-net condensed states”, *Physical Review B* **79**, 085118 (2009), arXiv:0809.2821.
- [113] Z. Y. Xie, H. C. Jiang, Q. N. Chen, Z. Y. Weng, and T. Xiang, “Second Renormalization of Tensor-Network States”, *Physical Review Letters* **103**, 160601 (2009).
- [114] Z. Y. Xie, J. Chen, M. P. Qin, J. W. Zhu, L. P. Yang, and T. Xiang, “Coarse-graining renormalization by higher-order singular value decomposition”, *Physical Review B* **86**, 045139 (2012), arXiv:1201.1144.
- [115] G. Evenbly and G. Vidal, “Tensor Network Renormalization”, *Physical Review Letters* **115**, 180405 (2015), arXiv:1412.0732.
- [116] G. Evenbly and G. Vidal, “Tensor Network Renormalization Yields the Multiscale Entanglement Renormalization Ansatz”, *Physical Review Letters* **115**, 200401 (2015), arXiv:1502.05385.
- [117] S. Yang, Z. C. Gu, and X. G. Wen, “Loop Optimization for Tensor Network Renormalization”, *Physical Review Letters* **118**, 1 (2017), arXiv:1512.04938.
- [118] M. Hauru, C. Delcamp, and S. Mizera, “Renormalization of tensor networks using graph independent local truncations”, arXiv:1709.07460 (2017), arXiv:1709.07460.
- [119] M. Hauru, private communication.
- [120] Z. Yang, P. Hayden, and X. L. Qi, “Bidirectional holographic codes and sub-AdS locality”, *Journal of High Energy Physics* **2016**, 1 (2016), arXiv:1510.03784.
- [121] F. Pollmann, S. Mukerjee, A. M. Turner, and J. E. Moore, “Theory of Finite-Entanglement Scaling at One-Dimensional Quantum Critical Points”, *Phys. Rev. Lett.* **102**, 255701 (2009), arXiv:0812.2903.
- [122] V. Stojevic, J. Haegeman, I. P. McCulloch, L. Tagliacozzo, and F. Verstraete, “Conformal data from finite entanglement scaling”, *Physical Review B* **91**, 035120 (2015), arXiv:1401.7654.
- [123] M. Fannes, B. Nachtergaele, and R. Werner, “Finitely correlated states on quantum spin chains”, *Communications in Mathematical Physics* **144**, 443 (1992).

-
- [124] S. Östlund and S. Rommer, “Thermodynamic limit of density matrix renormalization”, *Phys. Rev. Lett.* **75**, 3537 (1995).
- [125] G. Vidal, “Efficient simulation of one-dimensional quantum many-body systems”, *Physical Review Letters* **93**, 040502 (2004).
- [126] U. Schollwöck, “The density-matrix renormalization group”, *Reviews of Modern Physics* **77**, 259 (2005), arXiv:0409292v1 [arXiv:cond-mat].
- [127] L. Tagliacozzo, T. R. de Oliveira, S. Iblisdir, and J. I. Latorre, “Scaling of entanglement support for matrix product states”, *Phys. Rev. B* **78**, 024410 (2008).
- [128] F. Pollmann, S. Mukerjee, A. M. Turner, and J. E. Moore, “Theory of finite-entanglement scaling at one-dimensional quantum critical points”, *Phys. Rev. Lett.* **102**, 255701 (2009).
- [129] A. Läuchli, “Operator content of real-space entanglement spectra at conformal critical points”, arXiv preprint arXiv:1303.0741, 6 (2013), arXiv:1303.0741.
- [130] G. Evenbly and G. Vidal, “Local Scale Transformations on the Lattice with Tensor Network Renormalization”, *Physical Review Letters* **116**, 40401 (2016), arXiv:1510.00689.
- [131] V. Zauner, D. Draxler, L. Vanderstraeten, M. Degroote, J. Haegeman, M. M. Rams, V. Stojevic, N. Schuch, and F. Verstraete, “Transfer matrices and excitations with matrix product states”, *New Journal of Physics* **17**, 053002 (2015).
- [132] M. M. M. Rams, V. Zauner, M. Bal, J. Haegeman, and F. Verstraete, “Truncating an exact matrix product state for the XY model: Transfer matrix and its renormalization”, *Physical Review B* **92**, 235150 (2015), arXiv:1411.2607.
- [133] H. F. Trotter, “On the product of semi-groups of operators”, *Proc. Amer. Math. Soc.* **10**, 545 (1959).
- [134] M. Suzuki, “Relationship between d-dimensional quantum spin systems and (d+1)-dimensional Ising systems: equivalence, critical exponents and systematic approximants of the partition function and spin correlations”, *Progress of Theoretical Physics* **56**, 1454 (1976).
- [135] H. Betsuyaku, “Study of one-dimensional XY model by the transfer-matrix method”, *Physical Review Letters* **53**, 629 (1984).
- [136] J. Sirker and A. Klümper, “Real-time dynamics at finite temperature by the density-matrix renormalization group: a path-integral approach”, *Phys. Rev. B* **71**, 241101 (2005).
- [137] B. Pirvu, V. Murg, J. I. Cirac, and F. Verstraete, “Matrix product operator representations”, *New Journal of Physics* **12**, 025012 (2010).
- [138] T. Abrudan, J. Eriksson, and V. Koivunen, “Conjugate gradient algorithm for optimization under unitary matrix constraint”, *Signal Processing* **89**, 1704 (2009).

- [139] R. Orús and G. Vidal, “Infinite time-evolving block decimation algorithm beyond unitary evolution”, *Phys. Rev. B* **78**, 155117 (2008).
- [140] G. Evenbly and G. Vidal, “Theory of minimal updates in holography”, *Phys. Rev. B* **91**, 205119 (2015).
- [141] G. Evenbly, R. N. C. Pfeifer, V. Picó, S. Iblisdir, L. Tagliacozzo, I. P. McCulloch, and G. Vidal, “Boundary quantum critical phenomena with entanglement renormalization”, *Physical Review B* **82**, 161107 (2010), arXiv:0912.1642.
- [142] G. Evenbly and G. Vidal, “Algorithms for entanglement renormalization: boundaries, impurities and interfaces”, *Journal of Statistical Physics* **157**, 931 (2014).
- [143] R. Hübener, V. Nebendahl, and W. Dür, “Concatenated tensor network states”, *New Journal of Physics* **12**, 025004 (2010).
- [144] R. N. C. Pfeifer, G. Evenbly, and G. Vidal, “Entanglement renormalization, scale invariance, and quantum criticality”, *Physical Review A* **79**, 40301 (2009).
- [145] G. Evenbly and G. Vidal, “Entanglement renormalization in noninteracting fermionic systems”, *Phys. Rev. B* **81**, 235102 (2010).
- [146] G. Evenbly and G. Vidal, “Entanglement renormalization in free bosonic systems: real-space versus momentum-space renormalization group transforms”, *New Journal of Physics* **12**, 025007 (2010).
- [147] I. Peschel and V. Eisler, “Reduced density matrices and entanglement entropy in free lattice models”, *Journal of Physics A: Mathematical and Theoretical* **42**, 504003 (2009).
- [148] P. Czarnik and J. Dziarmaga, “Variational approach to projected entangled pair states at finite temperature”, *Phys. Rev. B* **92**, 035152 (2015).
- [149] T. D. Schultz, D. C. Mattis, and E. H. Lieb, “Two-dimensional Ising model as a soluble problem of many fermions”, *Reviews of Modern Physics* **36**, 856 (1964).
- [150] D. Abraham, *Stud. App. Math.* **1**, 71 (1971).
- [151] Z.-C. Gu, M. Levin, and X.-G. Wen, “Tensor-entanglement renormalization group approach as a unified method for symmetry breaking and topological phase transitions”, *Physical Review B* **78**, 205116 (2008).
- [152] H. H. Zhao, Z. Y. Xie, Q. N. Chen, Z. C. Wei, J. W. Cai, and T. Xiang, “Renormalization of tensor-network states”, *Physical Review B* **81**, 174411 (2010), arXiv:1002.1405.
- [153] G. Evenbly, “Algorithms for tensor network renormalization”, *Physical Review B* **95**, 045117 (2017), arXiv:1509.07484.
- [154] E. Efrati, Z. Wang, A. Kolan, and L. P. Kadanoff, “Real-space renormalization in statistical mechanics”, *Reviews of Modern Physics* **86**, 647 (2014), arXiv:arXiv:1301.6323v1.

-
- [155] V. Bittorf, B. Recht, C. Re, and J. A. Tropp, “Factoring nonnegative matrices with linear programs”, arXiv:1206.1270 (2012), arXiv:1206.1270.
- [156] D. J. Williamson, N. Bultinck, and F. Verstraete, “Symmetry-enriched topological order in tensor networks: Defects, gauging and anyon condensation”, arXiv:1711.07982 (2017), arXiv:1711.07982.
- [157] M. Hauru, G. Evenbly, W. W. Ho, D. Gaiotto, and G. Vidal, “Topological conformal defects with tensor networks”, *Physical Review B* **94**, 115125 (2016), arXiv:1512.03846.
- [158] N. Gillis and N. G. Be, “Sparse and Unique Nonnegative Matrix Factorization Through Data Preprocessing”, *Journal of Machine Learning Research* **13**, 3349 (2012), arXiv:1204.2436.
- [159] D. Donoho and V. Stodden, “When Does Non-Negative Matrix Factorization Give a Correct Decomposition into Parts?”, (2004).
- [160] K. Huang, N. D. Sidiropoulos, and A. Swami, “Non-Negative matrix factorization revisited: Uniqueness and algorithm for symmetric decomposition”, *IEEE Transactions on Signal Processing* **62**, 211 (2014).
- [161] S. A. Vavasis, “On the Complexity of Nonnegative Matrix Factorization”, *SIAM Journal on Optimization* **20**, 1364 (2010), arXiv:0708.4149.
- [162] D. D. Lee and H. S. Seung, “Learning the parts of objects by non-negative matrix factorization.”, *Nature* **401**, 788 (1999), arXiv:arXiv:1408.1149.
- [163] Y.-X. Wang and Y.-J. Zhang, “Nonnegative Matrix Factorization: A Comprehensive Review”, *IEEE Transactions on Knowledge and Data Engineering* **25**, 1336 (2013).
- [164] N. Gillis, “The Why and How of Nonnegative Matrix Factorization”, in *Arxiv preprint*, edited by M. S. J.A.K. Suykens and A. Argyriou (Chapman & Hall/CRC, 2014), pp. 1–25, arXiv:arXiv:1401.5226v2.
- [165] C. Boutsidis and E. Gallopoulos, “SVD based initialization: A head start for nonnegative matrix factorization”, *Pattern Recognition* **41**, 1350 (2008).
- [166] P. A. Knight, “The Sinkhorn–Knopp Algorithm: Convergence and Applications”, *SIAM Journal on Matrix Analysis and Applications* **30**, 261 (2008).
- [167] D. Perez-Garcia, M. M. Wolf, M. Sanz, F. Verstraete, and J. I. Cirac, “String order and symmetries in quantum spin lattices”, *Phys. Rev. Lett.* **100**, 167202 (2008).
- [168] J. Fuchs, I. Runkel, and C. Schweigert, “TFT construction of RCFT correlators I: partition functions”, *Nuclear Physics B* **646**, 353 (2002).
- [169] J. Fröhlich, J. Fuchs, I. Runkel, and C. Schweigert, “Kramers-Wannier Duality from Conformal Defects”, *Physical Review Letters* **93**, 070601 (2004), arXiv:0404051 [cond-mat].
- [170] J. Fröhlich, J. Fuchs, I. Runkel, and C. Schweigert, “Duality and defects in rational conformal field theory”, *Nuclear Physics B* **763**, 354 (2007), arXiv:0607247 [hep-th].

- [171] O. Buerschaper, M. Aguado, and G. Vidal, “Explicit tensor network representation for the ground states of string-net models”, *Physical Review B* **79**, 085119 (2009), arXiv:0809.2393.
- [172] Y.-Z. Z. You, Z. Bi, A. Rasmussen, K. Slagle, and C. Xu, “Wave Function and Strange Correlator of Short-Range Entangled States”, *Physical Review Letters* **112**, 247202 (2014), arXiv:1312.0626.
- [173] V. Petkova and J.-B. Zuber, “Generalised twisted partition functions”, *Physics Letters B* **504**, 157 (2001), arXiv:0011021v3 [arXiv:hep-th].
- [174] V. B. Petkova and J.-B. Zuber, “Conformal Boundary Conditions and what they teach us”, *Non-Perturbative QFT Methods and Their Applications*, 1 (2001), arXiv:0103007 [hep-th].
- [175] G. E. Andrews, R. J. Baxter, and P. J. Forrester, “Eight-vertex SOS model and generalized Rogers–Ramanujan-type identities”, *Journal of Statistical Physics* **35**, 193 (1984).
- [176] R. J. Baxter, *Exactly solved models in statistical mechanics* (Dover Publications, 2007), p. 498.
- [177] C. Heinrich, F. Burnell, L. Fidkowski, and M. Levin, “Symmetry-enriched string nets: Exactly solvable models for SET phases”, *Physical Review B* (2016) 10.1103/PhysRevB.94.235136, arXiv:1606.07816.
- [178] L. Chang, M. Cheng, S. X. Cui, Y. Hu, W. Jin, R. Movassagh, P. Naaijken, Z. Wang, and A. Young, “On enriching the Levin–Wen model with symmetry”, *Journal of Physics A: Mathematical and Theoretical* **48** (2015) 10.1088/1751-8113/48/12/12FT01, arXiv:arXiv:1412.6589v1.
- [179] M. Cheng, Z.-C. Gu, S. Jiang, and Y. Qi, “Exactly Solvable Models for Symmetry-Enriched Topological Phases”, (2016) 10.1103/PhysRevB.96.115107, arXiv:1606.08482.
- [180] A. Belavin, A. Polyakov, and A. Zamolodchikov, “Infinite conformal symmetry in two-dimensional quantum field theory”, *Nuclear Physics B* **241**, 333 (1984).
- [181] J. Haegeman, V. Zauner, N. Schuch, and F. Verstraete, “Shadows of anyons and the entanglement structure of topological phases”, *Nature Communications* **6**, 8284 (2015), arXiv:1410.5443.
- [182] U. Grimm, “Spectrum of a duality-twisted ising quantum chain”, *Journal of Physics A: Mathematical and General* **35**, L25 (2002), arXiv:0111157 [hep-th].
- [183] R. König, B. W. Reichardt, and G. Vidal, “Exact entanglement renormalization for string-net models”, *Physical Review B* **79**, 195123 (2009), arXiv:0806.4583.
- [184] G. Evenbly, “Implicitly disentangled renormalization”, (2017), arXiv:1707.05770.
- [185] H. A. Kramers and G. H. Wannier, “Statistics of the Two-Dimensional Ferromagnet. Part II”, *Physical Review* **60**, 263 (1941).